SISSA
Scuola
Internazionale
Superiore di
Studi Avanzati

Neuroscience Area

PhD course in Neurobiology

Spike-response properties of neocortical cells: an *in silico* study

Candidate:
Andrea Stacchetti

Advisor:
Michele Giugliano

Academic Year 2022/23

Declaration of Originality

I certify that this thesis, and the research to which it refers, are the product of my own work, and that any ideas or quotations from the work of other people, published or otherwise, are fully acknowledged in accordance with the standard referencing practices of the discipline.

Copyright Declaration

1 Acknowledgments

Here, I will say THANKS! to the big group of people that helped and supported me during this big journey of almost five years.
The first person I would like to thank is Georgi Hristov Spasov, without his presence and support, especially during the second half of my PhD, I couldn't reach the end. Sincerely thanks!
Then I thank my parents who supported me in whatever I did, even though at times we had quarrels. Yes, without a discussion there is no personal growth.
Then, I would like to thank my supervisor, Michele Giugliano, for the opportunity of a PhD! Thank you also for the stay abroad, in Antwerpen, and for encouraging me to attend the Master of HPC. I also recognize your help, during the very last months, when I was doubting I would have reached the end. I am aware we had not been always in good terms but it has been for a short time. Once again, thank you for your support, your kind words, and encouragements over these years. THANKS!
Then, I want to thanks my old friends from high school, especially Davide, Martina and Elisabetta! I am also grateful to my friends from Turin, particularly Claudia, Sara and Noemi: your support had no equal. Furthermore, thank you Arturo, despite we lost touch for most of my PhD. I am glad we got back in touch: without you, this adventure would have not even got started!
Then, I am grateful to would say thanks to friends from Antwerp, especially my neighbours Steven and Goisa, and my Brazilian friend Filipe, whom I have met during my stay in Belgium. Thinking of my former colleagues from the lab in Antwerp, I would like to thank Pat and Antonella: you have been really helpful and supportive.

I wish to thank as well Giulia, whom I have met during my stay at IIT: thank you a lot for your advice and supportive words! they helped me a lot! Then, in my current stay in Trst, there is a lot of people whom I would like remember and add to my "Thanks you-list". I am grateful to all our lab members, especially Matteo and some of our former members, such as Diletta, Alice and Valentina. A particular thought to Oyku, with whom I collaborated toe to toe. Working with you was an amazing experience, and even more as you are really a nice person!
Then, at SISSA, I would like to thank my mathematician friends Luca, Diego and Giacomo and all the SISSA's volleyball team, especially our captain Valentina and the two Francesco.
I won't forget of my office-mates, and especially Torre's lab members (Renza, Simone, Federica, Melania), the two Elenas, Irene and Laura.
Then, thanks to my colleagues from the Master of HPC: Iara and Keshvi, you helped me a lot during a very stressful period!
And, in the end, a very big thanks to Alex, Enzo and Paolo: it is also thanks to you if I survived throughout these years! I hope I gave credits to all the people who helped me during this very long and crazy journey... Anyway, thank you all!

2 Abstract

The input-output (I-O) properties of cortical excitatory neurons have been intensively studied in the past. Recently, theoretical work has demonstrated that the I-O properties in the high-frequency (HF) domain are not universally determined solely by neuronal properties, but also depend on the interplay between these neuronal properties and input statistics. This study aims to validate the aforementioned theoretical work using an extensive set of numerical simulations on state-of-the-art multi-compartmental cortical neuron models from the Blue Brain Project (BBP). The simulations are conducted using NEURON software with Python and Julia on high-performance computers (HPC). The results reveal variations in the strength of the hypothesized effect among different neurons, with some neuronal models not exhibiting this effect at all. Additionally, a notable anti-correlation has been identified between total dendritic length (TDL) and sensitivity to input statistics. This suggests that more extensive neurons are less sensitive, or even insensitive, to the theorized effect. Instead, they tend to exhibit the previously established universality behavior in the HF domain.

Contents

3 Introduction

3.1 Aims of this thesis

During the last decades the dynamical properties of the neurons have been extensively studied. Thanks to the linear response theory, it has been described the evolution over time of the neuron membrane potential and, more in general, the excitability of a single neuron and as well as of neuronal networks. The neuronal excitability has been described in the frequency domain describing the gain or magnitude and the phase shift between the output signal and the input one. It has been found out the gain of a neuron depends over the frequency of modulation of the input, it is affected by background noise at low and intermediate frequency, but is not at HF. Whatever inputs have injected in a neuron (current or conductance like) the neuron HF answer is not affected and depends only by the properties of the neuron itself. It has been formulate the idea of the universality of the HF response of a neurons, thus it depends only the neuronal properties themselves. On that regard a recent theoretical work by Richardson, (Richardson, 2018) has demonstrated that the HF response of a neuron depends by not only the neuronal properties themselves but as well as by the statistic of the input.

My PhD project has the goal to verify the validity of the Richardson's theory in real neurons, using more complex models than EIF, such as the state of the art multi-compartmental neuronal models of the excitatory neurons of the rat neocortex. Another goal is to understand if the effect theorised by Richardson could be seen in an experiment and give an idea of the amount of times and quantity of data (e.g. AP occurrence time) are needed to possibly see the aforementioned effect at HF. The expected outcomes from my project are:

- the possibility to perform *in vitro* experiment to reproduce the Richardson's theory in real neurons such as in acute slices

- The excitatory neurons of the neocortex show in the HF domain the Richardson's effect, confirming the interplay between the statistics of the input and the neuronal properties of the neurons themselves.

3.2 Background & Motivation: cellular electrophysiology in neuroscience

Throughout the entire human history, the inquire about nature of the world and of the human experience have been a constant focus. Over time, various methods have been employed to attempt to make progress in understand. From ancient mystic religions to philosophy and ultimately to the scientific method, the ways in which humans approached the pursuit of knowledge changed significantly. With respect to the nature of the brain and of the mind specifically, there was a notable shift away from "intuitions" and "analogies" towards a more philosophical approach grounded in "pure reason" and in subjective experience (Lamb, 1925).

After the appearance of Homo sapiens and 9000 years and the Agricultural Revolution (Harari, 2015), the center of emotions and thoughts was still considered the heart; once a person was dead its heart was weighted respected than a feather and as a function of this comparison the person afterlife destiny was settled (Papyrus of Ani, 0 BC). Many centuries later, the first person to track up the sensory nerves up to the brain was Alcmaeon of Croton around the 450 BC; he considered the brain the centre of the sens organs and thoughts (Tannery, 1887). From that time on, the prototype of the neuroscience has born. Around 100 years later, thanks to the Alcmaeon works Plato $\approx$ 360 BC believed that our head was the centre of thinking and reasoning, the *logos*. His idea come from the globe shape of the head, similar to Earth and since it is at the top of the body; closer to heaven and reflecting the image of God (Lamb, 1925).

In the same ages, Aristotle had its own idea: the soul was equally located through the body, was imperishable and self-existing and was the only sign of difference between plants and animals. In addition, he stated that the centre of sensation and emotion was the heart and, on the other hand, the brain was only an organ dedicated to cool down the heat produced by heart (Hicks, 1907).

When the Scientific revolution happened around 500 years ago, it has been recognise the ignorance of the human kind and a new path of exploration of the unknown was embarked (Harari, 2015). Around the 1543, Vesalius was the first to distinguish the grey and the white matter while dissecting human corpses (Vesalius and van Calcar, 1543). Around the 18th century, the father of the microscope, van Leeuwenhoek, observed a " fine vessels" within a nerve (van Leeuwenhoek, 1719). After 150 years, through carmine stain "vessels", "globules" and "protoplasmic processes" have seen as a unique cellular unit, the nerve; that later, thanks to the studies of Cajal, they will be named as neuron by Waldeyer (Waldeyer, 1891).

As before mentioned, the father of neurons is Santiago Ramón y Cajal that from the end of the 19th has contributed with discoveries and theories to forge the modern Neuroscience and Neuroanatomy (Ramon y Cajal, 1909) . Using and improving the Golgi silver stain, he was able to focus his attention on the central nervous system cells. He proved that neurons aren't continuous, but rather are contiguous; since they have a gap between them, the synapses. His work furnished evidences to prove the neuron doctrine by H. Waldeyer-Hartz later.

In 1952, Hodgkin and Huxley introduce their model that is a milestone of the neuroscience: the Hodgkin-Huxley model. They recorded the membrane potentials of a squid axon, to quantify for the first time the active mechanism together to the not passive properties of the cell membrane. They were able to quantify the flowing current and then, they fitted the experimental results with a mathematical model composed by a set of differential equations. The model well described and quantified the time evolution of the neuronal membrane potential (Hodgkin and Huxley, 1952).

From that time until now, the human knowledge has advanced and diversified, allowing us nowadays to approach complex problems such as the complexity of the brain or more specific how a network of neurons or a single neuron work.

On regard of that, a lot of questions are still open in neuroscience, i.e., how our

brain can generate complex mechanisms, such as perception, memory, language, cognition and taking decision from environmental stimuli; from a computational point of view, the brain receives inputs, elaborates them and responds with outputs. To investigate and dig into this exciting research field that still has big open questions, the theoretical neuroscience comes out with experimental data interpretation in order to make simpler the observations and build mathematical models that represent ideas (Gerstner et al., 2012). An example of model to study the nervous system is the black-box approach, that allows to understand, model, infer, describe how the brain generates outputs from input stimuli. One of the main brain area in charge of this input-output relationship is the cerebral cortex. However, it is still not completely understood how neuron populations and networks encode the incoming information and how they translate it. Many questions find room in these partial knowledge; how populations of interacting neurons make possible several complex tasks? How do they represent the information at the neuronal level with their structure and physiological properties?

Even if,nowadays, quite a lot is known about the the input-output properties of neurons, we are still far away to know,in details, how information is represented by neuronal activity. To make deeper the comprehension on how the neuronal networks perform the more complex tasks, it is necessary to investigate the microscopic scale and to understand the intrinsic neuronal properties and how neurons communicate between them as a network. Hence, to understand the brain complexity is helpful to investigate the physiology of the most "atomic" neuronal network blocks: neurons and synapses.

To accomplish this goal is useful to recall that the brain is composed by billion of neurons; for example considering a single cortical column of neocortex, there are around 10^5 neurons connect to each other with a number of synaptic connections as 10^9 (Dasgupta and Greenwald, 2001).

A neuron is an electrically excitable cell, it mostly communicates through synapses with other neurons releasing into the synaptic gap chemicals: the neurotransmitters. Neurons can be classified in several ways through their morphology, electrical "phenotype", on their functionality, as function of the emitted synaptic potential if positive or negative and etc. Neurons,in general consists in three main parts: soma, axon and dendrites. The soma is the neuron core, it contains the cell organelles and the biochemical machinery of the neuron. The dendrites are branched extensions that start from the soma and propagate electrical stimuli received from other cells to the neuron. The axon is a long projection of a neuron, it conducts the electrical impulses, the action potentials, from the soma to the external.

The synapses are structures that allow the transmission of the electrochemical signals between neurons; they are the main structures through neurons communicate. A synapse is composed by three main parts: a presynaptic terminal, the synaptic gap and a postsynaptic membrane. Synapses can be classified as electrical and chemical synapses.

So far, neurons and synapses have been introduced and they are the fundamental bricks of neuronal networks. However how neurons communicate? They do through action potentials, APs!

The electrochemical basis of neuronal communication is the action potential (AP) that has similar features whatever neuron has generated it, indeed the AP is stereotyped, hence whether the neuron generated it has always the same features.

An action potential is a sudden rise of the membrane potential values, afterwards it overcame a certain threshold value; then, the membrane potential comes back to a more negative values than the starting point. After a couple of milliseconds the membrane potential is at the starting point.

3.3 Conventional characterisation of the "electrical phenotype" cells

As it has briefly described before the AP is the key point of the communication between neurons; however to better understand the different phases of an action potential; before it is essential to have a deeper understand of the membrane potential basis.

The processing of the information depends not only by the synaptic circuitry, but also on the neurons electrophysiological properties as well as are affected and tuned by neuroactive substances. Considering, for example, two neurons with the same morphological features, they could respond in different ways due to intrinsic cellular properties (McCormick, 2004). Studying the electrophysiological and pharmacological properties of a single neuron helps to understand the functionality and the synaptic organisation. The neuron behaviour is determined by the heterogeneous ionic currents distribution and by the neurotransmitter action that can modulate the amplitude and the properties of the ionic currents (McCormick, 2004).

3.3.1 The electrical activity of a neuron: the basis

One way to study the activity of a neuron of a network of them is to measure their electrical activity. Neurons communicate between them through emission of single or a train of action potentials (APs). An action potential is a temporary variation of the membrane potential toward more positive values respect than a resting condition. The mammals neurons in resting condition have as a values of membrane potential -65 mV (also called resting potentials, V_{rest}), meaning that the inside of a cell is more negative than outside. This negative membrane potential is due the different concentration of the ions ($Na^+, K^+, Cl^-, Mg^{2+}, Ca^{2+}$) inside and outside of the cell membrane, where the main difference of concentration from the side of the membrane is a bigger extracellular concentration of Na^+ and conversely a bigger

K^+ intracellular concentration.

The cell membrane is a lipid bilayer, it is impermeable to ions and for that reason an ions concentration difference is set between the inside and outside of the membrane. As a consequence, a driving force is established and the lipid bilayer can be electrically modelled as an insulator. The only way that ions can cross the two sides of the membrane is through the ion channels, that are proteins into the lipid bilayer, that acts like a pores. One feature of the ion channels is the selective permeability to a certain ionic species, (i.e.sodium channels are called after the ion are more permeable of); for some of them the permeability depends on their gating properties. This means that ions channels can be open or close state. This "class" of channels are called active channels and only in the open state ions can permeate through. In addition, their gating properties and as consequence their permeability are a function of several factors (i.e. membrane potentials for voltage-gated channels and ligands concentration for chemically-gated channels). For the other channels, the passive ones, their permeability doesn't change in response to membrane potential variations. Between the two side of the membrane there is a continuous exchange

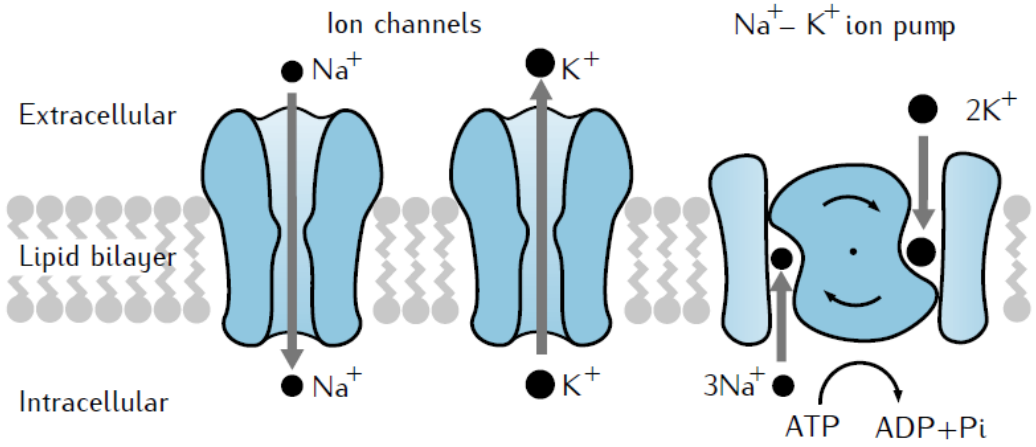

,

Figure 1: Example of active ion channels into a cells membrane, taken and modified from (Sterratt et al., 2011)

of ions also at the equilibrium, ions diffuse from one side to another, following

their gradient, however there are some ionic pumps that keeps constant the potential difference, such as the sodium–potassium exchanger that pushes K^+ into the cell and the Na^+ outside; for each of two K^+ ions pushed inside three Na^+ are pumped out. All this work against the equilibrium gradient requires energy. To describe the flux of a particle that flows following his gradient in a free environment; so basically its diffusion, the Fick's law comes to help (Fick, 1855) giving us the molar flux J_A, for a certain particle A and a certain a diffusion coefficient D_A, the derivative $\frac{dA}{dx}$ represents the difference in concentration of the particle A along the dimension x. It is necessary to consider the particle follow the concentration gradient, hence, with a positive value of the derivative,the diffusion goes towards the less concentrated region from where the particle is more concentrated. The Fick's law is:

$$J_{diff,A} = -D_A \frac{dA}{dx}. \tag{1}$$

However, ions are particles with electrical charge and the difference of potential affects their flux as well, they are accelerated by the electric field with a drift speed:

$$J_{drift,A} = -\frac{D_A \cdot F \cdot z_A \cdot [A]}{RT} \frac{dV}{dx} \tag{2}$$

where T is temperature, R and F are, respectively the gas and Faraday constants, z_A is the ions valency and V is the electrical potential. To consider both phenomena, the total flux is the sum of both contribution, $J_A = J_{diff,A} + J_{drift,A}$:

$$J_{,A} = -D_A \cdot (\frac{dA}{dx} + \frac{F \cdot z_A \cdot [A]}{RT} \frac{dV}{dx}) \tag{3}$$

That is called the Nernst-Plank equation.

Nevertheless, in neuroscience the ionic flux is usually described by the current I,

where:

$$I = z_A \cdot F \cdot J_A \tag{4}$$

the current is relate to the difference of potential to the Ohm's law, a milestone of the physics of electric phenomena:

$$V = I \cdot R \tag{5}$$

where R is the resistance, sometimes the law is expressed $I = GV$, where G is the conductance and is the reciprocal of the R. Conductors that behave as described as the Ohm's law are called ohmic.

Considering the difference of V between the sides of the membrane, this value is also affected by the different membrane permeability of the lasted to the different ion species; the membrane is very permeable to K^+,due to the passive or leak channels. Nonetheless, the membrane is less, but still permeable to Na^+ and Cl^-, through other and less numerous passive channels. A considerable amount of K^+ ions from inside to outside the membrane following the gradient concentration causes a rising of an electrical gradient due the unbalance of positive and negative sides of the membrane; when the two fluxes become equals in strength, the K^+ equilibrium potential is reached. It is possible to calculate the equilibrium potential of an ion through the Nerst's equation:

$$E_A = \frac{RT}{F \cdot z_A} \cdot \ln\left(\frac{[A]_{out}}{[A]_{in}}\right) \tag{6}$$

The different ion concentrations between outside and inside of the membrane, due to the membrane insulator behaviour has risen a query about the capacitance value in the past. From the work of Gentet and colleagues (Gentet et al., 2000), it has been found that the general capacitance value for neurons is $0,9\frac{\mu C}{cm^2}$ and usually accepted

$\approx 1,0\frac{\mu C}{cm^2}$.

Summarising all the notions stated so far, such the Nernst's equation,the Ohm's law, the single ions equilibrium potential, the diffusion and drift flux can be introduced the Goldman-Hodgkin-Katz equation, that predicts the ions current I_A, when the potential has a certain value V. Considering a membrane permeable to Na^+, K^+, Cl^-, it can be calculated the reversal potential (so the ion potential value in which the membrane current reverse direction) for all these ions. In addition, some assumption are necessary:

- The current flux is zero when the voltage is equal to the equilibrium potential
- The current changes direction at the equilibrium potential when the potential V is less than the equilibrium potential; for this reason the equilibrium is called reversal potential
- The single ion doesn't follow Ohm's law since there is not proportionality between current and potential
- the I-V characteristic of K^+ and Ca^{2+} promotes respectively, outward and inward rectification.

Now, it is possible calculate the reversal potential assuming that only Cl, K , and Na ions are present:

$$E_m = \frac{RT}{F} \ln \left(\frac{P_K[K^+]_{out} + P_{Na}[Na^+]_{out} + P_{Cl}[Cl^-]_{out}}{P_K[K^+]_{in} + P_{Na}[Na^+]_{in} + P_{Cl}[Cl^-]_{in}} \right) \tag{7}$$

with respectively P_K, P_{Na}, P_{Cl}, the membrane permeability of these ions. T

3.3.2 The action potential

The membrane potential in a neuron is not always stable at resting potential value,its brief changes can bring to rapid signalling in neurons. The most characteristic of them is the action potential or spike, which can be fire once or in sequence, as train of action potential or spike trains. Hodgkin and Huxley in their work on a squid axon, for the first time using the voltage clamp technique recorded action potentials (Hodgkin and Huxley, 1952). This technique allowed them to measure directly the transmembrane current, which is responsible for the electrical neuron behaviour. In addition, the ionic composition of the membrane had been control by Hodgkin and Huxley; showing that the very fast action potential upswing is due to an increase of the transient sodium current $I_{Na,t}$. The activation of the $I_{Na,t}$ appears when the depolarisation of the membrane reaches a value around —50 to —55 mV; in these range of values the activation of the $I_{Na,t}$ is strong enough to overcome its same inactivation. The depolarisation of the membrane potential rapidly activated the $I_{Na,t}$,causing a increase of the Na^+ ions which are entering into the cell, pushing the membrane potential towards more positive values. The sudden depolarisation is spread to the membrane close regions, via electronic current flow; causing the action potential propagation along the axon. The repolarisation of the membrane potential then occurs due to two processes: the inactivation of the $I_{Na,t}$ and the activation of the I_{K^+}. The I_{K^+} is slower than the I_{Na^+} and allows the K^+ ions to leave in the cell and is activated by the depolarisation of the membrane potential. At a certain time,while the K^+ are leaving, they overcame the Na^+ entering in the cell; causing the end of the action potential the repolarisation of the cell. From the Hodgkin and Huxley work, it has been shown that the $I_{Na,t}$ current is preponderant in AP generation (Hodgkin and Huxley, 1952). In the image 2 an AP of the squid giant axon is shown; the currents that contribute to the AP shape before mentioned are shown in the same image. However, also other current play a role in the AP generation like Ca^{2+}

voltage-gated current in somatic and dendritic regions. On the contrary of the squid axon, in dendrites and soma of mammalians the AP repolarisation is due to a variety of I_K repolarisation of action potentials currents.

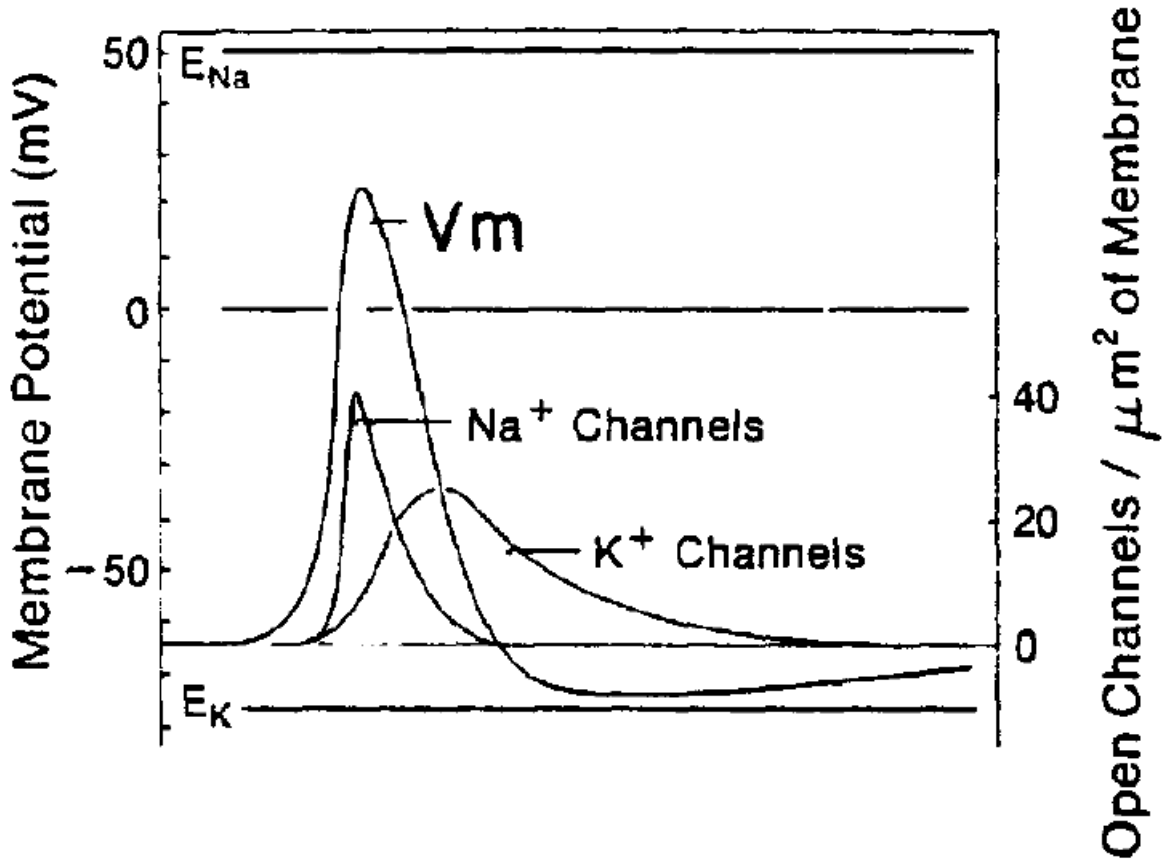

Figure 2: AP in a giant squid axon, The membrane potential scale together the equilibrium potentials are shown to the left.The k^+ and Na^+ conductances changes are scaled on the right per membrane μm^2 Changes in Na+ and K+ ionic conductances are scaled on the right in terms of calculated open channels per square micrometer of membrane. Taken and modified by (McCormick, 2004)

3.3.3 Types of ionic currents

The membrane potential of a neuron is not constant at the resting potential, through the cell membrane there is a constant flux of ions; so several ionic current are activated and deactivated. These currents are characterised by the ions they conduct as well as by membrane potential and neurotransmitter sensitivity and time course

(McCormick, 2004) (McCormick and Huguenard, 1992). The ionic currents once discovered were classified in two type: the ones sensitive to membrane potential changes and the one sensitive to neurotransmitter and second messengers; some of them have been shown to belong to both classes. Many currents are activated by membrane potential depolarisation, usually, they don't remain activated once they are, even if in presence of a constant depolarisation. Hence, ionic currents have states of activation and inactivation as well. If a small displacement from the resting membrane potential activates the current, that current is called low threshold, on the contrary, if a non-trivial positive displacement is needed the current is called high threshold current. Furthermore, if the membrane potential is kept constant and the current has only a transient response, it takes the names of transient or current; on the other hand if the current persists, it is known as persistent or long lasting current. the ionic currents are essential to determine the neuronal firing rate and, for this reason, have been intensively investigated. Some example of them are discussed below.

The transient and persistent sodium current $I_{Na^+,t}$ $I_{Na^+,p}$, they differ from their properties. They are both activated by depolarisation, however the transient sodium current, as mentioned before, is one of the key current to generate action potentials. On the other hand, the persistent one, brings the membrane potential from the resting value to a close value of the action potential firing threshold. Then, adding Na^+ ions enhances the neuron response to the excitatory inputs. The $I_{Na^+,p}$ determines the neuronal baseline firing rate and in some neurons appears to keep the intrinsic pacemaker activity also in absence of synaptic inputs (McCormick, 2004) . An example, could be cortical pyramidal neurons 4 (McCormick and Prince, 1987).
The high-threshold calcium currents contributes to generate APs in mammalian neurons; adding part of the depolarisation of the APs and, more significantly, allowing the Ca^{2+} to enter into the cell causing an activation of the Ca^{2+}-activated K^+ current

(Sah and Faber, 2002). On the other hand, the low-threshold calcium currents play a role on generating in rhythmic bursts of action potentials. A very clear example of this APs pattern is in the mammalian brain in thalamic relay neurons, which receive from the visual system a direct input from the retina and then, transmit the information to the visual cortex. An example of this phenomena, it is the generation of spontaneous synchronised activity by thalamic relay cells bursting in sleeping animals (McCormick and Bal, 1997).

On regard of the K^+ currents, they are responsible of the repolarisation of the membrane potential; therefore they have a role on determining the probability of generation of an action potential for a given time. An example of K^+ currents which significantly affect the neuronal firing rate are the Ca^{2+}-activated K^+ currents; which two of them have been identified I_C and I_{AHP} (Sah and Faber, 2002). In cortical and hippocampal pyramidal neurons, they contributes on decreasing the firing rate; a phenomena called spike frequency adaptation. The I_C contributes only for short interspike intervals due to short time course. On the other hands, the I_{AHP} contributes more on the timescale since it has a slower activation 4 (McCormick, 2004). Other example of K^+ that affect the neuronal firing rate are the muscarinic current I_M and K^+ transient current, known as I_A. The first one is activated by depolarisation ($\approx -60mV$) and with more positive potential is rapidly inactivated; it responses to a sudden depolarisation of the membrane potential and its jobs is to delay the onset of the first AP. It also play a role on to repolarise the membrane potential, when a constant depolarisation has been kept: it can slow down the firing frequency of a neuron; an example of its action is shown in the figure 3. The I_M is activated $\approx -65mV$, when the membrane potential is depolarised: it has been found in pyramidal neuron of hippocampus and cortex. Since it low amplitude and slow kinetics, it doesn't affect a single AP, but contributes to frequency adaptation, when a constant depolarisation is kept. The figure 3 shows the effects of the currents

previously described added on top of the Hodgkin-Huxley model. The figure 4 shows the different spiking shapes in different brain regions;all they are due to the contribute of the several types of currents. Some examples are the panel C where the current $I_{Na^+,p}$ generates some potential plateau (arrowheads) in the Purkinje cells. Another example is the strong presence of the I_{AHP} after every action potentials in medial Habenula, generating the intrinsic "peacemaker" discharge in panel F (arrows).

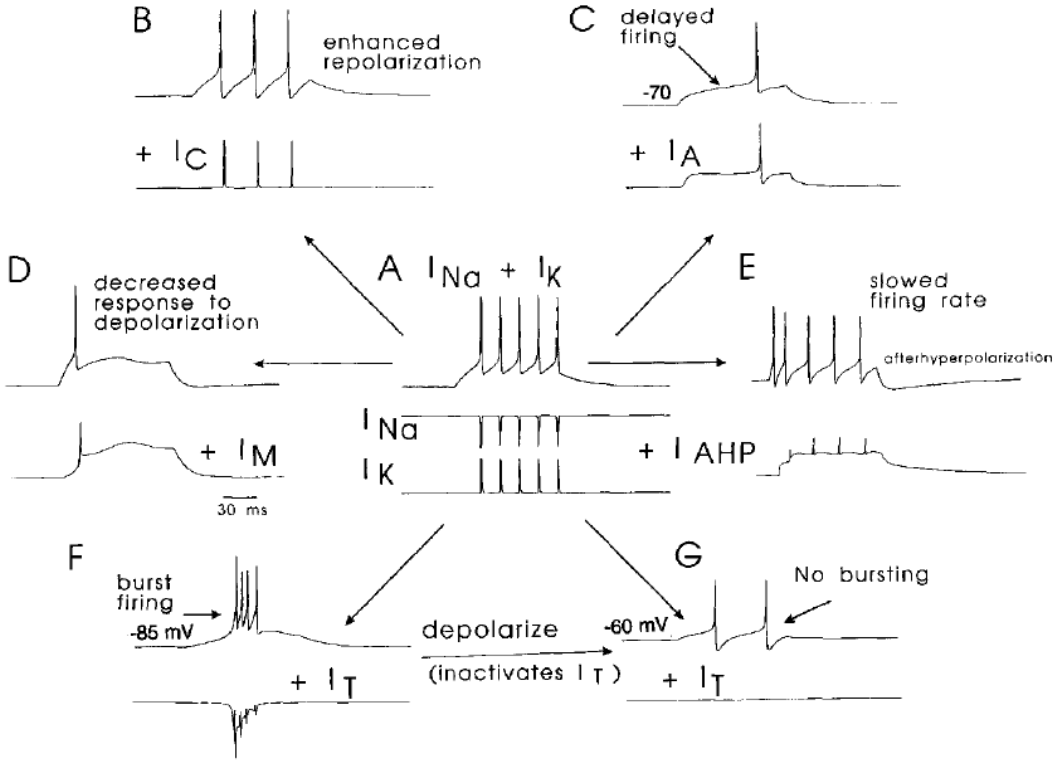

Figure 3: A combination of a classic Hodgkin-Huxley model firing pattern shown in panel A, with several types of voltage-gated currents and the impulse firing patterns in response of a steady depolarising current injection. B: I_C and high-threshold $Ca^{2+}I_L$ makes easier the repolarisation of each action potential. C: the addition of the I_A, a transient K^+ current activated by depolarisation. The result is in delaying the onset of an AP. D: The addition of the K^+ persistent current I_M brings in a substantial decrease of the neuronal excitability. E: The addition of the slow K^+ current Ca^{2+} activated generates spike frequency adaptation and a slow hyperpolarisation after a train of APs. F: Adding the slow threshold and transient Ca^{2+} current causes the generation of an action potential burst at ^-85mV. G: Considering the panel F and adding the inactivation of I_T current and a depolarisation at $-60mV$ generates a train of two action potentials. These traces were originally *in silico* results from Huguenard and McCormick, (Huguenard and McCormick, 1994).Taken by (McCormick, 2004)

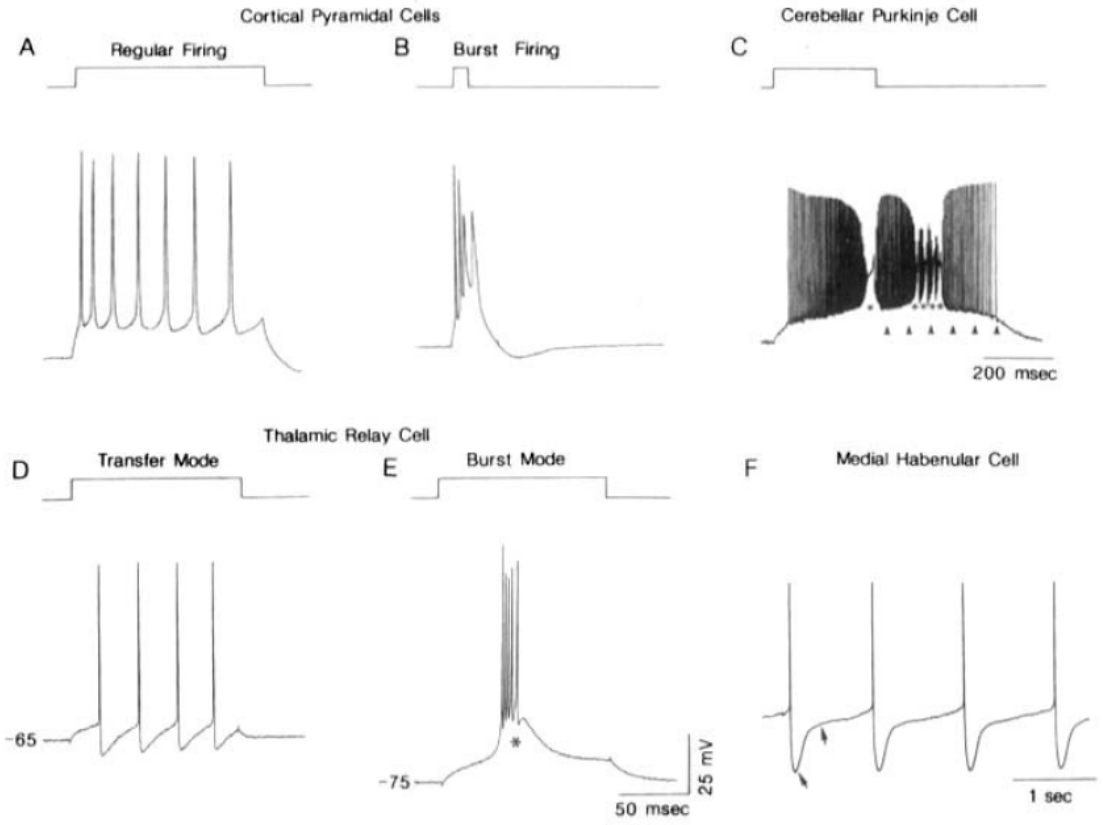

Figure 4: From different mammalian brain regions, the electrophysiological behavior of different neurons. A: Regular firing cortical pyramidal neuron. The injected depolarising current pulse (top trace) generates an AP train that occur undergoes to spike frequency adaptation. B: On the other hand in other cortical pyramidal neurons, an injection of depolarizing current pulses turns into a neuronal output "burst", so a generation of an APs cluster on top of a slow potential. C: Response of cerebellar Purkinje cell in response to an intracellular depolarising current pulse injection. At the first, in the soma, a fast and high-frequency discharge of Na^+-dependent action potentials. This phenomena is modulated by the $Ca2+$ dendritic spikes occurrence (asterisks). The discharge outlasts the duration of the intracellular injection(at the top). This is due to the presence of a plateau potential, generate by the $I_{Na^+,p}$ and calcium currents (arrowheads). D: Thalamic interneuron depolarisation generates an AP train of four action potentials when the membrane potential is slightly more positive than —65 mV. A burst of action potentials it is generated when the cell is more negative or at —75 mV E: The asterisk indicates a burst discharge due to low-threshold Ca^{2+} spike. F: A neuron in the medial Habenula, it generates an intrinsic "pacemaker" discharge. From intracellular recording, it has been revealed a large after hyperpolarisation following each AP. They affect the rate at which the neuron fires (arrows).

3.3.4 Conventional characterisation of the "electrical phenotype" cells

The physiological properties of the neurons, like the currents properties and their effects on the neuronal output response, have been often studied using the black box approach, injecting an input and recording the output of the neuron. It has led to the study of the unique output behaviour of each different neuronal type: their electrophysiological fingerprint. At single neuronal level, the study of the incoming synaptic inputs and their transformation into APs trains has been extensively explored injecting into neuronal soma depolarising DC square steps, meanwhile recording the membrane potential. Injecting into the neuronal soma a current step lead to a certain current values that overcome a threshold and the neurons start to fire APs. Then, it is possible to quantify the mean firing rate as the ratio of the number of the APs fired on the duration of the stimulus. Repeating this procedure for different current step values ends up to build the firing rate-current curve, that is the electrical "fingerprint" of a neuron.

In literature during the past decades, many experiments have been performed to study the input-output properties of the neurons. The transfer function of the neurons has been investigated in different animal species, such as rats, cats and guinea pigs as well as in motoneurons (Granit et al., 1963) (Granit et al., 1966), cortical neurons (McCormick et al., 1985) and visual cortical neurons *in vivo* (Nowak et al., 2003).

In the work of McCormick and colleagues (McCormick et al., 1985) have been used slices of sensorimotor and anterior cingulate cortex of guinea pig to study the electrophysiological properties of neurons throughout intracellular recordings. They injected current square suprathreshold steps into the neuronal soma to investigate the input output properties of the neuron, they found a linear relationship between injected current step and mean firing rate figure 5. Their study was a pioneer work in the neocortex that reproduced the earlier one performed on rat and cat motoneurons by Granit and colleagues.

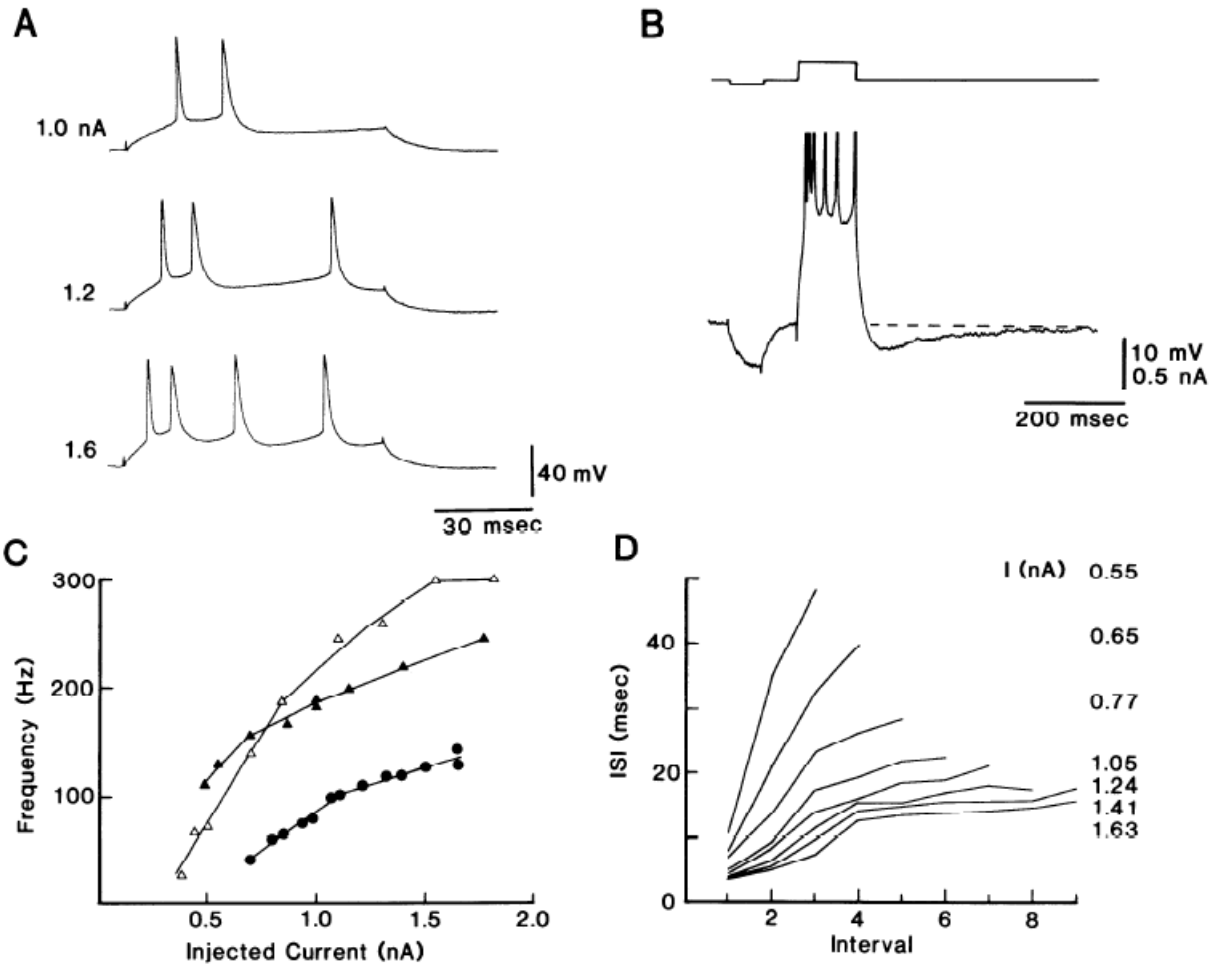

Figure 5: Regular spiking response of a depolarising intracellular current injection (McCormick et al., 1985)

In the works such of (McCormick et al., 1985) and (Nowak et al., 2003) firing rate-current curve has been essential to classify neurons as function of exhibition or not of adaptation as well as on the slope of the firing rate-curve slope. The mean firing rate-current slope is considerably higher in the Fast-Spiking (FS) cells, than the other neurons like Regular Spiking (RS), Intrinsically Bursting (IB), and chattering neurons figure 6.

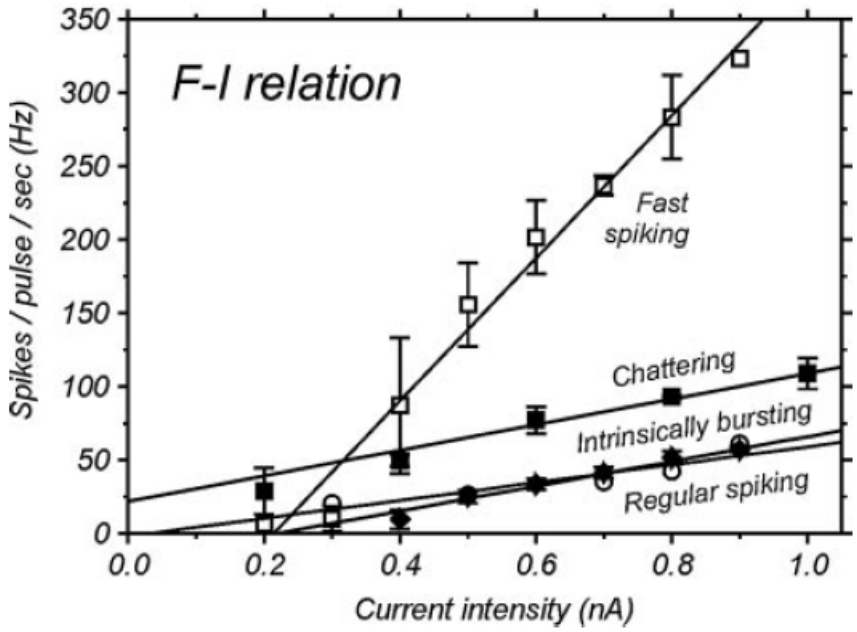

Figure 6: Different examples of Frequency-Current (F-I) curves. The slope of the firing rate-current curve changes significantly as function of the cell electrical "phenotype". Every point is the mean firing rate for a given current value of between 2- 10 repetitions. The bars represent standard error (Nowak et al., 2003)

3.4 Dynamical Systems, System identification, and input-output characterisation

In physics, a dynamical system is a an object or an ensemble of objects which have an evolution over time of quantities that describe its state. The time evolution is described by one or a system of differential equations. The resolution of a differential equation can be performed analytically, from pen and paper, when the resolution is simple to a numerical resolution through computer if supercomputer when is too difficult. On regard of this last mention, the numerical resolution can span from a simple system of differential equations solvable with a short simulations up to a numerical simulations that requires an huge number of resources in a supercomputer. In mathematics, a dynamical system is characterised by a set of time B, a space state A or phase state. If A is continuous, and C is a rule that describes the evolution as C:A$\times$B$\rightarrow$A. For any element a of A, which are called initial state, whereas any element of B are called evolution parameters. The rule C is called evolution function of the dynamics system.

The birth of dynamical systems has roots in Newtonian mechanics. The study of the dynamical system is widespread between a lot of branches of science, from mathematics, physics, biology, neuroscience etc. The evolution rule gives a prediction to the next state or states for a short amount time (in future). The evolution rule is deterministic if gives as a consequence of the only an unique consequent; otherwise if there are more than one possibility of consequent the rule is stochastic. To solve the system time evolution and to determine at all future times all the possible states, it means to integrate the differential equation, iterating in a discrete way (small time steps). If the system is solvable, given a certain initial point, it is possible to determine all possible future states, the ensemble of them is called trajectory or orbit. In the study of system evolution a type of a trajectory could be more important than another one. For example, some of them can be periodic or can move between

several different states of the system. The classification of the trajectories types has lead to a qualitative study of the dynamical system, such as, some properties that don't change is presence of coordinate change. An example of dynamical system whose a type of trajectory is solvable are the linear systems.

3.4.1 Nature and dynamical systems

The dynamical system are the focus of the dynamical system theory, which has a very broad range of applications in several fields; such as, physics, mathematics, engineering, oncology (Gevertz et al., 2015), neuroscience (Brunel and Wang, 2003)(Fourcaud-Trocmé et al., 2003) (Qi and Gong, 2022) etc... In addition, dynamical system are also a crucial matter of chaos theory and bifurcation theory.

An example of dynamical system in neuroscience is the whole brain or region of it or its neuronal networks that compose it or, even, a single neuron. To dive in more a level of a single neuron, consider sensory inputs coming from the external environment to neurons in a more physiological manner respect than a simple structured constant step of current; they have definitely a more complex time and statistical structure. In nature there are example of a more complex inputs like sinusoidal ones that are usually analysed in the auditory path frequency-wise (Cheng et al., 2021) (Gerstner et al., 1996). An other example in the animal world, it is the male of *Sternopygus macrurus* in a presence of a female emits a sinusoidal discharge to attract her in his hideout(Knudsen, 1974).

Another example of sinusoidal or, more in general dynamical system, is the fireflies; the winged beetles male of the order Coleoptera use their bio-luminescence to attract mates(Ravignani and de Reus, 2019).

The relevance of the sinusoidal waves is not only because is a very well widespread communication paradigm among the animal kingdom, but also because is widely

used as a established standard to define the transfer function and the resonance analysis of a dynamical system. From these information is possible to predict the system response of any inputs, given the hypothesis that the system is linear.
In order to study the dynamical properties of a cortical neuron, such as the transfer function, neurons have been stimulated by injection of several sinusoidal inputs at different frequency, (current or conductance based) (Tchumatchenko et al., 2011)(Linaro et al., 2017) (Köndgen et al., 2008) (Boucsein et al., 2009); then, their output has been collect and the properties of the transfer function analysed to infer their characteristics in frequency.

3.4.2 Differential Equations

From the mathematical point of view a differential equation is an equation which relates a function of more to their derivatives. They usually define relation between some physical quantities and their change rates. In not mathematical pure sciences, the important part of the differential equations are the solutions and their properties. Very often, an analytical solution for the differential equation is not available;then, numerical approximation is used through simple computers or high performance ones. From the point of view of dynamical systems the qualitative resolution of a differential equation is more important,while numerical methods are more focused to find solutions with certain accuracy degree. The differential equation are mostly divided in 2 "families" the ordinary and the partial ones. The "ordinary" term means that the derivation could be on more than one independent variable in contrast with the "partial" derivatives. The ordinary differential equations can be considered a subclass of partial differential equations; since they correspond to functions of a single variable.
Partial differential equations (PDE) are equations which compute partial derivatives of a function with more than one variable and the same function. It is quite difficult to

write an explicit resolution formulas for PDE, hence is common in science that PDE are widely study to find methods which provide the best numerical approximations with a certain degree of accuracy using computers.

3.4.3 Linear Response Theory

Linear systems are mathematical models that from an input x(t) time dependent maps an output y(t) using the black box approach.
They are part of the family of dynamical systems, however, they have features much simpler than the non-linear ones. A dynamical system is a linear system if satisfies the superposition principle, therefore, every linear combination of the system inputs is a linear combination of the zero state outputs (which means an output with initial condition set to zero) (Phillips and Riskin, 2008) (Bessai, 2005).

In addition, a dynamical system that satisfies the homogeneity and the additive properties are consider as well linear (Sundararajan, 2008). Considering two inputs of continuous-time system $x_1(t)$ and $x_2(t)$,their zero output-states such as $y_1(t) = H(x_1(t))$ and $y_2(t) = H(x_2(t))$; the linear system must satisfies the follow equation:

$$H[\alpha * x_1(t) + \beta * x_2(t)] = \alpha * y_1(t) + \beta * y_2(t)$$

with α and β two scalars. In this fashion, complex inputs can be modeled as a sum of simpler inputs, making easier to represent the solution for the linear system. The above mentioned concept is at the basis of the time-invariant system input function description as unit of impulses or frequency components; which for the continuous case are well adapted to be analysed by the Laplace transform.

3.4.4 Pulse Response and Fourier Domain Transfer Function

Whenever an external change acts over a dynamics system, the system reacts. The external change is the input of the system and the reaction of the system its own response, the output. Considering as input a brief one, like an impulse, the system response will be the impulse response function over the time (IRF). The input pulse contains all the frequency spectrum,for example the Dirac delta $\delta(t)$, thus, the impulse response will define the response of a linear time-invariant system (LTI) to that input for all frequencies. A signal continuous over time can be modeled with a train of Dirac delta $\delta(t)$, that is a very suitable idealisation of a very short pulse in time with a very high peak in amplitude and in the Fourier analysis contains all the frequencies contributions making the Dirac delta a very useful test tool. Given a LTI system continuous in time, the output signal y(t) is defined by the convolution integral between the input x(t) and h(t) that is the impulse response of the system to an impulse $x(\tau) = \delta(\tau)x(t)$:

$$y(t) = (x * h)(t) = \int_{-\infty}^{\infty} h(t)x(t-\tau)\,d\tau$$

The transfer function is the Laplace transform of the impulse response and can be used to characterised the LTI systems in the frequency domain. The convolution integral in the time domain, in the frequency domain is equivalent to a multiplication between the input $X(\omega)$ and the transfer function $H(\omega)$.

$$Y(\omega) = X(\omega)H(\omega)$$

3.4.5 Fourier Decomposition of Input Signal

Considering an input continuous over time, x(t), it can be always decomposed into Fourier frequencies, as a sum of trigonometric functions. The decomposition is

performed by the Fourier Transform (FT), which maps the time domain into the frequency one. Taking into account a single output-input differentiable dynamical system of degree n with the input being differentiated m times, can be expressed as following:

$$\sum_{k=0}^{n} a_k \frac{d^k y(t)}{dt^k} = \sum_{k=0}^{m} b_k \frac{d^k H(t)}{dt^k} \tag{8}$$

where $y(t)$ is the output and $H(t)$ is the input. In the case under consideration, $H(t)$ represents the injected current to which has been applied a RELU function as showed in (Köndgen et al., 2008), (Linaro et al., 2017). Using the linearity and the property of the FT the linear dynamical system can be written as an algebraic equation of the first order for y and n degree for ω in the left hand-side and an a first order equation in $H(t)$ on the right hand-side where $n < m$ to ensure the transfer function causality.

$$\sum_{k=0}^{n} a_k (i\omega)^k \hat{y}(\omega) = \sum_{k=0}^{m} b_k (i\omega)^k \hat{H}(\omega) \tag{9}$$

The equation 9 is equivalent to the algebraic relation $\hat{y}(\omega) = \hat{X}(\omega)\hat{H}(\omega)$ in which the $\hat{y}(\omega)$ and $\hat{H}(\omega)$ are the FT of $y(t)$ and $H(t)$ respectively, and $\hat{X}(\omega)$ is the transfer function defined as

$$\hat{X}(\omega) = A \frac{(i\cdot\omega + z_1)\cdot(i\cdot\omega + z_2)\cdot\ldots(i\cdot\omega + z_m)}{(i\cdot\omega + \pi_1)\cdot(i\cdot\omega + \pi_2)\cdot\ldots(i\cdot\omega + \pi_n)} \frac{\pi_1\cdot\pi_2\cdot\ldots\pi_n}{z_1\cdot z_2\cdot\ldots z_m} \tag{10}$$

where $i = \sqrt{-1}$ and A is a real number representing the low-frequency gain and $\{\pi_i\}_{i=0}^{n}$ and $\{z_i\}_{i=0}^{m}$ are the roots of the polynomial with coefficients $\{a_i\}_{i=0}^{n}$ and $\{b_i\}_{i=0}^{m}$ called poles and zeroes of the transfer function, i.e. (Köndgen et al., 2008) and (Linaro et al., 2017). For a band-pass filter, these roots act as upper and lower cut-off frequencies. Considering the I-O properties, i.e. the magnitude (gain) and the phase shift, are fully specified by A and the number and values of the unique zeroes and poles,i.e. z_i and π_i. Having a look more at the high frequency (HF) domain,

where $f \to +\infty$, the phase and the gain of $\hat{X}(\omega)$ have a power-law as $\omega^{-\alpha}$, where $\alpha = n - m$ and $\alpha \in \mathbb{Z}$, in which n is the number of poles and m the number of zeros (Linaro et al., 2017) (Köndgen et al., 2008). From experimental and theoretical works, i.e. (Fourcaud-Trocmé et al., 2003), (Köndgen et al., 2008) (Linaro et al., 2017), it has been found using the best fit, a single zero at very low frequencies and two or three poles; the largest poles is a low pass filter cut-off frequency measure (Linaro et al., 2017).

.

3.5 Recent applications of System theory in Cellular Electrophysiology

In this brief section, there are reported some example of recent applications of the system theory in cellular electrophysiology. The main focus are the papers of Fuhrmann et al., 2002; Köndgen et al., 2008 and Linaro et al., 2018. The first paper analysed the importance of the spike frequency adaptation (SFA) in neocortical pyramidal neurons with patch-clamp experiments technique and phenomenological model, i.e. a leaky integrated-and-fire-model by (Tuckwell, 1988) with an addition hyperpolarising potassium current, such as the adapting current by (Treves, 1993). The meaning of the work is studying the effect of the SFA onto the modulation of the I-O properties in a neocortical pyramidal neuron embedded in a noisy input. It has been found out through simulations that the preferred frequency of a single neurons guides the large network oscillations rhythms. In this study, it is very interesting the neuronal response to an oscillatory input; which has the following form:

$$I(t) = I_0 + I_1 \sin(2\pi * ft) \tag{11}$$

On top the sinusoidal form has been added white noise. It is important to notice that the input and the output has the same the same frequency of oscillation, most of the time the difference between the two signals is the phase. The phase shift is affected by the neuronal parameters of the simulations, such as the input resistance and adaptation current parameters and by the frequency of the injection current (Fuhrmann et al., 2002). Fuhrmann and colleagues found out that low frequency of oscillation causes a negative phase shift of the mean firing rate response, hence the output advances the input (negative shift) ; on the contrary higher frequency (between 30-40 cycles/s) cause on the mean firing rate a delayed response phase, hence a positive phase shift. The figure 7 shows the phase shift as a function of

the oscillation frequency input. As the Bolzano's theorem demonstrated, between a positive and a negative quantity there is always a zero. It happens as well for the relative phase shift of the neuronal model response, in which the zero phase shift happens at a certain input frequency oscillation; this frequency is called preferred frequency γ, see the figure 7. The reason behind the 0 phase shift is an equilibrium between two opposite mechanisms; the firing rate dynamics has a time constant τ_e, which tends to delay the neuronal response and it is dominant at the HF domain; on the other hand, the dynamics of the adaption current I_a tends to cause an advance of the phase shift and it is dominant at the lower frequencies.

the author in their work noted that the γ slightly depends of the input conductance as well as from some parameters of the adapting neuronal model such as the input resistance, R_{in}, the neuronal model parameters, (α, $\overline{g}_k$,τ_N), the neuronal model capacitance C, and the time constant of the firing rate dynamics τ_e. See in the following equation.

$$\gamma = \frac{1}{2\pi}\sqrt{\frac{R_{in}\alpha\overline{g}_k C}{\tau_e} - \frac{1}{\tau_N^2}} \tag{12}$$

They have been demonstrated that lowering the conductance input value, brings to a lower values the γ. It has been also showed in their paper (Fuhrmann et al., 2002) in figure 4 8.

To add a further analysis, γ some other dependencies on the input values, it has been shown that the preferred frequency that γ has some dependencies as well on the DC level and the amplitude oscillation level (I_0 and I_1) see equation 11; since an higher value of I_0 brings the membrane voltage closer to the threshold value, lowering the constant time of the firing rate dynamics τ_e. However, the dependency on the I_1 is much weaker than the one of I_0, an increase of I_1 lowers the γ value, see the figure 6 9 of the paper (Fuhrmann et al., 2002).

Considering a small network of identical neurons (adapting neuronal model), driven by an external oscillatory input; when all neurons have the same discharge

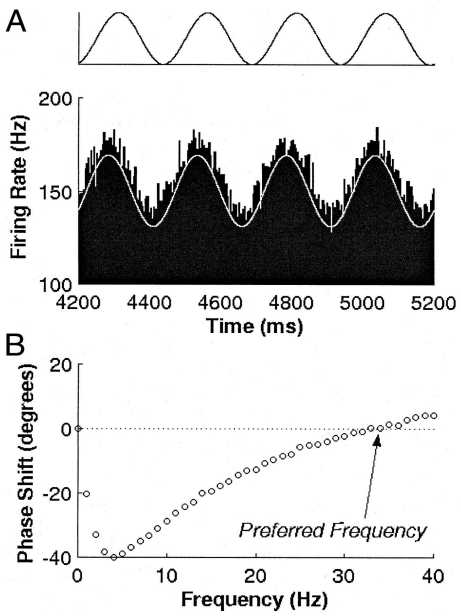

Figure 7: Response of an adapting neuronal model to an oscillatory input. The caption A is the peristimulus histogram (PSTH) of the neuronal model response to an oscillatory input of 4 Hz with (bottom) and without (with) noise. The mean current value is 1 nA with plus or minus 50 pA. the noise has $\sigma_I = 53pA$. The caption B is the output phase shift relative to the input as a function of injected input frequency. To note the arrow, which indicates the preferred frequency γ in which there is 0 phase shift relative to the input current. Image from the article of Fuhrmann et al., 2002 (Fuhrmann et al., 2002)

phase shift relative to the external input, the synchronous oscillation is achieved. In the figure 10 there is a network of four neurons, in which only one of them receives an oscillatory input, instead the others receive only a DC input to keep their firing rate at the same mean rate. It is important to underline, they are identical neurons, hence they have the phase-frequency curve (Fuhrmann et al., 2002). It has been expected that neurons would have been synchronised at their preferred frequency γ. Nevertheless, a new synchronisation frequency has been achieved at a lower value, in which all the neurons phase shift is opposite to the one produced by the synapse delay at that frequency. That frequency is called corrected preferred frequency (Fuhrmann et al., 2002). In other words, the input frequency for which the neurons exhibit synchronisation and have zero phase shift. It has been expected that the preferred

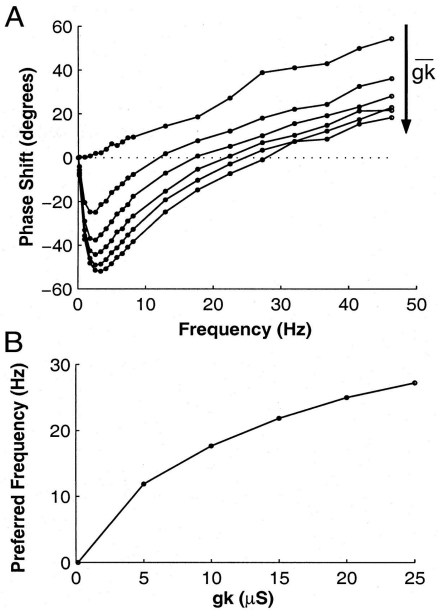

Figure 8: The phase shift as a function of the different values of $\overline{g}_k$, caption A shows how is varying γ lowering $\overline{g}_k$. In caption B is clear the dependency between γ and $\overline{g}_k$; increasing the input conductance means increasing the preferred frequency. Image taken from the article of Fuhrmann et al., 2002 (Fuhrmann et al., 2002)

corrected frequency determines the neocortical network rhythms (Fuhrmann et al., 2002).

The authors in their work have tested later the previous prediction in a large network of two hundred identical adapting neurons, in which each of them has an injection of uncorrelated noisy current with constant mean to induce spontaneous firing rate 11. The emergent property of the population rhythm is a network property, since the oscillation input has been injected to none of the neurons in the network. The synchronised oscillation frequency is 6,64 Hz and remains constant over time. However, has a small expected modulation since each neuron in the network experiences a slightly modulation due to the noisy input current and the random connections. A representative I_0 and I_1 have been used to built the phase-frequency curve for a single neuron in the homogeneous network considering the synaptic delay. The found corrected preferred frequency of the neuron was 6,7 Hz; hence, the emerging

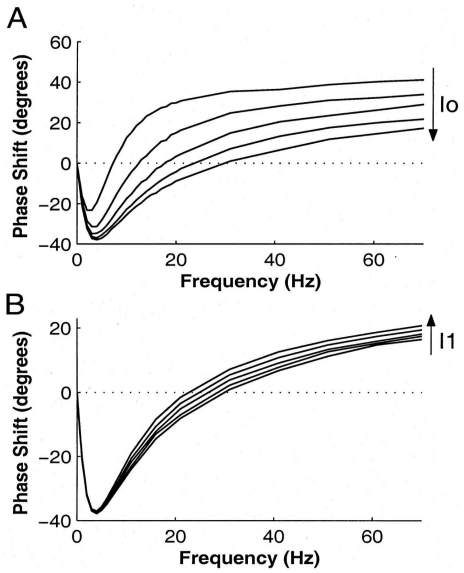

Figure 9: The image shows the dependency of the phase shift of the phase-frequency curve on changing the values of I_0 and I_1 in caption A and caption B respectively. In caption A, I_0 changes between 200-600 pA and I_1 is kept constant at 75 pA. In caption B, $I - O$ is constant at 600 pA and I_1 has values (70,100,130,160, 190) pA. The results have been obtained from the neuronal adapting model. Image taken from the article of Fuhrmann et al., 2002 (Fuhrmann et al., 2002)

network population rhythms in a large network as well can be predicted by the single neuron corrected preferred frequency.

An obvious criticism is if the emerging network population rhythms is still predicted by the single neuron corrected preferred frequency in a more realistic network composed by heterogeneous neurons (different neuronal models). The authors verified it using the same network and randomly distributing the value of the parameter $\overline{g}_k$, keeping the other constant; founding the same result present in the homogeneous network (Fuhrmann et al., 2002), see caption D in image 11.

The other two applications of System Theory to the fields of Electrophysiology and Neurobiology are more focused on experimental data of patch clamp technique; their result are very relevant for the HF domain of the response function of neocortical Layer V pyramidal neuron. The first paper of reference is (Köndgen et al., 2008), in

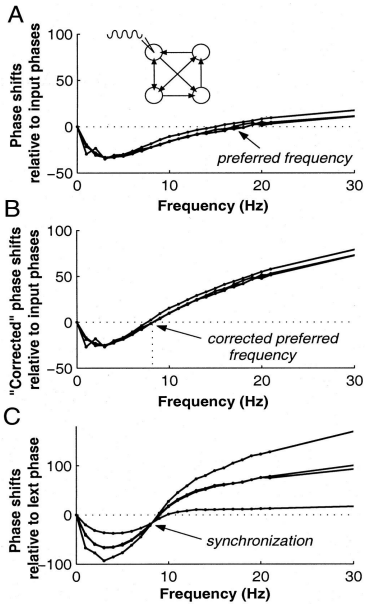

Figure 10: Effects of the corrected preferred frequency on a small network of identical neurons with asymmetry in connection. In caption A, the phase-frequency curve of each neuron related to their input. In caption B, The same as A, considering the synaptic shift. In caption C, phase-frequency curve for each neuron relative to their input, note the intersection of all the curve is the preferred corrected frequency of the neurons, where the synchronisation is achieved. The mean firing rate of the neurons is 53 cycles/s. Image taken from the article of Fuhrmann et al., 2002 (Fuhrmann et al., 2002)

which the authors for the first time studied the cortical neuronal response function in a wide frequency range (1-1000 Hz) of input frequency analysing the role of the background noise. The idea of a network can sustain a higher emission rate that a single neuron is easy to image, since a neuron cannot fire higher than its peak firing frequency, hence, it cannot fire at every cycle. In a network there are several neurons and while one is silent (i.e. refractory period) another one can fire; this make possible to sustain fast rhythms. Therefore, it is interesting understand how a background noise affected the neuronal response to input varying over time (Steriade, 2001). Some important past studies had underlined the importance of the background noise to ease the neuronal response and to decode without mistake the input fast time rhythms, i.e. (Gerstner, 2000) and (Knight, 1972). Another important theoretical

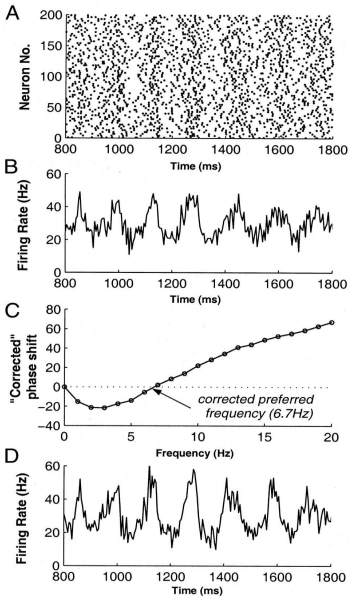

Figure 11: The image shows the implication of the preferred frequency for a synchronised large oscillating network composed by two hundred adapting neurons with same parameters. In caption A, there is the raster plot of the network, only one over three neurons have been shown. In caption B, the rhythm population emerges at 6,64 Hz. The bin size is 5 ms. In caption C, The phase-frequency curve of a single neuron is built, taking into account the experienced synaptic delay and mean input current parameter $I_0 = 253pA$ and $I_1 = 12,5pA$. The corrected preferred frequency is 6,7 Hz. In caption D, the heterogeneous network is the same network as the homogeneous one, except for a random distributed value of $\overline{g}_k$. The population histogram has the same bin size as caption B, the population rhythm is the same as the homogeneous network. Image taken from the article of Fuhrmann et al., 2002 (Fuhrmann et al., 2002)

study (Brunel et al., 2001a) had confirmed the previous studies importance, through a more detailed mathematical model to describe the link between the time correlation background inputs, such as the synaptic filtering, with the dynamic response. However, independently from the background input noise the cut-off frequency at HF domain is dominated by low-pass filter behaviour, which is predicted by a linear response of conductance-bases integrate-and-fire neurons (Fourcaud-Trocmé et al., 2003) (Fourcaud-Trocmé and Brunel, 2005). To study the neocortical layer V pyramidal neuron dynamics response into acute slices, in vivo-like condition a noisy

current has been injected into the neuronal soma in the current-clamp configuration. A deterministic sinusoidally modulated current has been superimposed over the background noise, with f_{mod} the frequency of modulation in the range of (1-1000) Hz:

$$I(t) = I_0 + I_1 sin(2\pi f_{mod} t) + I_{noise}(t) \tag{13}$$

In which the $I_{noise}(t)$ is a realisation of the Ornestein-Uhlenbeck stochastic process with zero mean and unitary variance (Uhlenbeck and Ornstein, 1930). The noisy background is exponentially white filtered and is meant to mimic the in vivo barrage of which a neuron undergoes from excitatory and inhibitory synaptic inputs at the soma. The variance of the noise was meant to reproduce the voltage fluctuation observed in the cortical recordings in vivo (3-5 mV) (Paré et al., 1998). The authors approach is to transform the input signal,i.e. the sinusoids, into the firing rate r(t), in which this transformation depends on the background noise statistics. On the other hand, in the time domain the linear filtering is into the frequency domain comes from equation 10. The input is filtered and then, the transformation from the time domain domain to the frequency one happens as described in the previous section Fourier Decomposition of Input Signal. The main result of the paper is to study the impact of background activity on neuronal response and network oscillation. To perform it the linear response function has been evaluated for a single neuron over its firing rater r(t) in response to a current composed by background noise plus small sinusoids. The firing rate r(t) has been estimated by PSTH, in the limit of small amplitude, such as when $I_1 < I_0 * 0,3$. The limit of small amplitude is kept to fulfill the validity of the linear approximation, allowing to ignore higher harmonics; which could be relevant with higher values of I_1. r(t) is well described by a sinusoidal wave with the same f_{mod} of the input current, see figure 12 :

$$r(t) = r_0 + r_1(f_{mod}) sin(2\pi f_{mod} t + \Phi(f_{mod})) \tag{14}$$

in which r_0 is the mean firing rate, $r_1(f_{mod})$ is the modulation amplitude and $\Phi(f_{mod})$ the phase shift relative tom the input. The values of r_0 was in the range of 10-20 cycles/s, with $r_0 > r_1 > 0$. In the context of Fourier decomposition signal as an input

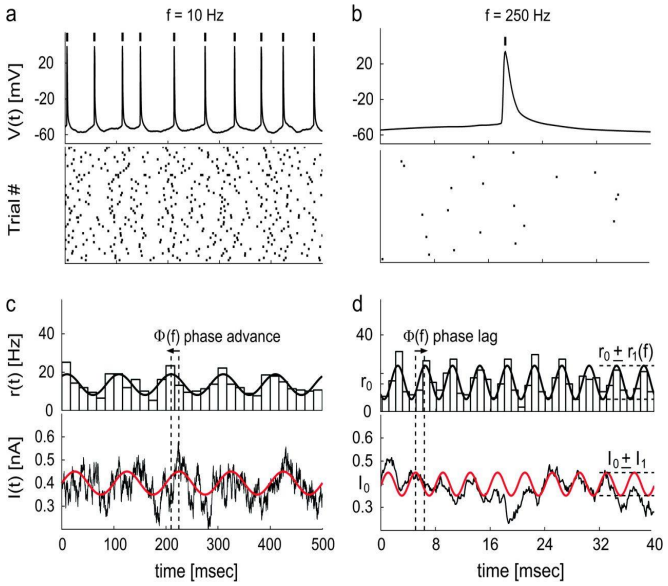

Figure 12: Analysis of the firing rate in response to a current sinusoidally modulated over a noisy background mimicking the synaptic inputs. The AP occurrence times is referred to its peak. The lower panel are the associated raster plots. The f_{mod} are 10 Hz and 250 Hz (a,b). The upper panels in (c,d) are the PSTH revealing a sinusoidally modulation of the firing rate $r(t)$. In the bottom panels, for comparing the sinusoidal component$I(t)$ is plotted in red, over the total $I(t)$. Nevertheless r_0 is constant, r_1 and Φ are f_{mod} dependent. Taken from (Köndgen et al., 2008)

for a neuron, the $r_1(f_{mod})$ and $\Phi(f_{mod})$ give back the information about how much a neuron attenuates and delays every component of the input f_{mod}. In the figure 13, cortical layer V pyramidal neuron showed a wide magnitude bandwidth ($\frac{r_1}{r_0}$) and an output phase-shift Φ. It has been showed that r_1 decreases for $f_{mod} > 100 - 200$ Hz, completely unaffected by the correlation time of the noise. The membrane impedance is dominated at low frequencies (5-10) Hz, by the voltage-dependent resonance by h-currents and M-currents and by low-pass filter behaviour at HF domain with strong attenuation $\sim 50Hz$ is not matched by the $r_1(f_{mod})$ behaviour. Over 200 Hz the

magnitude decays with a negative power-law, which in the figure 13 is straight since is a double logarithmic plot (the dashed one). The exponent estimated by the linear regression in 13 is $\alpha = -1,80$, and matches the average exponent obtained by single experiments $\alpha = (-1,81 \pm 0,31)$, see figure 14. From previous theoretical studies, It has been anticipated this results (Gerstner, 2000), (Knight, 1972) and can be replicated by nonlinear integrate-and-fire neuron and conductance based models (Fourcaud-Trocmé et al., 2003). A look on the HF domain of figure 13 suggests an $\alpha = 1$, on the contrary figure 14 panel a suggests $alpha = 2$; numerical simulations showed as well that the HF asymptotic behaviour can be reached at higher frequencies than the cut-off frequency (Fourcaud-Trocmé et al., 2003), letting still open the precise determination of the α value. The linear system at HF domain the phase shift saturates, on the other hand the cortical pyramidal neurons does not the same, see figure 14 panel b. This phenomena happens since there is a delay between the input and the output in the range of $0,3-1,1ms$ and it is much larger than the rising phase of the AP, which is in the range $0,3-0,5ms$. This mismatch observed in some neurons could be explained as an additional axo-somatic and somato-axonic propagation time (Köndgen et al., 2008) (Palmer and Stuart, 2006).

Considering The noisy input a neuron can be brought by membrane voltage fluctuation to spike overcoming the threshold even if its average input is subthreshold. The authors chose to have two different discharge regimes the suprathreshold or weak-noise regime and the strong-noise regime or subthreshold (Köndgen et al., 2008). In the weak-noise regime, the standard deviation of the input was set at $20-50pA$ and I_0 was set above threshold. On the contrary, in the regime of strong-noise the I_0 was set under the threshold, and the standard deviation was increased up to the r_0 value was matching the value reached in the other regime. The background noise is mimicking the presynaptic firing their cross-correlation (Rudolph and Destexhe, 2004), affecting the neuronal response especially at intermediate frequencies, smoothing resonances

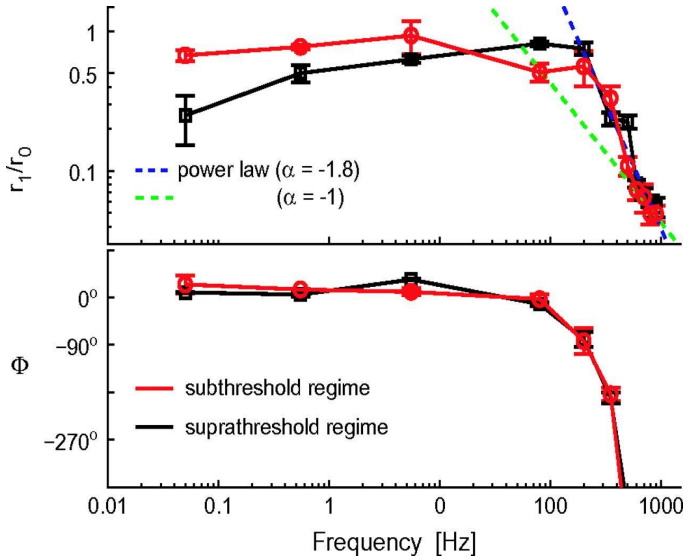

Figure 13: Normalised magnitude $\frac{r_1}{r_0}$ and phase shift Φ of response to a input current composed by a noisy background and an oscillatory foreground. Cortical pyramidal neurons showed that can track up to several hundred cycles per second. Their HF response goes as the power-law $r_1 \sim f_{mod}^{-\alpha}$ with a linear shift, $\Phi \sim f$. The results are on 67 cells. The error bars represent the SE across the data (32 ± 25). The color black stays for suprathreshold or weak-noise regime, the red stays for subthreshold and strong-noise regime. Mean rate $r_0 \sim 20$. Taken from (Köndgen et al., 2008)

and flattening the the neuronal response (Fourcaud-Trocmé et al., 2003) (Knight, 1972) (Brunel et al., 2001b). The most important result, however, is that at HF (f_{mod} > 100-300 Hz) the r_1 is attenuated in both regimes. At low f_{mod}, less than 20 Hz, there is always a phase-advance; see figure 15 16.In general, the HF domain neuronal response is not affected by background noise changes (Köndgen et al., 2008).

The timescale background fluctuations was changed systematically, the time constant of the noise is set to mimic the synaptic current time constants. Some previous studies have underlined the dependence of the Φ on the synaptic noise (Brunel et al., 2001b), leading to a zeroing the phase-lag as well as reducing the magnitude attenuation (Gerstner, 2000) and (Knight, 1972). The authors have been explored the constant time domain, τ from 5 to 100 ms to mimic the fast (AMPA-

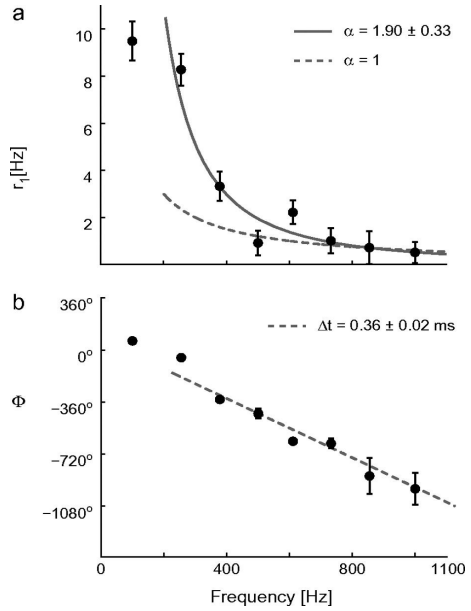

Figure 14: The HF cortical pyramidal neuronal dynamics response properties. In panel a, the modulation amplitude $r_1(f_{mod})$ shoes a power-law as $f_{mod}^{-\alpha}$ with $\alpha \sim 2$. In panel b, the phase shift decreases linearly as the increase of the f_{mod}. Taken from (Köndgen et al., 2008)

and $GABA_A-$)and slow(NMDA and $GABA_B$) synaptic currents. the r_1 and Φ showed at intermediate frequencies sensitivity to τ as showed 16.

.

The second paper of reference is from Linaro and colleagues. In their work they investigated the I-O properties of layer V pyramidal neurons using an input modulated in time with a noisy conductance background. Previous studies have experimentally investigated the existence of mathematical models of AP initiation, it has been reported a very large very large cut-off frequency in rodents (Köndgen et al., 2008) (Tchumatchenko et al., 2011) (Ilin et al., 2013) (Boucsein et al., 2009) and even large in humans (Testa-Silva et al., 2014). Furthermore, both experimentally and in mathematical model, the broadband transfer has been linked to the rapidity of the AP onset (Fourcaud-Trocmé et al., 2003) (Naundorf et al., 2006). In general, the authors extended the previous studies of the cortical dynamical response function to a

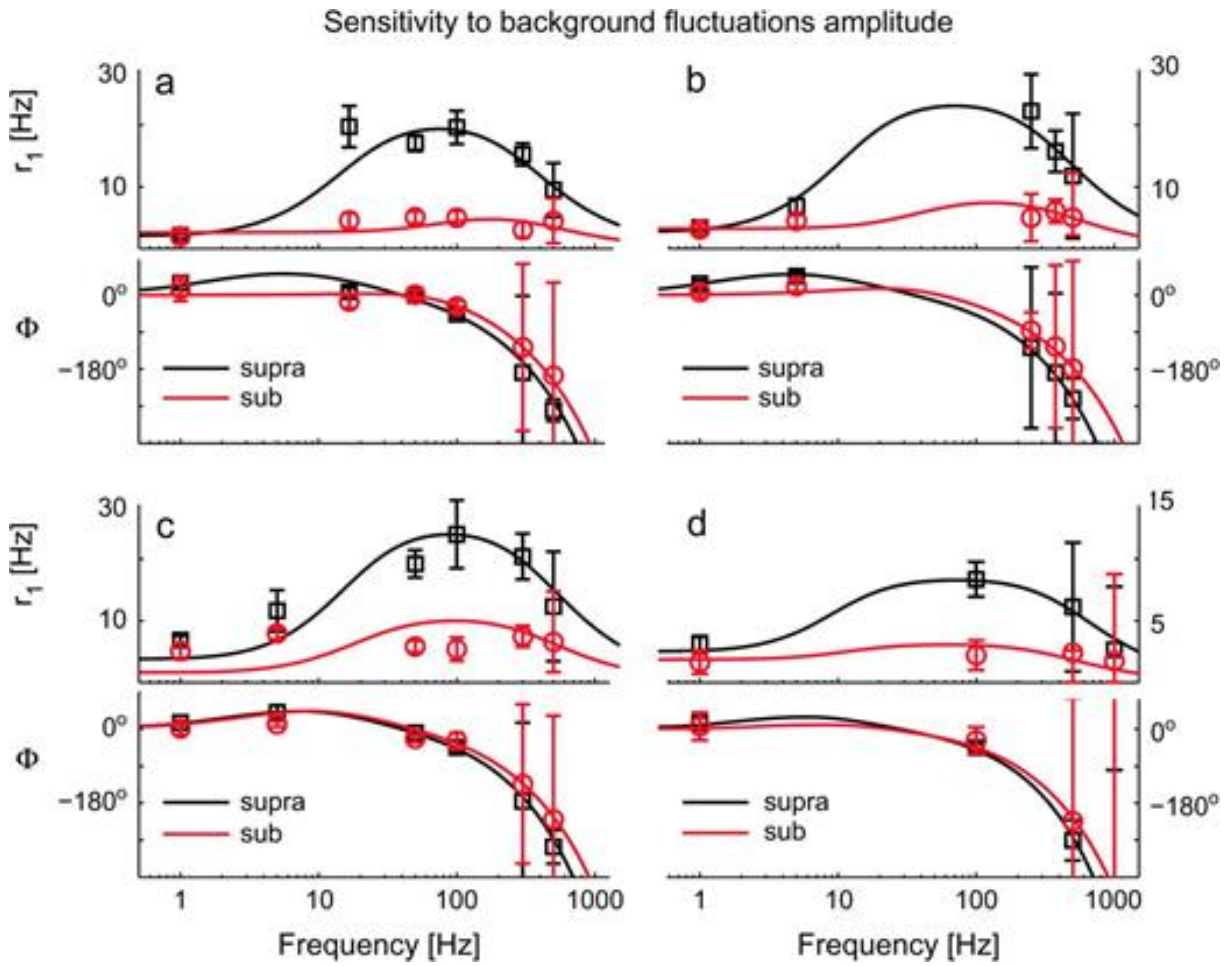

Figure 15: The background noise intensity affects the dynamical cortical neuronal response. On 4 cells, the impact of the noise variance has been examined for several values of f_{mod}. The $r_1 f_{mod}$) is smoothed at intermediate frequencies. All the panels show at the top $r_1(f_{mod})$ and at the bottom the Φ. the suprathreshold and the subthreshold regime are identified by different markers and colors. Experimental data and their best-fit from the model are plotted together. Error bars are at 95% of confidence interval. In the HF domain the error bar are big since the signal-to-noise is poor. Taken from (Köndgen et al., 2008)

more physiological settings (conductance -driven instead of current-driven) through dynamic clamp *in vitro*; recreating the barrage of irregular synaptic background observed *in vivo* (Destexhe et al., 2003). Before this study, in experiments, it has been only used current clamp to reproduce the noisy in vivo-like synaptic background see (Giugliano et al., 2008) in rodents (Köndgen et al., 2008) (Tchumatchenko et al., 2011) (Boucsein et al., 2009) (Ilin et al., 2013) and in human cortical neurons

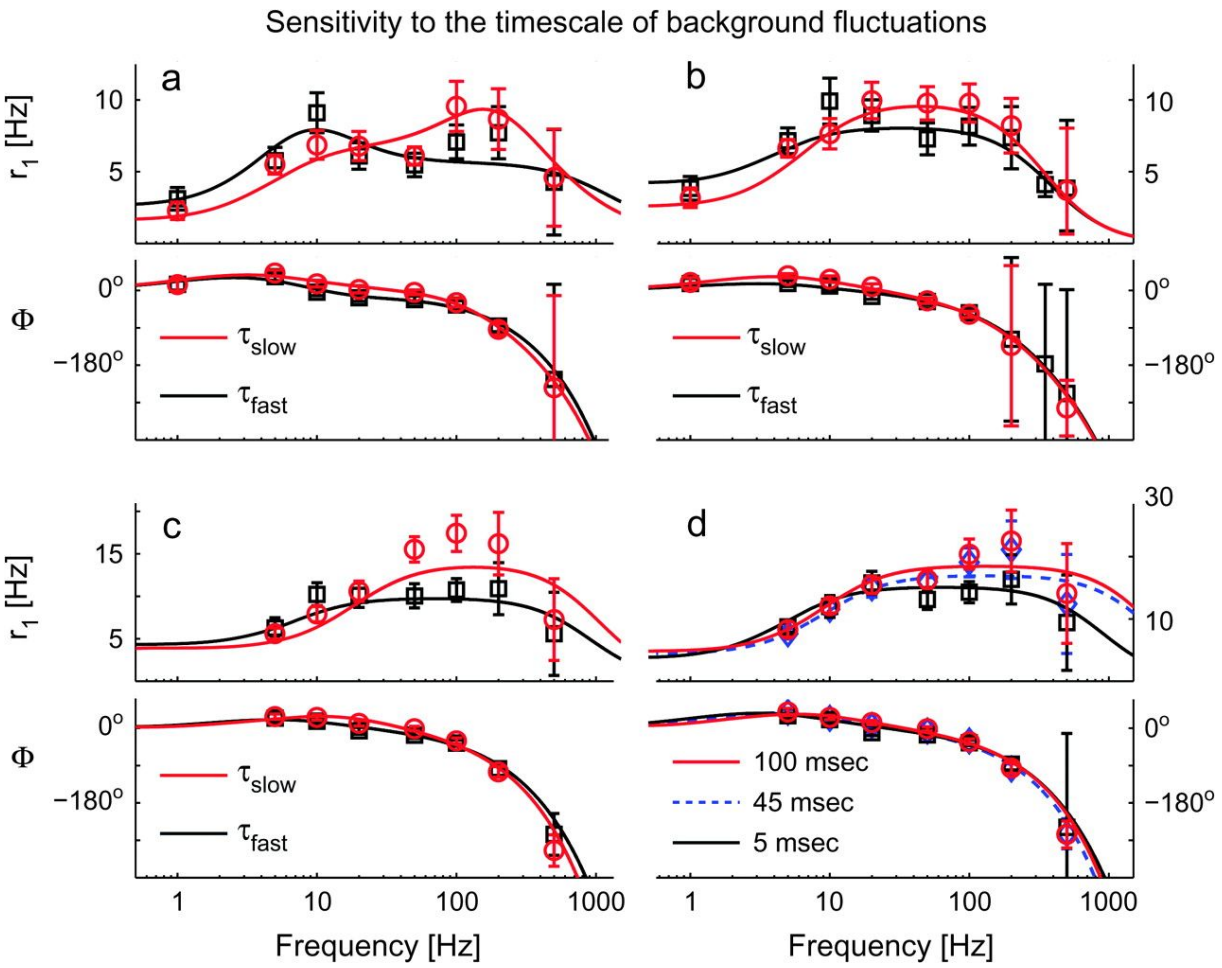

Figure 16: The timescale of fluctuations of background affects the dynamical cortical neuron response. the timescale effects was analysed among several f_{mod}. In the HF domain, cortical pyramidal neurons are not insensitive to white and colored background noise. All the panels show at the top $r_1(f_{mod})$ and at the bottom the Φ. The $r_1(f_{mod})$ and Φ has different shape and color for indicating the different simulation regimes τ_{slow} (red) and τ_{fast} (black). Experimental data and t has heir best-fit from the model are plotted together. τ_{fast} has value of 5 ms and τ_{slow} has values between 45-100 ms. Experimental data and their best-fit from the model are plotted together. Error bars are at 95% of confidence interval. In the HF domain the error bar are big since the signal-to-noise is poor. Taken from (Köndgen et al., 2008)

(Testa-Silva et al., 2014). The injected current $I(t)$ was generated in real-time by the computer and it is described by the following formula (Destexhe et al., 2003) (Linaro et al., 2014) (Bal and Destexhe, 2009) (Biró and Giugliano, 2015):

$$I(t) = G_E(t)(E_E - V(t) + G_I(t)(E_I) - V(t)), \tag{15}$$

Where $G_E(t)$ and $G_I(t)$ are the randomly fluctuations amplitude of excitatory and inhibitory synthetic synaptic conductances, with reversal potential $E_E = 0mV$ and $E_I = -80mV$ and membrane potential instantaneously recorded $V(t)$. Their fluctuations are the results of asynchronous activation of several presynaptic afferents, which their own synaptic conductances and exponential decays g_E, g_I and τ_E, tau_I; they are collectively activated by a stationary point Process τ_k with a parameter rate R_E and R_I. To study the effect of weak or strong background synaptic activity, the authors chose two different values of excitatory presynaptic rate R_E: 7 and 14 kHz. The first goal of the paper is to investigate the generalisation of the previous work of Ködgen and colleagues with a input time-varying current with background conductance fluctuations:

$$I(t) = I_0 + I_1 sin(2\pi ft) + G_E(t)(E_E - V(t)) + G_I(t)(E_I - V(t)), \tag{16}$$

where I_1 and f are the amplitude and frequency of sinusoidal injected current oscillation and I_0 is a term of offset current used to set the neurons at low (3-9 Hz) or high (15-25 Hz) output firing rate. A more biophysical set of input is with a time varying rate for the background conductance fluctuations; as $R(t) = R_0 + R_1 sin(2\pi ft)$. Having the rate time-varying means that the two OU process that reproduce the $G_E(t)$ and $G_I(t)$ have the same frequency of modulation f_{mod}, but not the same I_0 and I_1 leading to a non-stationary phenomena. To keep the neuronal response in linear regime the amplitude of I_1 and R_1 has been kept between the 5-20% of I_0 and R_0. In their experiments the authors explore the f_{mod} domain between 1-1000 kHz, they evaluate the phase $\phi(f_{mod})$ and the normalised gain or magnitude of the output as $\frac{r_1(f_{mod})}{r_0}$, which have been calculated by a PSTH over a period of the input oscillation through the estimate of the instantaneous firing rate $r(t)$:

$$r(t) \sim r_0 + r_1(f_{mod}) sin(2\pi ft + \phi(f_{mod})), \tag{17}$$

Then, the same analysis has been repeated on surrogate data to establish the level of significance. As explained in Ilin and colleagues (Ilin et al., 2013), from each spike train has set 100 surrogate date obtained by shuffling the original interspike intervals (Ilin et al., 2013); then, magnitude and phase has been evaluated as the mean of a hundred best fit over the a hundred realisation of the surrogate data for the each f_mod. The significance level has been set as the mean of the one hundred repetitions plus the standard deviation. The data analysis has been already discussed previously in section Fourier Decomposition of Input Signal. The *in vivo*-like regime has been recreated **in vitro** by dynamic-clamp technique to recreate the presynaptic inputs injecting random synthetic fluctuations of excitatory and inhibitory input conductances. It has been employed four different ways:

- an injection of an additional sinusoidal current, ΔI
- a weak modulation of the activation rate for excitatory ΔR_E or
- for inhibitory ΔR_I
- both modulation simultaneously ΔR_E and ΔR_I

Using as input the second protocol such as ΔR_E 17 the conductance rate mean and variance change over time by the $R_E(t)$ modulation (panel A); then, it has recorded and analysed the neuronal sparse response and computed the PSTH for estimating the $r(t)$ (panel B and C). The PSTH at each f_{mod} showed a strong attenuation over the frequency of $300 cycles/s$; note that the mean firing rate is always kept the same, even at frequencies in which a strong attenuation is present, see 17 panel C. The output oscillations are characterised by phase, mean, and magnitude; as showed by the panel C they depend on the f_{mod}. The characterisation in the frequency domain is reminiscent of the electronic filters which possess a bandwidth, a cut-off and low- or/and high-pass frequency. On the other hand, considering the protocol in which

ΔR_I is present means having an additional phase shift and upfront attenuation "in cascade" to the neuronal response.

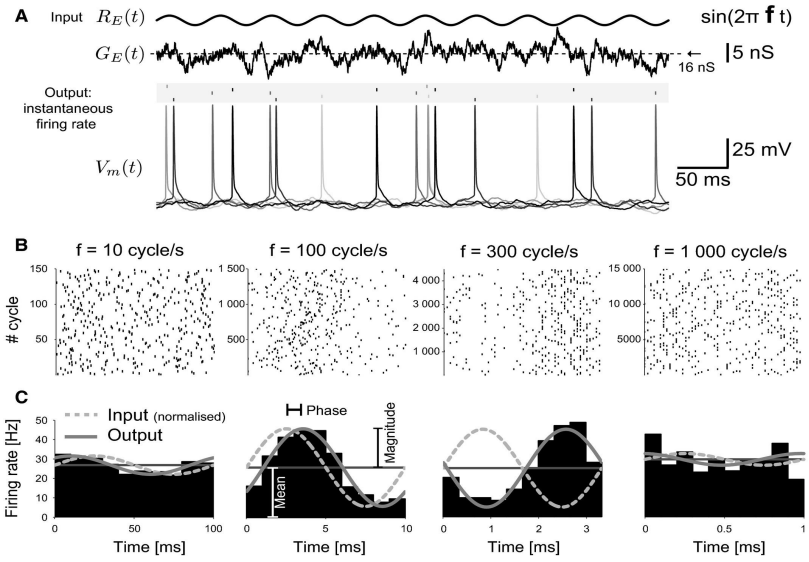

Figure 17: The instantaneous firing rate of a neuron is able to track the rapid modulations of the synaptic inputs. In panel A, it is showed one of the protocol applied, in which the mean and variance of $G_E(t)$ are modulated by sinusoidal presynaptic input $R_E(t)$. At the bottom, the neuronal response, such as a sparsely AP firing. The output firing rate is revealed by the raster plot and the PSTH; it is temporal modulated by the same input frequency f_{mod} up to $300 cysles/s$ (panel B and C). Note that magnitude and phase depend on f_{mod}. Taken from (Linaro et al., 2017)

The aim of the study is investigated the single cell contribution of the dynamical transfer properties; measuring normalised magnitude and phase with the highest signal-to-noise ratio for all the frequency domain (1-1000 Hz). Hence, the synaptic filtering has been compensated without affecting the spectral properties of the synaptic fluctuations, see figure 18 bottom panel. If the synaptic filtering is not compensated its attenuation doesn't allow the investigation of modulation at higher frequency of 30 or 15 $cycles/s$ (Linaro et al., 2017).

The figures 19 and 20 demonstrate the dynamical transfer response of the entire experimental dataset at different regimes and input modulation protocols. The plotted

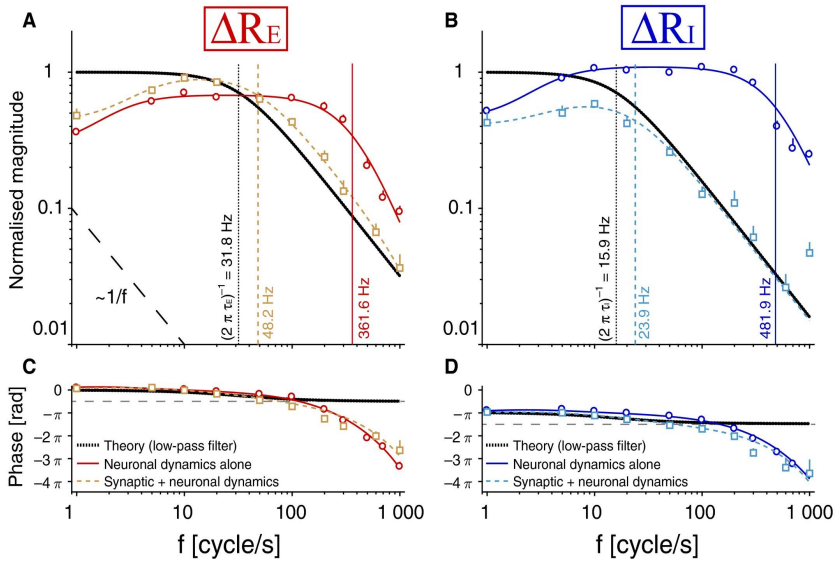

Figure 18: Neuronal dynamics response to fast input oscillations compensating the injected synaptic filtering. two different protocols have been used by the authors, instantaneous (circle markers) or induce filtered (square markers) oscillations of the input conductances. The vertical lines are cut-off frequencies by the optimal fit from the phenomenological model. On the left, in red, the excitatory time varying conductance on the side, in blue the inhibitory one. The black dashed line indicates the slope of $\sim \frac{1}{f}$ in A. Taken from (Linaro et al., 2017)

data in figure19 and 20 are the normalised magnitude and the phase, respectively, for each f_{mod}. The data are averaged over the neuron number, markers indicated mean and the bars the SEM. In figure 19 the black dashed line is the minimal significance level of the neuronal output response; on the other hand, the red one is the best fit of the power-law ($Bf_{mod}^{>}\alpha$): where the α value is indicated in each panel. In figure 20, the grey dashed line is used to identified to the phase value at 0 or $-\pi$. The value of the Δt above each panel derives from the slope of each curve. The obtained results are underling the main features of the neuronal dynamical response:

- A broadband up to $200-400 cycles/s$

- the power-law that describes the attenuation at HF domain is f_{mod}^{α}, with a negative exponent -(1.23 $\pm$ 0.15) in the range of -[0.9,1.5]
- at slow input modulation there is a phase advance
- A linear decrease which is not saturating for the phase in the HF domain.

The article work demonstrate neurons can track very rapid time-varying input signals, much faster than single cell and passive membrane filtering respectively around 25 and 50 $cycles/s$; since for all the f_{mod} the results stay above the minimum significance level. A further addition about the phase, when injected a time varying inhibitory conductance, there is a further phase offset of $-\pi$; basically the output rate reaches is minimum when the input rate is at its maximum (maximum of inhibition); resulting as an opposition of phase. Then, at HF domain the phase quickly decreasing lagging behind the input. For higher values of f_{mod} then the cut-off frequency in continuous line in figure 18 the phase linearly decreases as the product of $\Delta t f_{mod}$, reminiscent of the delay time Δt in the Fourier domain.

As showed in figures 19 and 20 there are two different regimes, the output mean firing rate has been varied identifying two different level of activity low (4-9) $spikes/s$ and high (15-25) $spikes/s$. High and low firing rate are associate to high and low coefficient of variability of the interspike intervals. In a similar fashion increasing the R_E from 7 to 14 kHz, it has been tuned different conductances intensities of synaptic activity, such as, weak and strong background; hence in the end the total possible regimes are four. As shown in figure 21 and 22 the cut-off frequencies at HF domain and in general the bandwidth are unaltered by a change in the background synaptic fluctuations and by a different output firing rate regime. However, it is not the true anymore at low and intermediate frequencies where there is an attenuation. Considering all together the result is possible to conclude that the cortical pyramidal neurons behave as band-pass filter which is affected (not only at HF domain) by both the output mean firing rate and by the presynaptic firing rate

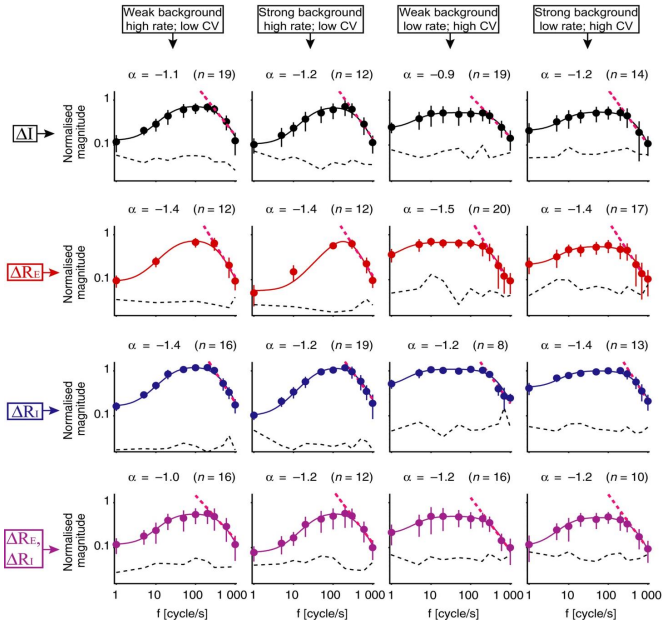

Figure 19: The neuronal normalised magnitude reveals some features, i.e., broadband-pass band, high cut-off frequency, and a power-law attenuation at HF domain. The panels show the magnitude as a function of the f_{mod} across different physiological regimes. The continuous lines are best fit of the phenomenological model, see section Fourier Decomposition of Input Signal. The red dashed line are best fit for the power law f^{α}. Row-wise are organise by the type of injected modulation and column-wise by the type of regimes. The black dashed line is the minimum level of significance threshold. For each panel is indicated the values from the best fit of α and the number of cells. Taken from (Linaro et al., 2017)

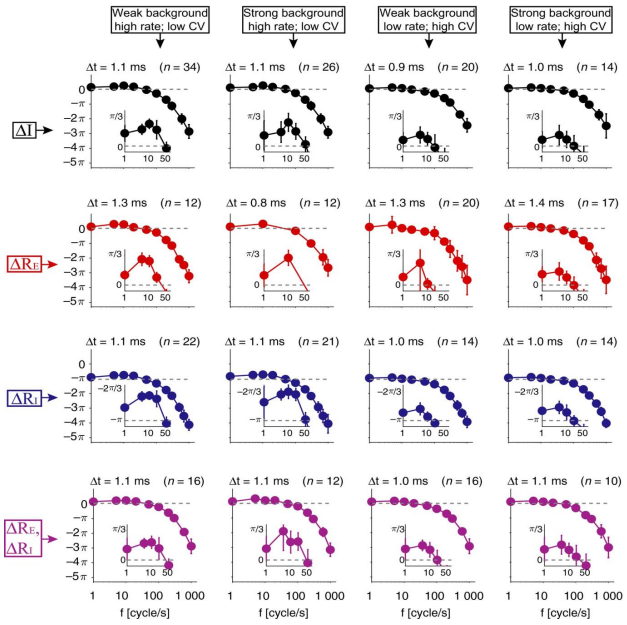

Figure 20: Across the f_{mod}, the neuronal phase response shows: phase advance at low frequency domain and phase lag for intermediate and HF domain. Then, a linear increase, i.e. $\sim \Delta t\, f_{mod}$ at very HF. As the figure 19, the vertical and horizontal organisation is the same. The grey line indicates represents 0 or $-\pi$. For each panel, it is indicated the values from the best fit of Δt and the number of cells. Taken from (Linaro et al., 2017)

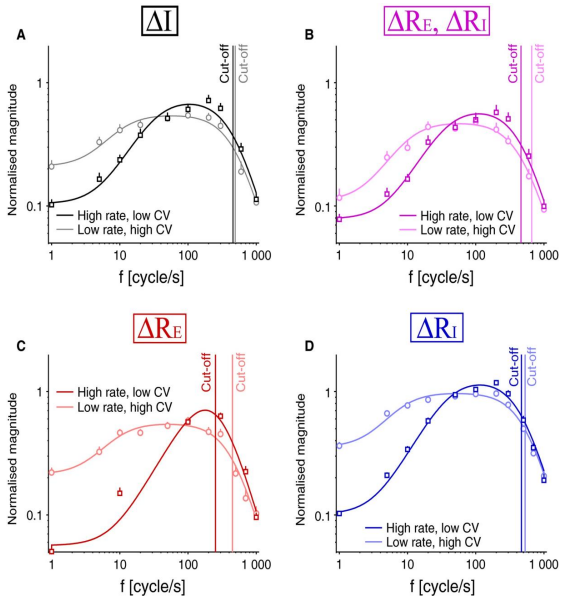

Figure 21: The increase of the output mean firing rate leave at HF domain the cut-off frequency of the gain not altered. Instead, at transfer function at slow f_{mod}. All the panel are under strong background fluctuations, while the several type of input are time modulated. The circular/square markers are the magnitude of the transfer function to an injection of instantaneously modulated conductances at low/high output firing rate. The vertical lines are cut-off frequencies by the optimal fit from the phenomenological model. Taken from (Linaro et al., 2017)

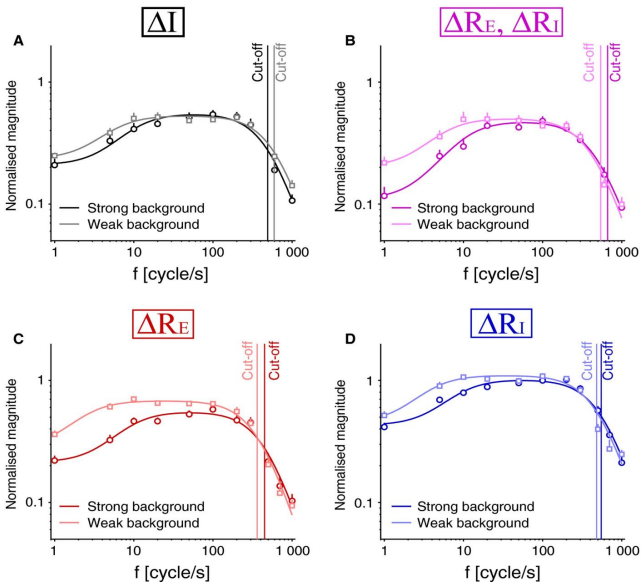

Figure 22: The increase of the output mean firing rate leave at HF domain the cut-off frequency of the gain not altered. All the panels show the magnitude of the output instantaneous firing rate as function of f_{mod} at low output mean firing rate,while the several type of input are time modulated. The square/circular markers are the magnitude of the transfer function to an injection of instantaneously modulated conductances under weak/strong background synaptic fluctuations. The vertical lines are cut-off frequencies by the optimal fit from the phenomenological model.Taken from (Linaro et al., 2017)

3.6 Studying cortical responses under in vivo-like recreated regimes

3.6.1 High-conductance state

The spontaneous activity in neurons is very different between *in vitro*, i.e. acute brain slice and *in vivo* experiments. The main reason is the loss of a lot of connections due to the severed 3D structure. In addition, neurons *in vivo* are more depolarised and have a lower input resistance (Steriade, 2001) (Matsumura et al., 1988) (Baranyi et al., 1993). The intact brain structure at the level of the cortex has a high connectivity between 5-60 thousands synaptic connections; mostly of them come from the cortex itself (DeFelipe and Fariñas, 1992); however some of them comes from external regions such as the thalamus (Brown et al., 2012). In awake animals, neurons have high spontaneous firing rate (Steriade, 2001), this constant and irregular synaptic bombardment, called high conductance state, affects the neuronal response and the mechanisms behind it are still unclear... It is surely challenging and useful evaluated the effect of the "high-conductance state" *in vivo*, however it is very difficult, since doesn't allow the same control that is possible to reach *in vitro*, such as with acute slices. Nevertheless, the use of some experimental techniques has allowed to improved the knowledge about the synaptic integration in cortical neurons (Williams and Stuart, 2003), it is also known that the network activity might affect the integration property of a cortical neuron; for this reason the study of the computational models is essential to integrate the experimental results obtained *in vitro* and *in vivo* as well. In the end, *in vitro* and *in vivo* approach cane be merged using dynamic-clamp, in which in vitro experiment high-conductance states are generated by a computer are used to mimic the synaptic bombardment. The *in vivo* experiment in awake animals are, usually, for mostly mechanical reasons with anaesthetized animals, with barbiturate anaesthesia. The first experiment was obtained in motor neurons in cat spinal cord (Brock et al., 1952); since then, recordings have been performed in all cortical regions. Unluckily, the barbiturates profoundly suppress

cortical excitability, leading to an electroencephalographic (EEG) similar to the one observed to slow-wave sleep. The slow wave are associate with synchronised bust-silence in cortical neurons; in contrast to the EEG low-amplitude, fast activity associated to asynchronous and irregular firing. Some few studies in waking animals (Steriade, 2001) (Matsumura et al., 1988) (Woody and Gruen, 1978) and others, have shown a low input resistance (R_{in}) ($5-10M\Omega$), a more depolarised membrane potential ($-60mV$) with stronger fluctuations $\sigma_V = 2-6mV$ causing an irregular discharge in the frequency range or 5-40 Hz 23 (Steriade, 2001). Furthermore, to have a complete characterisation of the cortical neurons during activated states,it must perform EEG recording in parallel with intracellular recordings. Considering the waking animals and the up state of KX anaesthesia, cortical neurons have a lower input resistance, the V_m is depolarised, neurons fire spontaneously at rest and experience a V_m continuous fluctuations; this state is called high conductance state. The latter state is very different from the *in vitro*, where neurons lack of connections and spontaneous firings, have higher input resistance and are hyperpolarised 23 panel b and d. To study the contribution of synaptic activity on high-conductance states recording of *in vivo* of intracellular neurons, they have been compared between the the very same neuron before and after microperfusion of tetrodotoxin (TTX) (Paré et al., 1998). The TTX application produces a stabilisation and an hyperpolarisation of V_m and increases the input resistance see figure 24. After applying the TTX *in vivo*, the R_{in} is the same as observed *in vitro* (Paré et al., 1998); this means that damaging with electrode the cells with *in vivo* electrodes doesn't count as important point between *in vivo* and *in vitro*. More exactly, these experiments underline that the difference in R_{in} and the depolarised V_m is due to the spontaneous activity. To summarise the neocortical neurons are considered in "high-conductance" state if they have the following features:

- a large membrane conductance

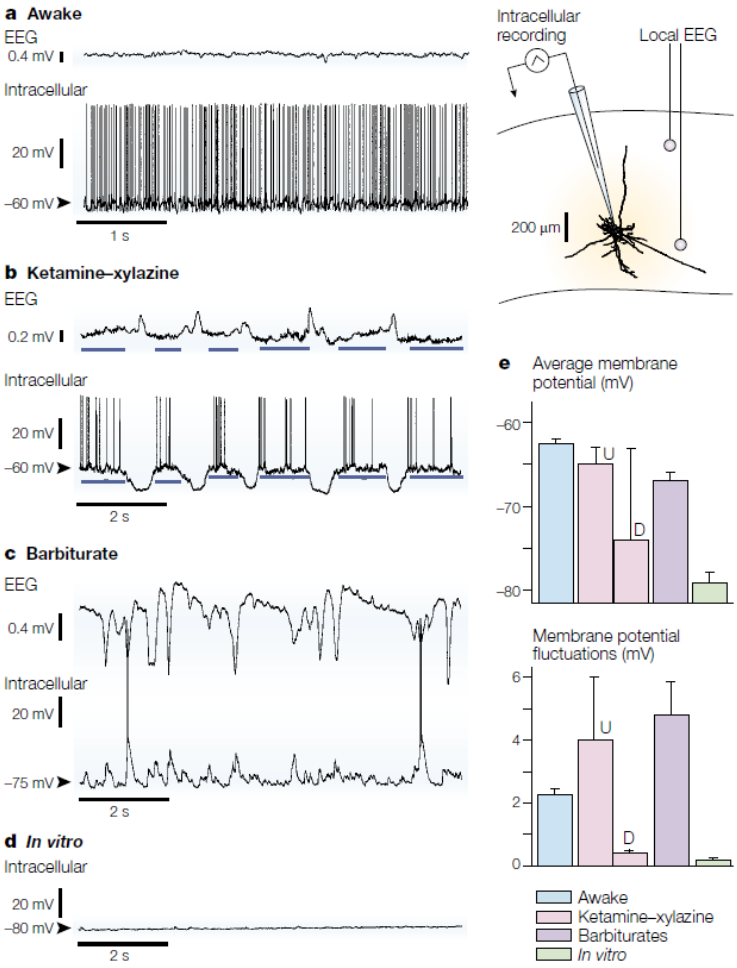

Figure 23: Parallel EEG and intracellular recordings during activate states. In panel a, it is showed an awake animal, the EEG recording is de-synchronized, on the hand the intracellular one has a depolarised and highly fluctuating membrane potential, which is associated with irregular firing. In panel b, the animals undergoes to ketamine–xylazine (KX) anaesthesia; it is showed an oscillation between two phases by the EEG recording, one is a de-synchronised periods (up states), indicated by bars, with fast irregular EEG oscillations; and slow waves. In this state the fast EEG activities are absent or strongly reduced. The intracellular recording shows that during the de-synchronised periods (bars), there is an high fluctuations and a depolarisation for the membrane potential, on the other hand, there is an hyperpolarisation during slow waves. In panel c, the animal undergoes to barbiturate anaesthesia, slow waves are present in the EEG recording, whereas the intracellular signal has an hyperpolarised baseline on top of which there are depolarized bursts. In panel d, *in vitro* recordings are obtained in cortical slices using sharp electrodes. The network activity is reduced, basically the activity is silent. In Panel e, it is compared the mean value of the membrane potential and its standard deviation across different states. Taken from (Destexhe et al., 2003)

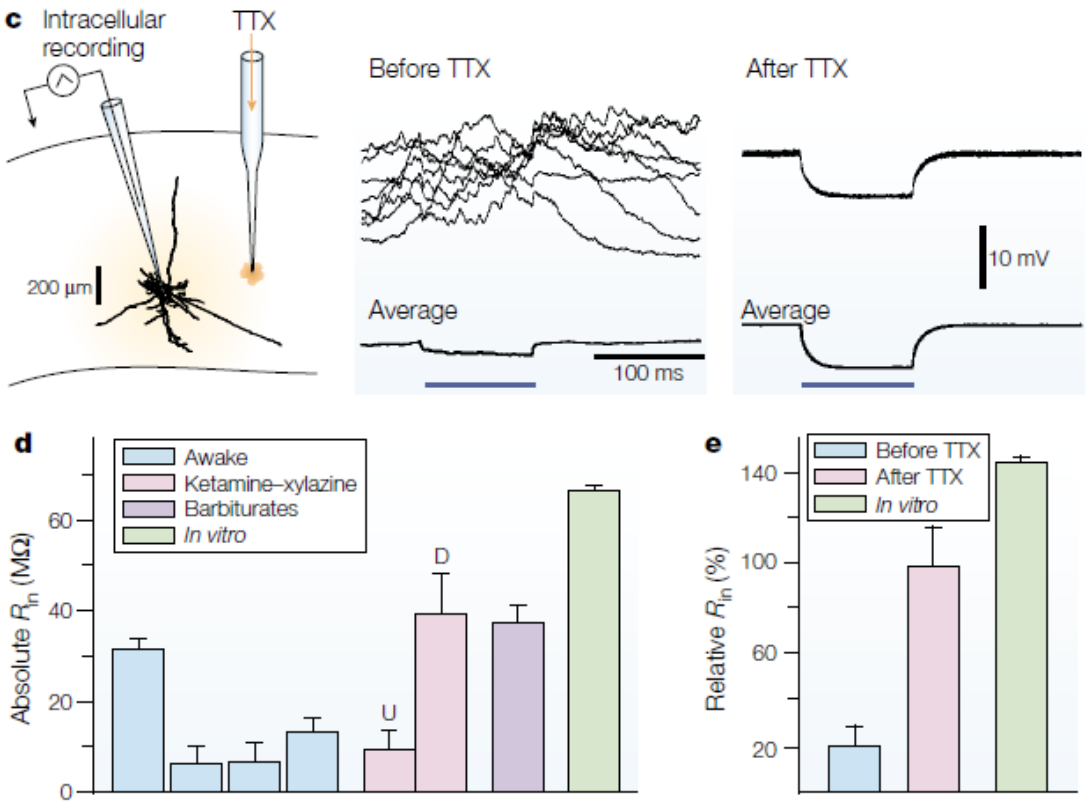

Figure 24: In panel c, from the left to the right, the experimental setup; a pipette was used to perform a tetrodotoxin (TTX) microperfusion *in vivo*. Then, in the middle, response to the current injection during an up state of a KX anaesthesia, individual response at the top, averaged at the bottom. On the right, the same current response after the TTX suppression of the activity. The R_{in} and time constant τ_m are five times larger than the up state. The results are similar to the *in vitro* measurements. In panel d, absolute values of R_{in} measurements in different studies in awake animals. From left to right, data from (Steriade, 2001),(Matsumura et al., 1988), (Woody and Gruen, 1978),(Baranyi et al., 1993); KX data from (Destexhe and Paré, 1999),(Paré et al., 1998); barbiturate and *in vivo* data from (Paré et al., 1998). In panel e, before and after TTX, relative R_{in} values in the same cells. Taken from (Destexhe et al., 2003) and modified

- an average V_m between (-65,-60) mV more depolarised than the natural resting level between (-80,-70) mV
- big membrane potential fluctuations with σ_m between (2-6) mV up to tenfold larger than in absence of activity.
- a dominant inhibitory conductances $g_i \sim 4g_e$

To study the integration properties of cortical neurons in high-conductance states, it is necessary combined several "ingredients", such as *in vivo* data with detailed biophysical dendritic excitability measurement. To perform this study are useful the multi-compartmental models, which reconstruct the three-dimensional morphological structure of a neuron. Neuronal simulators environments, such as NEURON (Hines and Carnevale, 2001), make possible to integrate the cable equation over morphological data using isopotential group or set of compartments. This model contains as well all the biophysical information of the modelled neuron. Several models of compartmental ones have been proposed to mimic the synaptic bombardment in cortical neurons (Bernander et al., 1991) (London and Segev, 2001) (Destexhe and Paré, 1999); more recently, the stochastic OU process is used to reproduce the synaptic bombardment which a cortical neuron undergoes *in vivo*. In figure 25 is showed some example of "synaptic noise", for example the model in 1b comes from an *in vivo* model of animal under KX and comes from the up states previously discussed. This model is able to reproduce the high-conductance features, such as $0.5-3Hz$ and $4-8Hz$ of release frequency for miniature synaptic events of respectively,excitatory and inhibitory synapses. In the panel c 25, the approach is different is a single-compartment model with multiple afferent synapses (Salinas and Sejnowski, 2000) (Tiesinga et al., 2000), or already containing an "effective" synaptic conductance (Destexhe et al., 2001). Instead the case d, the synaptic conductances are modelled by a stochastic process, which reproduce the spectral and statistical properties of the synaptic conductances 25. All these models are able to reproduce the the features of high-conductance states listed above 3.6.1.

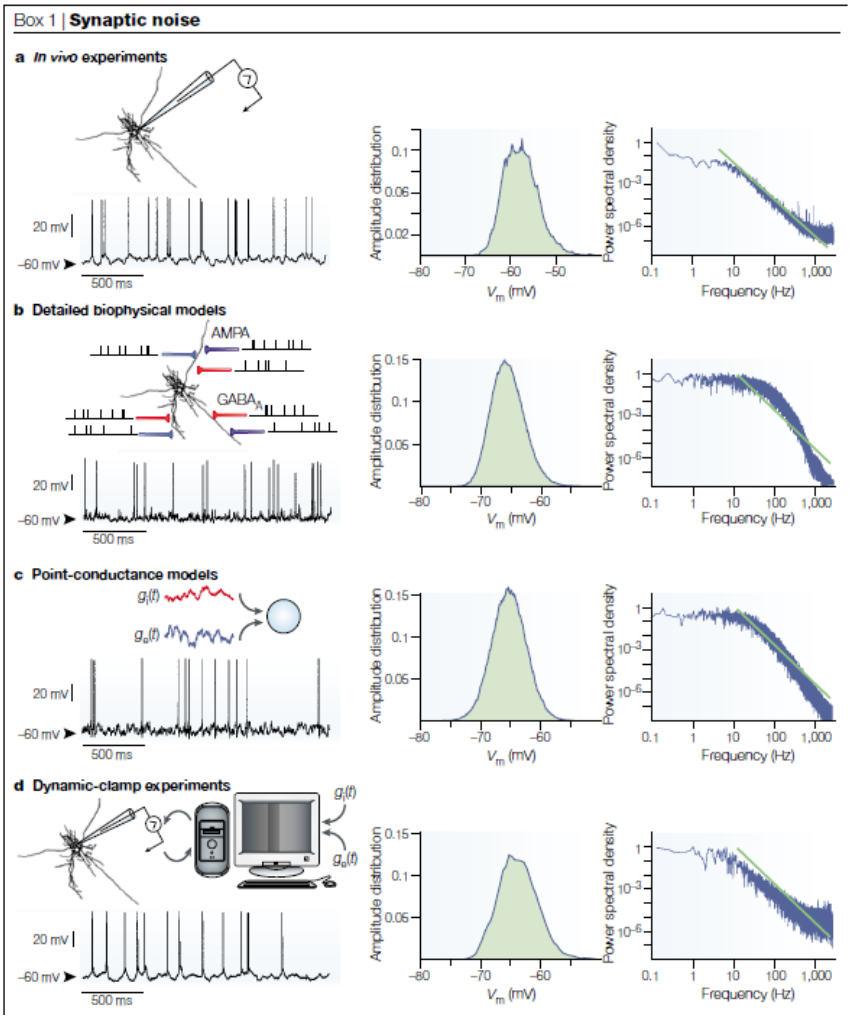

Figure 25: The synaptic noise terminology has used to describe the barrage of the synaptic bombardment in which a neuron undergoes. It is an *in vivo* subthreshold dynamics due to the irregular discharge of a large number of presynaptic neurons. This dynamics is indeed a information carrier, however it seems random and has a stochastic dynamics on the V_m; it has a statistical properties as well as a broadband power spectrum coloured noise (Destexhe et al., 2003). in the panel a, it is showed an *in vivo* recordings in neocortical neurons during activated periods with EEG. In panel b, it is showed a very detailed model of synaptic noise in a reconstructed layer VI pyramidal neuron. It contains, in the soma and in the dendrites, both Na^+ and K^+ channels. A random release of excitatory and inhibitory synapses has been modeled using AMPA and $GABA_A$, respectively the synapses quantity was four and sixteen thousands. In panel c, it is showed a synaptic noise "point conductance model"; a single-compartment model with two excitatory (g_e) and inhibitory (g_i) synaptic conductances. In panel d, it is showed the synaptic-clamp result of an induction of synaptic noise in neocortical neurons *in vitro*. From left to right, there is an example of the V_m, the amplitude distribution and the power spectral densities is computed with no spikes. The power spectral densities is broadband and at HF has a negative exponent in the power-law of f^{α}, with $\alpha = 2,6$ behaving as low-pass filter. The data used for the analysis are provided by M. Badoual and T. Bal. Taken from (Destexhe et al., 2003) and modified

In general, the high conductance test has several consequences on the cortical neurons integration. On of them is the responsiveness, that is completely different in presence of absence of the high-conductance states; such as neurons respond scholastically, since their behaviour is described by a probability function, see for an example 26. The probability to evoke an AP at the soma given a certain synaptic input shows contrasting results (Destexhe et al., 2003). In the panel b of 26, it is compared the same compartmental model at three different states: quiescent in pink, a green one in which the synaptic input is simulated as panel b of 25 and a blue one, in which the synaptic activity effect was incorporated with an additional conductance leak. The cortical neuron purely *in vitro* behave as all-or-none response function, having a tiny threshold as function of the input intensity 26. However, in presence of the "synaptic noise" the response function changes, see green in panel b, 26; on the other hand, the presence of high-conductance states decreases the responsiveness, see the blue panel b in 26. From the panel b of figure 26 it is possible to see that in presence of high-conductances states there is a probability of response even with sub-threshold inputs, see the asterisk. This is due to the stochastic resonance, which has been found in non-linear system (Wiesenfeld and Moss, 1995), in simple models (Doiron et al., 2001), in theoretical (Rudolph and Destexhe, 2001) and experimental (Stacey and Durand, 2001) models. Another effect of high-conductances state is over the temporal processing. There is a reduction of the membrane time constant (Destexhe and Paré, 1999), (Bernander et al., 1991) which come is visible from experimental data in response to fast injection of current see figure 24 panel c.

The reduction of the time constant should favor a finer discrimination (on the temporal domain) of the distant synaptic inputs (Bernander et al., 1991). Considering active dendrites structure, having a small membrane time constant facilitates a fast AP propagation, having as consequences a less prominent location dependence of EPSPs timing (Rudolph and Destexhe, 2003a) and a facilitation of association of

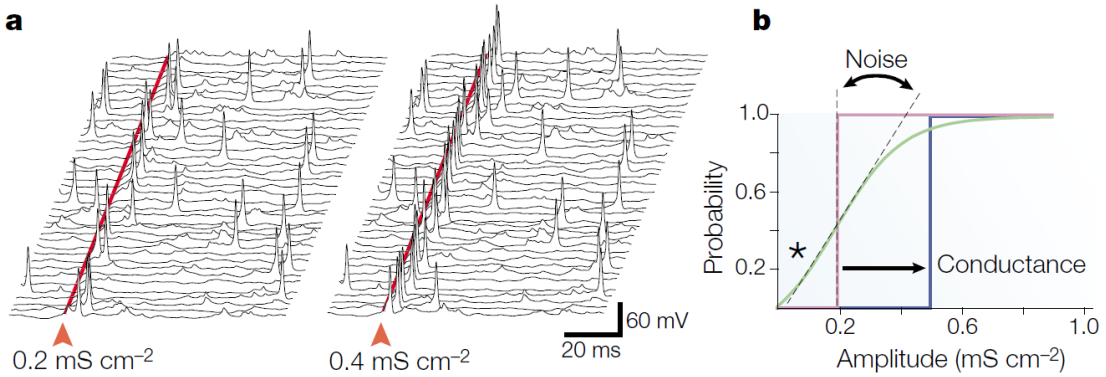

Figure 26: the responsiveness is enhanced during high-conductance states. In panel a, it is shown in presence of membrane potential fluctuations by spontaneous network activity, which triggers the synaptic AP probabilistic dynamics. A cortical pyramidal neurons has been simulated in high-conductance state using the same model of panel b in 25. It was stimulated by synapses of AMPA (see the arrow; two different stimulus intensities are shown). In panel b, it is shown the responsiveness enhancement by voltage fluctuations. The response curve, such as the probability somatic spike response as a function of stimulus amplitude has three different states: quiescent (pink, which means no synaptic activity), static conductance (blue, an addition of a constant conductance, such as the average conductance during high-conductance states) and high-conductance state (green, the same in panel a). The presence of the static conductance input shifts the response curve towards a higher threshold (single arrow), whereas the presence of "synaptic noise" during high-conductance states changes the slope of the response curve (double arrow). In the last case, there are evoked subthreshold response as well as to small inputs (asterisk). Taken from (Destexhe et al., 2003) and modified

distal inputs with higher temporal resolution. Taking all of this together, a relationship between high-conductance states and the irregular and random firing of the neocortical neurons has been found and (Rudolph and Destexhe, 2003a) (Salinas and Sejnowski, 2000). One of the main consequence of high-conductances states in cortical neurons is the possibility to track higher frequency inputs than in quiescent states (Rudolph and Destexhe, 2003b). Other advantages have been find in computational models due to slightly variation of the large values of the inhibitory and excitatory conductances allowing the neurons to track faint changes of their inputs temporal correlation (Halliday, 2000). To summarize the high-conductance states in models has been predict to give advantages such as a finer discrimination of the input in the

temporal, spatial and of the amplitude. However, there are also drawbacks such as the system is stochastic and responds only with a certain probability; on the other hand, this is highly compensated by the neuronal population which can process the information in parallel (Shadlen and Newsome, 1998). The high-conductance states can be recreated in intact network through an injection into the cell using the dynamic clamp technique see figure 27 panel a, which is used to mimic the high-conductance measured *in vivo* (Destexhe et al., 2001). Using the dynamic-clamp means to add a "virtual" conductance in the neuron membrane and reproducing this technique in cortical slices, leads to have a depolarising and fluctuating membrane, a reduced input resistance, voltage with an irregular firing; hence all the features observed *in vivo* see as reference the panel b of figure 27 and panel d of 25. The limitation of this approach is the possibility to inject the "virtual conductances" only around the electrode, but actually, the synaptic input are distributed all over the dendrites. On the other hand, the dynamic-clamp, is able to catch the interplay between the current of the proximal region and benefits of the fine control that is possible to apply *in vitro*.

3.6.2 Diffusion approximation and "noise" injection

The diffusion approximation is a technique in which there is a replacement of a complicated and intractable stochastic process by an appropriate diffusion process, which is a strong Markov process having continuous sample paths.

The diffusion approximation approach is comparable to the normal approximation for sums of random variables, since using the central limit theorem allows to replace intractable stochastic process with an appropriately chosen normal random variable. In neuroscience, the diffusion approximation approach is used to inject into a single neuron, i.e. in cortical acute slices, to recreate the synaptic bombardment that a neocortical neuron undergoes *in vivo*, as discussed in the previous sectionHigh-

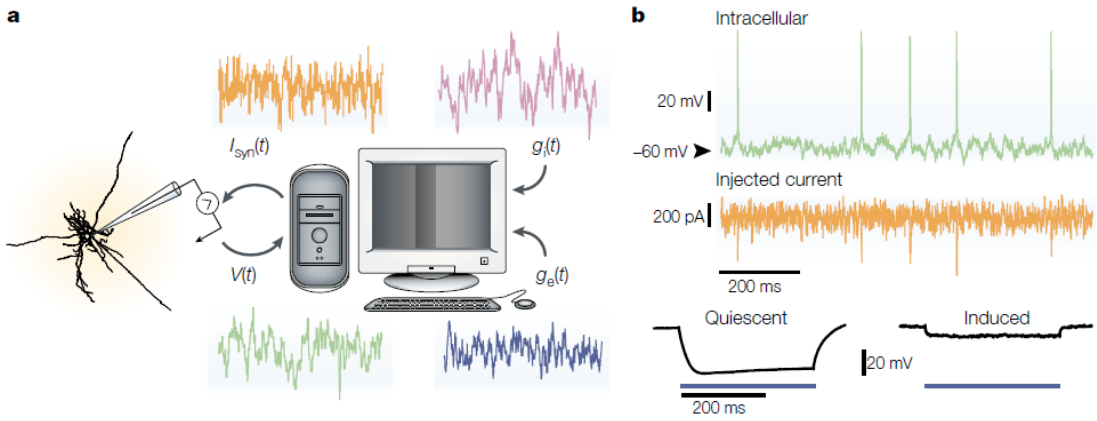

Figure 27: *In vitro* dynamic-clamp experiment reproducing the high-conductances states. In panel a, the dynamic-clamp protocol. In green, there is the recording of the $V_m(t)$ by intracellular recording combined by the computational model of stochastic conductance $g_e(t)$ and $g_i(t)$. The result of the effective synaptic current in orange, the resulting effective $I_{syn}(t) = g_e(t)(E_e - V(t)) + g_i(t)(E_i - V_m(t))$; where E_e and E_i are the reversal potentials for the excitatory and inhibitory conductances. It is injected into the cell in the current-clamp mode, inducing a neuronal stochastic activity, see as reference the panel c in figure 25. In panel b, It is shown an *in vitro* injection of high-conductance states. At the top: in orange, the injection of noisy current (orange), induced a stochastic activity, which is characterized by a depolarised and fluctuating membrane potential and irregular discharges (the green traces, as reference see the panel d in figure 25. At the bottom: The membrane has an (induced) reduced input resistance R_in, which causes a less prominent response to injected currents (blue bars; see as reference the panel c in figure 24). Taken from (Destexhe et al., 2003) and modified

conductance state. In literature, the diffusion approximation is a very well establish approach to extent the frequency-current curve from a injection of a step of a current to a more physiological injection of current/conductances which recreate the *in vivo* synaptic bombardment, see the review (Camera et al., 2008) and other works (Giugliano et al., 2004) (Arsiero et al., 2007) and others. Adding on top of the synaptic bombardment a time varying signal allows to study in a more generale way the frequency-currnet curve, which becomes the transfer function of a neuron, see the review (Giugliano et al., 2008) some other more recent works: (Köndgen et al., 2008), (Tchumatchenko et al., 2011), (Boucsein et al., 2009), (Linaro et al., 2017) and others. A recent paper from Richardson (Richardson, 2018), it recreates the

diffusion approximation as one possible case of another stochastic process, which seems to be more general and more indicated to investigate the I-O neocortical neuronal properties; however it will be discussed later subsection Lack of universality of the response function, for realistic synaptic input "models". The diffusion approximation is applied in neuroscience as "synaptic noisy" input and it is recreated with the stochastic process of OU previously mentioned. Hence, here it is a short explanation over the stochastic OU process. The process of Ornestein-Uhlenbeck $x(t)$ see equation 18 is a continuous in time and values stochastic process wth a lot of application in physics, finance and computational neuroscience. It can be defined by the following first-order stochastic differential equation, complemented by the (deterministic) initial condition $x(t_0) = x_0$:

$$\tau \frac{dx}{dt} = \mu - x + \sigma\sqrt{2\tau}\xi(t) \tag{18}$$

In equation 18, $\xi(t)$ is not a conventional function; it is instead a *Gaussian white-noise* and it is not differentiable. However, exploiting the analytical solution of first-order ordinary differential equations it is possible to derive the statistical properties of $x(t)$. In the end, note that $\xi(t)$ is characterised by zero mean, unitary variance, autocorrelation function, and probability density distribution as follows:

$$< \xi(t) > = 0 \tag{19}$$

$$< \xi(t)^2 > = 1 \tag{20}$$

$$< \xi(t)\xi(t+T) > = \delta(T) \tag{21}$$

$$p_\xi(Z) = (\sqrt{2\pi})^{-1} e^{-Z^2/2}. \tag{22}$$

Sometimes in literature, the equation 18 is without the leading τ on the left hand side, or while renaming the term $\sigma\sqrt{2\tau}$ as $\sqrt{2D}$. Here, it has the advantage that the

steady-state mean and variance are clearly identifiable by direct inspection of its right hand side and, most importantly, as the physical units of $x(t)$, μ, and σ are the same (e.g. *pA*). The *relaxation* time (or autocorrelation time length) τ is measured in the units of t ($[t]$, e.g. *ms*) and $\xi(t)$ in $[t]^{1/2}$.

As equation 18 is linear, the probability density distribution of $x(t)$ is also Gaussian. Proving this statement requires deriving the *Fokker-Plank* equation associated to equation 18, which is a partial derivatives differential equation where the unknown is $p(x,t)$ the probability density function of x at time t. It follows that the expected value, the variance, and the autocovariance (or the autocorrelation function) of $x(t)$ fully determine the OU process. It has been derived all analytical derivation, of the statistics of $x(t)$.

The expected value of $x(t)$ is time-varying and converging to μ, over a time of the order of τ:

$$m(t) \; = < x(t) > = \; x_0 e^{-(t-t_0)/\tau} + \mu \left(1 - e^{-(t-t_0)/\tau}\right) \longrightarrow \mu \tag{23}$$

The variance of $x(t)$ is time-varying and it converges to σ^2, over a time of the order of τ:

$$s(t)^2 \; = < [x(t) - m(t)]^2 > = \; \sigma^2 \left(1 - e^{-2(t-t_0)/\tau}\right) \longrightarrow \sigma^2 \tag{24}$$

The covariance of $x(t)$, defined as $< [x(t) - m(t)]\,[x(t+T) - m(t+T)] >$, is also time-varying and converges to $\sigma^2 e^{-|T|/\tau}$, over a time of the order of τ:

$$Cov_x(t,T) \; = \; \sigma^2 e^{-|T|/\tau}(1 - e^{-2(t-t_0)/\tau})) \longrightarrow \sigma^2 e^{-|T|/\tau} \tag{25}$$

In the end, $x(t)$ can be simulated numerically by the following *exact* iterative expression

$$x(t+\Delta t) = e^{-\Delta t/\tau}\, x(t) + \mu\left(1 - e^{-\Delta t/\tau}\right) + \sigma\sqrt{1 - e^{-2\Delta t/\tau}}\;\phi \tag{26}$$

where ϕ is a uncorrelated Gauss-distributed random variables, with zero-mean and unitary variance, and where it is not required for Δt to be infinitesimal.

3.6.3 Stein's process and *diffusion* approximations

The Stein's (S) process $y(t)$ is another continuous-time continuous-valued stochastic process, applied in Neuroscience in the very same contexts of OU. It is defined by the following first-order stochastic differential equation, complemented by the (deterministic) initial condition $y(t_0) = y_0$:

$$\tau\frac{dy}{dt} = -y + \tau J\sum_k \delta(t - t_k) \tag{27}$$

In equation 27, the train of Dirac's Delta functions $\sum_k \delta(t - t_k)$ captures the effect of incoming external events, whose occurrence times $\{t_k\}$ are random as in a *shot-noise*. These events cause the variable y to suddenly increase its current value by a (fixed) amount (i.e. as a *jump*) specified by J, while in the interval between two successive events y decays exponentially towards zero with time constant τ. This can be easily demonstrated by integrating both sides of equation 27 around each time of occurrence of an external event (i.e. let say in the range $(t_k^-; t_k^+)$. The statistics of occurrence of the events is independent on the previous history (i.e. renewal property) and expressed in terms of the equation 28 as follow:

$$Prob\,[an\ event\ occurring\ in\ [t; t+\delta t)] = \lambda\,\delta t + O(\delta t) \tag{28}$$

When λ - representing the *rate* of occurrence is constant in time, the set $\{t_k\}$ identifies a homogeneous *Poisson point process*. It is easy to show that the associated probability density function of the inter-event times is exponential. One can for instance define the *survival* probability $S(\Delta)$ as the probability that the next event (e.g. say t_{k+1}) will occur after at least a time interval of length Δ, given that one previous event occurred at the beginning of the interval (i.e. $t_{k+1} > t_k + \Delta$). Then, one can easily conclude that $S(0) = 1$ and that $S(\Delta + dt) = S(\Delta)\,(1 - \lambda dt)$. Rearranging the last expression, and also using the first one as initial condition, allows one to prove that in the limit of $dt \to 0$, $dS(\Delta)/dt = -\lambda S(\Delta)$ and hence $S(\Delta) = e^{-\lambda\Delta}$. The probability distribution for the inter-event times (i.e. $Prob\,[interval < \Delta]$) is the complementary of the survival probability (i.e. $1 - S(\Delta)$) so that the probability density is the derivative of $1 - S(\Delta)$ with respect to Δ, thus $\lambda\ e^{-\lambda\Delta}$.

Under the hypothesis of infinitesimal J and infinitely frequent occurrence rate λ (i.e. so that the product $J\ \lambda$ remains finite) and whenever explicitly or implicitly under the sign of integration, one can replace the process $\tau J \sum_k \delta(t - t_k)$ by a *Gaussian white-noise* $\mu + \sigma\sqrt{2\tau}\xi(t)$, with parameters chosen as:

$$\mu = J\ \lambda\ \tau \qquad \sigma = J\ \tau\sqrt{\frac{\lambda}{2\tau}} = J\sqrt{\frac{\lambda\,\tau}{2}} \tag{29}$$

The equation 29 *diffusion approximation* and allows to use the Ornstein-Uhlenbeck through equation 18 instead of the Stein's process through equation 27. Incidentally, the above expressions provide in all the cases (i.e. even for finite J and λ) steady-state mean and standard deviation of $y(t)$, avoiding manipulating directly the Dirac's Delta functions. The Stein process is more realistic than the OU one, it is a generalisation of it to a finite value of J and finite frequency of input. As previously mentioned, from a recent work of Richardson (Richardson, 2018), the process of Stein has been showed as a generalisation of the diffusion approximation and provided a very intriguing results from a mathematical integration of the Fokker-Plank equation on

the membrane voltage evolution over time of a EIF model with a shot noise input (Stein process). In the next paragraph it will be further discussed this topic.

3.7 Lack of universality of the response function with realistic synaptic input models

The characterisation of a dynamical linear system it is universal and only based on the system features without any dependencies on the external input or stress provided to it. Whatever will be external input, the frequency system response will only depends on the system features themselves, an example could be taken from the electronics: the RC circuit, which has its characteristic poles and zeros at different frequencies of modulation of the input, which determine the pass-band behaviour of the circuit. The RC system has its cut-off frequency starting from there the signal is attenuated from a factor of $\frac{1}{\sqrt{2}}$. The RC circuit description has been applied over neuron to describe their electrical behaviour over the frequency domain and neuron has been studied as dynamical linear system. The neuronal I-O relationship considering a time-varying input has the goal to study the neuronal behaviour in a wide brand of frequencies; as it has been shown in the previous section section Recent applications of System theory in Cellular Electrophysiology. From the literature, firstly, it has been established that neurons behaves as the linear dynamic system; however from a recent study, i.e. (Linaro et al., 2017) and (Köndgen et al., 2008), it has been showed that at low and intermediate modulation frequency the intensity of the synaptic background and of the output firing rate affected the magnitude of the signal. On the other hand, the HF domain was unaffected by any of those conditions and hence, only depending on the neuronal properties. Nevertheless, the Richardson's study previously mentioned, it has been shown that the diffusion approximation predict only an universal exponent for the power-law at HF, which however is a particular case of the more general process of Stein used in Richardson's work, which shows a non-universal exponent which depends on the interplay between statistic of the input and neuronal properties. A well establish approach is to model the the synaptic barrage, which a neuron undergoes *in vivo* with a Gaussian white-noise as input with high rate and very low

amplitude and short temporal correlation (Richardson, 2018). The synaptic barrage has been reproduce in the leaky integrate-and-fire neuron using the OU process with a threshold reset applying the Fokker-Planck formalism (Johannesma, 1968) (Ricciardi, 1977) to calculate the instantaneous firing rate, spike-train spectrum at the level of single neuron or unconnected population (Lindner et al., 2002). The synaptic potentials in quiescent tissue of neocortical pyramidal neurons have an amplitude log-normal distribution (Song et al., 2005), having as mean value between 1-2 mV (Reyes and Sakmann, 1999) (Perin et al., 2011). A value of 1-2 mV is huge, considering the voltage membrane V_m fluctuations, a input of that magnitude can easily bring the cell from the resting value to the threshold one during the network activity; this happens since the V_m is below, but not far from the threshold value and only few inputs are enough to provoke an AP firing (Destexhe et al., 2003) (Sanchez-Vives and McCormick, 2000). A positive correlation within the presynaptic population likely increase the occurrence of the presynaptic inputs at the same time, improving the synapse pulses amplitude (Deniz and Rotter, 2017) (DeWeese and Zador, 2006), on the other hand, short-term synaptic depression acts on the opposite way reducing the afferent inputs in the same time window (Abbott et al., 1997). From the outcome of experimental results it has been suggested that the synaptic amplitude distribution is a function of the network state (in active network) and the diffusion approximation approach is not reliable. However, the diffusion approximation approach with small amplitude and high rate is currently used in a lot of studies and with different models; investigating subthreshold voltage fluctuations (Wolff and Lindner, 2008) (Hohn and Burkitt, 2001), firing properties (Cain et al., 2016) (Iyer et al., 2013) and many others. A very good idea is to provide to the neurons a more biophysically detailed input of synaptic drive than the diffusion approximation; for instance neurons driven by shot-noise respond faster (Helias et al., 2011) and have a different response to HF modulation (Richardson and Swarbrick, 2010). There is also an important

difference to underline between the diffusion approximation and the shot-noise, the first one has the inhibitory fluctuation which contribute to the voltage variance of the input which contributes to bring the V_m across the threshold; on the contrary, the shot-noise has only the excitatory component which is the one causing the APs. Another important aspect is that the shot-noise derived results have been obtained with the leaky integrate-and-fire neuron (LIF), which leaks of an accurate description of the V_m over time in the region close to the threshold for spike initiation; since the current-voltage relationship is non-linear due to the activation of the spike-generating sodium current (Hodgkin and Huxley, 1952). Other models have been proposed to better describe the voltage dynamics of a neurons especially during an AP initiation, a model which shows a very accurate agreement with the experimental data is the exponential integrate-and-fire neuron (EIF) model (Fourcaud-Trocmé et al., 2003) of the neocortical pyramidal cells in layers II,III, IV and V (Badel et al., 2008b) (Harrison et al., 2015) and fast-spiking interneurons (Badel et al., 2008a).

The EIF suggested a reduction to few parameters and a reduction to one variable which has a nonlinear current-voltage relationship composed by a linear term plus and an exponential non-linearity close to the AP initiation threshold (Fourcaud-Trocmé et al., 2003).

From experiments, it has been measured a voltage range around the spike initiation threshold, which is between 0,5-1,5 mV, this range will be called dT. The spike onset sharpness dT has a key role in setting the cut-off frequency at HF domain for a population of EIF having as input a synaptic drive; smaller is dT, higher is the cut-off frequency (Fourcaud-Trocmé and Brunel, 2005). Experimentally, the synaptic amplitude values are around the value of $1mV$, which is the same order of magnitude of dT. The question of the author is whether there is an interplay between the input statistic such as the mean of the synaptic input a_s and the dT, playing a role on the neuronal integration.

Considering a population of neurons, each of them has its own value of membrane voltage v and receive and independent realisation of Poissonian shot-noise $s(t)$ with a rate $R(t)$, see the general differential equation below 30.

$$\frac{dv}{dt} = s(t) + f(v) \tag{30}$$

The Poissonian distributed pulse over time t_k has as well an amplitude distribution with coefficient a_k drawn independently from $A(a)$; in general the shot noise is written as equation 31:

$$s(t) = \sum_{t_k} \delta(t - t_k) a_k. \tag{31}$$

The amplitude distribution A(a) is considered to go beyond the diffusion approximation approach and is $A(a) = \delta(a - a_s)$ considering fixed, bus not necessarily small the mean synaptic amplitude a_s. Later, the A(a) will be changed to match a more physiological barrage. It is important to consider that the previously mentioned rate of the presynaptic rate is sinusoidally modulated by $f = \frac{\omega}{2\pi}$, and written in its complex form, such as the equation 32:

$$R_s(t) = \overline{R}_s + \hat{R}_s e^{i\omega t}. \tag{32}$$

Considering the EIF model and its voltage dynamics, the equation 30 can be rewritten as:

$$\tau \frac{dv}{dt} = \tau s(t) + -v + dTe^{\frac{(v - v_T)}{dT}} \tag{33}$$

together a value of threshold v_{re}, which reset the V_m when goes to infinity. *tau* is the membrane time constant and dT is smaller than v_T and are positive parameters which characterise the onset of the action potential or spike. The biophysical meaning of dT and v_T are respectively, the rapidity of the sodium current activation which generate the APs and the threshold found which minimise the I-V of the EIF (Fourcaud-

Trocmé et al., 2003). Combining the EIF model with the finite-amplitude synaptic drive $A(a)$ have been firstly investigated the HF behaviour of the model. From the work of Badel and colleagues the model has been shown to provide an accurate description of experimental data (Badel et al., 2008b) maintaining a good level of mathematical tractability. The diffusion approximation driving the EIF model through the synaptic drive has been an extensively matter of study, in the limit of an high input rate R_s and a small amplitude of a_k bringing to a Gaussian white-noise process.

The HF behaviour firing rate response is shown 34

$$\hat{r}(\omega) \sim \frac{\tau\bar{r}}{i\omega\tau}\left(\frac{<a>}{dT} + \frac{<a^2>}{2dT^2}\right) \tag{34}$$

where $\bar{r}$ is the steady-state rate. The diffusion approximation approach predicts an universal exponent for the HF, such as $\hat{r} \sim \frac{1}{i\omega^{\beta}}$ where $\beta = 1$ which is universal, since it is not depending on the parameters of the externally imposed synaptic drive. Considering the amplitude distribution $A(a)$ as $A(a) = \delta(a - a_s)$, the HF behaviour is given:

$$\hat{r} \sim \hat{R}_s \frac{\tau\bar{r}}{i\omega\tau}\left(e^{\frac{as}{dT}} - 1\right) \tag{35}$$

which is close to $\frac{1}{\omega}$ for small value of the fraction $\frac{as}{dT}$. Now introduce a more physiological description for the distribution $A(a)$:

$$A(a) = \frac{e^{\frac{a}{a_s}}}{a_s} \tag{36}$$

where a_s is the mean of the distribution. From the work of Song and collaborators (Song et al., 2005) the distribution of isolated synaptic amplitude is log-normal for layer V pyramidal neurons; nevertheless is important to consider additional process present in a neuronal network like short-term depression/facilitation and presynaptic

correlation. For the author, an exponential distribution tail is a reasonable choice for the presynaptic amplitude in a active network.

With this new more physiological input, the next step is comparing the I-O response curve at HF and see if it changes; as expected the Stein process (the input) will affect the I-O response curve HF domain. To perform an accurate analysis has been distinguish three different cases:

- a_s smaller than dT
- a_s equal to dT
- a_s bigger than dT

Consider an output synaptic rate R_s adjusted to have a firing rate equal 5 Hz. See the figures 28 and 29 for more details.

Considering the figure 29 the case with a_s smaller and equal than dT are reproducing the diffusion approximation approach; on the other hand the case a_s bigger than dT the input amplitudes below the v_T contribute more significantly than the local jumps. Then, considering the HF domain of the three different cases, it has been obtained:

$$a_s < dT$$

$$\hat{r}(\omega) \sim \hat{R}_s \frac{\bar{r}\tau}{i\omega\tau} \frac{a_s}{dT - a_s} \tag{37}$$

$$a_s = dT$$

$$\hat{r}(\omega) \sim \hat{R}_s \frac{\bar{r}\tau}{i\omega\tau} log(i\omega\tau\tilde{\kappa}) \tag{38}$$

$$a_s > dT$$

$$\hat{r}(\omega) \sim \hat{R}_s \frac{\bar{r}\tau I_s}{(i\omega\tau)^{\frac{dT}{a_s}}} \Gamma(\frac{dT}{a_s} + 1) \tag{39}$$

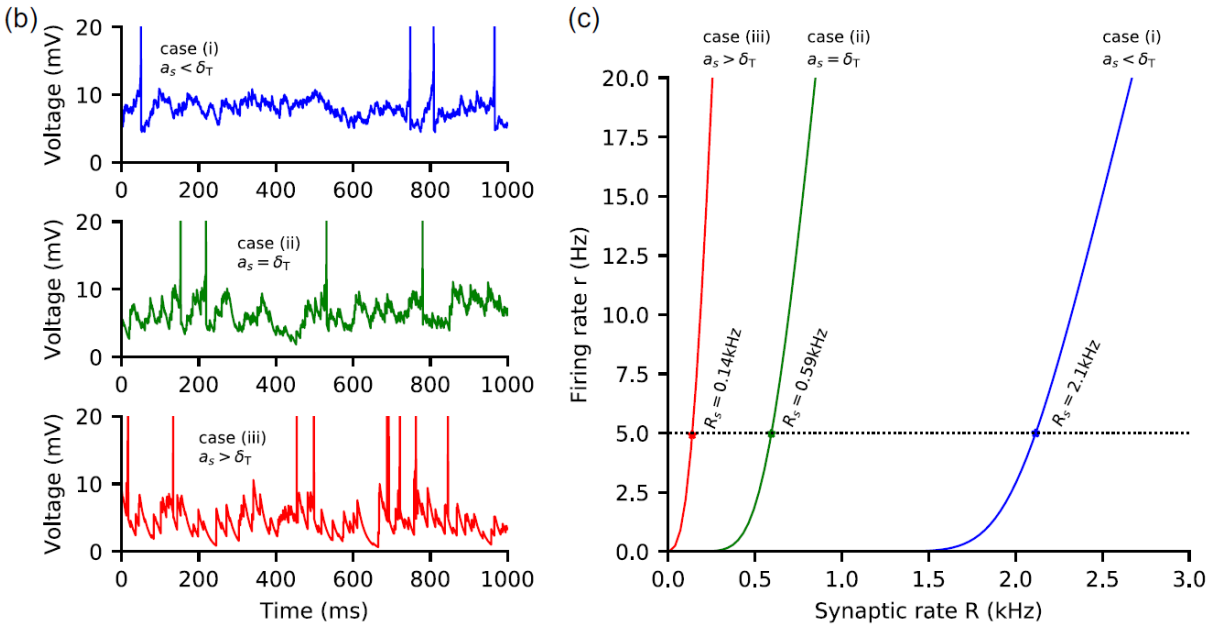

Figure 28: EIF neuron steady state properties, the driven input is a shot noise with an amplitude distribution as in the equation 64, hence an exponential distribution. The parameters used are $\tau = 20ms$, $v_T = 10mV$ and $dT = 0,6mV$. In panel b, the membrane voltage V_m over time for all the three cases, with a_s smaller, equal or bigger than dT. The mean value of a_s are $a_s = 0.2$, 0.6, and 1.8 mV, respectively. The synaptic rate $\overline{R}_s$ is r = 5 Hz. In panel c, the output firing rate $\bar{r}$ versus the synaptic rate $\overline{R}_s$, the intersection of the dotted line and the firing curve is the reference at 5Hz. Other parameters used are $v_{re} = 5mV$ and $v_{th} = 30mV$. The figure is taken and modified from (Richardson, 2018).

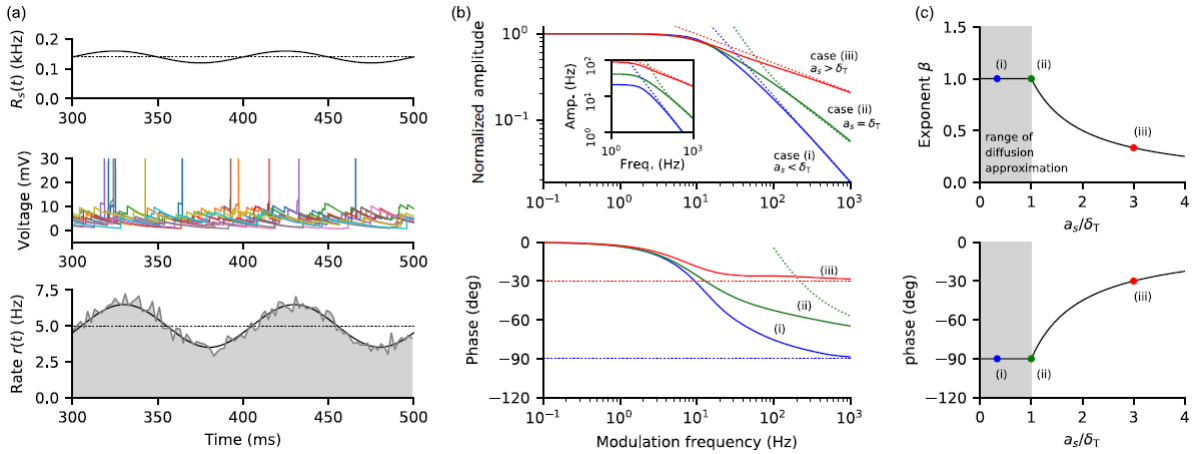

Figure 29: The response of an EIF population neurons driven by synaptic rate. In panel a, at the top, weak sinusoidal modulation from equation 32 of the synaptic rate $R_s(t)$; it induces a population sinusoidal modulation of the firing rate $r(t)$ around its steady state (middle panel and bottom one, the histogram is compared to theory). The amplitude and phase shift of the firing-rate response are frequency dependent. In panel b, it has been shown the amplitude (top panel) and the phase (bottom panel) of $\hat{r}$ as a function of the modulation frequency of the three cases. The steady state of the output firing rate is 5 Hz. The amplitude is normalised over the low frequencies amplitude and the dashed line s show the asymptotic forms in equations 39 and 38. To consider the third case, it has 50 times the amplitude of the first case at HF ($R_s = 1000Hz$). The inset shows the unnormalized amplitude. In panel c, the HF exponent as a function of the ratio of a_s and dT at the top; in the diffusion approximation approach the exponent is stable at one at the HF domain; however when a_s is bigger than dT the value become smaller and smaller. The same idea for the phase shift between input and output; in this case as expected it passes from an advance of the phase to a delay. Model parameters are the same as figure 28. The figure is taken and modified from (Richardson, 2018).

where $\Gamma(m)$ is the standard gamma function, $\tilde{\kappa} = \kappa e^{\gamma - 1}$ with *gamma* the Euler-Mascheroni constant. The most important result, however is the HF domain in which the power-law attenuation has not an universal exponent! The fraction $\frac{1}{(i\omega)^\beta}$ the $\beta = 1$ predict by the diffusion approximation is still valid in the case of $a_s < dT$ and $a_s = dT$, in which the synaptic amplitude are small. On the other hand, when the synaptic amplitude aren't small, such as $a_s > dT$, the exponent is equal to $\beta = \frac{dT}{a_s}$ and is a function of the synaptic distribution. The figure 29 shows in panel c the phase and the HF exponent behaviour as function of the ratio $\frac{dT}{a_s}$.

It is important note that these very significant results have been obtained in the hypothesis the value of the voltage threshold value v_{th} is infinite (value at which an AP is recorded) and then, the V_m is reset to V_{re}. Although, this numerical setup is not even close to a real experiment; therefore a finite threshold for recording an AP is chosen as it is usual to do in an experiment. An obvious question to the author answered was: "Are the previous results still valid, when the modulation frequency crosses a certain value?" The authors found that the crossover frequency (cut off frequency) grows exponentially with v_{th}, hence the previous results remain correct. The crossover frequency can be calculated from the following equation:

$$F_c \sim \frac{1}{2\pi\tau} e^{\frac{v_{th}-v_T}{dT}} \tag{40}$$

The following result showed in the figure 30, for finite thresholds atv_{th} =12, 13, and 14 mV. In the panel a of figure 30 it is showed the EIF exponential term of $f(v)$ and the crossover frequency in the inset.

Moreover in the first b panel of figure 30,it is clearly showed the asymptotic behaviour with the $v_{th} = 12$ mV with a crossover at $\sim$ 130 Hz; this threshold is only bigger of 0,2 mV than the unstable fixed point. If the v_{th} is increased of 1 mV only the crossover frequency increases to $\sim$ 1000Hz (middle b panel of figure 30) and with a further of 1 mV to 2,3 mV above the unstable fixed point the crossover goes above 6000 Hz (last b panel of figure 30).

Another important step more of realism is the synaptic filtering due to the finite closing time of the excitatory synaptic channels. This effect can be taken into consideration by including a dynamics for the synaptic drive. such as:

$$\tau_s \frac{ds}{dt} = -s + \sum_{t_k} \delta(t - t_k) a_k \tag{41}$$

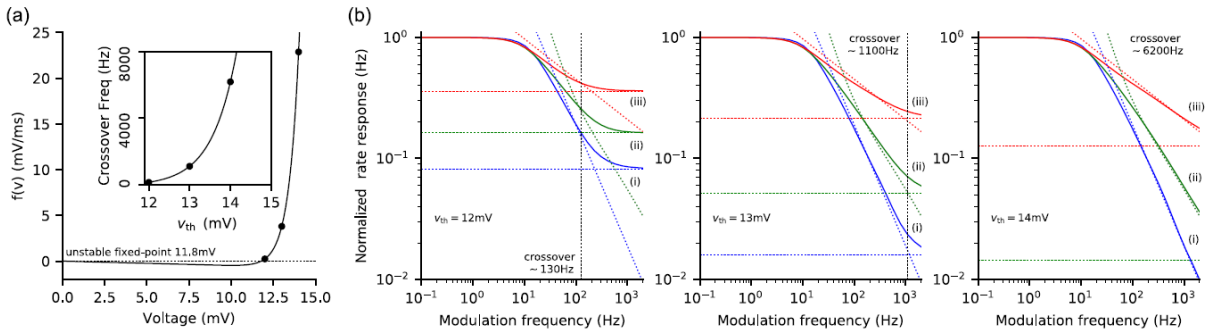

Figure 30: Effect of a low spike threshold on the modeled high-frequency response. In panel a, the forcing term $f(v)$ and in the inset the crossover frequency, the spike threshold are marked $v_{th} = 12$, 13, and 14 mV. In panel b, the firing rate response curve for these three different thresholds, with the infinite-threshold asymptotic in equations 38 and 39. Together there is as well the corresponding finite-threshold HF constant asymptotic (dotted horizontal lines) for each of the three cases. The crossover frequency are the vertical dotted line, which increase exponentially with the threshold v_{th}. Parameters are the same as for figure 28 unless marked. The figure is taken from (Richardson, 2018)

where the τ_s is the time constant of the synaptic filtering and a_k comes from the exponential distribution of before, see the equation 36.

The synaptic filtered drive modifies as well the postsynaptic potential giving it a two exponential form considering τ and τ_s in the same time scale for an isolated input and t >0, see the following equation:

$$v(t) = a_k \frac{\tau}{\tau - \tau_s}(e^{\frac{-t}{\tau}} - e^{\frac{-t}{\tau_s}}). \tag{42}$$

From experiments, the τ_s time scale has a mean around $1,7$ ms (Häusser and Roth, 1997) and in the range of $1,3$–2 ms (Kleppe and Robinson, 1999); without considering the dendritic filtering that can increase the value up to $(2,9 \pm 2,3)$ ms (Markram et al., 1997). in the figure 31 panel a, around the firing-rate steady state, r = 5Hz the τ_s and the $\overline{R}_s$ are numerically extracted. In the panel b the four graphs of figure 31, the normalised amplitude is measured plotted for the different τ_s values, from $\tau_s = 0$ ms to 3 ms. The numerical simulations are compared to the solution of the master equation like the panel b of figure 29. In the same panel, τ_s spans from 0 to 3

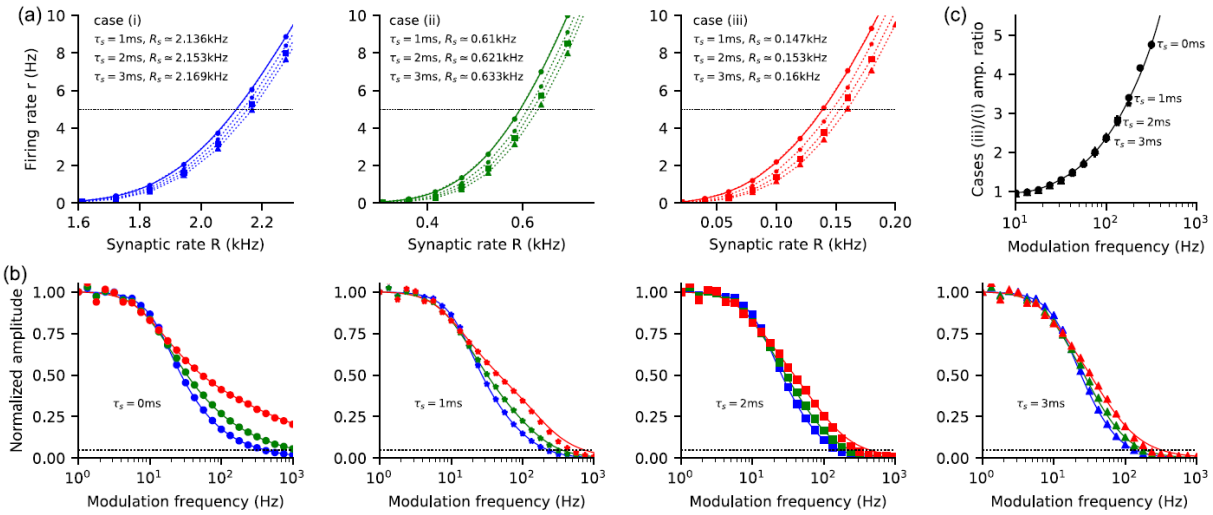

Figure 31: he Effect of shot noise with synaptic filtering. In panel a, the three cases (blue, green,red) have shown their steady-state rates for different τ_s values 0,1,2,3, ms. The synaptic rate for 5 Hz are showed in the panels. In panel b, the normalised amplitude of the rate modulation comparing the three cases for four different time constants τ_s. There is a very strong suppression in the HF domain. In panel c, it is shown the amplitude ratio between the cases $a_s > dT$ over $a_s < dT$ for synaptic time constants. The increased responsiveness of $a_s > dT$ respect than $a_s < dT$ is still present even in presence of synaptic filtering at least up to 100 Hz. The figure is taken from (Richardson, 2018)

ms; corresponding and an heuristic fit was perform to obtain the corresponding $\hat{r}_0$ in presence of synaptic filtering:

$$\hat{r}_s \sim \frac{\hat{r}_0}{\sqrt{1+(\omega\tau_s)^2}} \tag{43}$$

The heuristic fit gives indications about the behaviour at intermediate frequencies of the amplitude, but in the HF domain the modulation is suppressed (especially over 300 Hz), see the figure 31 panels b. The panel c of figure 31 shows the ratio of the cases when $a_s > dT$ over $a_s < dT$ (red divided by blue) from the panel b. It is showed the HF domain response is different and still stronger in the first case, to demonstrate it the amplitude ratio is showed as a function of the modulation frequency for the four different τ_s. The black line is the numerical solution ratio of the master equation

for τ_s =0 ms. It is possible to note that the heuristic form gives the same result for τ_s =0 ms, since the ratio makes τ_s-independent the amplitude.

3.8 Review of neuronal dynamics *in silico* studies from single neuronal model to multi-compartmental ones

3.8.1 Modelling cells: the Exponential Integrate-and-Fire model

The description of the cells electrical behaviour of excitable cells is no recent. At the end of the 18th century, precisely 1790, Luigi Galvani, using a frog, applied an electrical stimulus on a nerve, observing the innervated muscle contract itself. An year later, he described his discover in his book: "De viribus electricitatis in motu musculari". He was, more in general, sure about the electrical stimuli come from the brain and through the nerve transmit to the muscles. Then, having a big jump over centuries, we will arrive to the most important description of an electrical behaviour of a neuron from an axon squid by Hogdkin and Huxley in the half of the 20th century. From their experiments, they formulate a mathematical model able to describe the time evolution of the cell membrane potential. The model is composed by four ordinary differential equations (ODEs), describing the time evolution of the K^+ and Na^+ concentration as well as the total current. The Hogdkin and Huxley model (HH model) is the basis of the further conductance-based models, such as the Integrate-and-fire models. There are many models which are HH based; some examples could be the FitzHugh-Nagumo model which is a mathematical reduction of the HH model, the model proposed by Wang and Buzsáki (WB) (Wang and Buzsáki, 1996); which is a HH based modified model with 3 ODEs, describing the time evolution of the leak current, fast Na^+ current activation and the delayed rectifier K^+ current. This model very well describes the interneurons network discharge. From the work of N. Fourcaud-Trocmé (Fourcaud-Trocmé et al., 2003), it has been introduced the exponential integrate-and-fire neuron (EIF) as one-variable conductance based model to describe the dynamics of neuronal membrane voltage. The model is very well in accordance with the WB model and it replicated the exponential upswing of

an APs due to the Na^+ channel activation than the previous leaky and quadratic integrate-and-fire models (LIF,QIF) (Fourcaud-Trocmé et al., 2003). The authors theoretically investigated the neuronal response to fluctuating inputs over time using analytical and numerical simulations.

Considering the model EIF and QIF, the parameters have been chosen to have the firing onset at the injection of a constant current able to reproduce the WB model close enough to the current threshold see figure 32

The figure 32 shows that the firing rate evoked in response to an injection of an input current is very close in EIF and WB models (up to 200 Hz). QIF neuronal model well reproduce the WB model at low frequency, but not at HF. The LIF, on the other hand, can reproduce reasonably well at the HF the WB model; however at low frequencies it cannot since there is a difference mathematical dependency of the firing rate over the current. Considering the figure 32 panel B; it shows the F-I curve of the different models in response to a noisy current input. As before, the QIF and EIF F-I match very well the WB F-I, however the match between the WB model and the EIF one covers a broader input current range.

To have a deeper insight of the spiking dynamics of these models, the figure 33 is very accurate. The voltage traces of the different models are the neuronal answer to the same input current. The figure 33 panel A shows the same models behaviour in a large time scale. Nevertheless, to appreciate the difference between models, it is necessary have a more refined look of the voltage traces as shown in panel B. The best match with the WB neuron is the EIF model, on the contrary LIF and QIF spiked or before or after. The same behaviour of the EIF and WB models is due both by the same leak current present in the models and since their I-V are very similar close to the threshold voltage (V_T). This last similarity stays since the WB model activation curve for the fast Na^+ current can be very well approximate by an exponential function, see panel C in figure 33. As previously mentioned, the membrane potential

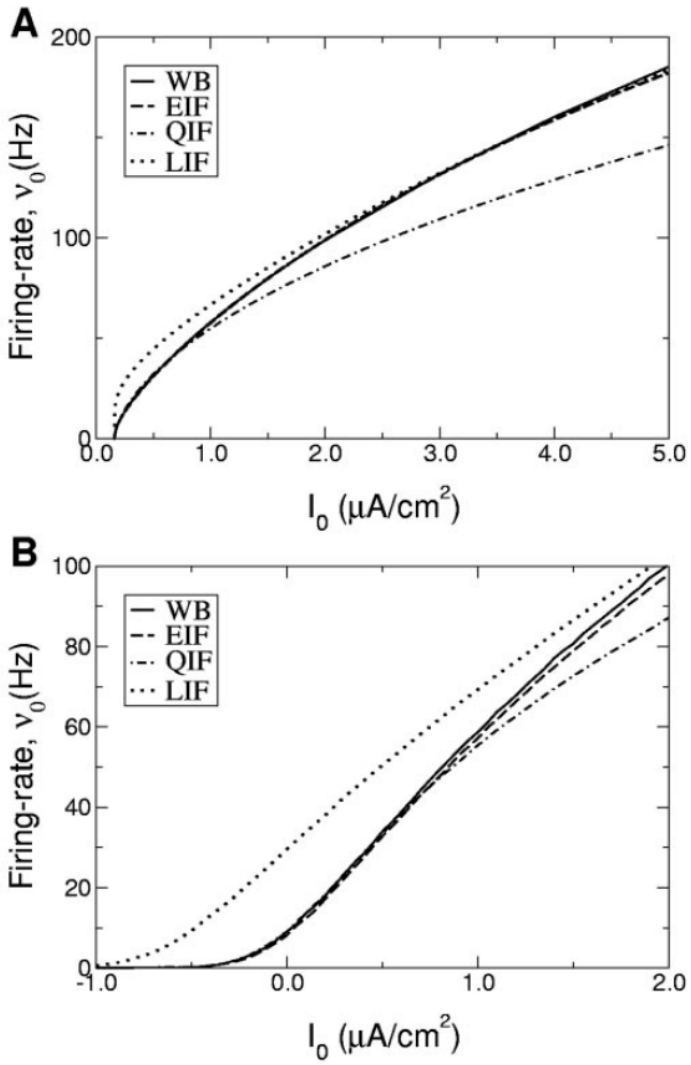

Figure 32: In panel A and B are showed the LIF , QIF, EIF and WB neuronal models that undergo to an injection of input constant current in A and a noisy input current in B (Gaussian white noise with σ = 5mV). The firing rate range of the F-I curve of QIF and WB models matches, however the match is smaller than the one in which EIF and WB match as well. On the contrary the LIF model doesn't match at low frequencies since the different dependencies of the firing rate on the input current doesn't allow an accordance. On the contrary, considering the HF domain the LIF can match the WB considering a good choice of parameters. Figure taken from (Fourcaud-Trocmé et al., 2003).

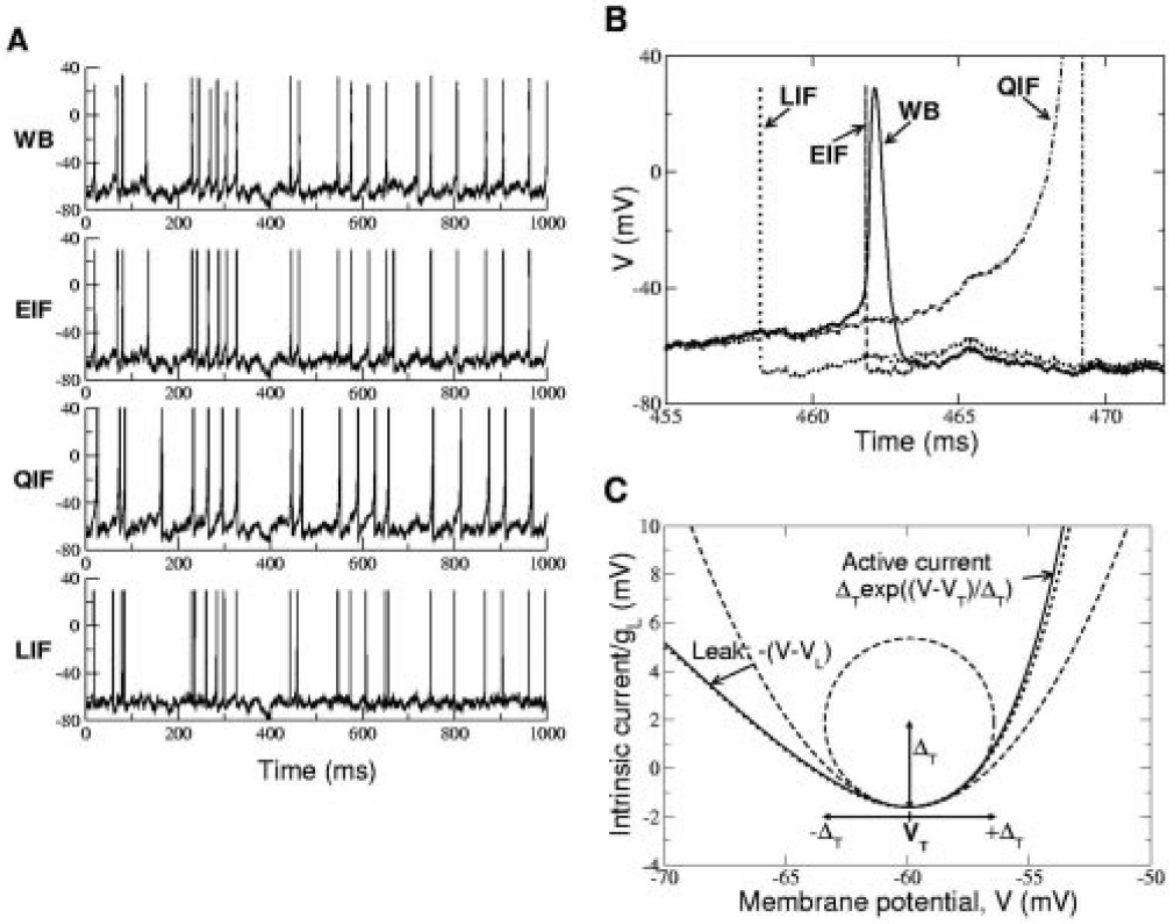

Figure 33: In panel A, the voltage traces of WB, EIF, QIF and LIF are shown for the same noisy input current. In panel B, it is shown the same as A, but an higher resolution. The focus is over a spike time; LIF and QIF spike at the wrong time, one before and one after the WB model; on the other hand, the EIF spikes at the same WB onset. In panel C, it is shown the I-V curve of WB and EIF neuronal models, respectively solid and dotted lines. The threshold V_T is the minimum of the I-V curve. The slope factor Δ_T is proportional at the curvature radius of the I-V at its minimum.

dynamics at the spike onset is very close for the EIF and WB models. After the onset, it is independent from the synaptic input and depends only by the Na^+ and K^+ channel dynamics. Furthermore, the spike shape is invariant between models (at the onset), however, after the spike peak the spike shape is different; causing a small delay independent by the input between the two models spikes (around 0,2 ms), see figure 33 panel C.

3.8.2 Cable Equations

Dendrites and nerve axons have been seen as conductors since their external and internal liquid are conducting electricity and usually are simplified and seen as cylinder in their structure. Their electrical membrane resistance is definitely bigger than the one along their interior or exterior core; hence a current inside of them flows parallel to the cylinder axis for a long distance before any leakage. In this very simple model the length of the cylinder is definitely bigger than the diameter, this lead to:

- uniform membrane properties such as (membrane capacitance and resistance, electromotive force, intracellular resistance)
- the cable equation can be simplified to one dimension equation, hence along the cylinder axis the intracellular voltage V_i is a function of time and only one direction of space (Sterratt et al., 2011).
- the intracellular potential gradient can be expressed:

$$\frac{\partial V_i}{\partial x} = -r_i i_i \tag{44}$$

where I_i and r_i are, respectively, the intracellular current and resistivity per unit of length.

Applying on both side the derivative over the space to the equation 44, it will be obtained (Koch and Segev, 1998):

$$\frac{\partial^2 V_i}{\partial^2 x} = -r_i \frac{\partial i_i}{\partial x} \tag{45}$$

the derivative of the current indicates the current flux over a certain discrete unit of δx and in absence of any external source of external current for continuity the membrane current density can be defined as (Koch and Segev, 1998):

$$i_m = -\frac{\partial i_i}{\partial x} \tag{46}$$

Combining the the equation 45 together to 46 and multiplying both sides for r_m the membrane resistance for unit of length, it is still necessary to consider that the extracellular potential and the resting potential E_m are isopotential and independent from time and space. In addition, considering a passive uniform neurite and its value per unit per length of capacitance c_m and a resistance r_m, it is possible to express the membrane current density as (Koch and Segev, 1998):

$$i_m r_m = \tau_m \frac{\partial V}{\partial t} + (V - E_m) \tag{47}$$

where τ_m is the membrane constant time. A next step to the cable equation, is to define the length constant λ as (Koch and Segev, 1998):

$$\lambda = \sqrt{\frac{R_m}{R_i}\frac{d}{4}} \tag{48}$$

In the end, putting all together "the ingredients" listed above the cable equation is ready to be introduced, hence, the analytic approach to solve the passive properties of a neurite.

$$\lambda^2 \frac{\partial^2 V}{\partial x^2} - (V - E_m) - \tau_m \frac{\partial V}{\partial t} = 0 \tag{49}$$

Considering the equal to 0 nA the injected current I_{inj}, V the difference between the internal potential and the external one, τ_m is the membrane time constant and λ has previously defined 48.

In a more realistic situation such as a dendrite branch different "cables" with different properties are connected to each other; to guarantee the continuity of the cable equation some boundary condition are needed. As shown in figure 34 there are three different kind of boundary conditions: sealed end, killed end and leaky end.
In a condition when the tiny end of a neurite is intact,sealed end, the final tip has a very high resistance and there is not current flowing outside of the membrane;the $\frac{\partial V}{\partial x} = 0$. In the case of a killed end, where for instance a dendrite has been cut, its cytoplasm ans the external medium are in direct contact so the difference between and outside is 0 mV.The leaky end boundary condition there is a current flowing through the resistance R_L, equal to $\frac{(V-E_m)}{R_L}$. If a current is injected in a neurite with a sealed end boundary condition, it gets another type of boundary condition, that is defined as $\pm\frac{\partial V}{\partial x} = r_i I(t)$, where I(t) is the injected current.
Another very useful as well as basic idea is the semi-infinite cable, that starts at x=0

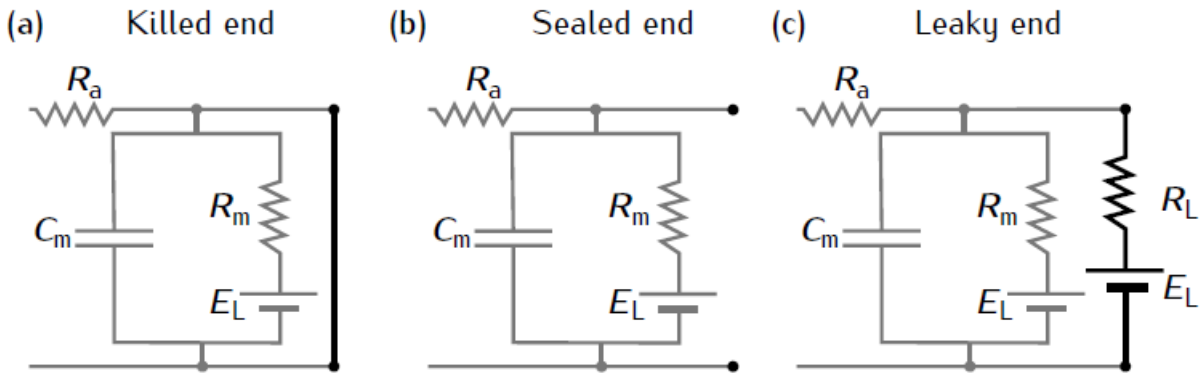

Figure 34: The boundary condition for the cable equation, taken from (Sterratt et al., 2011)

and has a sealed distance at infinite distance with an injection of current equal to I_{inj}. Although it is no realistic, it is a good approximation on how much the potential decay as a function of the length of the cable, and is simply describe by the following equation:

$$V(x) = E_m + R_\infty I_{inj} \exp \frac{-x}{\lambda} \tag{50}$$

with $R_\infty = \frac{R_m}{\pi d \lambda}$ is the input resistance of the semi-infinite cable and λ is the necessary distance to along the cable to decrease by a factor $\frac{1}{e}$ the membrane potential. In a simpler scenario, with $I_{inj} = 0nA$ and with a boundary condition as V= V_0 at x=0. The equation solution of this case is $V(x) = V_0 \exp \frac{-x}{\lambda}$.

3.8.3 Multi-compartimental models

The idea is based on compartimentalisation of neurons (axons and dendrites) in small cylinders and each of them is an isopotential and spatially uniform for its own properties (Koch and Segev, 1998); the difference in voltage are only between the different compartments (RaIl, 1964)(Holmes and Rall, 1992). According to this idea, every cylinder is a compartment with a certain length l, diameter d and surface area: $a = \pi dl$; within each compartment the current flows into the capacitance and the resistance and can flow to the extracellular media and through the cytoplasm in a longitudinal way. Furthermore, the extracellular media has a negligible resistance if compared to the intracellular resistance, hence $R_{ext} \approx 0$, and it is considered as isopotential reference, in other words the ground of the circuit (RaIl, 1964).

Every compartment represents an electrical circuit, hence we can introduce the the N as a total number of compartment, where k $\in$ [1,N]; the potential of the k-th compartment is V_i as well the injected current $I_{inj,k}$ etc. Considering three cylindrical segments of a dendrite,which are sufficiently short to be considered isopotential (Koch and Segev, 1998), then it is possible to reconsider the idea of the I_m now can

flow to adjacent compartment and is no longer true that every compartment is an isolated system; hence I_m is different from zero.

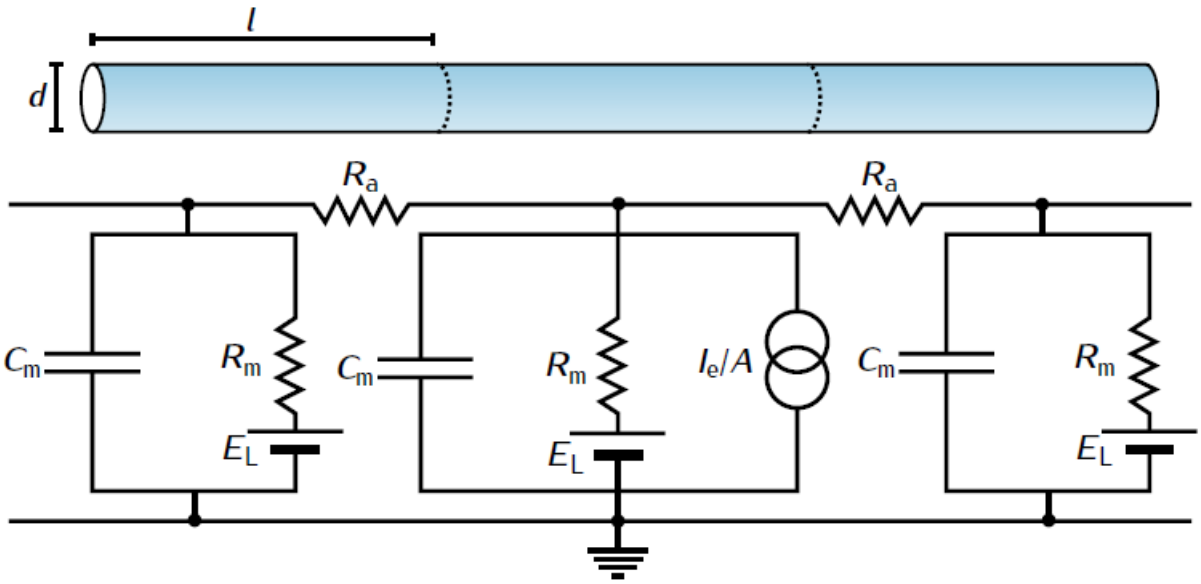

Figure 35: Three adjacent compartments that represent an isopotential part of a neurite, taken and modified from (Sterratt et al., 2011)

The next equation takes care of what happens to the current between neighbouring compartments, such as between the k-1 and k+1 compartment 35.

$$I_{inj,k} + I_{m,k}a = I_{c,k}a + I_{i,k}a = \frac{V_{i+1} - V_i}{\frac{4R_a l}{\pi d^2}} + \frac{V_{i-1} - V_i}{\frac{4R_a l}{\pi d^2}} + I_i \tag{51}$$

with R_a is the axial resistance between a compartment to another and it is defined the resistivity properties of the intracellular medium.

Then, completing the mathematical substitutions, and dividing by the surface area $\pi l d$:

$$C_m \frac{dV_k}{dt} = \frac{E_m - V_k}{R_m} + \frac{d}{4R_a}\left(\frac{V_{k+1} - V_k + V_{k-1} - V_k}{l^2}\right) + \frac{I_{i,k}}{\pi d l} = \frac{V_{i+1} - V_i}{\frac{4R_a l}{\pi d^2}} + \frac{V_{i-1} - V_i}{\frac{4R_a l}{\pi d^2}} + I_i \tag{52}$$

This equation can become way more difficult is the diameter of the neurite change over its ramification. To make easier the integration of the time evolution of the voltage membrane the neurite is divided in cylinders which fixed voltage making a compartments varying over the diameter the sum of small cylinders of constant d. A common rule to divide an unbranched dendrite with more cylinders could be to divide from the starting point to each diameter increment is bigger than 0,1 μm along the dendrite. It is import with the simple geometry shape of the electric circuit. NEURON has packages specifically designed for building compartmental (Carnevale and Hines, 2006) providing a cylinders as the only solution to represent a complex morphology. However, a soma that is spherical, should be translated as a cylinder with the same surface area. In some cases there are some simulation packages, which allow a representation that reflect the division between morphology and electrical compartments. All of this makes easier to change the compartments number of the electrical representation of the morphology. Once the cylinder are set they need to be divided into electrical compartments, these last ones have been assumed to be isopotential. Once the morphology has been represented as a set of cylindrical sections, they must be divided into electrical compartments. Each compartment is assumed to be isopotential. The compartmental models used in simulations have a finite amount of compartments; big enough to make tolerable the error on simulated the real morphology. The error come from the assumption of each electrical compartment is isopotential. A small compartment during the simulation makes smaller the error; on the other hand makes bigger the computational burden. A general accepted rule is to have the compartment size no longer than 10% of the length constant λ_f. Compartmental model could be based over the morphology of real neurons, the use of transgenic approach, tissue fixation or fluorescent dyes. In the idea to reconstruct an entire neurons with its axons and dendrites more slices

are needed to be aligned, There are some software that help in this process such as Neurolucida; which is the one used to reconstruct the BBP neuronal models. Neuronal simulator, like NEURON, can simulate big multi-compartmental models; it could be some cases in which a simpler models more desirable. This happens since a neuron morphology simplifications could lead to an identical electrical compartmental models with a reduced number of compartments and complexity.

In the work of Rall 1964, (RaIl, 1964), he discovered that passive dendrites can be equivalently modelled by a single cylinder that follows the undermentioned rules:

- The membrane resistance R_m and the axial one R_a fave to be the same in all the branches
- The end of each terminal branch must have the same boundary conditions
- The terminal branch end need to be at the same electrotonic distance from the tree base.
- The relation between the parent branch and the two child branches is: $d_1^{\frac{3}{2}} = d_2^{\frac{3}{2}} + d_3^{\frac{3}{2}}$

These rules may seem very restrictive; in fact some of the real neuronal trees such as apical trunks of cortical pyramidal neurons, violate the 3/2 rules. The difference between following the above mentioned rules or not is on the V_m along the tree; if the rule is followed there is a decrease like in a single and equivalent comportment; on the other hand there is an abrupt change in the branch point.

3.8.4 NEURON simulator and robust numerical methods

NEURON (http://www.neuron.yale.edu) is a simulation environment for modelling single neurons as well as neuronal networks. It can simulate: single neurons via section that can be divided into individual compartments, neuronal properties, i.e.

complex branching morphology, multiple channel types, inhomogeneous channels distribution, secondary messenger effects and ionic diffusion (Hines and Carnevale, 2001). It provides tools for handling complex models without requiring a strong computational or coding background. Regarding to simulate single neurons, they are divided into sections and furthermore sections are divided as well into single compartments. In addition, to sections can be assigned properties which can vary continuously along the section length. In this way, it is possible to separate the physical properties from the numerical issue of spatial compartments size helping a more focus investigation on the biophysics/biology of the phenomena, rather than numerical details (Hines and Carnevale, 1997). Sections can be connected together to make cables and branched cables.

It has been mainly developed by T. Carnevale and J.W. Moore with the idea of facilitate the simulation of complex membrane properties and where the geometry plays important roles on it (Arbib, 1998). Later, it has been added other facilitation for studying the longitudinal ionic diffusion and efficient computation representation of neuronal connections (Hines and Carnevale, 2000). NEURON has as primary interface HOC, however, currently is more used a Python interface. Parallelisation is supported by the MPI protocol. NEURON is able to perform diffusion-reaction models and integrating diffusion functions into cellular-network and synapses models. The properties of the membrane channels of the neuron are simulated using compiled mechanisms written using the NMODL language (Hines and Carnevale, 2000). More in details, an user definition of the membrane or cytoplasmic biophysical definitions are described in sets of differential equations and kinetic schemes (Hines and Carnevale, 2001). These models are compiled and the membrane voltage can be efficiently computed using an implicit integration method for branched structures (Hines and Carnevale, 2000). More in general, NEURON is born to facilitates the creation of computational models, which are able to matches the knowledge (Koch

and Segev, 1998) so far and helps to further investigate the physiology of neurons and neuronal networks in many aspects. The possible applications of NEURON make it functional in wide range of research topics, from the basic cellular mechanisms which shred a light on the physiology of a neuron encoding information, which is involved in many process such as memory, learning, consciousness, perception an even helping into the comprehension of some disease like epilepsy, multiple sclerosis, learning and memory disorders (Hines and Carnevale, 2001).

To simulate neurons of network of them, it is necessary to consider the continuity of time and space, chemical and electrical signals spreading are governed by partial differential equations in which potential and flux are smooth function in time and space (Rall, 1977) and others. An establish way to perform the resolution of the set of equations before mentioned is solve them numerically, see for example (Crank, 1980) and(Carslaw, 1986). This approach is similar to solve the original continuous system by another one which on the contrary is discontinuous; this is the NEURON approach on the words of its major contributors (Hines and Carnevale, 1997). The way in which NEURON works is computing continuously some variables over a set of discrete space points called nodes for a certain number of time steps. NEURON has a method to correct the integration, which is of the second of accuracy while integrating the system via linear interpolation on the intermediate temporal and spatial step. Obviously, the step size is a key point to simulate correctly the the system phenomena. I want to stress about how much is important a good choice of the best size for the time and temporal steps; a poor choice can lead to a numerical error and a wrong interpretation of the biological phenomena which is wanted to simulate.

In the paper of Hines and Carnevale, a set of figures, figures 36, 37 and 38 underline the importance of good choice for the time and temporal step, in figure 36 the finest dt is the best choice to emulate the analytical solution. In these figure a not

appropriate step size can lead to wrong or not accurate solutions as well as to correct solutions which have an exaggerated computation burden. In addition, considering the NEURON second order of integration it can oscillate if the spatial step is too large see figure 38 back line, however to prevent any oscillations in the numerical solution time and spatial increments are normalised.

One of the most fundamental problem in NEURON was the spatial decay of a transient signal. The neuronal membrane properties of a single neurons act as low-pass filter, so fast transient signal are cut or greatly distorted and/or attenuated with distance. Hence, to resolve an HF signal in space is necessary a fine grid.

The authors proposed a criterion based on the length constant λ_f, that is computed at a certain frequency f, that is high enough to have the transmembrane current mostly capacitive.

this last current and the ionic one are equal at the frequency$f_m = \frac{1}{2\pi\tau_m}$, hence R_m has a small effect on the propagation of the signals $\geq 5 f_m$.

Usually, cells have membrane time constant τ_m bigger than 8 ms ($f_m \sim$20 Hz), so the distance of an adjacent node should not be bigger that a certain fraction of the constant length at 100 Hz, λ_{100}. This frequency is reasonably high to be insensitive to ionic conductance shunting, however not so high compared to fast EPSPs and spikes that are around 1 ms, that corresponds to $\sim$400 Hz.

$$\lambda_f \sim 0,5\sqrt{\frac{d}{\pi R_a C_m}} \tag{53}$$

where d is the diameter, C_m the membrane capacitance e R_a the access resistance. In NEURON the lambda rule is implemented by the CellBuilder, which allows to specify the anatomical distance between the grid points as a fraction of λ_{100}, the adjustable parameter that care of this is called d_lambda; the default values is 0,3. The figure 39, panel A, shows how works the d_lambda rule in a model of rat

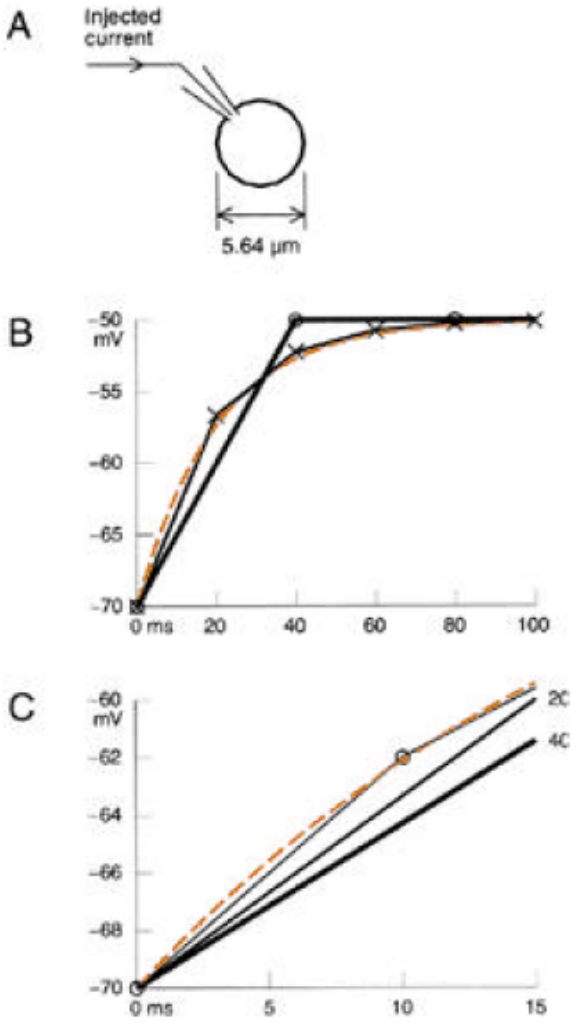

Figure 36: In Panel A, a simple model represent a spherical cell with surface 100 mm^2. The resting potential, V_{rest} is -70 mV and the membrane capacitance is $1\frac{mF}{cm^2}$, the membrane resistance is $20\Omega cm^2$ time constant $\tau_m = 20ms$. A 1 pA of depolarising current is injected at t =0 ms. In panel B, the orange dashed line is the analytic solution for the first 100 ms for the V_m, the solid line are the computed solutions; with dt 40 ms (circle) and dt =20 ms (cross). In panel C, the graph is in an expanded scale. Circle are for a dt of 10 ms and 20 and 40 ms are labelled.

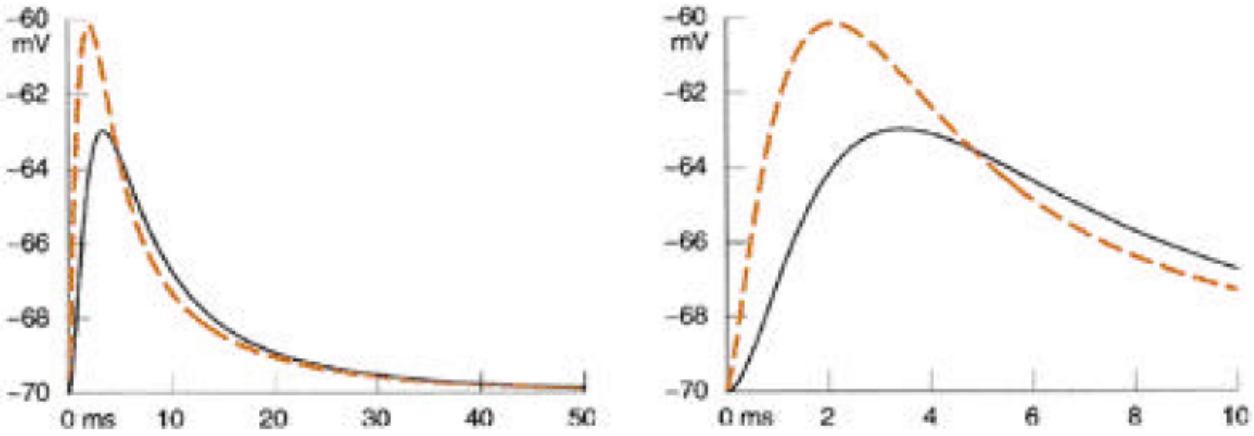

Figure 37: For both images there is the V_m over time at the synapse location. The analytical solution is orange, the black is the computed one. The dt is 1ms (left). Right, an expanded view for the first 10 ms.

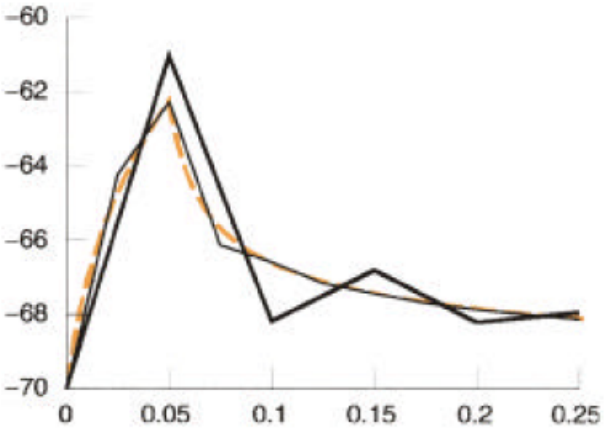

Figure 38: Considering a dendritic model the response of an injection of current of 250 pA lasting 0,05 ms, applied in the midpoint. The spatial grid has 125 nodes, 20 mm of distance; the oscillation of the solution occurs at dt bigger than 0,128 ms. The orange dashed line is the analytical solution and the black lines are the computed solutions with dt 0,05 and 0l.025 ms. The numerical solution starting from 0,0125 ms is indistinguishable from the analytic solution.

hippocampus granule cell from the dentate gyrus, see the model by Dennis Turner (http://www.neuro.soton.ac.uk/cells/ cellArchive.html).

In panel B of figure 39, the time evolution of V_m at the soma is computed using a dt of 25 ms, using three different methods for specifying the spatial grind; one or three nodes in each branch, (thick blue and black lines) and d_lambda = 0,3. Furthermore, solutions with dt = 25 ms and 30 ms are indistinguishable; hence the d_lambda is a good way to fix an accuracy standard.

However, it is important to consider as well the time steps, for example to compute a somatic ESPs with only 3 nodes and the spike timing is important a finer grid is mandatory see figure 40 panel C. However, the best accuracy reached without any drawbacks on accuracy has been achieved with the grid set by d_lambda = 0,3 and 110 nodes.

As same as the important of the spatial grid step, there is the time step dt. In neuronal network as well as in single neurons some signals can vary or propagate quickly; ergo a tiny step is a very good choice. On the other hand, it is true an adaptive time step lead to the user the freedom to tune the local accuracy as well as make lighter the overall computational burden. To this purpose NEURON has adopted the CVODE (Cohen and Hindmarsh, 1994), package written in ANSI standard C to solve ODE problems. It solves both stiff and non stiff systems. In the first case, it has several options to treat the system Jacobian, including dense an interative preconditioner solver (Krylov) and dense and band matrix solvers. Using CVODE the user can specify the maximum possible absolute error instead of the dt, then, the integrator will dynamically adjust the dt to adjust the local error of each variable state. Talking about computational performances, a topic which I am very care about; CVODE is able to achieved a runtime 10 time faster with the same accuracy of the most accurate solution with a fixed time step (Hines and Carnevale, 2001). The reason is simple, having the ability to dynamically change the dt step during the integration,

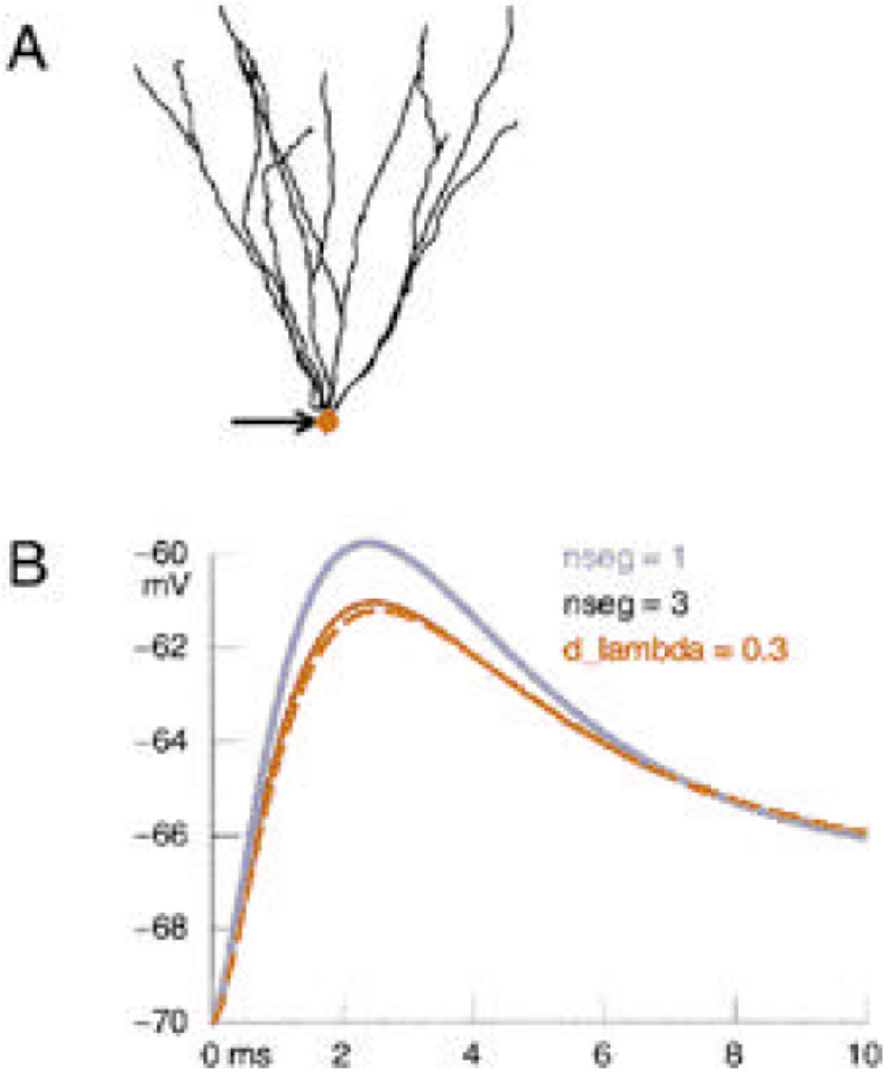

Figure 39: In panel A, it is shown an anatomical detailed model of a rat hippocampus granule cell from dentate gyrus. A fast AMPA synapse is attached to the some, orange dot. In panel B, with a spatial grid of one or three nodes per branch or in dashed orange the d_lambda value as 0,3; it is showed the V_m of the some over time.

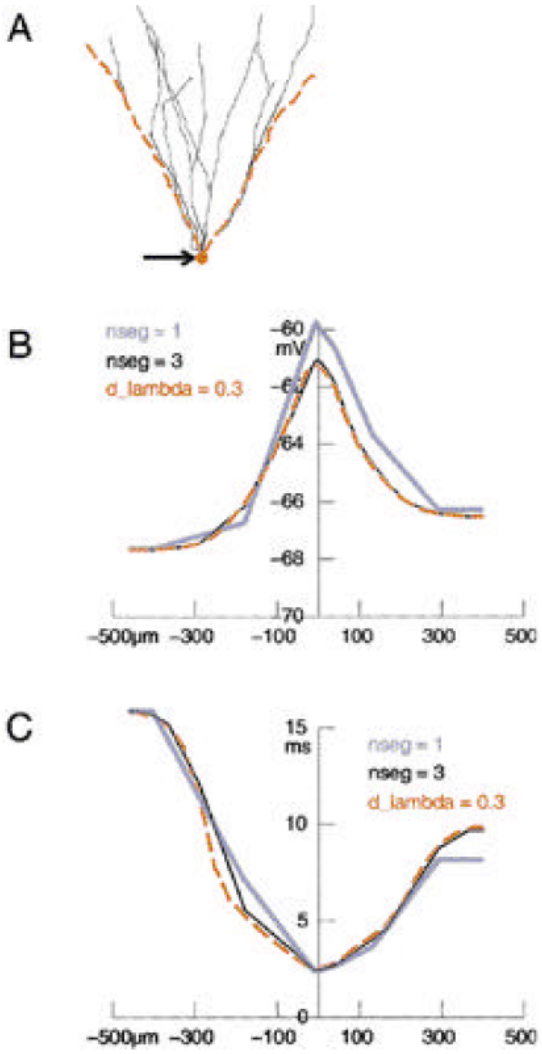

Figure 40: In panel A, an EPSP is evoked from a synapse activation on the soma, which is spread along the dendrites, with a transient depolarisation becoming smaller smaller with distance. Along the orange dashed path the panel B and C show the timing and depolarisation magnitude changes along the orange path. In panel B, it is showed the peak amplitude of the dendritic depolarisation along the orange path; the model computed with nseg =3 (black line), it is identical to the accuracy standard for d_lambda = 0,3. In panel C, along the dashed orange path is showed the peak dendritic depolarisation time as a function of the soma distance. Between $\sim$ -150 to 300 mm there is an evident difference between the computed curve with 3 nodes and the accuracy standard (thin black trace versus the orange dashed trace).

it cans squeeze the dt only in needing steps relaxing it elsewhere. In the figure 41 panel B, it is showed the control which CVODE has over the integration steps, slicing the time step in the there is a rapid change into 0.01 ms pieces up to relaxing the time step up to around 4,4 ms during long interbust. The integration of CVODE in NEURON, however has allowed the use of whatever NEURON integration method to simulate carefully any neuronal model biophysical mechanism.

It is important to underline that the NEURON default integration is a fixed-step-first-order implicit, which is numerically stable when extremely stiff ODEs and for algebraic equations are present in the system; such as in presence in the model of voltage clamps. The simulation cited so far in the article of Hines et al (Hines and Carnevale, 2001), they have been perform with NEURON's Crank-Nicholson like integration method or CVODE. The Crank-Nicholson like method has algorithm performance very close to the first-order implicit method (Hines, 1984), but when there is linearity between the membrane channel current and voltage, it is second-order correct. Therefore, to shorten the run-time and achieving the same accuracy of the first-order, it is possible to use a larger dt.

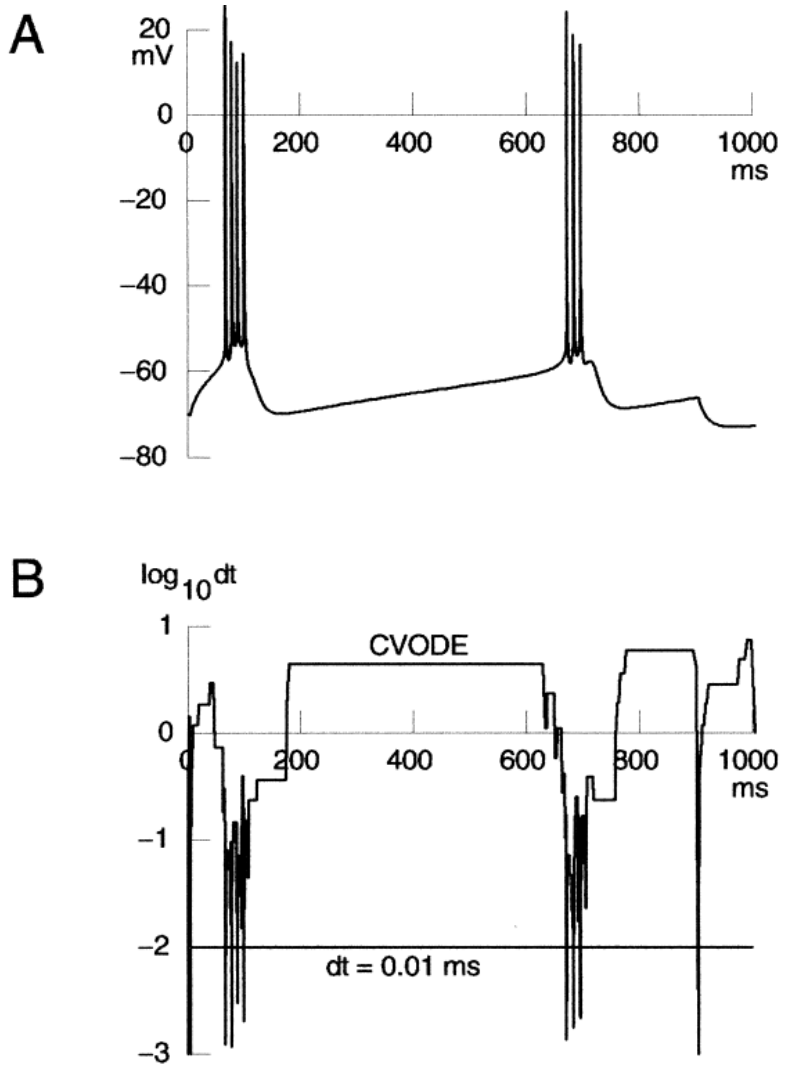

Figure 41: in panel A, the neocortical layer V pyramidal neuron somatic V_m over time undergoes to a long depolarisation pulse. The solution computed with fixed and variable time step are indistinguishable. In panel B, the CVODE dt varied over a wide range, from below 0.01 ms during every AP and at three different times: at the simulation beginning and at the sudden start and end of the current pulse injection(5 ms and 905 ms).On the other hand, for most of the simulation the dt was much larger than 0.01 ms. The integration order ranged from 2 to 5, with most steps using second or third-order of integration.

3.8.5 3D reconstructions of the morphologies into NEURON

In this section of my thesis I report two very good example of 3D reconstruction of neuronal morphologies. The two examples are the works of Markram and colleagues (1997) and the work of Erik De Schutter and J.M. Bower (1994). In the work of Markran et al (Markram et al., 1997), it has been experimentally performed an all-embracing work from the morphological structure and physiology to the synaptic connection and physiology of pyramidal neuron of layer in the rat neocortex. In this brief section the focus will be on the morphological structure of the pyramidal neurons. In their works they used acute slices of neocortex of juvenile rats, to perform somatic whole-cell recordings, in which some neurons were filled with biocytin. It has been analysed the following morphological parameters of pyramidal layer V neurons synaptically connected. The analysis was quantitative:

- soma location within the layer 5
- soma diameters (vertical and horizontal)
- the maximum span and the number of dendritic fields of basal apical and terminal tuft dendrites
- the distance between the soma and the fist bifurcation of the apical dendrite
- maximum horizontal and vertical extent and number of axonal collaterals.

In addition, it has been mapped the number of synaptic contacts had by two neurons and the distance of those synapses to the two somas from the main apical trunk, basal or apical oblique dendrites. The compartment models have been build from a camera lucida, the dimension (length and diameter) of the neuron have been measured from the enlargement coming from the camera lucida drawings; they haven been tabulated in the NEURON package (Hines, 1993). Compartmental models were constructed from camera lucida drawings of pairs of pyramidal neurons. The lengths

and diameters of all dendritic branches were measured from enlargements of these camera lucida drawings, tabulated and entered in the program package NEURON (Hines, 1993). Assuming the properties of passive cable the values are R_{int}= 155 Ωcm, C_m = 1μF cm^{-2} and R_m = 7000 Ωcm, where R_{int} is the internal resistivity, C_m is the membrane capacitance and R_m is the membrane resistance.

It is important to take in consideration that simulation could be subject to inaccuracies (Markram et al., 1997). The drawings of camera lucida are morphological projection into a plane of 3D structure. Corrections for the z-axis aren't take into considerations. This issue is not for all the dendrites, since the apical ones are parallel to the plane projection. The others, instead appear to be too short from the reconstruction. The electrotonic as well as the geometric length has been estimated to be the 20% underestimated on average. The shrinkage due to the fixation procedure hasn't been compensated. Observing the apical dendrites, the wiggles seen there suggest the reconstructed cells have a shrinkage of the 10% respect their environment, it may happen to the product used to stabilise them. The shrinkage due to the biocytin-filled neurons is around 5%, which is in agreement with the comparison results of soma diameter measured using the IR-DIC and the camera lucida drawings.

From the figure 42 is possible to see example of adjacent thick tufted pyramidal neurons of layer 5. The soma sizes is between 15 and 25 μm, and the probability to have a simultaneously recording of synaptically connected neuron is $\sim$ 0,1 for a sample of 500 paired recordings; however, in one brain slice, it has been found an higher probability of connections between two pyramidal neurons.

The figure 43 shows the somatosensory cortex location of thirteen anatomically reconstructed pyramidal neurons synaptically connected. The whole patch-clamp voltage recordings have been obtained exclusively from layer V thick tufted pyramidal neurons.

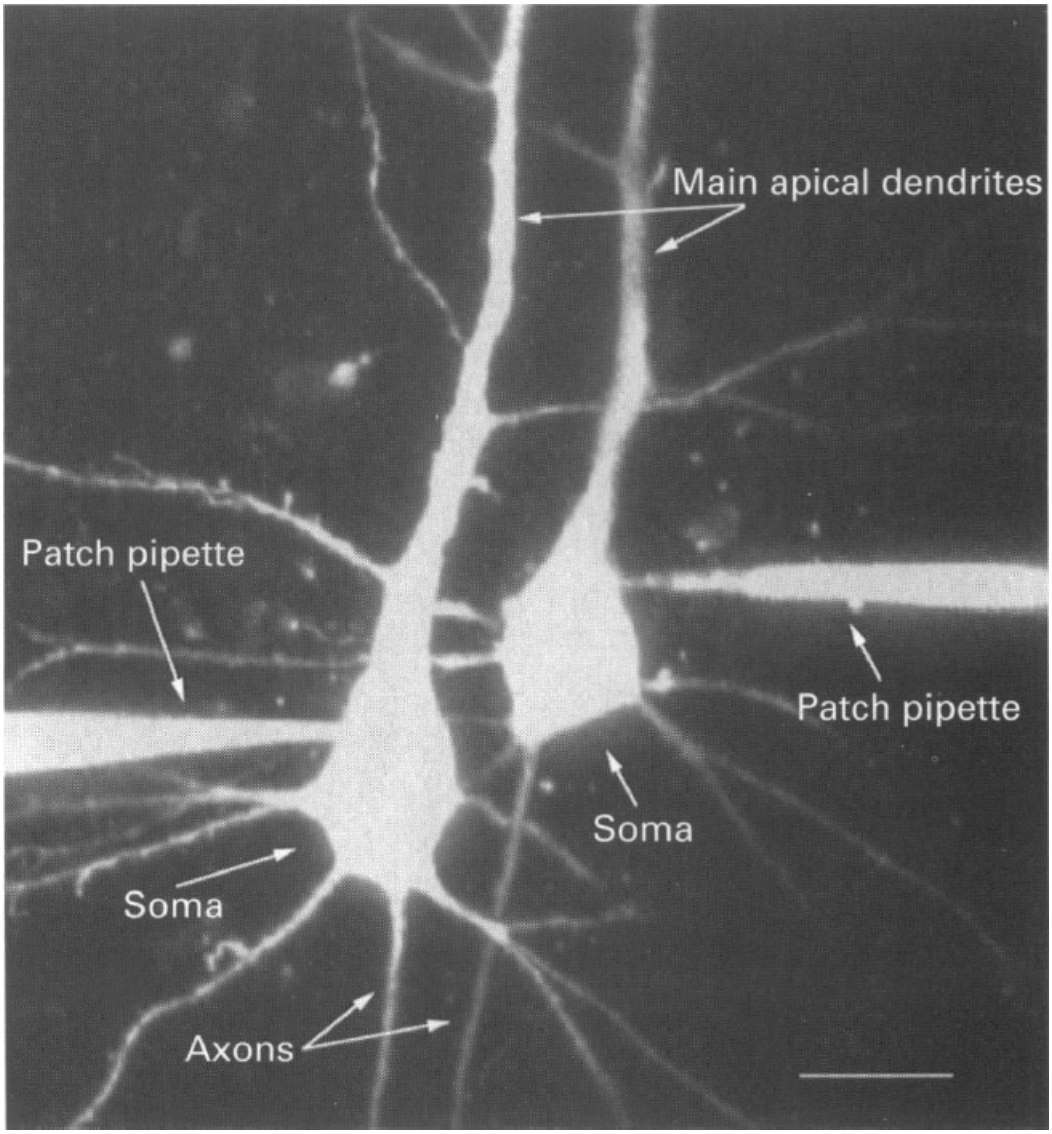

Figure 42: Using a confocal microscopy (stack of 30 images, 1 μm of depth) a pair of adjacent pyramidal neurons of layer V has been reconstructed, they are sinaptically connected. They have been identified using IR-DIC microscopy and recorded with patch-clamp pipettes. Taken from (Markram et al., 1997)

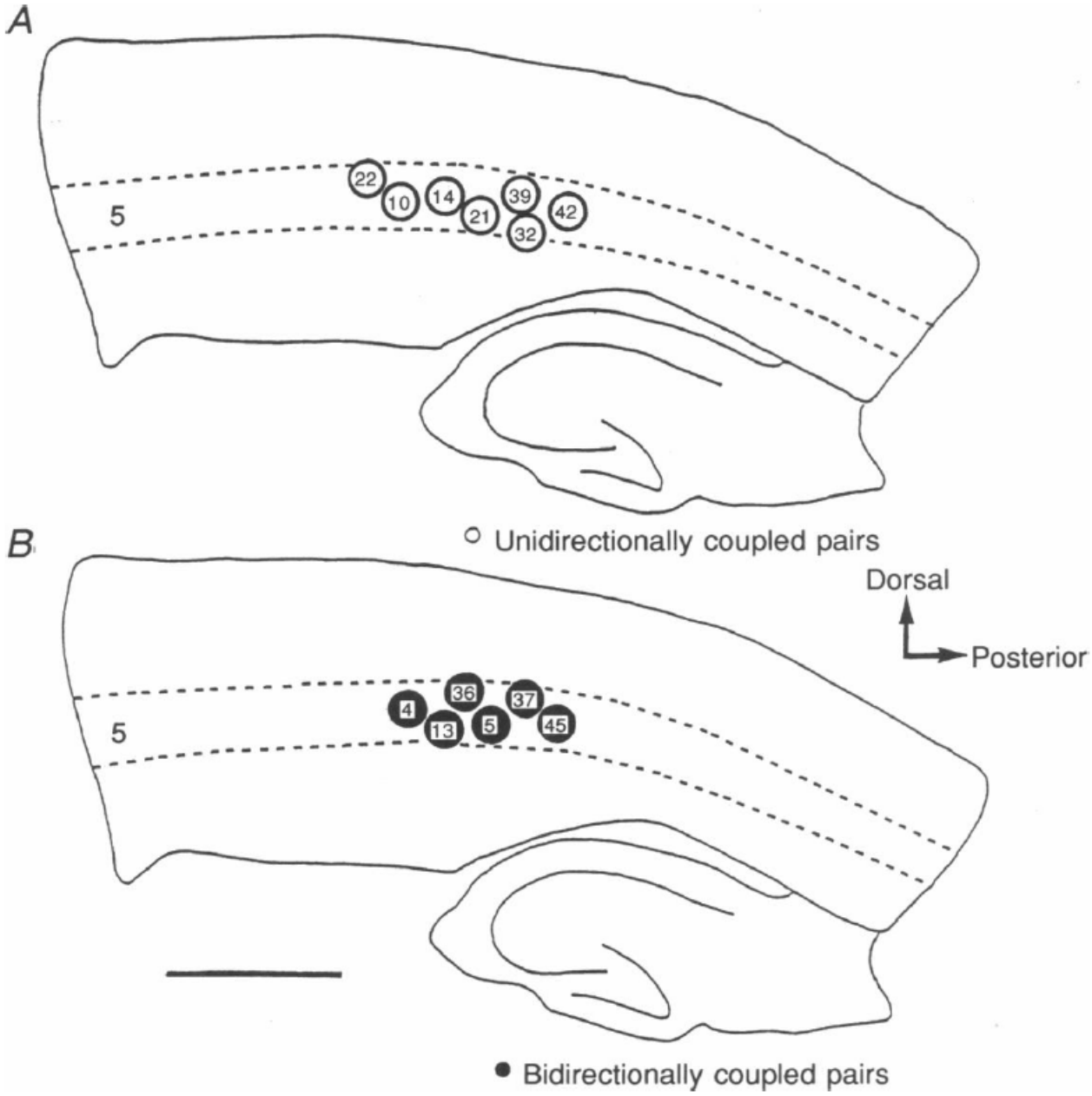

Figure 43: Here, it has been shown the location of synaptically connected pair of layer V pyramidal neurons morphologically reconstructed. The panels show two drawings of the sections, Panel A, it shows the unidirectionally reconstructed location in panel B are showed the bidirectional ones. All the neurons are located inside the somatosensory cortex. The numbers into the circles are the internal reference numbers.Figure taken by (Markram et al., 1997).

fourteen neuron, so seven pairs of neurons were unidirectionally connected and reconstructed studied in detail on the base of their dendritic location of the synaptic contacts(both pre- and post-synaptic location). Figure 44 shows a pair of connected neuron low magnification already filled with biocytin as figure 42. In addition, in the other panels B-D, are showed at higher magnification the synaptic contacts at different dendritic locations.All the neuron have been reconstructed thanks to the camera lucida use, as well as the potential synaptic sites on the neurons have been marked with the camera lucida as showed in figure 45.

The above mentioned unidirectionally synaptic contacts are an example of 3D morphological reconstruction of layer 5 pyramidal neurons of the somatosensory cortex using the camera lucida. The same method is used to reconstruct the bidirectionally contacts between pair of neurons; nevertheless I will not show here. In conclusion, here I reported an example of a past work which reconstructed the complex morphological structure of the layer V pyramidal neurons, that later has been implied into the NEURON simulator to simulate those reconstructed neurons.

Another very important example of a 3D reconstruction of cerebellar Purkinje cell by Erik De Schutter and J.M. Bower. Their work is inserted in the context of signal integration of the neuron; it is really affected by the dendritic geometry. To underline this concept the general conclusion is the synaptic inputs dendritic location is important (Rall et al., 1967).

The Purkinje cells have a large dendritic tree, with an huge number of excitatory parallel fiber synapses (Harvey and Napper, 1991). The molecular layer of the cerebellar has a morphology which the parallel fibers makes synaptic contact with each Purkinje cell whose contact.

Hence, the distal synaptic inputs are attenuated in the Purkinje cells, since the parallel fiber at the top of the molecular layer has a smaller impact over the Purkinje somatic response. Since the Purkinje cells are the only output of the cerebellar cortex

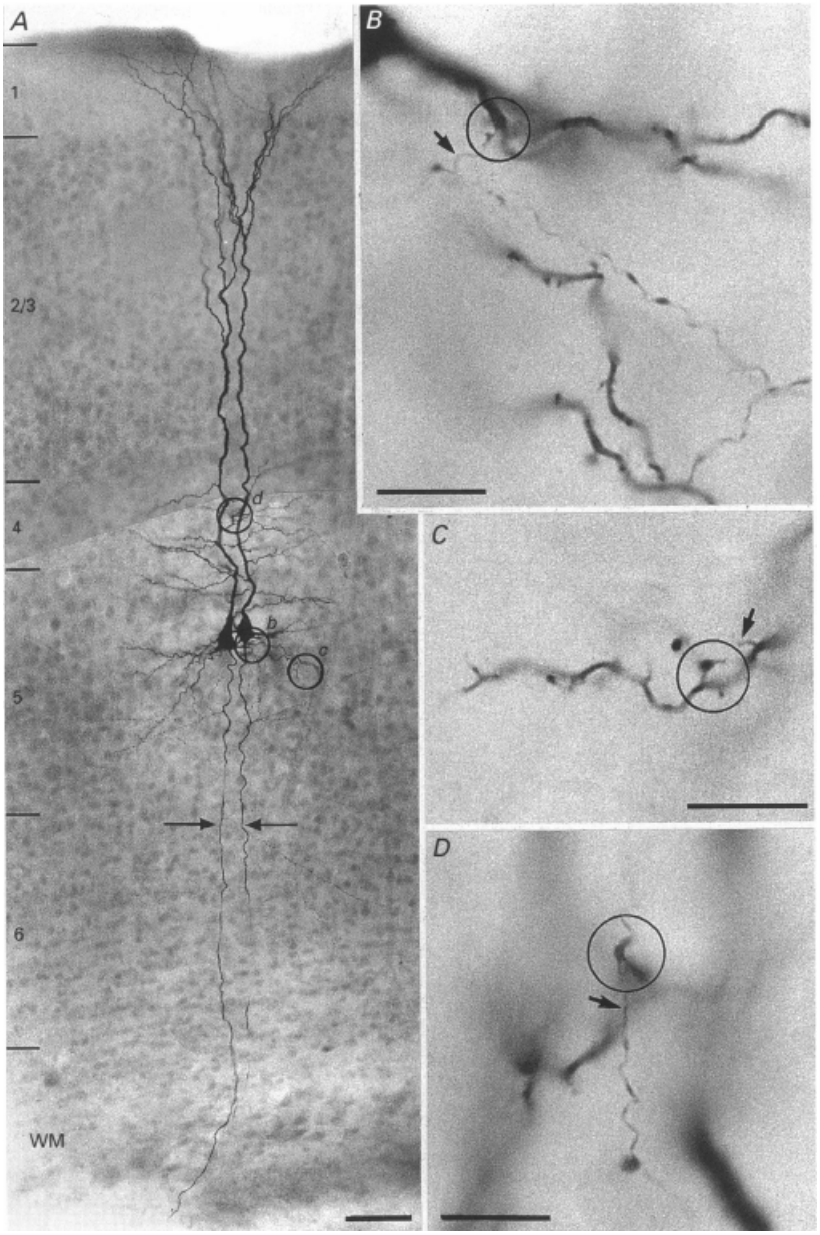

Figure 44: Unidirectionally connected couple of pyramidal neurons of layer V. In panel A, low magnification of a connected couple of neurons filled by biocytin. the circles show an autaptic contact (in panel B) and synaptic contact between the pair of neurons. in higher magnification are showed in panel B,C,D. The main axons are indicated by arrows. The contacts have been identified at the electron microscope, scale is 100 μm in panel A and 50 in the others. Figure taken by (Markram et al., 1997).

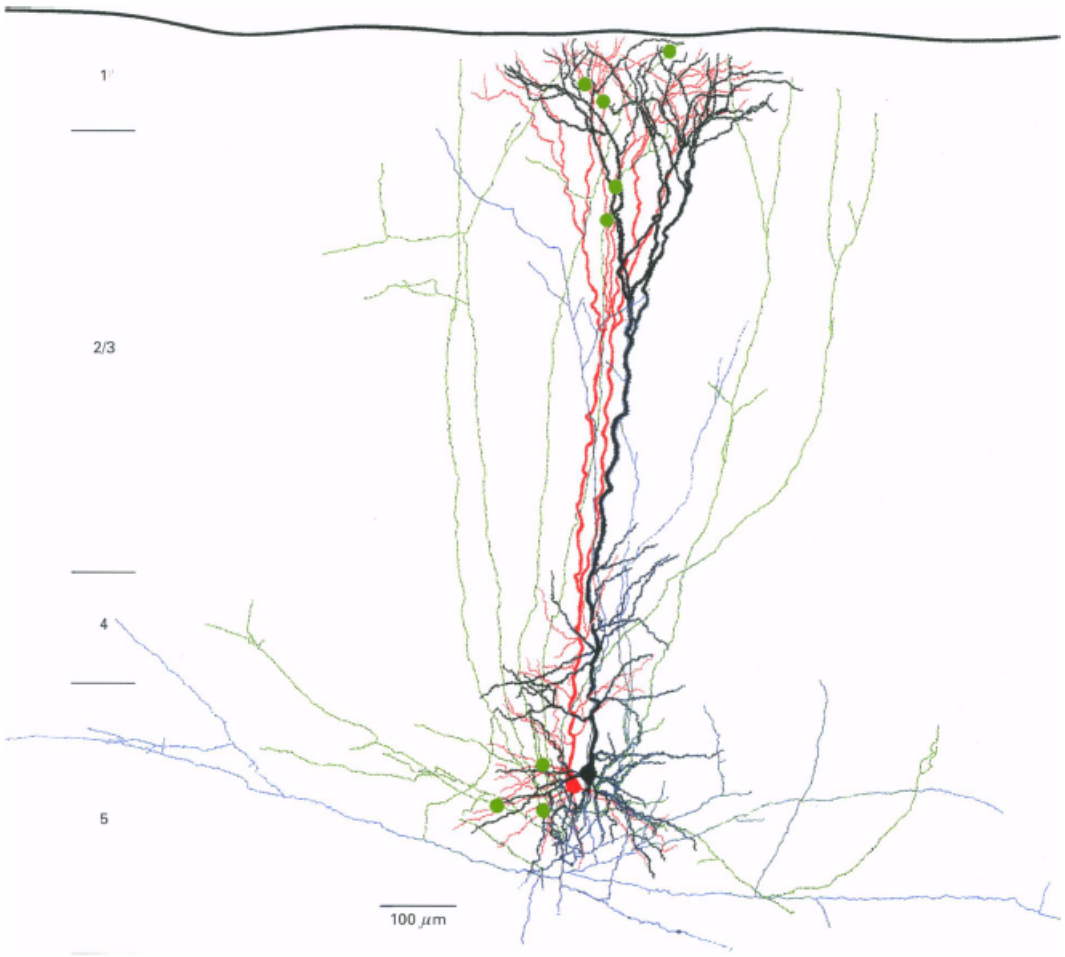

Figure 45: Unidirectional dendrites connections on apical tuft dendrites. the target neuron dendritic arborisation is in red, the axonal one in blue. The black color indicates the dendritic morphologies of the projecting neuron, the green is the axonal one. The green circles shown the synaptic contacts by the projection of the neuron on the target one, hence black/green neuron to red/blue one. Figure taken by (Markram et al., 1997).

(Ito, 1984) many cells have smaller influence over their integration. In their paper, they showed that Purkinje cell model (Schutter and Bower, 1994) have dendritic active properties and that they interactions with the synaptic background inputs; in addition, the passive electrical properties amplify the distal signal, neglecting the distance. Their model has a very powerful results showing that all the granule cells has the equal access to the Purkinje soma cells. All the simulations used a compartmental model of the Purkinje cells with reconstructed dendritic anatomy (Rapp et al., 1994). The model was simulated using GENESIS. The morphological structure of the Purkinje cells and the dendritic spines were modeled using more than 4500 compartments; considering overall the model, all the dendritic compartments excluding the one simulate the spines; contain:

- Ca^{2+} channels P- and T- type
- two Ca^{2+}-activated K^{+} channels, with a persistent K^{+} channel
- soma fast and persistent Na^{+} channel
- delayed and rectifier A current, persistent $K+$

The soma is completely passive which allows the recording of the EPSPs. The active membrane model was also compared to the passive one to have the same leak conductance. The model is able to replicate the current injection of *in vitro* data as well as generate correct response of synaptic inputs by climbing fibers, parallel fibers, and inhibitory neurons (Schutter and Bower, 1994). Furthermore, this model is able to replicate the spontaneous firing rate of Purkinje cells *in vivo* (Gilman and Arbor, 1983).

The somatic EPSPs amplification is linearly related to the distance from the soma to the input for distances beyond 100 μm; this is not due to an EPSPs amplification big increase, since the spine head amplification is small. In the passive model description, EPSP amplitudes in the spine heads are smaller on the proximal dendrites

(27,0 $\pm$ 1,0) mV than the ones in the distal dendrites (41.6 $\pm$ 3.0) mV. This is due to the sink effect present in the large, leaky soma (Jack et al., 1975). The distal inputs big amplification come from an interaction between the P-channel activation and the electronic structure of the neuron; this interaction is illustrated in figure 46. The P-channel spread activation adds an additional dendrite depolarisation, nevertheless is not enough to trigger a full-blown dendritic spike. This increased current flows P channel into the dendrite causing a more somatic depolarisation. P-channel activation in other dendrite parts occur only in presence of background parallel fiber inputs, which contribute to maintain the dendrite around -50 mV, panels A and G of figure 46; very close to the channel activation threshold around -40 mV (Regan, 1991); hence any small additional depolarisation caused by an EPSPs passive spread could activate the channels. Meanwhile the synaptic inputs activate the P channels in the dendrite, the geometrical structure f the Purkinje cells makes the proximal dendrites effect less effective (in terms of amplification). In the proximal regions the current sink caused by the soma large dimension stop further depolarisation spread to the adjacent branchlets; not allowing any P channels current to be recruited (panel G-I in figure 46). The firing model responses ha been shown to be similar to experimental *in vivo* recordings of Purkinje cells response (Bower and Woolston, 1983).

In addition, the response haven't been affected by the inputs clustering over a single branchelet, since an input distribution over eight branchelets gave the same response. It is important to underline that, for physiological firing frequencies the amplification mechanism is robust for the model, on the contrary, for small firing frequencies below 2 Hz, the model fails showing a realistic description. The failure at low frequencies was due to the impossibility to the very low input synaptic spontaneous activity to depolarise the dendrites and activate the P-channel current.

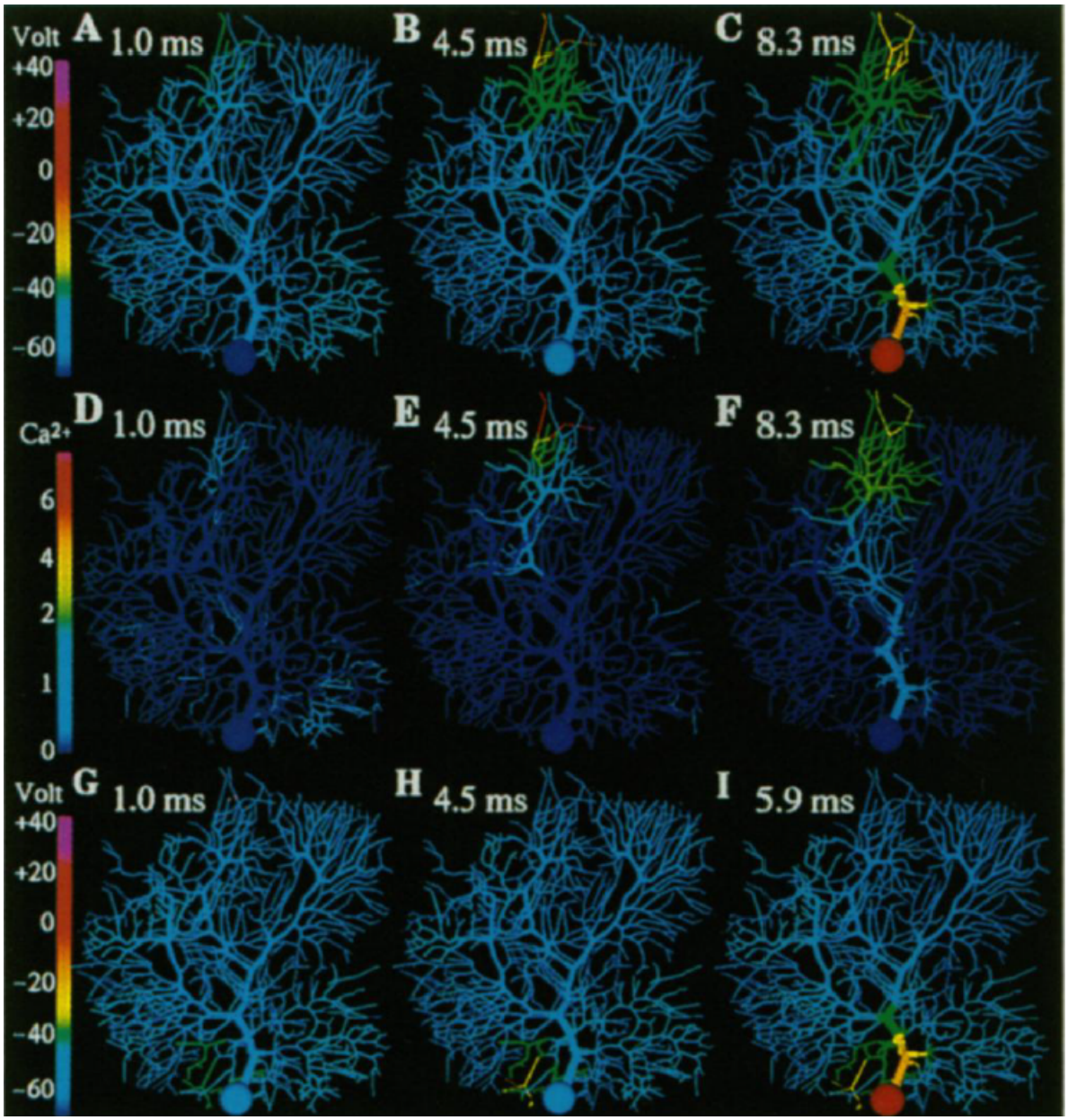

Figure 46: Purkinje cell model response to a synchronous synaptic response in a distant branchelets false color image, (branchelet 44, from panel A to F) and a proximal one (branchelet 3) from G to I panels. From A-C and G-I membrane potential and submembrane $[Ca^{2+}]$ at the times after the input are shown. At 1 ms the starting depolarisation is localised to the input providing branchelet (panel A and G). For both inputs, P-channel activation have increased the depolarisation at 4,5 ms (panel and H);the consequent Ca^{2+} influx increased the Ca^{2+} concentration (panel E). On the regard of the distal input, the surrounding parts of the dendrite were depolarised as well (panel B) and when the neuron fire an AP (panel C), P channels have activated in a large surrounding input area of branchelet 44 (panel F). On the other hand, for proximal input, the activation of the P-channel and the depolarisation are restricted only to the site of the synaptic input (panel I).

I want to underline the morphological reconstruction of the morphological structure and the dendritic arborisation due in this work showed in figure 46their physiological.

It is known that Purkinje cells are the only one adult neuron in the mammalian kingdom which hasn't NMDA channels. One of the reason of insensitivity of synaptic inputs clustering could be exactly the absence of the NMDA channels. This channels lack suggests a very different way to perform a signal integration than the pyramidal neurons.

3.8.6 Birth of a series of approached in "large-scale simulations" cortex, hippocampus and cerebellum

In this section I want to include three work of Markram, Migliore and D'Angelo; which are large simulation of somatosensory cortex, hippocampus and cerebellum. The Markhran's work is the fist microcircuitry somatosensory cortex digital of juvenile rat. It has been reconstructed an anatomical neocortical column of the volume $(0{,}29 \pm 0{,}01)\ mm^3$ containing 31 thousand neurons; in patch clamp studies identify 55 specific morphological layers and 207 morphoelectrical sub-types of neurons.

In the past decades neuron have been analysed and classified ion different terms:

- their electrophysiological behaviors, see (McCormick et al., 1985) (Kasper et al., 1994)
- their morphological features, see (Larkman, 1991) (Wang, 2002)
- their different expression of Ca^{2+}-binding peptides, see (Toledo-Rodriguez et al., 2005) (DeFelipe, 1993).

Nevertheless, there is no agreement on an objective classification of the neuronal types. It still lacking a comprehension of the total view of the each layer number of neuronal types. With the help of the paired techniques, it has been possible to study the anatomical and physiological properties of synaptic connections between neuronal types, see (Gupta et al., 2000) (Frick et al., 2007) and others. Talking about the functional level, neocortical slices have been studied and has been investigated emergent behaviour (Cunningham et al., 2004) (McCormick et al., 2003), correlated activity (Silberberg et al., 2004) (Hasenstaub et al., 2005), and the functional impact of single neurons across the layers, which has been studied *in vivo* and the somatosensory and other cortical areas (Wilson et al., 2012) (Reyes-Puerta et al., 2014). Nonetheless, it still lacking a comprehension of the cellular and synaptic

mechanisms and roles of the different layers even in the simplest behaviour. It is known the several types of neurons are connected among them through synapses with different dynamics and strengths, the connections are located in on dendrites, axons, soma etc... However the functional significance of this specific organisation remains unclear.

In this work Markran and colleagues have presented a complementary approach to the prior computational studies and have reconstructed a column of neuronal microcircuitry across the somatosensory cortex layers (1-6) of a two weeks old Wistar rat. The authors recorded and digitally reconstructed neurons starting from acute slices, the neurons have been classified in their morphological types see figure 47, then located in a proper volume estimated by experimental data into the proper layer of belonging as shown in figure 47 and then, the connectivity between neurons have been reconstructed as shown in figure 47. Neurons have been classified into their electrical types (e-types), using an extended version of the work by Ascoli and colleagues, 2008 (Ascoli et al., 2008) into electrical types (e-types), then the models reproduced to capture their characteristic electrical behavior see figure 47. The simulations have explored some emergent behaviours of the reconstructed micro-circuitry, they were able to reproduce previous *in vivo* and *in vitro* providing findings as well as clues about functioning of the neocortical microcircuitry. Differences among neurons are a lot and really well spread, the differ in location, morphology, electrical properties, location and functionalities, i.e. (protein expression) (Harris and Shepherd, 2015). At the first sight, the neuronal digital reconstruction took into account only layer, electrophysiology and local morphology. The e-types of the Petilla convention (Ascoli et al., 2008) were used as sub-types. On the hand, they have been included, when the whole brain tracing data were sufficient in quantity for a decent number of neurons(e.g. L5_TTPC_CT as cortico-tectal sub-types). In this work the authors have recorded and labelled more than 14 thousand of neurons

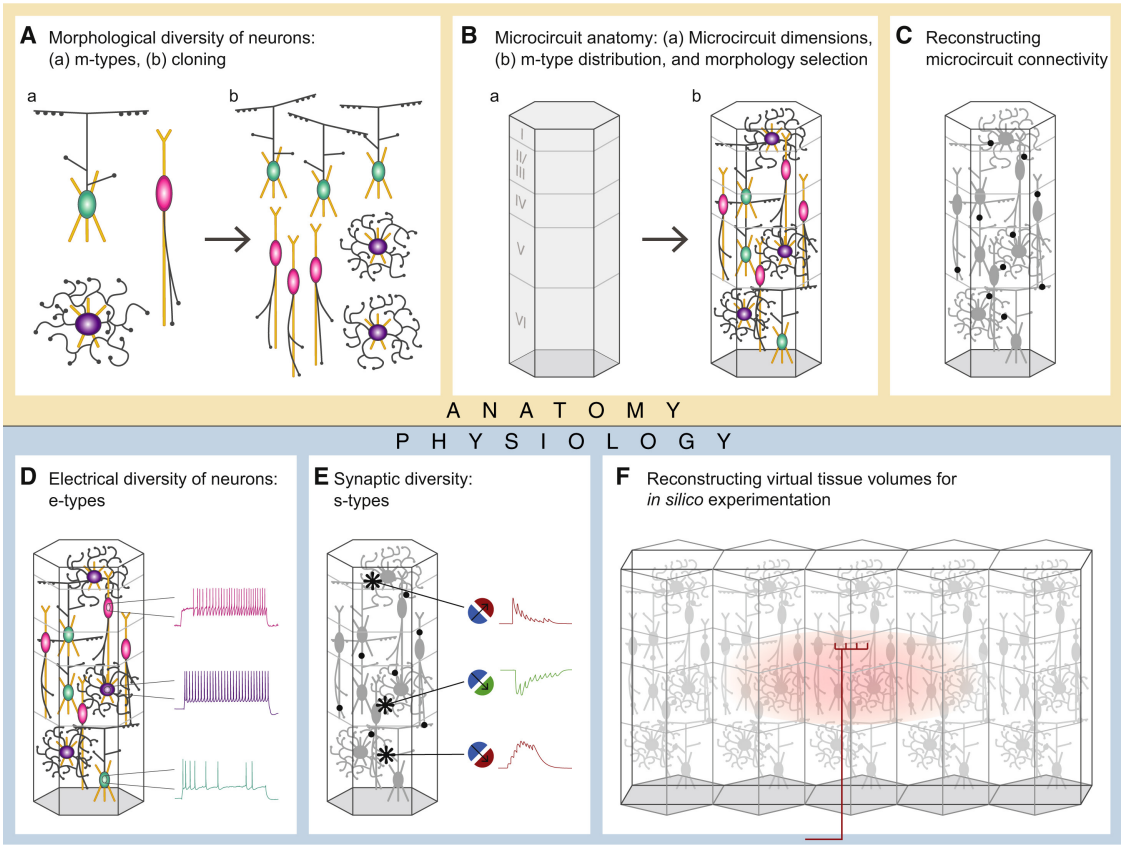

Figure 47: Data-driven Reconstruction workflow of neocortical microcircuitry Panel A, neurons morphological diversity. a) Identify the morphological types in the microcircuit (m-types). b) The m-types are repaired and then cloned with a statistical variations to have more exemplars in Panel B, anatomy of microcircuit, a) the definition of the spatial dimension of an unitary microcircuit. b) Single neurons assembly of individual neurons in the 3D space as a function of the occurrence of m-type per layer. In panel C, Reconstruction of the microcircuit connectivity. Based on the synaptic connectivity rules, it has been derived the number and location of the synaptic contacts into the microcircuit between neurons. in panel D, neuron electrical diversity, map and models of electrical types (e-types) for each m-types to consider the morpho-electrical sub types. in panel E, neurons synaptic diversity. According to the rules of synaptic physiology, there are map and model of the synaptic type (s-type) found pre- and post the combination of me-types. In panel F, the virtual reconstruction of the tissue volume. It has been as well insert synapses coming from the thalamocortical fibers. Figure taken from (Markram et al., 2015)

.

from all the somatosensory cortex six layers of a P14 Wistar rat. The experiments have been performed in acute slices using patch-clamp technique. More than two thousands of well stained neurons were necessary to classify the neuronal m-types, the characteristic features of arborisation of axon and dendrites was the "key" for the classification (Larkman, 1991) (Ramon y Cajal, 1909) (Wang et al., 2004). However, some rare m-types haven't their morphological reconstruction since they were rare and they "substituted" with types of same morphology of close layers (Markram et al., 2015). Even if, the "missing" m-types were reported in literature like L6 sub-plate pyramidal cells(L6_HPC and L6_SPC) see (Ghosh and Shatz, 1993)(Hevner et al., 2001), however the stains quality was not sufficient and they were excluded. In the end, 55 m-types have been reconstructed, 67 if considering the missing ones and separating neurons between layer 2 and 3; see figure (were there reported only excitatory types) 48, which they are distinguished by their dendritic features. In addition, it could have been introduce a more refine, but less reliable classification between m-types since the pyramidal cells morphology changes as a function of depth an layers figure 48. Note that one of the pyramidal cell of the layer 6 has inverted axonal arbors. To generate an even larger pool of unique m-types exemplars have been jittered angles, branch angles and section lengths in the clone see figure 49.

This approach was validate against the features distribution of the neuronal features from reconstructed ones and allowed the authors to have a larger dataset respecting the biological variability.

From the side of the morphoelectric classification, neurons have been classified using current steps according to the criteria of Petilla convention (Ascoli et al., 2008). Then, since there weren't any significant traces of bursting behaviour in the excitatory neurons, they have been classified as continuous adapting neurons (CAD).

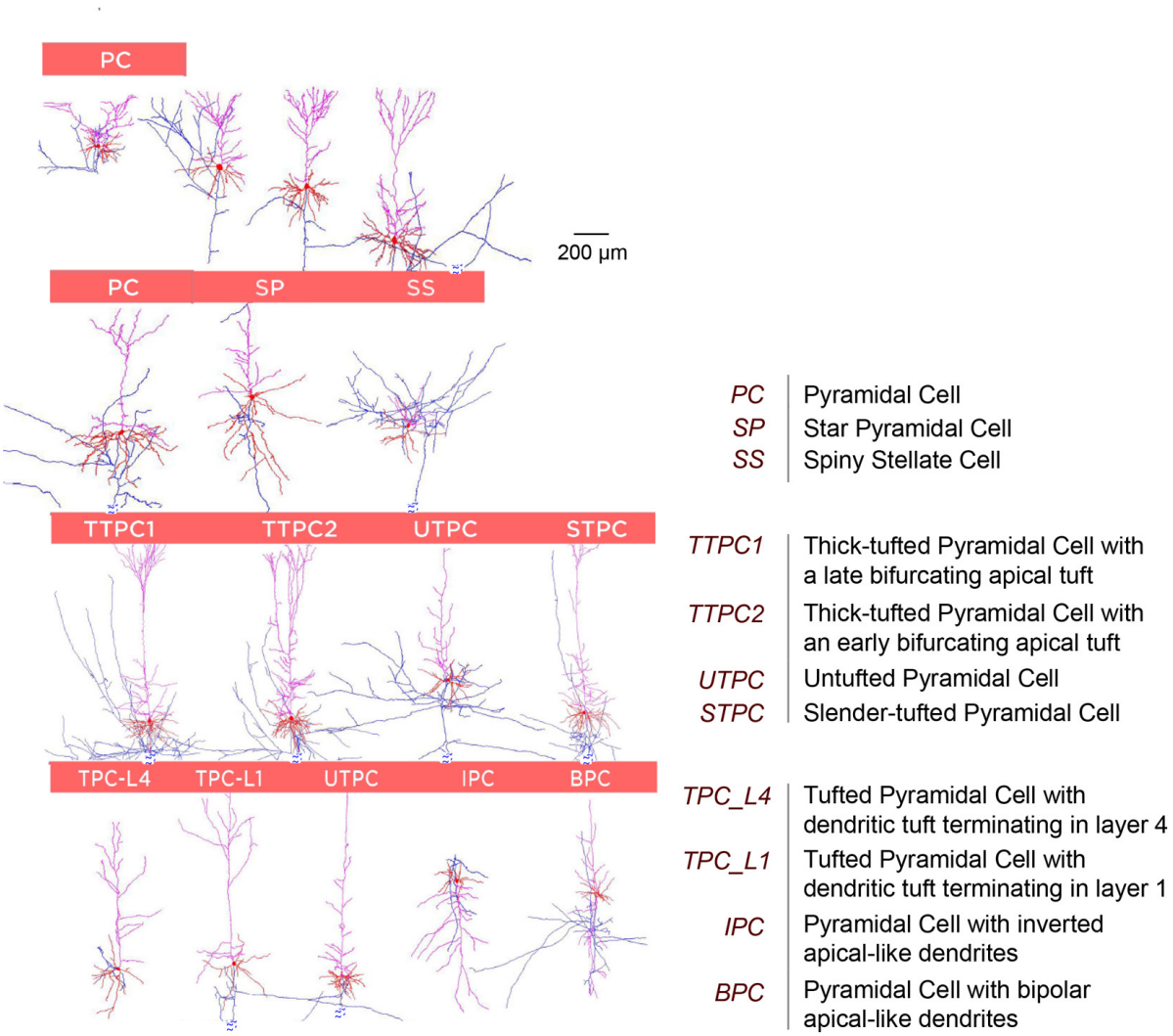

Figure 48: All the excitatory 3D reconstructions of m-types. Morphologies in L2 and L3 are not separated. The axon is in blue and the dendrites in red. To have further details look at figure FIGURE for the complete type arborisation.

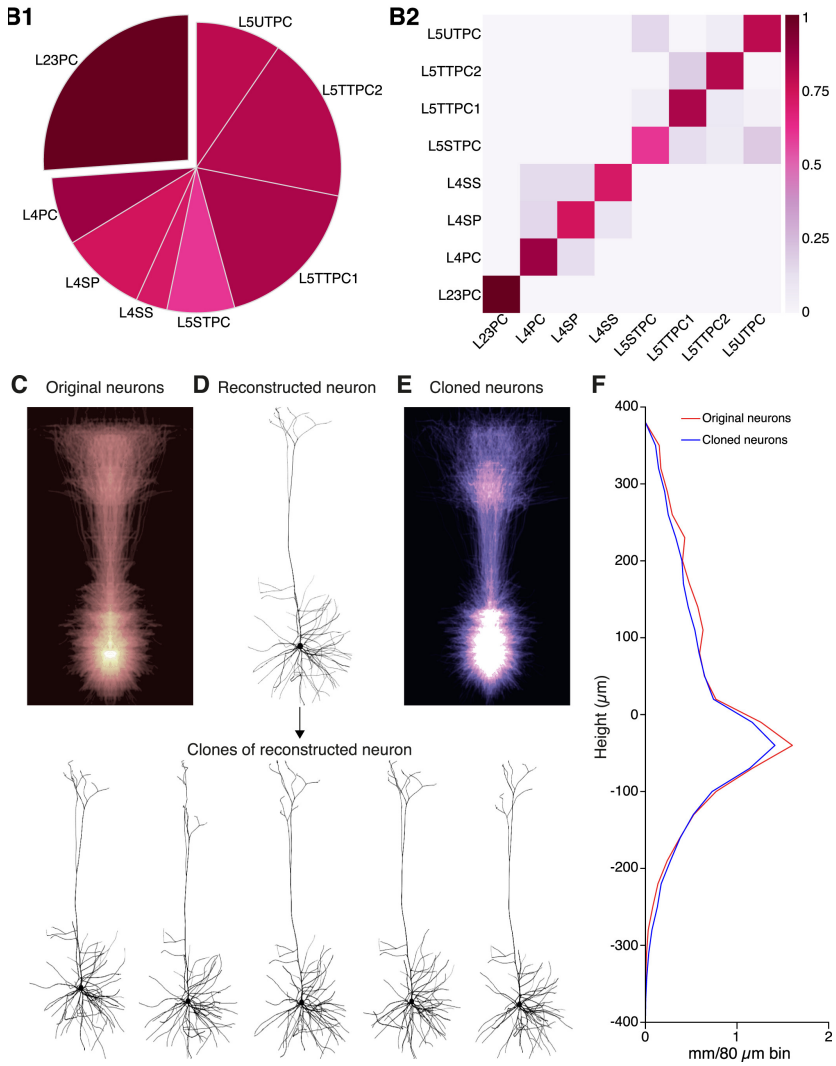

Figure 49: Classification robustness summary for L2-5 pyramidal cells in panel B1 and B2. The left one, B1 shows their relative population sizes. In the right panel there is the accuracy scale in colors The accuracy of the classification is the ratio between the successfully classified cells over their total amount of m-type cells. In panel B2, results of supervising clustering of selected features of (B2) Detailed results of supervised clustering with feature selection for pyramidal cell classes. In panel C, it is shown the image of L5TTPC repaired fiber density. In panel D, there is a neuron in the upper part of panel D, that has been cloned introducing variability of branch angles and lengths. In panel E, the same neuron present in panel C, for randomly selected clones. In panel F, fiber density plot of L5TTPCs, clones against original; which shows the mean fiber at different heights grouped in 80 μm bins. Figure taken and modified from (Markram et al., 2015)

Another very crucial work on performing a large-scale simulation is the work of Migliore and colleagues (Migliore et al., 1995) in the hippocampus. their work focused on the simulation of the CA3 neuron of hippocampus and some of their goals were:

- To understand if the bursting or non-bursting behaviour of CA3 was possible to be seen in a morphologically realistic model using a certain number of known ionic conductance behaviour
- it this model is solid among all the different morphologies.

The authors developed a model an very detailed model of membrane ions channel distribution ans densities in the hippocampal CA3 cells (bursting) and pyramidal neurons (non-bursting).The model was able to reproduce both the firing modes (Migliore et al., 1995). Furthermore, to test the model, it has been applied on six different CA3 hippocampal pyramidal neurons morphologically accurate reconstructions. To test model robustness, in each neuronal reconstruction, Ca^{2+} and its related process as well as Ca^{2+} channels reproduce the bursting and the non-bursting behaviour, for synaptic and somatic stimulations. In the end, simulations results suggested that CA3 pyramidal bursting neurons, don't need any specific distribution of Ca^{2+}-dependent channels and mechanisms. Then, the different firing modes were not dependent on Ca^{2+} and its related process as well as on some geometric cell constrains, on Ca^{2+}-dependent K^{+} channel distribution, but they depend on the densities and distribution of the latest channels only close to the soma. One of the typical hippocampal CA3 neurons features is they exhibit bursting behaviour (Migliore et al., 1995); however not all of them show it. Since their critical position within the circuit of the hippocampus, the bursting or nonbursting behaviour could have important biological consequences. The authors run the model on the NEURON simulator, with a timestep of 25 μs for a simulation lifetime of 1h for one CPU. The authors chose to target the dendritic shafts with the synaptic inputs and the spines modelling haven't a

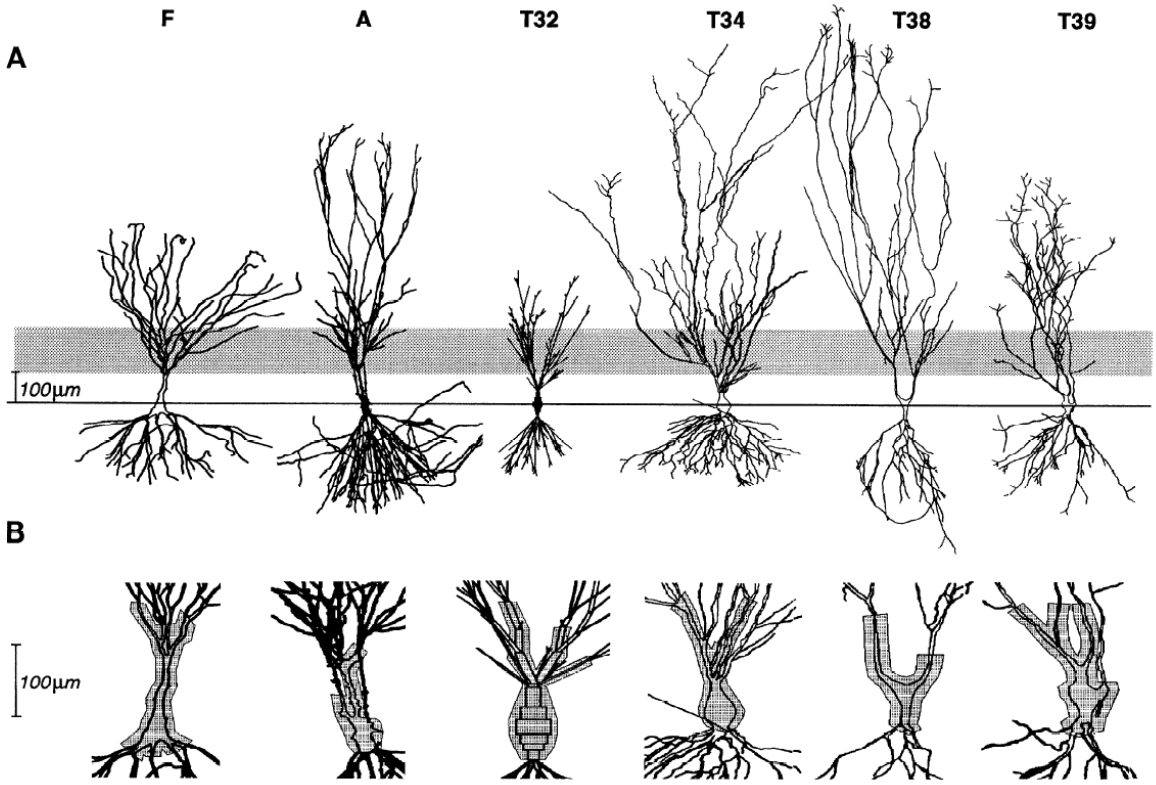

Figure 50: In panel A, drawings of reconstructed neurons (camera lucida reconstruction). Note that the T32 draw is not available, hence it is showed its compartmental model. The gray areas show the regions used to simulate the synaptic stimulation; 100-250 μm from the soma In panel B, it is shown an enlarged region for every neuron, the shaded area, as well as the somatic and proximal apical dendritic region, where the Ca^{2+}-independent K^+ channels were placed.

significant influence over the model electrical behaviour (Migliore et al., 1995). The figure 50 shows the neurolucida reconstruction of the neurons used in the simulations and the distribution of the Na^+ and Ca^{2+}-independent $K+$ channels used in each cells.

The used formalism for the conductances comes from the model of Hodgkin-Huxley equations for the state of the gating particle ($g_{K_{DR}}$,g_{K_A},g_{K_M}, $g_{K_{AHP}}$).

An interesting feature of CA3 neurons is their burst ability, which are a several APs over a slow depolarising envelope; they can be spontaneous or triggered by injection a step of current (Migliore et al., 1995). The channel distribution of the Ca^{2+}-independent K^+ channels was set *a priori* and was arbitrary, they have been

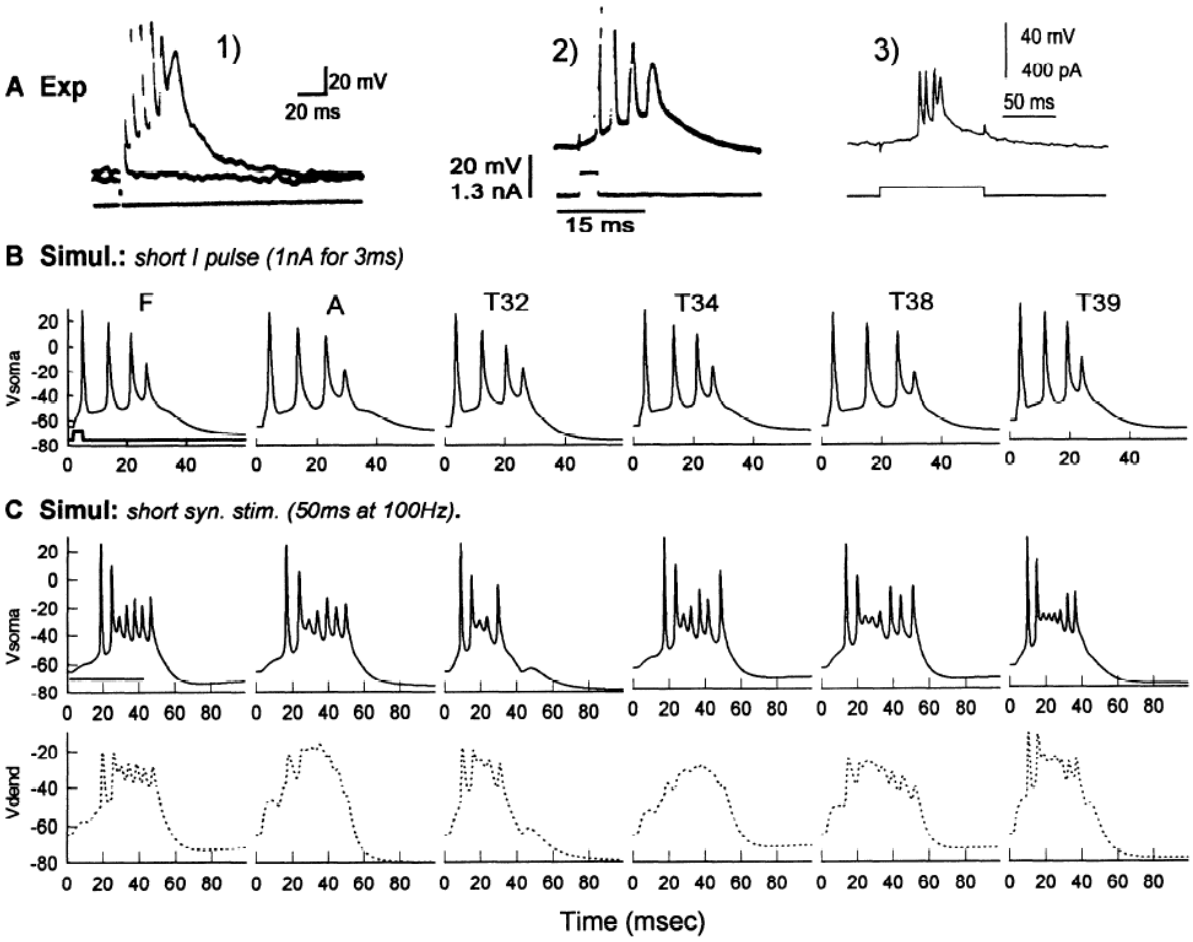

Figure 51: In panel A, example of bursts from experiments. Pictures come from the work of (Hablitz and Johnston, 1981) and (Wong and Prince, 1981). In panel B, bursts of cells obtained from a short somatic stimulation 1 nA for 3 ms. In panel C, membrane potential(–) and distal dendrite(..) are shown, after five short synaptic stimulations for 50 ms at 100 Hz, spaces 10 ms each.

places up to 100 μm from the soma as shown in the panel B of figure 50. Later, it was found that it does not play a very crucial role on the burst neuron ability as well as on the shape of the burst.

The figure 51 shows recorded CA3 bursts from experiments evoked after a short somatic stimulations.

From experiments (Wong and Prince, 1981) and (Hablitz and Johnston, 1981) and with simulations *in silico* (Traub et al., 1991), it has been seen that the CA3 bursts can be "turned off" by an appropriate hyperpolarisation pulse and it is possible to switch

from repetitive bursting to repetitive AP increasing the somatic current injection. To block the onset of a burst it is just necessary to increase the K^+ conductance, $g_{K_{DR}}$or g_{K_A}. To have a better agreement with the experiments the magnitude to increase is the mean potassium conductance, $\overline{g}_K$; which is the key difference between a CA3 pyramidal neurons being bursting or non-bursting. The obtained results showed bursting and spike frequency adaptation of CA3 hippocampal pyramidal neurons using the same model on six different neuronal reconstructions.

The last example of "large-scale simulations" is in the cerebellum by Solinas and collaborators from the 2010 (Solinas et al., 2010). In their work, the authors, analysed a wide aspect of the cerebellar granular layer using a realistic computational model to address some functional hypotheses:

- the HF response properties to bursts
- the neuron coherent oscillations in response of random activity
- the time windowing
- the center surrounded organisation.

The neuronal network has more than $4 * 10^5$ synapses and almost $4,4 * 10^3$ neurons; (Granule cells GrCs, Golgi cells GoCs, mossy fibers mfs, parallel fibers pfs). The authors results have shown that the input mossy fiber are firstly separated and processed in some layer sub-circuits and afterwords passed to Purkinje cells for more integration and pattern recognition (Dean et al., 2009). In addition, the model prediction is that the granular layer circuits act as spatio-temporal filter, with the features that can be adapted through long-term plasticity and can be synchronised with low-frequency oscillations structures. By an accurate reconstruction the model could track multiple granular layer activity dynamics recorded *in vivo* and *in vitro* to see the dynamics look at figure 52.

The firing pattern depends on the local excitation and inhibition, furthermore, neurons used to have a low and irregular firing rate, but could have oscillatory activity.

Consequently, the model demonstrates *in vitro* properties are enough to reproduce *in vivo* activity patterns plus providing the contribution basis of a single neuron to the network activity as well as the network influence on single neurons (Buzsáki, 2006) (Izhikevich and Edelman, 2008).

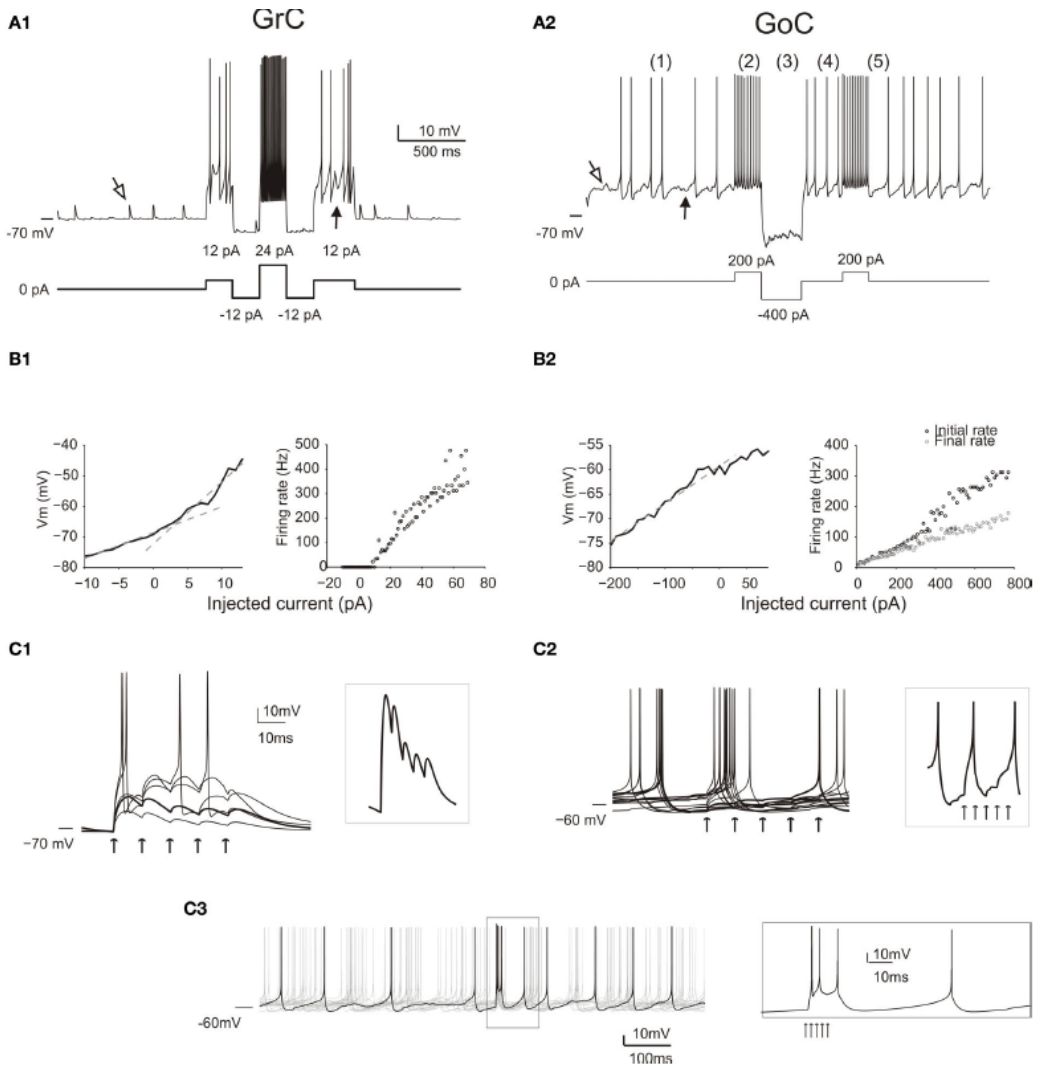

Figure 52: GrCs and GoCs response in the network. In panel A, GoCs A1) and GrCs A2) response of current injection. The background activity affected the neurons. GoC activity causes mf and IPSPs activity as well (filled arrow). GrCs show EPSPs (open arrow). GoC have low-amplitude synaptic noise, due to pf and mf EPSPs (open arrow) and by basket and stellate cells IPSPs (filled arrow). GoC shows as well low-frequency spiking due to pacemaker-like activity. Note that the GrC discharge is proportional to the injected current. GoC exhibits: spike frequency adaptation during depolarisation, reset after an HF bursts, pacemaker-like activity, sagging inward rectification. In panel B, have shown the I-O relationships for GrC (B1) and GoC in (B2) in response of a injection of current, since has been fitted with two straight lines with different slopes. On the contrary, the GoC has an almost linear spike F-I relationship up to 500 Hz. GrC has a linear spike F-I up to the 300 Hz and a very fast adaptation which is splitting in two the firing frequency. In panel C, spikeburst effects on GrCs (C1) and GoCs (C2,C3). With a presence of weak ESPs activation there is a short-term depression, meanwhile with strong activation GrCs fire spike bursts. In (C2), the traces show a reset phase that is antecedent to a pacemaker cycle activity spike occurrence at different phases. The showed bursts are composed by two or three spikes followed by a reset phase.

4 Materials and Methods

4.1 Automation and reproducibility of my own work

In this *in silico* study, it has been simulated an injection of a sinusoidally-modulated stochastic process, a Stein process, by patch clamp technique in current clamp configuration, in several multi-compartmental models of cortical pyramidal neurons (excitatory), through the NEURON simulator using Python (Hines, 2009); on top of that Julia has been used to perform a parallelisation of the simulations.

The cortical pyramidal models used are from the Blue Brain Project (BBP) (https://bbp.epfl.ch/nmc-portal/downloads.html), they are 65 distinct models of 13 electrical classes of excitatory pyramidal cortical neurons from rat somatosensory cortex with soma, accurate dendritic tree branches and membrane cell properties (Markram et al., 2015). The main steps of the current work are: Once the multi-compartmental neuronal models have been downloaded and compiled correctly, the first step is to determinate the dT magnitude, the sharpness of the AP onset, taking advantages of the experimental protocol of Badel and collaborators (Badel et al., 2008b). Then, to reproduce the theoretical work of Richardson (Richardson, 2018), it is necessary to set the average values of the input stochastic processes amplitude a_s and the event rate $r(t)$ of the Stein Process, which together define the rate and the mean amplitude of the input, the Poisson shot noise,for each the cortical pyramidal neuron models. All the simulation parameters have been saved in a .npz file, which is a dictionary-like file easy to read for both Python and Julia. Then, the neuronal models and the parameter file have been transferred to an high-performance computer, where the numerical simulations of the Richardson's work have been performed. To analyse the data, the results have been download in a cloud and analyse locally throughout scripts written in Julia and Python.

4.2 Determine the AP onset steepness, dT

The Badel and collaborators' method has been reproduced *in silico* in a Python script, see in the appendix (to reproduce the Badel's experimental protocol has been used the python script Badel_simulation.py and to perform the EIF parameters fit the extraction EIF_Extraction.py has been used). The first step has been load the function that produce the current input, i.e. the Ornstein–Uhlenbeck (OU), stochastic process (Uhlenbeck and Ornstein, 1930) (generateOU.py) and the function that load the .hoc files of the simulated neuronal models; such as morphology,biophysics, 3D structure and others (BBP_type.py). The input OU process is the only neuronal model input, since the simulation has been performed without any synaptic inputs. The general form of an OU process is:

$$\tau\frac{dx}{dt} = \mu - x + \sqrt{2\sigma^2\tau}\xi(t) \tag{54}$$

where $\xi(t)$ is a Gaussian white-noise function with zero mean,unitary variance and auto-correlation:

$$< \xi(t) >= 0 < \xi^2(t) >= 1 < \xi(t)\xi(t+T) >= \delta(T) \tag{55}$$

To numerically generate the OU process time has been discretized, in $dt = 0.025ms$ generating an OU process as:

$$x_{k+1} = (\frac{\mu - x_k}{\tau})dt + x_k + \sqrt{(}\frac{2\sigma dt)}{\tau}) * epsy \tag{56}$$

with epsy a pseudo-random function generator with unitary variance and zero mean. The injected OU process is the sum of two different OU processes, with different statistics; which means with two different values of relaxation time, $\tau, \tau_{fast} = 3ms$ and $\tau_{slow} = 10ms$ and variance, σ_{slow} and σ_{fast}.

To measure the dT of a neuron,the protocol considers eight injections of the current for 40s each, separated by 3s of silence between them as in (Badel et al., 2008b). Every 40s of the injected current, different values of mean and variance are used. The eight inputs are the combination of the four different mean values $\mu = [0.00, 0.02, 0.03, 0.06]$ combined with two different set of variances $\sigma_{slow} = \sigma_{fast} = 0.18$ and $\sigma_{slow} = 0.25$, $\sigma_{fast} = 0.36$, as show in image 53.

μ	σ_{fast}	σ_{slow}
0.0	0.18	0.18
0.02	0.18	0.18
0.03	0.18	0.18
0.06	0.18	0.18
0.0	0.36	0.25
0.02	0.36	0.25
0.03	0.36	0.25
0.06	0.36	0.25

Figure 53: Values of all the combination of the mean and variance of the two OU processes which compose the input (Badel et al., 2008b)

Then, to have as output the desired range of firing rate [1-15] cycles/s of the excitatory neurons, the input waveform has been multiplied by α, in the range of 1-1.5 nA.

The membrane potential and the injected current have been recorded for all the injection time, and the voltage membrane derivative over time has been calculated to extract the membrane capacitance of the cell, from the equation 57:

$$C\frac{dV}{dt} + I_m(V,t) + I_{noise} = I_{inj}(t) \tag{57}$$

where $I_{inj}(t)$ is injected current, I_m is the transmembrane current plus the equilibrating currents flowing between soma and dendrites/axon. I_{noise} is mimicking the weak synaptic background activity, which in this cases equal to 0 nA since the synaptic activity are turned off. I_m is the difference between I_{inj} and the membrane potential derivative. The capacitance value is determined minimising the variance of the equation 58, in which raw data from the Badel's protocol simulation have been filtered using the following rule (Badel et al., 2008b):

- only subthreshold voltage membrane which run up to the spike are included
- all voltage membrane data into 200 ms window after a spike are excluded

$$Var[\frac{I_m}{C_e} - \frac{dV}{dt}] = Var[(\frac{1}{C} - \frac{1}{C_e})^2 * I_{inj}] \tag{58}$$

In which C is the real capacitance to calculated and C_e is an estimate,the right-hand side of equation 58 is minimised when C_e is equal to C, obtaining the correct value of cellular capacitance 54.

Afterwards, the cellular capacitance estimation has been complete, the next step is the fit of EIF parameter values of the neuronal model, considering as more valuable the dT, the steepness of the AP upswing (Fourcaud-Trocmé et al., 2003). According to the equation 59, the F(V) is the voltage dynamics of the neuronal model EIF (Fourcaud-Trocmé et al., 2003), which is non-linear and contains the activation of

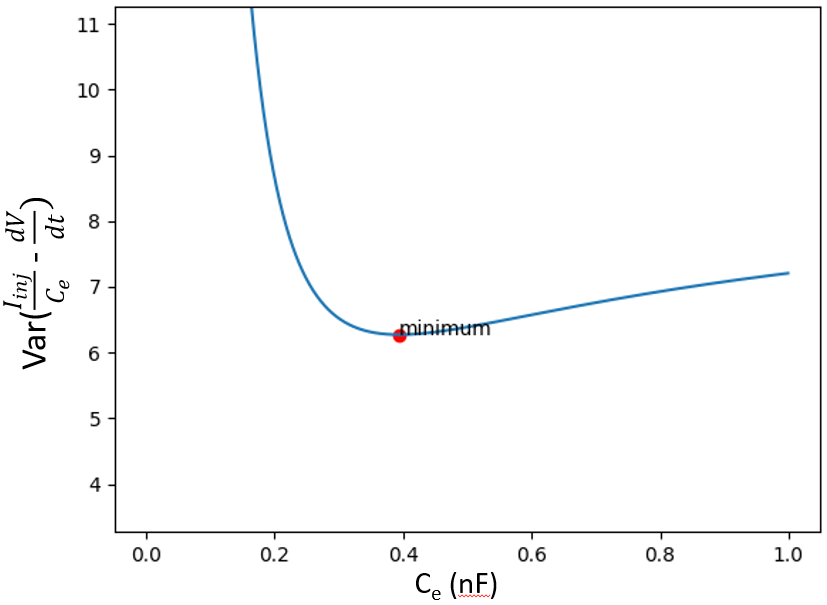

Figure 54: The reproduce method of Badel and collaborators to find capacitance. In this specific case the neuronal model is a thick tufted L5 pyramidal neuron, L5_TTPC1_cADpyr232_1, the $C = 395pF$ (Badel et al., 2008b)

the spike-generating sodium currents (Fourcaud-Trocmé and Brunel, 2005).

$$\frac{dV}{dt} = F(V) + \frac{I_{inj}(t)}{C} \tag{59}$$

Throughout the Badel's protocol is possible to measure directly the dynamic curve and comparing the equation 59 and 57 is possible to define:

$$F(V) = \frac{-}{I_d}C \tag{60}$$

where the I_d is the mean over time of $I_m(V,t)$, hence:

$$I_d(V) = Mean[I_m(V,t)] \tag{61}$$

The F(V) form is the EIF model 62 (Fourcaud-Trocmé et al., 2003), it has four parameters: the membrane constant time, τ_m, the resting potential E_m, the spike

initiation threshold V_T and the steepness of the AP onset, dT.

$$F(V) = \frac{1}{\tau_m}(E_m - V + dT \exp \frac{V - V_T}{dT}) \tag{62}$$

The EIF_Extraction.py is used to roughly extract the EIF parameter from the already filtered data, later a more refine look is necessary to check the consistence with the extremes of fit and the accordance of the fit instead with simulated data in the exponential upswing of the non linear function. The used extremes of fit are in the range of -90 mV and -[55,50] mV, with an exception for the model of the pyramidal neuron of 2-3 layer, which have a broader range up to -[45,44] mV. The filtered data used to determine the capacitance value have been filtered again to have values of voltage membrane between -95 and -29 mV to build the non-linear function of the neuronal model as a function of the voltage; to measure the EIF parameters. The data have been clustered in an histogram with bin of 0.5 mV; and then, the dynamical curve of the neuronal models have been reproduced, fitted and use to extract the dT value. Once the EIF parameters have been estimate according to the fit extremes and the best accordance between the *in silico* data and the fit; they have been saved in a .npz file and used as input data in the next script to determine the pool value of a_s.

4.3 Estimating the average current value and the stationary input frequency value

Starting from the dT determination for each of 65 neuronal models, the next step is the determination of input mean amplitude, which is mimicking the synaptic input amplitude, that is drawn by an exponential distribution with a mean amplitude a_s (Richardson, 2018). For each neuronal model, the values of a_s have been set to reproduce the theoretical work of Richardson, starting to the "case" in which $a_s = dT$

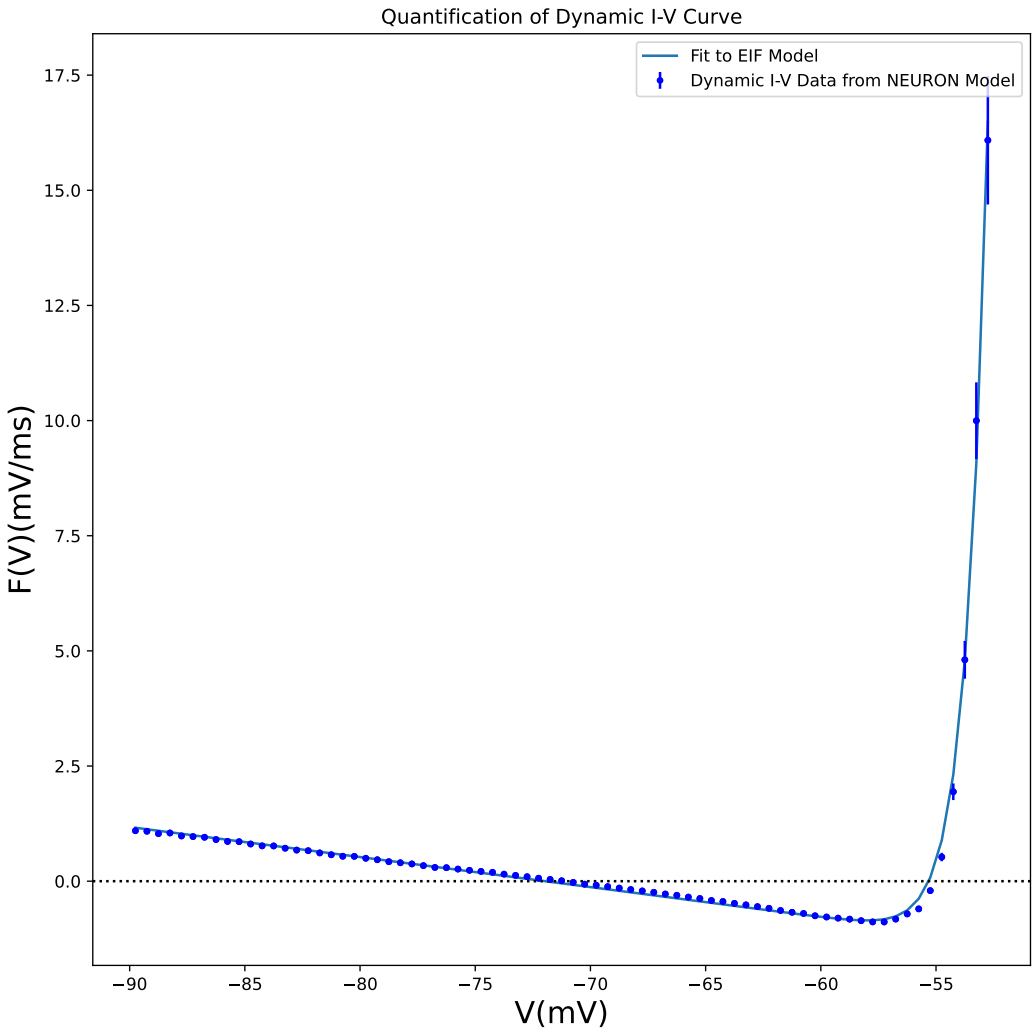

Figure 55: The reproduce method of Badel and collaborators to estimate the dT of the neuronal model. In this specific case the neuronal model is a thick tufted L5 pyramidal neuron, L5_TTPC1_cADpyr232_1, the dT≃0.92 mV(Badel et al., 2008b) in the extremes of fitting (-90,-52) mV

and then to obtain the case of $a_s > dT$ and $a_s < dT$ has been added $\pm$ 1 mV,if the dT is bigger than 1.15 mV. Then, in the cases dT is comprised between 1.15 and 0.6 mV, it has been added $\pm 0.5mV$. On the other cases, the a_s values have been set like: a_s = [dT-0.2*dT,dT,dT+0.2*dT,dT+0.4*dT] mV. After that, since the injected input is a Poisson sinusoidally-modulated current, once the a_s values are set, it is necessary

to determine the mean current values, a_sI,which can cause on the cell membrane the voltage drop equal to the a_s values. To determinate the a_sI values, it has been used the trivial approach of the trial and error; using a python script interfacing with NEURON (Automatic_J_setter.py). To determine each value of a_sI starting from 0 nA, it has been added 50 pA at every injected current step in the neuronal model; the injection of the current has been performed for 1.5s, considering a transient time of 1s, which has been discard to allow the model to stabilise around the resting potential. The current values have been accepted when was able to cause a voltage drop equal to a_s more or less the 5% of a_s. An extra caution has been considered, since the value of I_s was causing at time t a voltage drop less than $a_s - 0.05a_s$ and at time t+1 was generating a membrane voltage values bigger than $a_s + 0.05a_s$ bringing to an infinite back and forward loop. To avoid it, it has been set a step of bisection method, to set the mean between the two alternating values as a new starting point. When the a_sI have been determined, they have been saved in a .npz file and used as input for the next script, which calculates the stationary input frequency value r_0.

The next step is to set the stationary input frequency r_0 of the injected current; this current set the event rates of the Poisson shot noise to have as output frequency of the neuronal models a value around 5 cycles/s. The Julia script (automatic_r0_setter.jl) is using the secant method to determine the value of r_0. Then, it generated The above mentioned input, as a Poisson input with the event rate sinusoidally-modulated by a frequency of 0 Hz and the amplitude exponentially modulated by a_s. The mathematical form of the input rate is the following, in which f_{mod} and r_1 are 0 Hz and the signal phase shift is zero as well:

$$r(t) = r_0 + r_1 * cos(2 * \pi * f_{mod} * t/1000 + ph)/\lambda \tag{63}$$

with $\lambda = r_0 + r_1$. Then, the shot noise is generated as the product of the amplitude exponential distribution and the shot noise. A more detailed explanation will be done in the next section about the Poisson shot noise input. Then, the input is saved on memory and used as current input into the neuronal model throughout a Python script (execute_calibration.py), which, performs the simulation of the calibration for a total time of 30s, ignoring the first 500ms allowing the membrane potential to stabilise. Then, the output frequency r_{out} is saved on the disk and read by the Julia script; if it is not in the wanted range value ($r5.00 \pm 0.15$)cycles/s; the secant method is used once to generate the next possible value of r_{out} and the procedure is repeated up to the desired value of r_{out} is reached.

4.4 Richardson's effect reproduction on numerical simulations

Once all the parameters have been set and saved on disk for reproducing the Richardson's work in a set of numerical simulations; the neuronal models and the saved parameters have been transferred in the available high-performance computing (Ulysse at SISSA, Marconi and G100 of the CINECA consortium). The script that reproduced the Richardson's work (LSHPC.jl) is launched by an automatic batch script to the HPC queue to perform all the numerical simulations. More details will be discussed later. For each of the 65 neuronal model, it has explored the I-O relationship; in the frequency domain from 0 to 1000 Hz, which has been sliced in 25 frequencies (1, 3, 5, 10, 20, 50, 100, 150, 200, 250,300, 350, 400, 450, 500, 550, 600, 650, 700,750,800, 850, 900, 950, 1000 cycle/s), to which has been added a random number to avoid numerical errors. The twenty-five frequencies have been used as a modulation frequency of the current input, hence the f_{mod} value. To have a sufficient statistics to validate the obtained result every neuronal simulation has been repeated 61 times; obtaining as output around $3,05 * 10^5$ APs. This choice was imposed by the impossibility of building a unique longer simulation due to the limited cores memory

availability on the HPC nodes.Every simulation had a lifetime of $1 * 10^6 ms$. To have a more efficient explanation, consider the case of only one neuronal model, such as L5_TTPC1_cADpyr232_1, to reproduce numerically the Richardson's theory, it is necessary the shot Poisson input with:

- the a_s values drawn by an exponential distribution

$$A(a) = \frac{e^{-\frac{a}{a_s}}}{a_s} \tag{64}$$

- a sinusoidally-modulated $r(t)$ described in equation 63, with for each a_s value, a r_0 and r_1 values and twenty-five different f_{mod} to explore the frequency domain for each a_s

To generate the input a Julia script in library_function.jl is called by a python script, simulations_neuron.py, which is in charge to play the input inside the neuronal model, simulating the patch-clamp technique and collecting the output as the APs.

As above mentioned, the input is the product of an exponential distribution with mean a_s and the Poisson shot-noise sinusoidally-modulated by r(t). More in detail, the shot-noise has as well over the time an exponential distribution,which generates the time interval between events, depends on random numbers and it is normalised over the maximum of r(t), $\lambda = r_0 + r_1$. Then, for each time t, the sinusoidal rate r(t) is generated and normalised over λ and compared with a random number; if the random number is smaller, the event is happening otherwise no event takes place. Then, in every time interval is checked if and how many events have happened; then a multiplication between the exponential amplitude distribution of a_s and the time event distribution is set to generate the proper input to injected in the neuronal model.

4.5 Data Analysis, from APs to the transfer function

Once the simulations on HPC have ended, all the simulations results, the APs, have been downloaded and group by cell and a_s. The filename are unique for each f_{mod} and depend on the a_s, r_0 and f_{mod}. This make easy to group the data with the same modulation frequency. An automatic bash script (Analisi.sh) make all folders to store the data, then, check if the analysis is already performed on those data. Then, the proper analysis starts.The analysis is performed in Julia and Python scripts. The first script, is a Python script, KS_test_mp.py, it prepares the data for the Kolmogorov-Smirnov test, that will be done in a later stage. At this step, starting from a train of APs, using the circular static method (Ilin et al., 2013); the magnitude has been calculated for every AP trains and for each modulation frequency f_{mod}. Later, the AP trains are organised differently and are appended all together in a "unique simulation" for each f_{mod}. The Julia script ("append same file", ASF.jl) check as well if there are available data and if the data are readable and not corrupted; in those cases it raises exceptions and the data are ignored. The third step of the analysis is another Julia script, (Generation figures, GF.jl) It calculates the gain of the "unique simulation" for all the twenty-five frequencies; it calculated the gain using the circular static as describe in the following paper (Ilin et al., 2013). Considering the complex plane, each AP occurrence time has a real and a complex part, from which the output signal phase and magnitude can be obtained for every frequency of modulation for each a_s and neuron. As before mention, the gain has been calculated for the f_{mod} for each neuronal model and a_s; then, it has been normalised over the biggest value of the gain, at 5 cycles/s. All APs for each f_{mod} have been divided in one hundred chunks, for each of them has been calculated the magnitude. Then, the mean, the average and the error of the mean over all the chunks of the same frequency of modulation f_{mod} have been calculated. In the end, it has been obtained twenty-five mean values of magnitude with their error of the mean. To set an interval of confidence over

which the results are reliable; it has been calculated the gain of the surrogate data in the same manner as before mentioned excluding the normalisation passage. The surrogate data are made starting from the "unique simulation" for each f_{mod} and have been calculated the interspike intervals and then shuffled; after that, using the cumulative sum the AP time is reconstructed. This has been repeated for 100 times for each action potential trains; then, the average and standard deviation have been calculated and the mean plus two times the standard deviation has been used as the confidence interval (Linaro et al., 2017). The last step of the automatic bash script is making the plots of the gain as a function of the frequency modulation. All the data are plotted together to the interval of confidence, the ones are considered reliable, hence, they are over the interval of confidence have been kept to the next steps of analysis. Then, the Kolmogorov-Smirnov (KS) test has been performed only over the data considered significant, and the plot is repeated only for them. In addition, the KS test has been performed only over the HF f_{mod} in which the magnitude has a loss. The test ha been done coupling the f_{mod} of each "case" A vs B, B vs C and etc; to prove that are statistically distinguishable and different from each other. Afterwards, over the reliable data, it has been performed a linear regression in a logarithmic scale in which the magnitude is plotted as a function of the f_{mod}, in order to find the exponent of the power law that describes the magnitude attenuation at HF for the different "cases" (A,B,C, eventually D). From the linear regression the offset and the slope of the straight line has been extracted; the slope parameter is, for the logarithmic property, the exponent of the power-law of the magnitude attenuation. For each neuronal model and "case". The starting point of the linear regression is the cut-off frequency and continues up to all the set of f_{mod}.

4.6 Verifying the presence of a correlation between the slopes at HF domain and the Total dendritic length, TDL

The script that is carrying this analysis is written in Julia and import the library Scipy by Python; its name is "slope_vs_smth.jl". For correctly working the script need to have as 3 inputs, the name of the file of the magnitude to correlate with the slopes, such as "TDL.npz", the name of the magnitude, "TDL" and its unit of measure, "micrometers". Once the script is entered one by one in the folder of the 65 neuronal models of the BBP, it checks for the presence of the "TDL.npz" and the "fit_results.npz" files and read the TDL and slopes values and append them in the proper vector. Then, through a linear regression calculated the slopes of the slopes and save the result in the same directory in the file: "M_calculation.npz". Once this part has concluded, it goes for plotting all the magnitude against the TDL, and then calculate the Pearson test and the Tau-Kendall test for each paired magnitude taking advantes of the Scipy library.

4.7 Automation of my own work

From the beginning of the parameters setting and up to the data analysis my own work has been also to automatised the procedure as much as possible. The procedure has been divided in steps and every final output of the a script has been became the input of the next; to build more complex results step by step and in case of failure to not lose all the work, but just going back a step backward. However, the biggest effort has been to automatise the simulation schedule to easily perform a big number of them as requested. The repetition of the same computational load, such as the same calculation changing just some parameters is a typical example of embarassingly-parallel problem. The execution of the simulation on HPC node, in which each core has taken care of one simulation has been performed using the Julia library FLoops (https://github.com/JuliaFolds/FLoops.jl) A bash file, "Allrun_Case_input.sh" see

the appendix, which starting from the directory of the neuronal model, it checks on the output directories how many simulations have been done for each "case" and frequency of modulation f_{mod}. For each f_{mod}, the simulation number is checked, if the number is less than one desired, the missing ones has been scheduled. For each simulations a bash file is generated, (runSimulation.sh, in appendix), in which it has been requested between 6 and 9 hours, only one node, and a core for each f_{mod}; hence twenty-five. This last script has been modified as a function of the difference of the used clusters. Another common features of the runSimulation.sh are the environmental variables to perform the simulations. The difference between the two HPCs is the available RAM memory per node, On Ulysses on the regular2 queue wasn't possible to ask more than 4GB, on the other hand, on G100 and Marconi was possible to ask up to 180 GB for each node. On CINECA HPCs, on a single node was possible, for each core, schedules one simulations for each modulation frequency, f_{mod}, so twenty-five simulation for each f_{mod} on twenty-five cores. On the other hand, on Ulysses cluster due to the memory boundaries the the twenty-five modulation frequencies have been divided in three groups of six, nine and ten f_{mod}, each group of simulation has been scheduled independently on a node requesting the same number of core per f_{mod}; a scheme to help to understand the subdivision on the different HPC is present in figure 56.

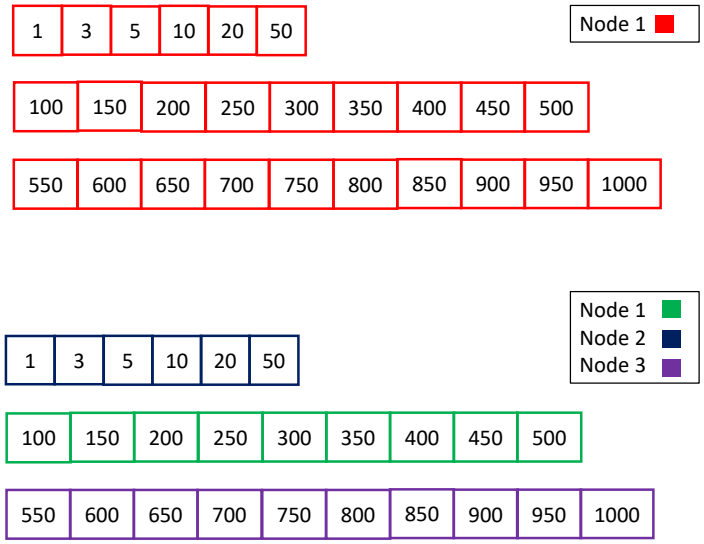

Figure 56: The different setting of the simulation on the used HPCs. In the CINECA's cluster was possible to schedule all the simulation for each f_{mod} in the same node. For lacking of necessary RAM on Ulysses the f_{mod} has been split into three different groups.

5 Results

5.1 Preliminary results on EIF model

In the previous sections, I have described the establish knowledge of the I-O relationship of a neuron, especially in the HF domain. As reported in the section section Recent applications of System theory in Cellular Electrophysiology, the HF behaviour of the I-O neuronal properties has shown an universal behaviour only dependent by the neuronal properties itself. On the other hand, an intriguing theoretical work has demonstrated the HF response function of a neuron depends by the interplay between the neuronal properties themselves and by the statistics of the input. The first part of the obtained results was the validation of the theoretical work using the same neuronal model, such as the EIF neuron. However, it has been used a different approach by the Fokker-Plank equation for evolving a probability distribution of the membrane potential which can assume a certain voltage value. The approach used in this work consists in evolving the membrane potential over time. As a first step, the equivalence between the two approaches has been established through the reproduction of the obtained results in the theoretical work for the particular test case. The obtained results are showed in figure 57. The equivalence between the approach and the reproduction of the same results has allowed us to investigate the presence of the theorised model in the state-of-the-art neuronal models, which are the more accurate possible models for real neurons. Since the Fokker-Plank equation cannot be obtained for the multi-compartmental models, the best approach is the evolution of state equation over time. The preliminary results are very promising since they guide us to underline the difference between the EIF simple model and the more accurate BBP neuronal models; BBP are not point neurons, but they have a dendritic length that have shown to play a role in the effect, see section section Further investigation on possible biophysical magnutide correlations. In addition,

they have shred a light on the total time necessary to see the effect in real neurons, suggesting the only possible approach the *in silico* one, since it is impossible to keep alive a cell in acute slices up to almost 17 hours.

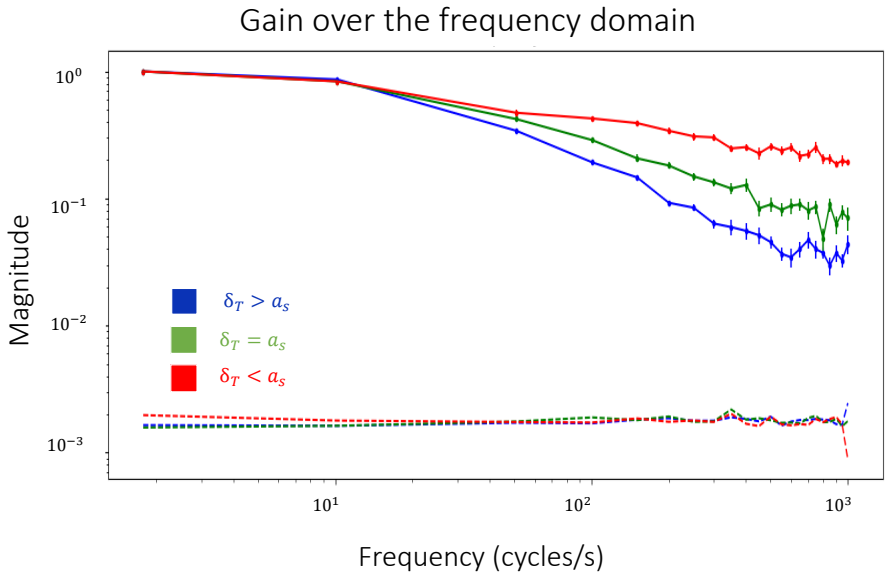

Figure 57: Preliminary results obtained by a numerical simulation using Julia for five repetition of lifetime simulation of 10^7 ms and a time step of 0,05 ms. It is noticeable at HF the different slope for the three cases of different value of a_s. The S/N at very HF frequency is less favourable than small and intermediate frequency, underline some oscillation on gain (magnitude) value. The gain value are normalised over the smallest frequency gain value. The results are all above the significance levels in dotted lines. The code color is included in the legend.

From now on, the code color means: blue, the dT is greater than a_s, green dT is equal to a_s red dT is smaller than a_s. The output frequency of the EIF model was kept at 5 Hz. The simulation code is in the section Appendix

5.2 Multi-compartmental models, dT extraction

The first overall result is the successfully reproduction *in silico* protocol of Badel and colleagues (Badel et al., 2008b) over all the excitatory pyramidal neurons of the neocortex. They are 65 models in total. For each of them has been extracted the dT parameter. The obtained results are the I-V curve examples; they have been chosen randomly as one neuron for each neocortex layer, see 58,59,60, 61. The data have been fitted with the EIF model to extract the neuronal dT value. The obtained results of the fit has been showed to be very sensible to the fit extremes; as a default the left extreme has been fixed as -90 mV; on the other hand, the right one was the crucial one for fixing how much of the exponential curve would have considered in the EIF fit. The right extreme has been chosen along some specific arbitrary constants, such as when the I-V curve is still growing positive and the $|F(V)|$ is bigger than value of 2. These choices has been put to guarantee a minimum of exponential trajectory to fit. The reproducibility of the result, surely, has been respected. In the following table see figure 62, it is possible to appreciate all the dT values of the 65 me-types of the excitatory neurons of the neocortex, the dT values have the second digits after the comma has uncertainty. To be clear, as specified in the subsection Birth of a series of approached in "large-scale simulations" cortex, hippocampus and cerebellum :"they are 65 distinct models of 13 electrical classes of excitatory pyramidal cortical neurons from rat somatosensory cortex with soma" that means five different "versions" of the same electrical type. From the histogram results of the dTs, it is possible to appreciate the tiny interval of all the excitatory neocortex neurons dT are located (0,76-2,26) mV. Furthermore, a total variation of the dTs values of ΔdT= 1,5 mV is compatible with the magnitude of the synaptic input amplitude $\sim$ 1mV (Richardson, 2018), meaning an a_s variation can easily become smaller or bigger than of a certain neuronal dT value; triggering the Richardson's effect illustrated theoretically in his paper (Richardson, 2018).

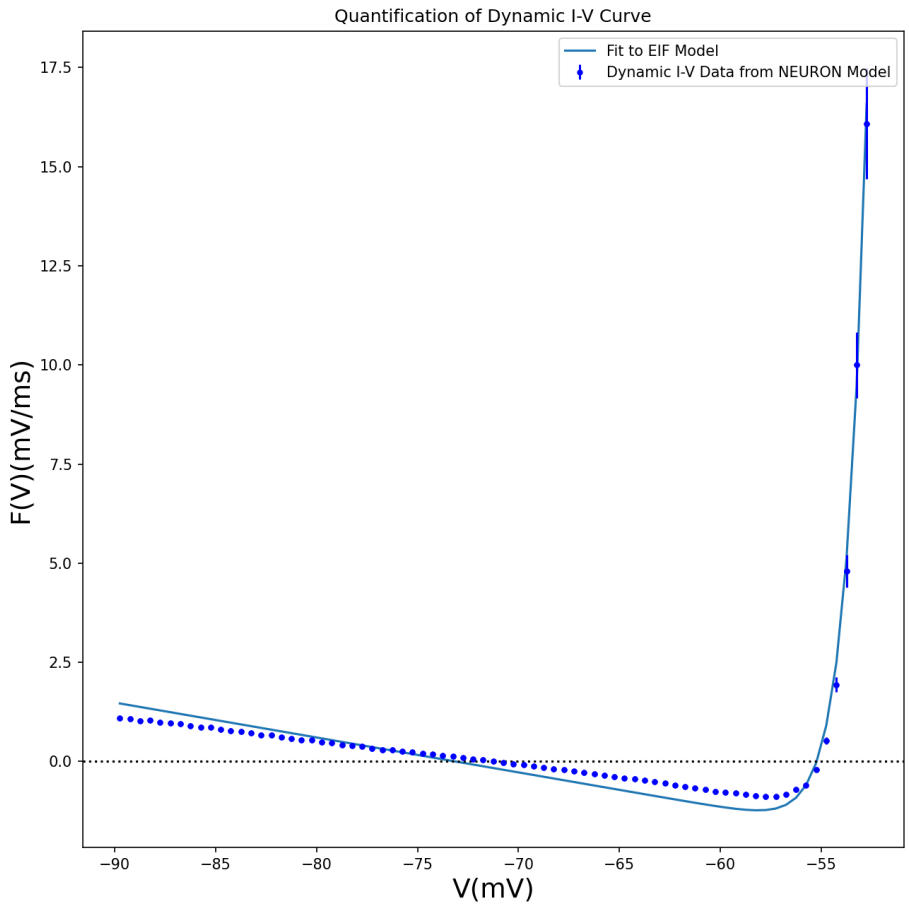

Figure 58: Obtained results by the Badel's work reproduction *in silico* fitted by the EIF model. Here, the extremes value are -(90,52) mV. The vertical bars in blue are the errors associated to the data. The neuronal model is one of the five different models of a thick tufted pyramidal neuron of the layer 5.

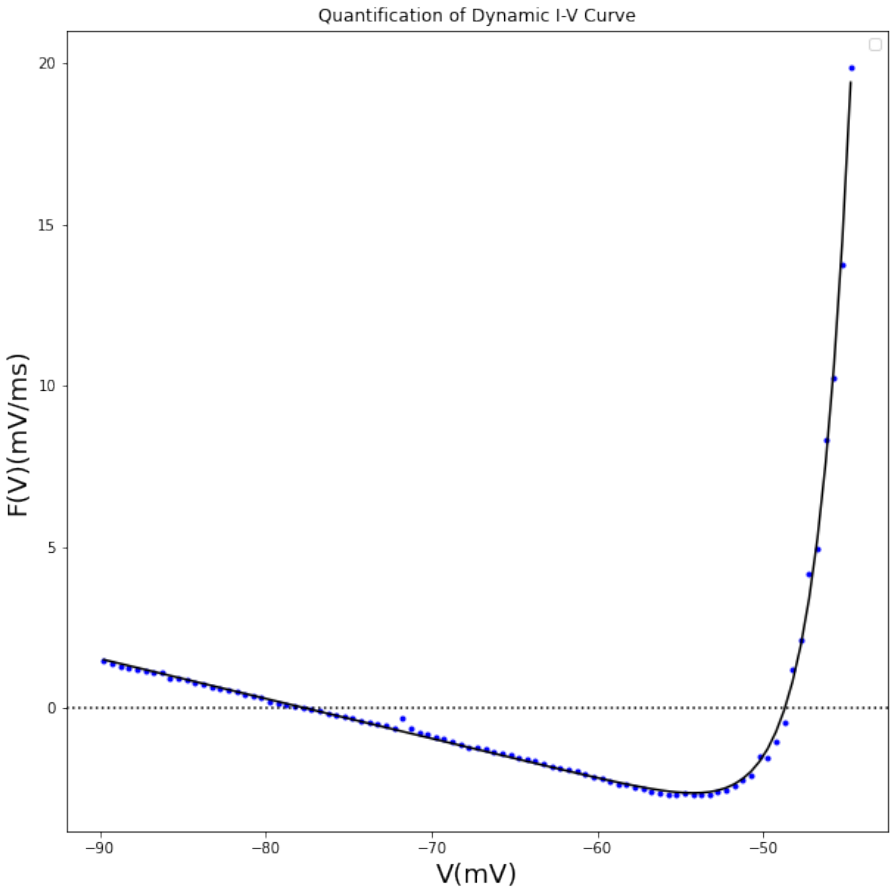

Figure 59: Obtained results by the Badel's work reproduction *in silico* fitted by the EIF model. Here, the extremes value are -(90,45) mV. The vertical bars in blue are the errors associated to the data. The neuronal model is one of the five different models of a pyramidal neuron of the layer 2/3.

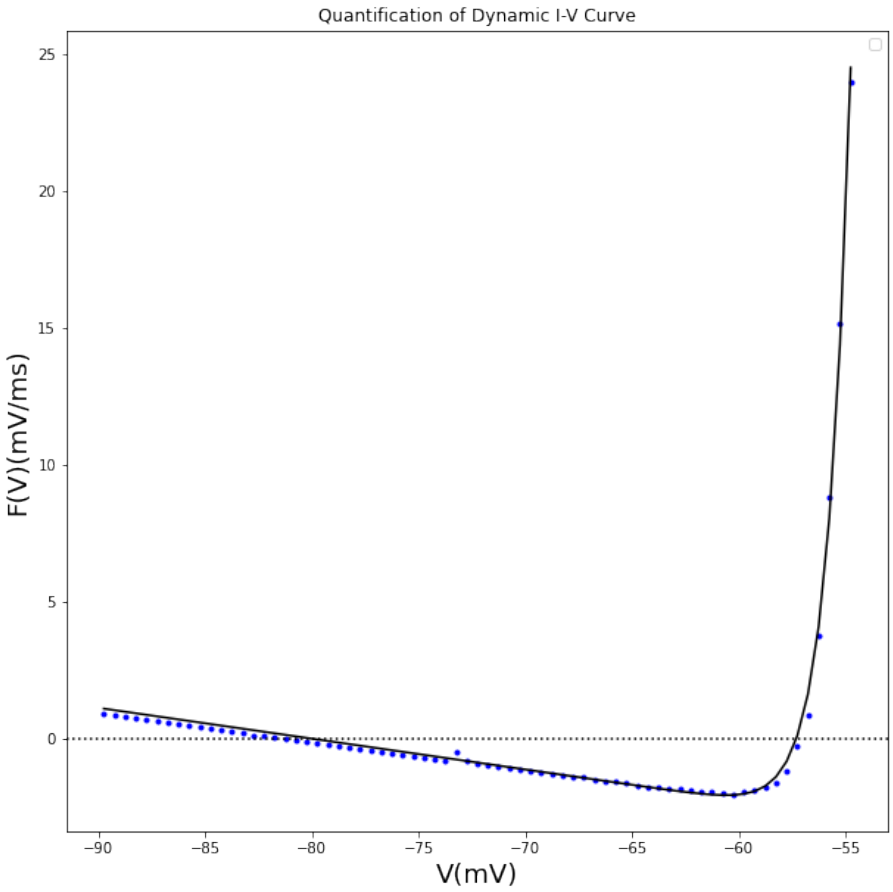

Figure 60: Obtained results by the Badel's work reproduction *in silico* fitted by the EIF model. Here, the extremes value are -(90,54) mV. The vertical bars in blue are the errors associated to the data. The neuronal model is one of the five different models of a spiny stellate neurons.

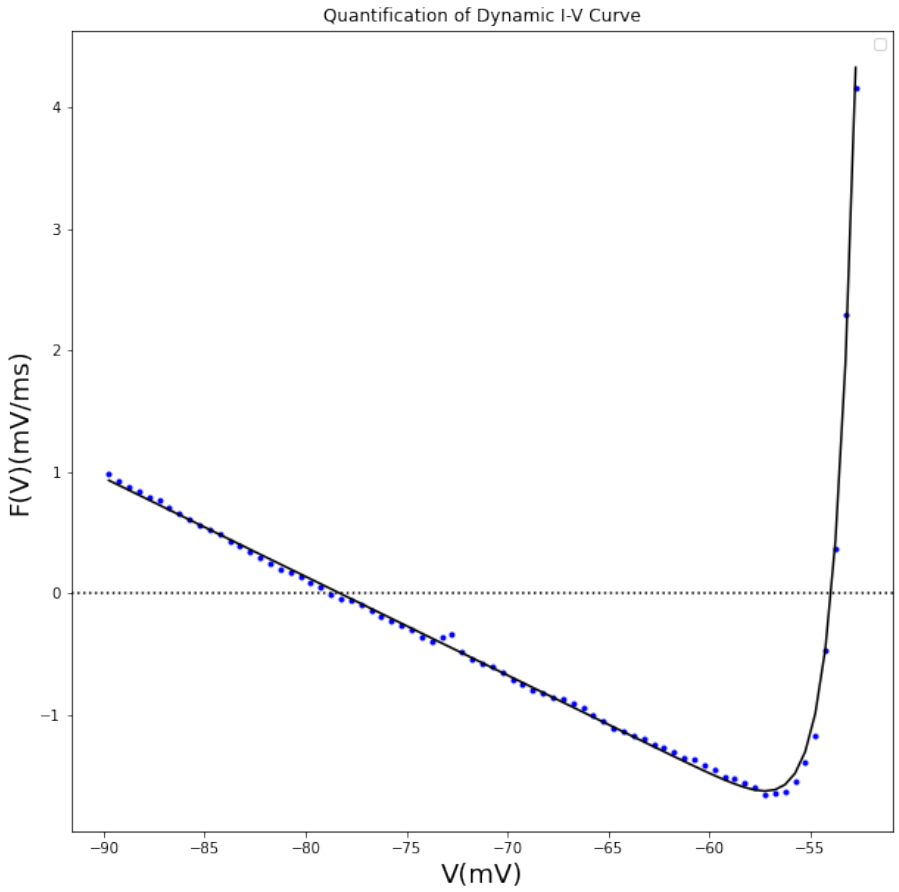

Figure 61: Obtained results by the Badel's work reproduction *in silico* fitted by the EIF model. Here, the extremes value are -(90,52) mV. The vertical bars in blue are the errors associated to the data. The neuronal model is one of the five different models of a bipolar pyramidal neurons.

Neuron	dT (mV)	fit_extremes (mV)	dT (mV)	fit_extremes (mV)	dT (mV)	fit_extremes (mV)	dT (mV)	fit_extremes (mV)	dT (mV)	fit_extremes (mV)
L6_BPC	1.03	(-90,-52)	1.54	(-90,-52)	1.04	(-90,-52)	1.10	(-90, -52)	1.55	(-90, -52)
L5_TTPC2	0.88	(-90,-52)	0.82	(-90,-52)	0.84	(-90,-52)	0.83	(-90,-52)	0.87	(-90,-52)
L6_TPC_L1	0.86	(-90,-52)	1.07	(-90,-52)	1.24	(-90,-52)	1.33	(-90,-52)	0.98	(-90,-52)
L5_UTPC	2.03	(-90,-47)	1.43	(-90,-47)	1.50	(-90,-47)	1.51	(-90, -52)	1.56	(-90, -52)
L6_TPC_L4	1.17	(-90,-52)	1.01	(-90,-52)	1.24	(-90,-52)	1.25	(-90,-52)	1.33	(-90,-52)
L6_UTPC	1.57	(-90,-50)	1.13	(-90,-50)	1.64	(-90,-50)	1.64	(-90,-50)	1.46	(-90,-50)
L5_STPC	0.91	(-90,-52)	2.17	(-90,-49)	2.10	(-90;-47)	2.26	(-90,-47)	1.56	(-90,-48)
L4_PC	0.92	(-90,-55)	1.18	(-90,-55)	1.10	(-90,-55)	0.87	(-90, 54.5)	1.22	(-90,-55)
L4_SP	0.76	(-90,-55.5)	1.05	(-90,-55.5)	1.11	(-90,-55.5)	1.01	(-90,-55.5)	1.02	(-90,-55.5)
L4_SS	1.05	(-90,-54)	1.08	(-90,-54)	1.04	(-90,-54)	1.07	(-90,-54)	1.03	(-90,-54)
L5_TTPC1	0.92	(-90, -52)	0.78	(-90, -52)	0.94	(-90, -52)	0.92	(-90, -52)	0.89	(-90, -52)
L23_PC	2.15	(-90,-45);	2.25	(-90,-45);	2.09	(-90,-45);	2.11	(-90,-45)	2.09	(-90,-46)
L6_IPC	1.74	(-90, -52)	1.19	(-90, -52)	2.21	(-90,-51)	1.63	(-90,-51)	1.10	(-90,-52)

Figure 62: In summary in this table, all the dT values of the 65 me-types and their respective range of fit are shown. The first columns stays for the first me-types of the neurons,the fifth column stays for the fifth realisation. All the fits are in the section Appendix. The uncertainty of the measure is on the second digits after the comma.

All the other pictures of the EIF fit concerning the other 61 models are in sectionAppendix. In the same section, it is possible to find the code used to reproduce the Badel's work and fit the data with EIF model.

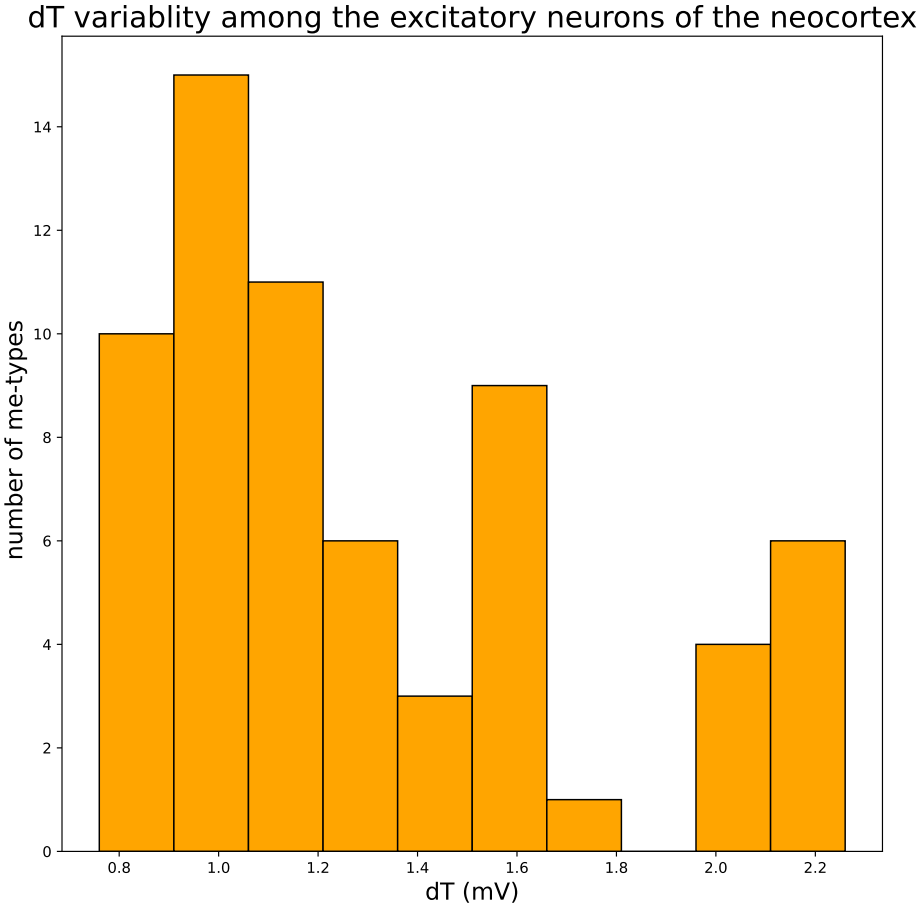

Figure 63: The histogram shows the dT values distribution of the neuronal multi-compartmental models. The distribution of them stays in a tiny interval that range from 0,76 mV to 2,26 mV. The total span of the interval is 1,5 mV, which is compatible with the experimental magnitude of the synaptic input amplitude of around 1 mV (Richardson, 2018).

5.3 Theory of Richardson verification on multi-compartmental models

The Richardson's theory has been verified over all the excitatory neurons of the neocortex of a rat. The multi-compartmental models of the neocortex has underline a variety of behaviour, first of all the effect needs a lot of statistic to be observed. More clearly, it was necessary repeat a lot of times the same simulation (around 61) to reach an APs number big enough to observe the I-O relationship of the neuron and whether the neuronal models were showing the effect theorised by Richardson (Richardson, 2018) at HF. A total of around $3 * 10^8$ AP events was necessary to describe the I-O neuronal behaviour in the HF domain. Then, after the data has been analysed and as a function of all the frequencies of modulation the I-O relationship has been shown, see 64. All the data above the minimal significance level of threshold (dashed lines in 64) have been accepted. In the HF domain, a linear regression model has extrapolated each slope of the different "cases" ("a_s < dT in blue, a_S= dT in green, a_s> dT in red and sometimes is present a_s» dT in black) in the frequency modulation range from 200 Hz to 1000 Hz see the example 64. A Kolmogorov-Smirnov (KS) test has been carried for each gain value in the HF domain of each case (A , B, C and eventually D) to prove that they are different cases and are not superimposable with each others and therefore they are distinguishable. In the results which will follow, the KS test will be indicates as stars over each f_{mod} 64. The slope of the linear attenuation at HF have been obtained with a linear regression model for each case and for each neuronal model. In the following results some multi-compartmental model show to reproduce clearly the Richardson's theory, furthermore, some other slightly reproduce the effect; on the other hand, the majority of the neuronal model seems to not reproduce the Richardson's theory. Over 65 neuronal models analysed in this work, around 34% (22 models) will be shown to reproduce the Richardson's

theory; on the contrary, the remaining 66% will not behave as predicted by the Richardson's theory. I will discuss more in detail about this later.

All the slope values extrapolated for each of the 65 neuronal models are reported in the figure 70. In the following images, it will be shown some neuronal models examples which are in agreement or not with the Richardson's theory. The neuronal models that show the Richardson's theory have a clear different slopes in the HF domain and the gain amplitudes of the "cases" is increase while a_s increase as well, in other words, when a_s is equal to dT the gain amplitude for each frequency in the HF domain should be bigger than when a_s is smaller than dT. This idea is valid as well when a_s in bigger than dT compared to the other "cases", see figure 2 in the paper of Richardson (Richardson, 2018). Here, there are some examples which show the Richardson's effect: the neuronal model of the thick-tufted layer V pyramidal neurons, L5_TTPC1_cADpyr232_1 and the tufted pyramidal neuron of the layer 6 which has dendritic tufts which end in the layer 1, L6_TPC_L1_cADpyr231_1 see figure 64 and figure 65; for a more numerical guide look at the figure 70. The slopes values of the neuronal models, considering their error over the linear regression; cannot be clearly be superimposed for both the models and for each "case". To summarise here are reported the slope values for both models: the thick tufted pyramidal of Layer 5: case A:(-1.24 ± 0.04), case B:(-1.03 ± 0.03), case C: (-0.86 ± 0.02). The same happens for the neuronal model L6_TPC_L1_cADpyr231_1: case A:(-0.87 ± 0.03), case B:(-0.80 ± 0.03), case C: (-0.69 ± 0.03).

Before in this subsection, I mentioned some other neuronal models which show a slightly presence of the Richardson's theory; some example are the models L23_PC_cADpyr229_3 and L4_PC_cADpyr230_1, which will be shown below. The values of the slopes are for both model different considering the linear regression error for the extreme cases, such as case A versus case C or D, however, the middle case (case B) it is not clearly different from the two extremes. Nevertheless, the

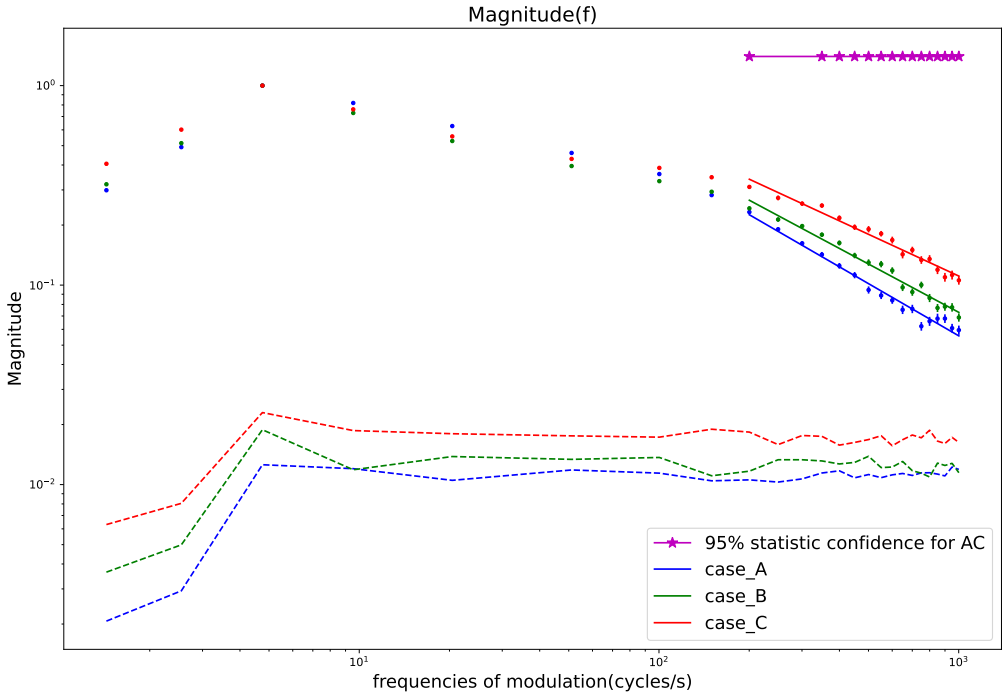

Figure 64: An example of the gain as a function of the modulation frequency of one of the 65 neuronal models, the model is the L5_TTPC1_cADpyr232_1 from the BBP project. The gain values are normalised over their maximum located around the $f_{mod} \sim$ 5Hz. The data of the different "cases" are shown; the color blue stays for when the dT > a_s, the green for when a_s = dT and the red for when a_s< dT. The dashed lines stay for each cases as the minimal level of significance threshold. The magenta line and the stars indicate for each f_{mod} value that the case A and C cannot be superimposed at the 95% of significance of the KS test. The solid lines of each color are the HF domain linear fit used to extrapolated the HF slope of the linear attenuation; the slopes values for each cases and neuronal models are in figure 70. In this neuronal models, the slope in the HF domain has three different values as a function of the mean synaptic value a_s if it is bigger, equal or smaller than the dT. The slopes values are shown in the figure 70.

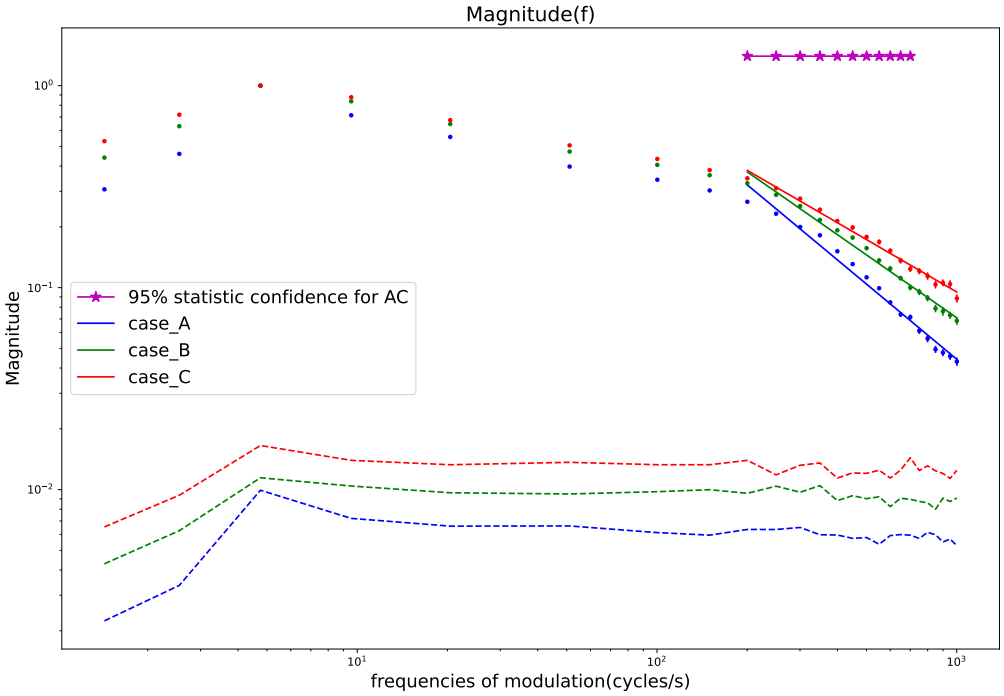

Figure 65: Another example of a neuronal model which shown the Richardson's effect at HF, the neuronal model of tufted pyramidal neuron with dendritic tufts terminating in layer 1. The slopes values are shown in the figure 70.

middle case is a tiny junction between the diffusion approximation regime, when a_s is smaller than dT and when happens the opposite. In this work, the presence of the Richardson's effect has still considered valid and present, even if, only the extremes cases shown a different HF domain slopes together with the correct area subtend to the I-O relationship see figure 66 and 67. To summarise here are reported the slope values for both models: the pyramidal neuron of layer 2-3, L23_PC_cADpyr229_3, has a very well distinguish the cases A and C, but not the case B with the others: case A: (-1.17 ± 0.04), case B:(-1.10 ± 0.04), case C: (-0.99 ± 0.04). For the pyramidal neuron of layer 4, L4_PC_cADpyr230_1 happens the same, with an additional case the case D. Even if the case D and the case C are not distinguishable, the extremes value has different slopes, underlining the the presence of the Richardson's effect. case A:(-1.0 ± 0.1), case B:(-0.8 ± 0.1), case C:(-0.7 ± 0.1), case D:(-0.7 ± 0.1).

As before mentioned, the 66% of the neuronal models are not showing the presence of the effect theorised in the Richardson's theory. Some neuronal models used as the L4_SP_cADpyr230_1 and L6_BPC_cADpyr231_1 have been chosen to underline the necessity to show for the different "cases" ($a_s < dT$ A, $a_s = dT$ B, $a_s > dT$ C and sometimes $a_s >> dT$ D) to have distinct linear slopes values in the HF domain and that the "case" with $a_s > dT$ should have bigger gain amplitude than the one with the $a_s < dT$; as reported in the paper of (Richardson, 2018). The examples are showed in the figure 68 and 69.

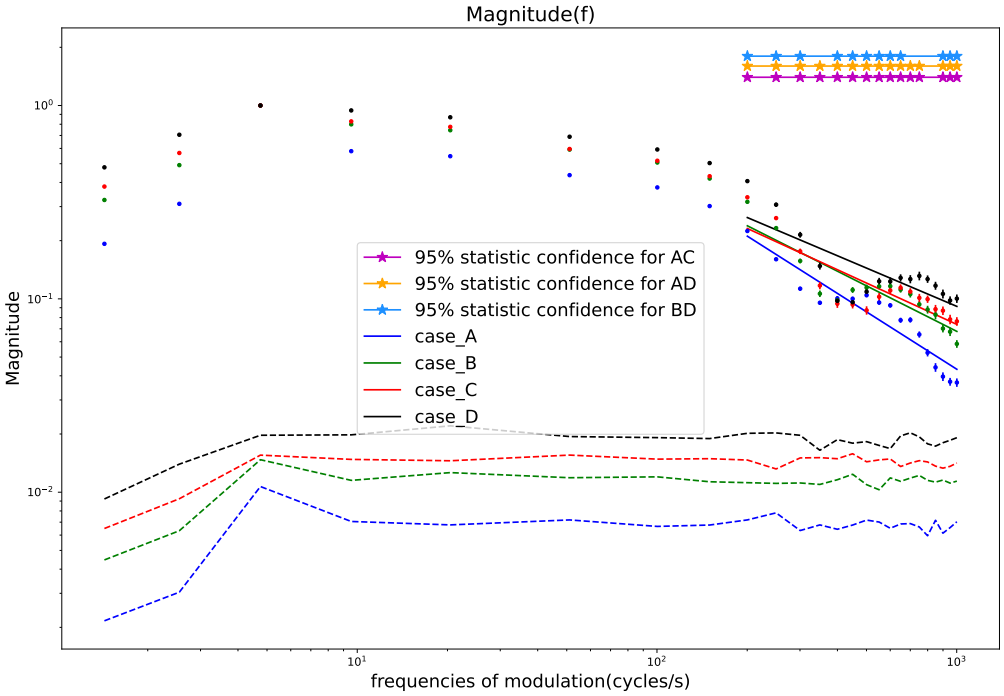

Figure 66: An example of a neuronal model, the L4_PC_cADpyr230_1, which shown the Richardson's effect at HF, only between the case A and Case C or D. However the effect is till present. The slopes values are shown in the figure 70.

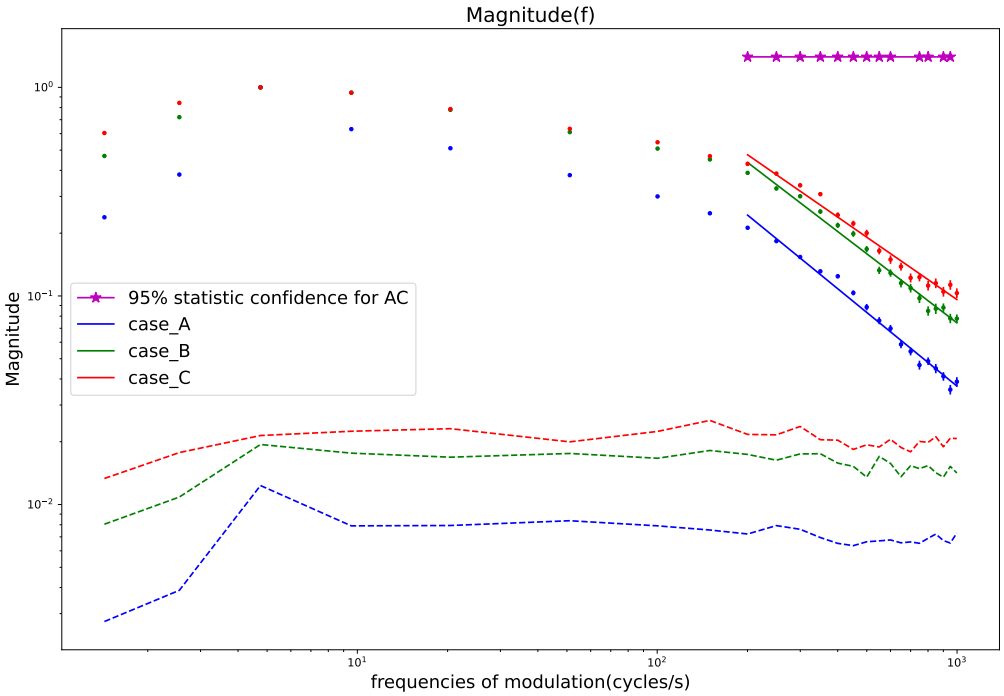

Figure 67: The neuronal model of the pyramidal neuron of the layer 2-3, L23_PC_cADpyr229_3, shows the Richardson's effect at HF, only between the case A and Case C or D. However the effect is still present. The slopes values are shown in the figure 70.

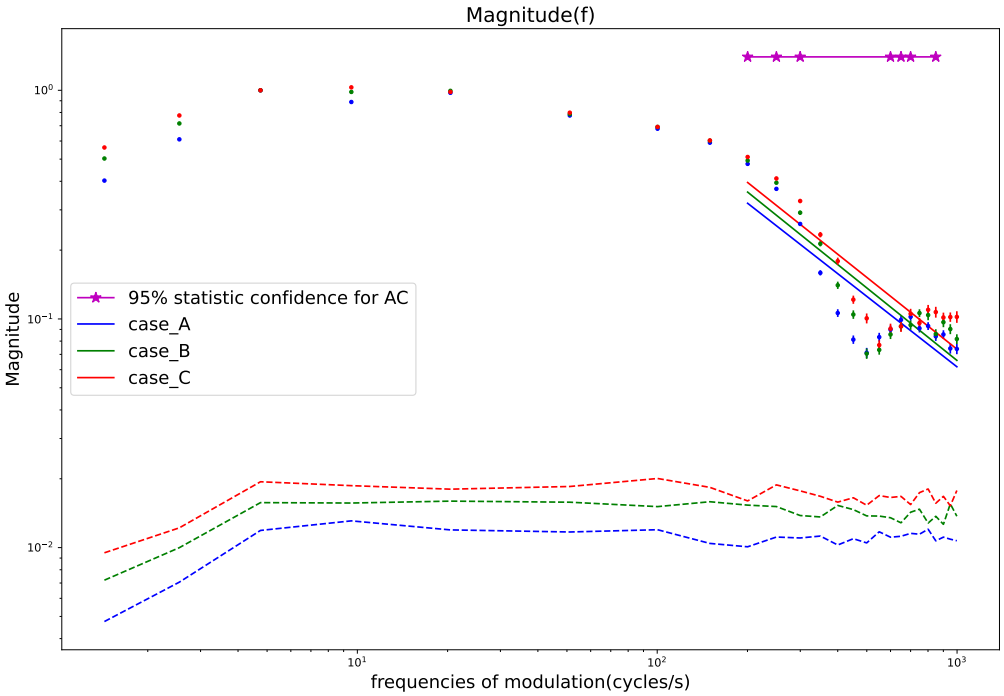

Figure 68: An example of a neuronal model, the L6_BPC_cADpyr231_1, it doesn't show the presence of the effect theorised by Richardson (Richardson, 2018), since the HF domain linear regression slope values are not distinguishable. The slopes values are shown in the figure 70.

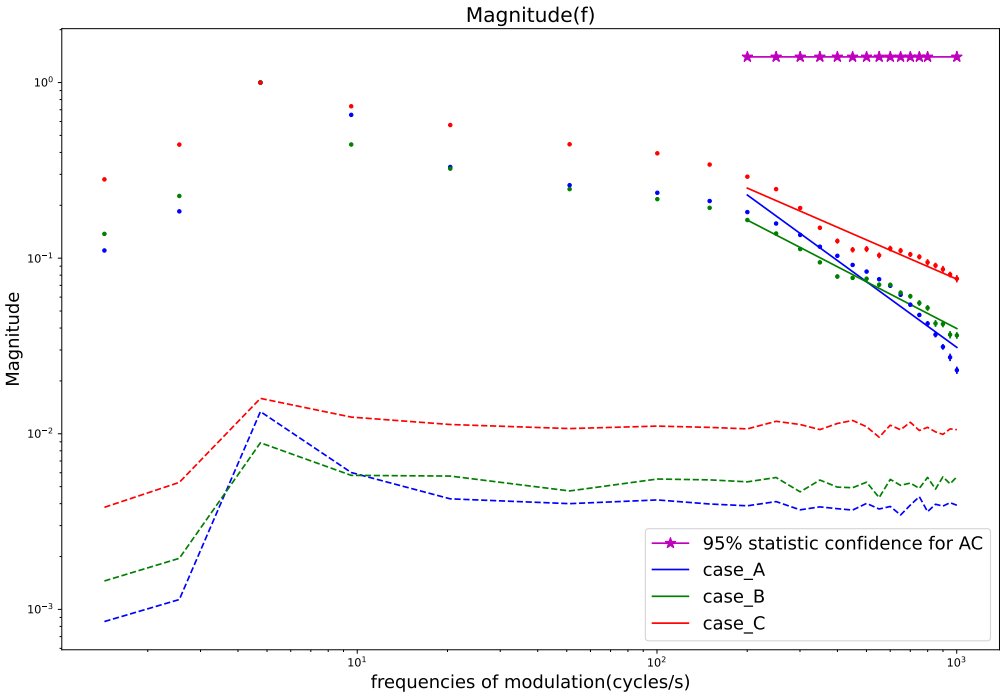

Figure 69: An example of a neuronal model, the L4_SP_cADpyr230_1, at the HF domain the slopes has distinct values, however the gain amplitude vales are not correct since the case A (a_s < dT has an higher amplitude than the case B a_s = dT). The slopes values are shown in the figure 70.

So far, it has been observed which in some models the effect theorised by Richardson is present and, on the other hand, in some other neuronal models seem to be absent. In addition, in all the me-types of the slender pyramidal neuron for the layer 4, such as L4_SP_cADpyr230_(1,2,3,4,5) and in the bipolar pyramidal neuron of the layer 6, L6_BPC_cADpyr231_(1,2,3,4,5) the effect is not present. All the other figure that show the I-O properties of the others neuronal models are in the subsection I-O properties at the HF for each neuronal models. From the results obtained so far, it is possible to say that the Richardson's theory is present in some of the multi-compartmental models, which are currently the state-of-the-art neuronal models; therefore it seems true that the interplay between the AP sharpness onset and the mean value of the synaptic input occurs plays a role in the I-O behaviour of an excitatory neuron in the domain of the HF. However, so far, even with further investigation there is not a clear reason about why some times the neuronal models show the Richardson effect and why sometimes not.

Neuron	slope_A	slope_B	slope_C	slope_D
L5_TTPC2_cADpyr232_3	(-0.70±0.02)	(-0.73± 0.03)	(-0.71± 0.02)	(0± 0)
L6_BPC_cADpyr231_4	(-1.09± 0.02)	(-0.98± 0.05)	(-0.94± 0.06)	(0± 0)
L6_TPC_L4_cADpyr231_5	(-1.35± 0.06)	(-1.00±0.05)	(-0.86± 0.04)	(0± 0)
L4_SS_cADpyr230_1	(-1.09± 0.03)	(-0.92± 0.03)	(-0.83± 0.02)	(-0.69± 0.02)
L5_TTPC1_cADpyr232_2	(-0.84± 0.03)	(-0.79± 0.03)	(-0.76± 0.02)	(-0.78± 0.03)
L6_TPC_L1_cADpyr231_2	(-1.04± 0.07)	(-1.0±0.1)	(-1.0±0.1)	(-1.0±0.1)
L4_PC_cADpyr230_3	(-1.09± 0.04)	(-0.94± 0.03)	(-0.85± 0.03)	(-0.75± 0.02)
L4_SP_cADpyr230_1	(-1.24± 0.08)	(-0.88± 0.04)	(-0.74± 0.06)	(0± 0)
L4_SS_cADpyr230_4	(-1.06± 0.04)	(-0.88± 0.02)	(-0.81± 0.02)	(-0.74± 0.03)
L5_TTPC2_cADpyr232_2	(-0.89± 0.02)	(-0.82± 0.03)	(-0.75± 0.03)	(-0.92± 0.07)
L6_IPC_cADpyr231_2	(-1.6±0.1)	(-1.02± 0.02)	(-0.84± 0.07)	(-0.78± 0.09)
L6_IPC_cADpyr231_3	(-1± 0.1)	(-1.0±0.1)	(-0.8± 0.1)	(0± 0)
L5_STPC_cADpyr232_2	(0.80±0.05)	(-0.76± 0.04)	(0.70±0.03)	(-0.70±0.03)
L4_PC_cADpyr230_5	(-1.25± 0.05)	(-0.87± 0.08)	(-0.7± 0.1)	(0± 0)
L23_PC_cADpyr229_2	(-1.37± 0.06)	(-1.10±0.08)	(-0.72± 0.09)	(-0.58± 0.09)
L6_UTPC_cADpyr231_2	(-1.30±0.04)	(-0.92± 0.07)	(-0.8± 0.1)	(0± 0)
L5_STPC_cADpyr232_3	(-0.62± 0.08)	(-0.6± 0.1)	(-0.56± 0.09)	(0± 0)
L5_UTPC_cADpyr232_1	(-0.8± 0.1)	(-0.67± 0.06)	(-0.58± 0.03)	(0± 0)
L4_SS_cADpyr230_2	(-1.08± 0.04)	(-0.89± 0.03)	(-0.82± 0.03)	(0.80±0.02)
L23_PC_cADpyr229_3	(-1.17± 0.04)	(-1.10±0.04)	(-0.99± 0.04)	(0± 0)
L5_UTPC_cADpyr232_5	(-0.8± 0.1)	(0.70±0.04)	(0.70±0.03)	(0± 0)
L6_UTPC_cADpyr231_5	(-1.0±0.1)	(-1.0±0.1)	(-0.9± 0.1)	(0± 0)
L6_IPC_cADpyr231_4	(-1.04± 0.06)	(-0.9± 0.1)	(-0.8± 0.1)	(0± 0)
L5_TTPC1_cADpyr232_5	(-0.64± 0.03)	(-0.68± 0.03)	(-0.68± 0.02)	(0± 0)
L5_STPC_cADpyr232_1	(0.80±0.05)	(-0.76± 0.04)	(0.70±0.03)	(0± 0)
L5_TTPC1_cADpyr232_4	(-0.80±0.04)	(-0.81± 0.03)	(-0.79± 0.02)	(0± 0)
L5_UTPC_cADpyr232_3	(-0.68± 0.06)	(-0.70±0.03)	(-0.69± 0.02)	(0± 0)
L6_BPC_cADpyr231_3	(-1.08± 0.03)	(-0.94± 0.02)	(-0.90±0.04)	(0± 0)
L6_TPC_L1_cADpyr231_4	(-1.06± 0.07)	(-1.0±0.1)	(-0.9± 0.1)	(0± 0)
L6_TPC_L4_cADpyr231_4	(-1.21± 0.05)	(-1.0±0.1)	(-0.8± 0.1)	(0± 0)
L6_TPC_L1_cADpyr231_3	(-1.23± 0.04)	(-0.93± 0.06)	(-0.8± 0.1)	(0± 0)
L6_UTPC_cADpyr231_3	(-1.24± 0.04)	(-0.9± 0.1)	(-0.8± 0.1)	(0± 0)
L6_TPC_L4_cADpyr231_2	(-1.18± 0.04)	(-0.98± 0.02)	(-0.85± 0.03)	(0± 0)
L5_TTPC1_cADpyr232_1	(-0.87± 0.03)	(-0.80±0.03)	(-0.69± 0.03)	(0± 0)
L6_TPC_L1_cADpyr231_1	(-1.24± 0.04)	(-1.03± 0.03)	(-0.86± 0.02)	(0± 0)
L4_PC_cADpyr230_4	(-1.18± 0.07)	(-0.89± 0.05)	(-0.81± 0.04)	(0± 0)
L5_STPC_cADpyr232_5	(-0.8± 0.1)	(-0.74± 0.07)	(-0.67± 0.04)	(0± 0)
L6_BPC_cADpyr231_5	(-1.07± 0.03)	(-1.0±0.1)	(-0.9± 0.1)	(0± 0)
L5_TTPC2_cADpyr232_4	(-0.66± 0.04)	(-0.73± 0.03)	(-0.69± 0.02)	(0± 0)
L4_SS_cADpyr230_5	(-1.09± 0.04)	(-0.96± 0.03)	(-0.84± 0.02)	(-0.77± 0.03)
L6_IPC_cADpyr231_5	(-1.23± 0.05)	(-1.07± 0.03)	(-0.99± 0.03)	(0± 0)
L5_STPC_cADpyr232_4	(-0.86± 0.02)	(-0.76± 0.03)	(-0.73± 0.03)	(0± 0)
L6_BPC_cADpyr231_1	(-1.0±0.2)	(-1.0±0.1)	(-1.0±0.1)	(0± 0)
L6_TPC_L4_cADpyr231_1	(-1.45± 0.06)	(-0.94± 0.02)	(-0.81± 0.05)	(-0.72± 0.07)
L4_PC_cADpyr230_2	(-1.5± 0.1)	(-0.83± 0.05)	(-0.72± 0.07)	(-0.6± 0.1)
L4_SS_cADpyr230_3	(-1.11± 0.05)	(-0.90±0.03)	(-0.82± 0.03)	(0± 0)
L6_TPC_L4_cADpyr231_3	(-1.5± 0.1)	(-0.94± 0.08)	(-0.8± 0.1)	(0± 0)
L23_PC_cADpyr229_1	(-1.29± 0.05)	(-1.31± 0.06)	(-1.13± 0.06)	(-0.98± 0.06)
L6_IPC_cADpyr231_1	(-1.06± 0.05)	(-1.0±0.1)	(-0.9± 0.1)	(-0.8± 0.1)
L5_TTPC2_cADpyr232_1	(-0.71± 0.03)	(-0.75± 0.02)	(-0.73± 0.02)	(0± 0)
L6_UTPC_cADpyr231_4	(-1.13± 0.03)	(-0.9± 0.1)	(-0.8± 0.1)	(0± 0)
L4_SP_cADpyr230_5	(-1.10±0.05)	(-0.91± 0.04)	(-0.82± 0.02)	(0± 0)
L5_TTPC1_cADpyr232_3	(-0.87± 0.03)	(-0.86± 0.03)	(-0.81± 0.02)	(0± 0)
L4_SP_cADpyr230_4	(-1.15± 0.05)	(-0.91± 0.03)	(-0.82± 0.03)	(0± 0)
L6_UTPC_cADpyr231_1	(-1.20±0.04)	(-0.96± 0.03)	(-0.86± 0.04)	(0± 0)
L6_TPC_L1_cADpyr231_5	(-1.09± 0.03)	(-0.99± 0.03)	(-0.93± 0.07)	(0± 0)
L4_PC_cADpyr230_1	(-1± 0.1)	(-0.8± 0.1)	(-0.7± 0.1)	(-0.7± 0.1)
L23_PC_cADpyr229_5	(-1.0±0.1)	(-1.0±0.1)	(-0.7± 0.1)	(0± 0)
L4_SP_cADpyr230_3	(-1.07± 0.04)	(-0.90.0±0.03)	(-0.82± 0.02)	(0± 0)
L5_UTPC_cADpyr232_2	(-0.7± 0.1)	(-0.71± 0.04)	(-0.66± 0.03)	(0± 0)
L6_BPC_cADpyr231_2	(-1.1± 0.2)	(-1.1± 0.2)	(-0.9± 0.1)	(0± 0)
L5_UTPC_cADpyr232_4	(-0.72± 0.05)	(-0.73± 0.02)	(-0.70±0.03)	(0± 0)
L4_SP_cADpyr230_2	(-1.14± 0.05)	(-1.03± 0.04)	(-0.98± 0.05)	(0± 0)
L5_TTPC2_cADpyr232_5	(-0.70±0.05)	(-0.76± 0.02)	(-0.73± 0.02)	(0± 0)
L23_PC_cADpyr229_4	(-1.16± 0.04)	(-1.11± 0.04)	(-0.92± 0.05)	(-0.88± 0.03)

Figure 70: Results of the linear regression at the HF domain (200-1000 Hz) for all the multi-compartmental models.

5.4 Further investigation on possible biophysical magnitudes correlations

Some additional investigations have been performed over the slopes values and over the dT values to verify if there was a correlation between dT with some biophysical neuronal magnitude, such as the total dendritic length (TDL). Furthermore, also the slopes of the HF domain for each "cases" and each neuronal model (65) have been used to calculate their the mean, the difference (maximum slope less minimum slope), and the slopes difference over their mean. In addition, it has been performed a linear regression over the slopes, to find a linear slopes of the slopes for each "cases" and neuronal model, (that will called slopes of the slopes).

The idea to correlate the dT and the HF slopes with the TDL, come from the work of Eyal and collaborators (Eyal et al., 2014), since it has been shown in their work that the increase of the TDL increases the sharpness of an AP as well as the cross-over (cut-off frequency) frequency. The result of the correlation between the dT and the different values calculated from the HF slopes has been shown in the following figures 73, 74, 76, 75, 72, 77 and 78. However, it has not been found any correlation between the TDL, the slopes and the dT. On the other hand, between the TDL and the slopes mean, the slopes difference, the difference over their mean and, in the end, the linear regression of the slopes(that will be called slopes of the slopes;) it has been found a fair correlation confirmed by both the tests performed, the Pearson and Kendall's "Tau" test. It has been performed a Pearson test and a non-parametric Kendall's "Tau" test to verify the presence of correlation between the magnitude considered in this analysis, both the tests agree for a fair (above ± 0.4) correlation or anti-correlation when it has been found with a p value way smaller than the significance level of $\alpha = 0.05$ see table 72. Furthermore, it has not expected a correlation between dT and the slopes at HF domain and between TDL and dT,

Neuron	TDL(µm)	TDL(µm)	TDL(µm)	TDL(µm)	TDL(µm)
L6_BPC	7371	9644	7526	7999	9654
L5_TTPC2	18153	15359	15236	15131	15345
L6_TPC_L1	9530	10163	5209	7183	10045
L5_UTPC	8798	7792	7943	9057	9285
L6_TPC_L4	7994	8241	7961	7755	7892
L6_UTPC	8502	8562	9231	9566	6908
L5_STPC	12397	11835	12325	12069	11642
L4_PC	10345	6654	6523	6500	5157
L4_SP	5199	4363	4184	4453	4430
L4_SS	5499	5434	4375	3337	3570
L5_TTPC1	18190	18196	18190	18194	15322
L23_PC	6090	5841	5557	5534	7030
L6_IPC	10776	5956	4850	10516	6377

Figure 71: Here,the total dendritic length (TDL) of the 65 multi-compartmental models are shown, the TDL results have been obtained from the morphology files of the BBP for each model.

since this last properties is a somatic one. In the following table, 71, there will be the total dendritic length (TDL) obtained from the 65 multi-compartmental models.

In the following table, it will be shown the presence or not of correlation and their respective values of tau, p-value and Pearson coefficient.

Summarising all the investigations performed in this work and focusing on the anti-correlation present between the slopes of the slopes and the TDL; it seems that bigger neurons, or more precisely, more 3D extended neurons, hence with a bigger TDL, have a less sensitivity of statistics of the input. The discover of this anti-correlation lead us to add some more words: The Richardson's effect (Richardson, 2018) is present and is valid; however, when a neuron resembles less and less a point-neuron, the effect seems to lose its relevance and the I-O relationship in the HF domain seems to depends only to the neuronal properties itself; going back to the universality of the I-O properties described by (Linaro et al., 2017).

test	dT and slopes	TDL and slopes of the slopes	TDL and the mean of the slopes	TDL and the max(slopes - min(slopes)	TDL and the (max(slopes - min(slopes))/mean(slopes)
Pearson	no correlation	fair anticorrelation	fair correlation	fair anticorrelation	fair correlation
tau-kendall	no correlation	fair anticorrelation	fair correlation	fair anticorrelation	fair correlation

test	dT and slopes	TDL and slopes of the slopes	TDL and the mean of the slopes	TDL and the max(slopes - min(slopes)	TDL and the (max(slopes - min(slopes))/mean(slopes)
Pearson	r ≈-0.03, pv =0.613	r =-0.54, pv $<10^{-5}$	r = 0.57, pv $<10^{-6}$	r = -0.48, pv $<10^{-4}$	r = 0.46, pv $<10^{-4}$
tau-kendall	r ≈-0,.09 pv =0.613	r =-0.54, pv ≈$3*10^{-6}$	r = 0.57, pv ≈$8*10^{-7}$	r = -0.48, pv≈$4*10^{-5}$	r = 0.46, pv $<10^{-4}$

Figure 72: Resume table of the presence or not of the correlation and their degree of correlation/anti-correlation between the considered magnitudes. The significance level is $\alpha = 0.05$

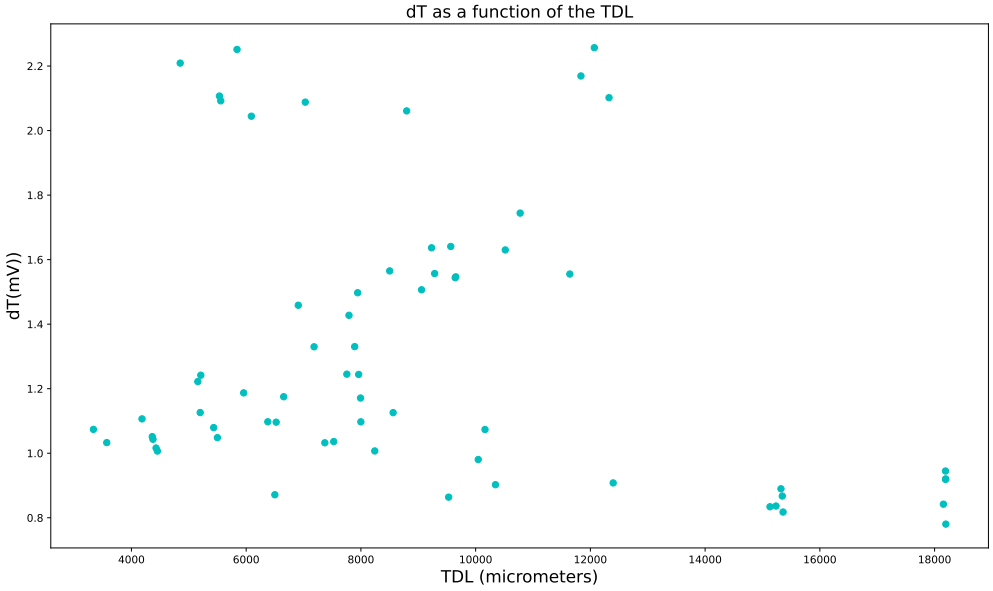

Figure 73: Here, it is shown the dT as a function of the total dendritic length. From both the tests, the Pearson and the Kendall's "Tau" there is not any correlation between these two magnitudes. the tau value and the p-value are: $\tau = -0.24$ and pv=0.613 with a level of significance of $alpha = 0.05$. See the above for detail the table 72

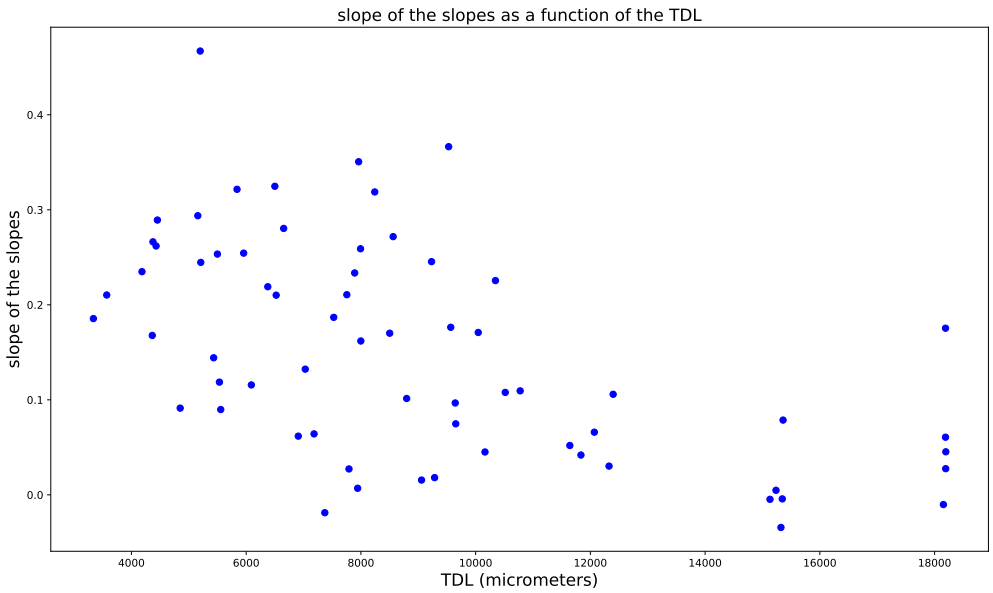

Figure 74: Here it is shown the slopes of the slopes as a function of the total dendritic length. From both the tests, the Pearson and the Kendall's "Tau" there is a fair anti-correlation between these two magnitudes. Hence, it means that bigger neurons are less sensitive to the statistics of the neuron compared to the smaller ones. The $\tau = -0.54$ and the $p - value \sim 3 * 10^(-6)$ with a level of significance of $alpha = 0.05$. See the above for detail the table 72

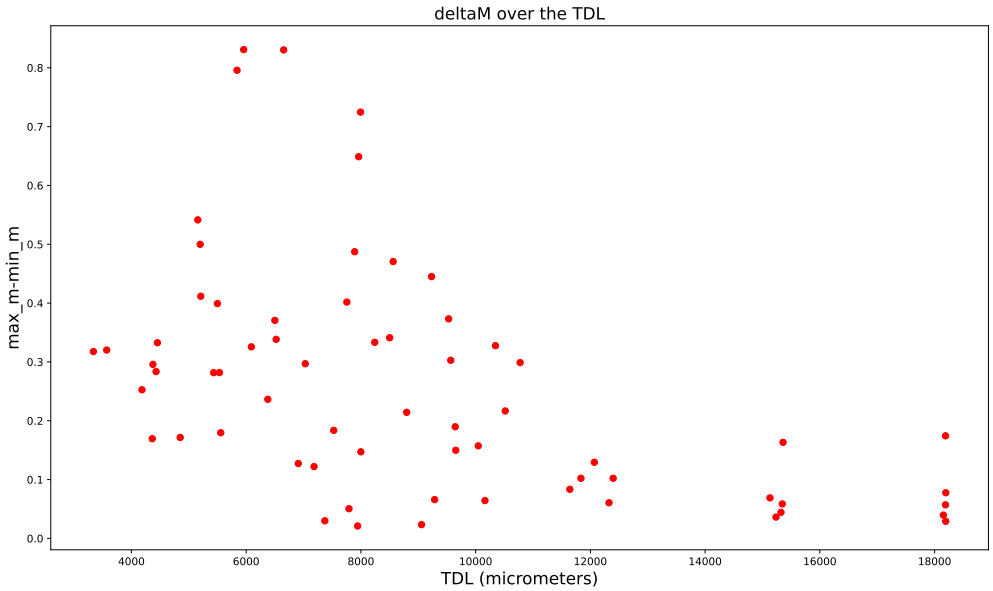

Figure 75: Here, it is shown the difference between the maximum and minimum values values of the slopes for each neuronal models as a function of the total dendritic length. From both the tests, the Pearson and the Kendall's "Tau" there is a fair anti-correlation between these two magnitudes. It means bigger neurons are less sensitive to the statistics of the neuron compared to the smaller ones as said in the figure 74. The $\tau = -0.48$ and the $p - value \sim 4 * 10^(-5)$ with a level of significance of $alpha = 0.05$. See the above for detail the table 72

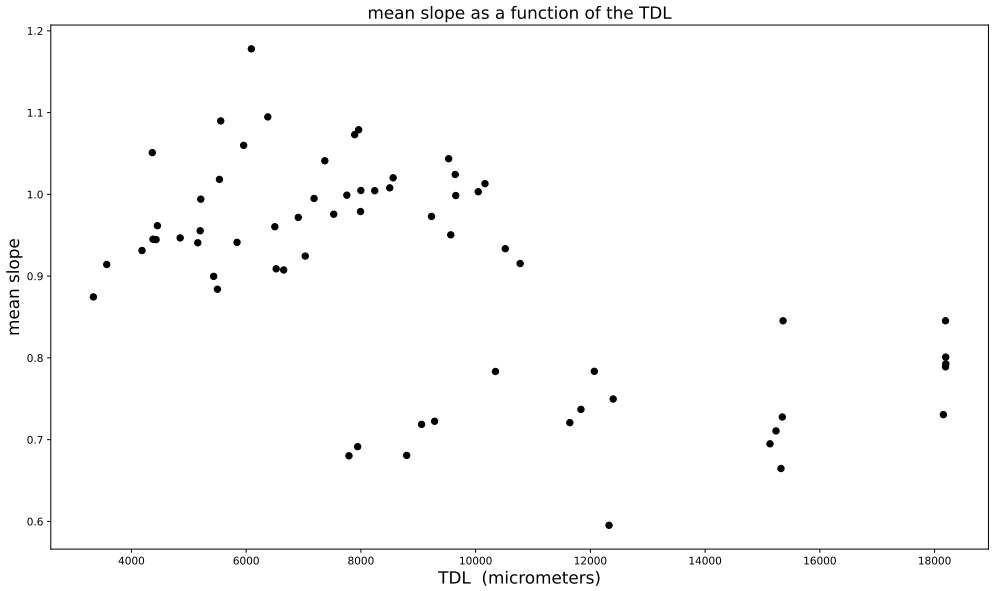

Figure 76: Here, it is shown the means of the slopes for each neuronal models as a function of the total dendritic length. From both the tests, the Pearson and the Kendall's "Tau" there is a fair correlation between these two magnitudes. It means for bigger neurons the slopes at the HF domain are bigger on average. Showing a less prominent effect than the smaller neurons. The $\tau = 0.57$ and the $p - value \sim 1 * 10^{(} - 6)$ with a level of significance of $alpha = 0.05$. See the above for detail the table 72

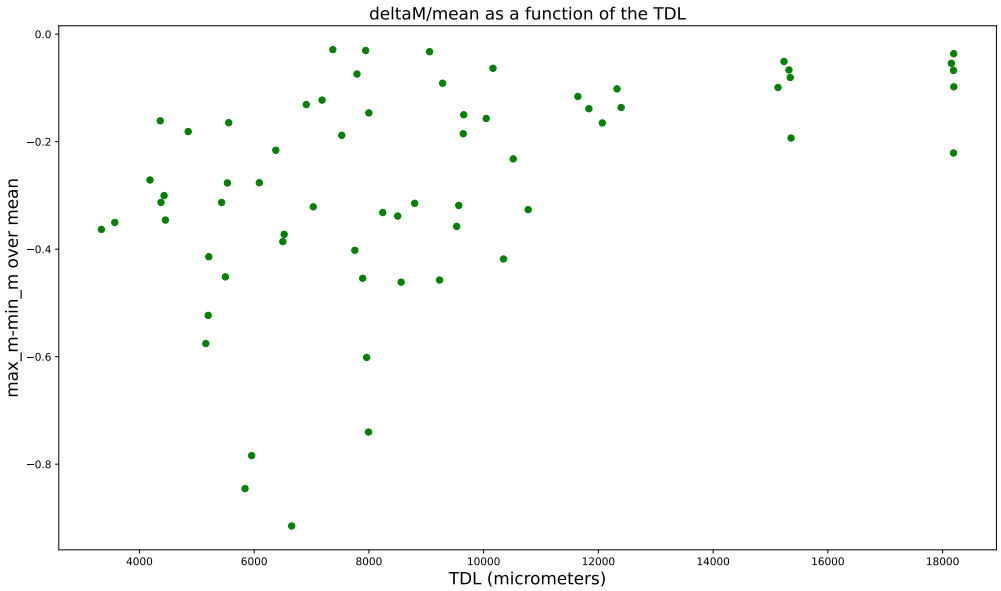

Figure 77: Here, it is shown the ratio between the difference between the maximum and minimum values and the values means of the slopes, for each neuronal models, as a function of the total dendritic length. From both the tests, the Pearson and the Kendall's "Tau" there is a fair correlation between these two magnitudes. It means for bigger neurons the slopes at the HF domain are bigger on average. Showing a less prominent effect than the smaller neurons. The $\tau = 0.46$ and the $p - value \sim 1 * 10^(-4)$ with a level of significance of $alpha = 0.05$. See the above for detail the table 72

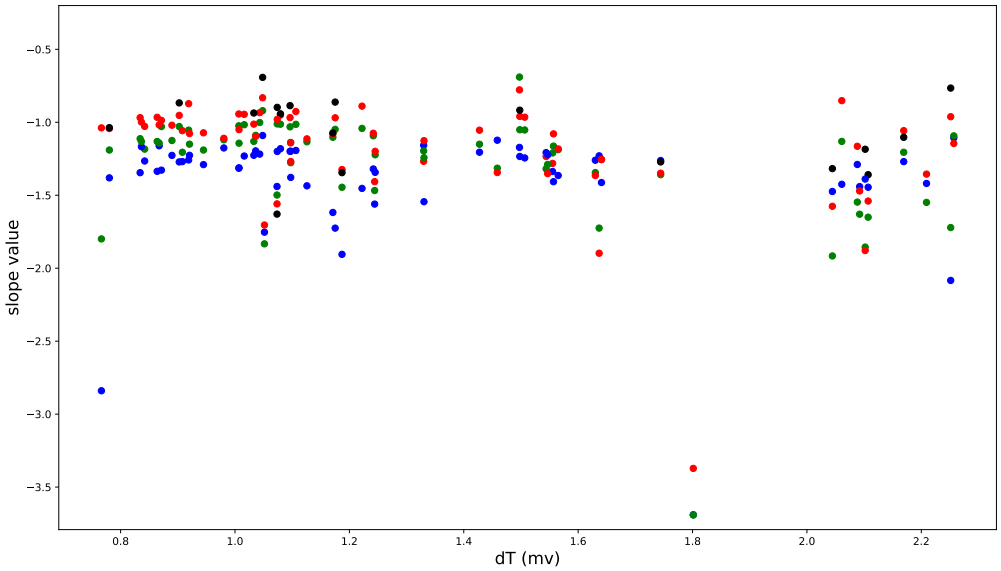

Figure 78: Here, it is shown the slopes as a function of dT. From both the tests, the Pearson and the Kendall's "Tau" there is not any correlation between these two magnitudes. the tau value and the p-value are: $\tau = -0.09$ and pv=0.613 with a level of significance of $alpha = 0.05$. See the above for detail the table 72

6 Discussion

In this last part of this work, I will discuss the obtained results and add some future perspectives. First of all, I would like to recall the context of my PhD project; with the work of (Köndgen et al., 2008), in which the authors studied the cortical neuronal response as a function of a wide frequency range (1-1000 Hz) of the input frequency, analysing the role of the background noise. Their work led to discover an unexpected ability of the neuron to track fast transients without attenuation up to 200 cycles/s. This frequency value is the cut-off frequency, which has an higher limit than the only passive membrane properties ($\sim 50Hz$) and it is not affect by any input changes. Above the cut-off frequency, the amplitude of the magnitude decays with a power-law $f_{mod}^{-\alpha}$, in which f_{mod} is the input modulation frequency and α, the exponent, does not depend by the membrane voltage fluctuations due to the background input. Then, with the work of Linaro and colleagues (Linaro et al., 2017),it has been proven that the HF I-O properties of a pyramidal neuron of the layer 5 are not affected by the input and, in addition, the gain in the HF domain has a linear decay after the cut-off frequency with an exponent value between -1 and -2. Furthermore, since the HF domain of the I-O properties are not affected by the input, they depends only by the neuronal properties, introducing the concept of universality of the I-O properties at high frequency. More clearly, no matter what input is presented to the neuron; its I-O properties in the HF domain depend only by the neuronal properties themselves. On the contrary, a recent publication by Richardson (Richardson, 2018), demonstrated that the HF I-O properties of a EIF model (a conductance based model, which well described the neuronal excitability of cortical pyramidal neurons) depends by an interplay between the neuronal intrinsic properties and the statistic of the input. The neuronal properties are represented by the dT parameter of the EIF model by Fourcaud-Trocmé and colleagues (Fourcaud-Trocmé et al., 2003); on the other hand, the statistic of the input is represented by the mean amplitude of the input

a_s. This work is set in this context, and is a large numerical study with the goal to be a preparatory work focused on testing the Richardson's thesis (Richardson, 2018) and then, to set the necessary parameters for making easier a future experimental validation. From the results obtained by my PhD research, the first results is that the dT parameter range of the excitatory cortical neurons spans from 0,76 mV to 2,26 mV as expected to be around 1 mV as reported in the work of Richardson (Richardson, 2018). However, a very good results is to have proven the presence of the Richardson's effect in the state-of-the-art multi-compartmental model of the BBP; although the effect is not present in all the neuronal models, since some of them seem to exhibit it with different "intensity" or seem to not exhibit it at all. After further researches, it has been found that the slopes of the slopes has a fair anti-correlation (correlation value bigger than ± 0.4) with the TDL (see subsection Further investigation on possible biophysical magnitude correlations); which means that more a neuron is extended in the three dimensional space less sensitive is to the statistic of the input and, therefore, to the Richardson's effect, see also figure 73. In other words, less a neuron is resembling a point-neuron, like the EIF model, less is sensitive to the Richardson's effect. The universality of the I-O properties in the HF domain seems to be replaced by the Richardson's effect for neuron with a small TDL. On the other hand, for neuron very well extended and with a big TDL value, it seems that the Richardson's effect is no longer present and the universality of the I-O properties at HF is again prominent, see figure 73 and subsection Further investigation on possible biophysical magnitude correlations. Another results from my work is that the Richardson's effect is modest, more clearly it needs a lot of exposure time to have been seen. During my simulation for each case and f_{mod} I need to acquire around to $3 \cdot 10^8$ AP to see the effect. In the domain this mean repeat around 61 time a simulation of 10^6 ms, leading to a total time of the experiment of about 17 hours; that is definitely bigger than the entire life-span of a neuron in an

acute slices preparation. I would like to add some further words on possible further perspectives. The first future develop could be from the point of view of the code; most of my scripts would benefit to make them more efficient and, in particularly an automatic minimisation of dT estimation is suggested, since doing by myself I can have accidentally introduced a bias. It has been beneficial doing neuronal model by neuronal model, since it was an exploration of the dT and gave me the idea that every model is different. I can speculate that it would be possible doing it, training a small neuronal network to perform the task replacing the user eyes, experience and a possible presence of an introduced human bias. The second future development for the sake of the Master of the High-Performance Computing I have attended, could be develop a version of my code for taking advantages of the speed up potential of the GPUs, using as a guide the following work of Roy Ben Shalom and colleagues (Ben-Shalom et al., 2022). The third future development to prove my previous hypothesis, such as the anti-correlation between TDL and slopes of the slopes. The idea focus on performing a very interesting experiment, such as taking one of the neuronal model with the highest TDL value and then "dissect it" removing step my step a piece of the dendritic tree, reducing the TDL and veryfing my previous hypothesis.

7 Appendix

7.1 All comprehensive results

Neuron	M_m	M_diff	mean_m	M_diff/mean_m
L5_TTPC2_cADpyr232_3	0.005	0.04	-0.71	-0.05
L6_BPC_cADpyr231_4	0.162	0.15	-1.00	-0.15
L6_TPC_L4_cADpyr231_5	0.234	0.49	-1.07	-0.45
L4_SS_cADpyr230_1	0.253	0.40	-0.88	-0.45
L5_TTPC1_cADpyr232_2	0.045	0.08	-0.79	-0.10
L6_TPC_L1_cADpyr231_2	0.045	0.06	-1.01	-0.06
L4_PC_cADpyr230_3	0.210	0.34	-0.91	-0.37
L4_SP_cADpyr230_1	0.467	0.50	-0.96	-0.52
L4_SS_cADpyr230_4	0.186	0.32	-0.87	-0.36
L5_TTPC2_cADpyr232_2	0.079	0.16	-0.85	-0.19
L6_IPC_cADpyr231_2	0.254	0.83	-1.06	-0.78
L6_IPC_cADpyr231_3	0.091	0.17	-0.95	-0.18
L5_STPC_cADpyr232_2	0.042	0.10	-0.74	-0.14
L4_PC_cADpyr230_5	0.129	0.28	-0.95	-0.30
L23_PC_cADpyr229_2	0.322	0.80	-0.94	-0.85
L6_UTPC_cADpyr231_2	0.272	0.47	-1.02	-0.46
L5_STPC_cADpyr232_3	0.030	0.06	-0.60	-0.10
L5_UTPC_cADpyr232_1	0.101	0.21	-0.68	-0.31
L4_SS_cADpyr230_2	0.144	0.28	-0.90	-0.31
L23_PC_cADpyr229_3	0.090	0.18	-1.09	-0.16
L5_UTPC_cADpyr232_5	0.018	0.07	-0.72	-0.09
L6_UTPC_cADpyr231_5	0.062	0.13	-0.97	-0.13
L6_IPC_cADpyr231_4	0.108	0.22	-0.93	-0.23
L5_TTPC1_cADpyr232_5	-0.034	0.04	-0.66	-0.07
L5_STPC_cADpyr232_1	0.106	0.10	-0.75	-0.14
L5_TTPC1_cADpyr232_4	0.028	0.03	-0.80	-0.04
L5_UTPC_cADpyr232_3	0.007	0.02	-0.69	-0.03
L6_BPC_cADpyr231_3	0.187	0.18	-0.98	-0.19
L6_TPC_L1_cADpyr231_4	0.064	0.12	-1.00	-0.12
L6_TPC_L4_cADpyr231_4	0.211	0.40	-1.00	-0.40
L6_TPC_L1_cADpyr231_3	0.245	0.41	-0.99	-0.41
L6_UTPC_cADpyr231_3	0.245	0.45	-0.97	-0.46
L6_TPC_L4_cADpyr231_2	0.319	0.33	-1.00	-0.33
L5_TTPC1_cADpyr232_1	0.175	0.17	-0.79	-0.22
L6_TPC_L1_cADpyr231_1	0.366	0.37	-1.04	-0.36
L4_PC_cADpyr230_4	0.325	0.37	-0.96	-0.39
L5_STPC_cADpyr232_5	0.052	0.08	-0.72	-0.12
L6_BPC_cADpyr231_5	0.075	0.15	-1.00	-0.15
L5_TTPC2_cADpyr232_4	-0.005	0.07	-0.69	-0.10
L4_SS_cADpyr230_5	0.210	0.32	-0.91	-0.35
L6_IPC_cADpyr231_5	0.219	0.24	-1.09	-0.22
L5_STPC_cADpyr232_4	0.066	0.13	-0.78	-0.17
L6_BPC_cADpyr231_1	-0.019	0.03	-1.04	-0.03
L6_TPC_L4_cADpyr231_1	0.259	0.72	-0.98	-0.74
L4_PC_cADpyr230_2	0.280	0.83	-0.91	-0.92
L4_SS_cADpyr230_3	0.266	0.30	-0.95	-0.31
L6_TPC_L4_cADpyr231_3	0.351	0.65	-1.08	-0.60
L23_PC_cADpyr229_1	0.116	0.33	-1.18	-0.28
L6_IPC_cADpyr231_1	0.109	0.30	-0.92	-0.33
L5_TTPC2_cADpyr232_1	-0.010	0.04	-0.73	-0.05
L6_UTPC_cADpyr231_4	0.176	0.30	-0.95	-0.32
L4_SP_cADpyr230_5	0.262	0.28	-0.94	-0.30
L5_TTPC1_cADpyr232_3	0.061	0.06	-0.85	-0.07
L4_SP_cADpyr230_4	0.289	0.33	-0.96	-0.35
L6_UTPC_cADpyr231_1	0.170	0.34	-1.01	-0.34
L6_TPC_L1_cADpyr231_5	0.171	0.16	-1.00	-0.16
L4_PC_cADpyr230_1	0.226	0.33	-0.78	-0.42
L23_PC_cADpyr229_5	0.132	0.30	-0.92	-0.32
L4_SP_cADpyr230_3	0.235	0.25	-0.93	-0.27
L5_UTPC_cADpyr232_2	0.027	0.05	-0.68	-0.07
L6_BPC_cADpyr231_2	0.097	0.19	-1.02	-0.19
L5_UTPC_cADpyr232_4	0.016	0.02	-0.72	-0.03
L4_SP_cADpyr230_2	0.168	0.17	-1.05	-0.16
L5_TTPC2_cADpyr232_5	-0.004	0.06	-0.73	-0.08
L23_PC_cADpyr229_4	0.119	0.28	-1.02	-0.28

Figure 79: in This table are present for each neuronal model values of the mean slopes, the difference between the maximum and the minimum values of the slopes, the ratio between the difference aforementioned and the mean and the slopes of the slopes.

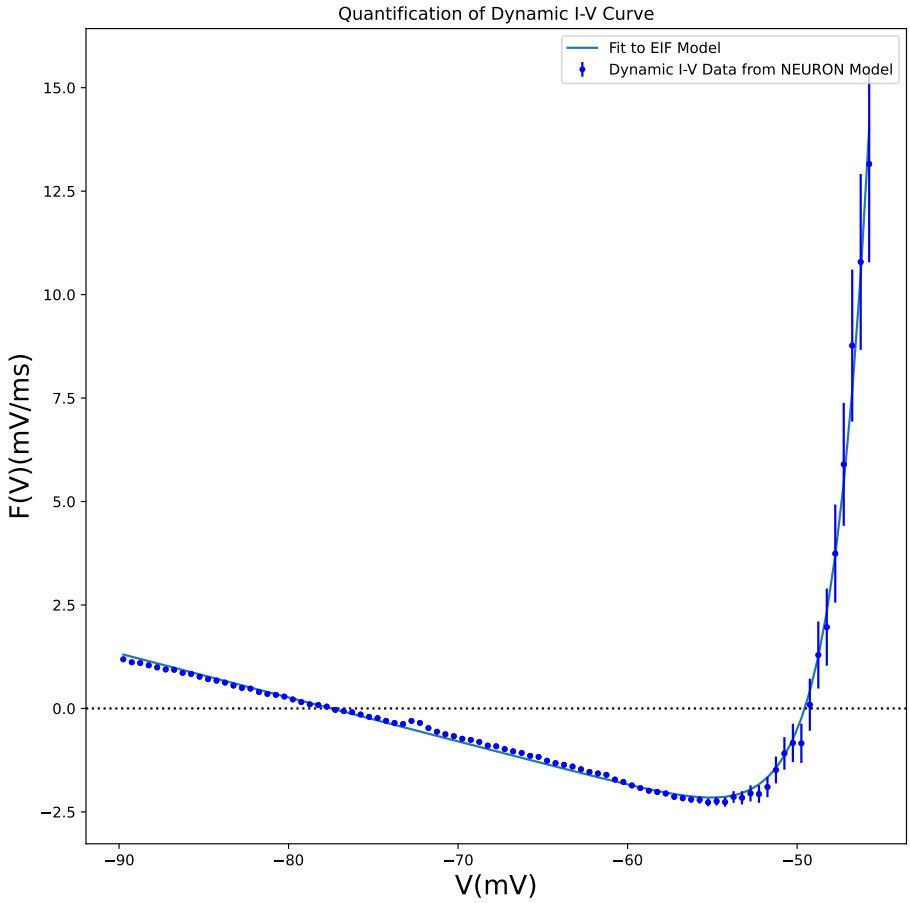

Figure 80: here it is shown the graph for the estimation of the dT parameter of the EIF model of the *in silico* data. The neuronal model is L23_PC_cADpyr229_1, the dT value is in the figure 62 in the extremes range of -90, -45 mV

7.2 dT extraction of all the neuronal models

Here. all the figure of the exponential regression to estimate the dT:

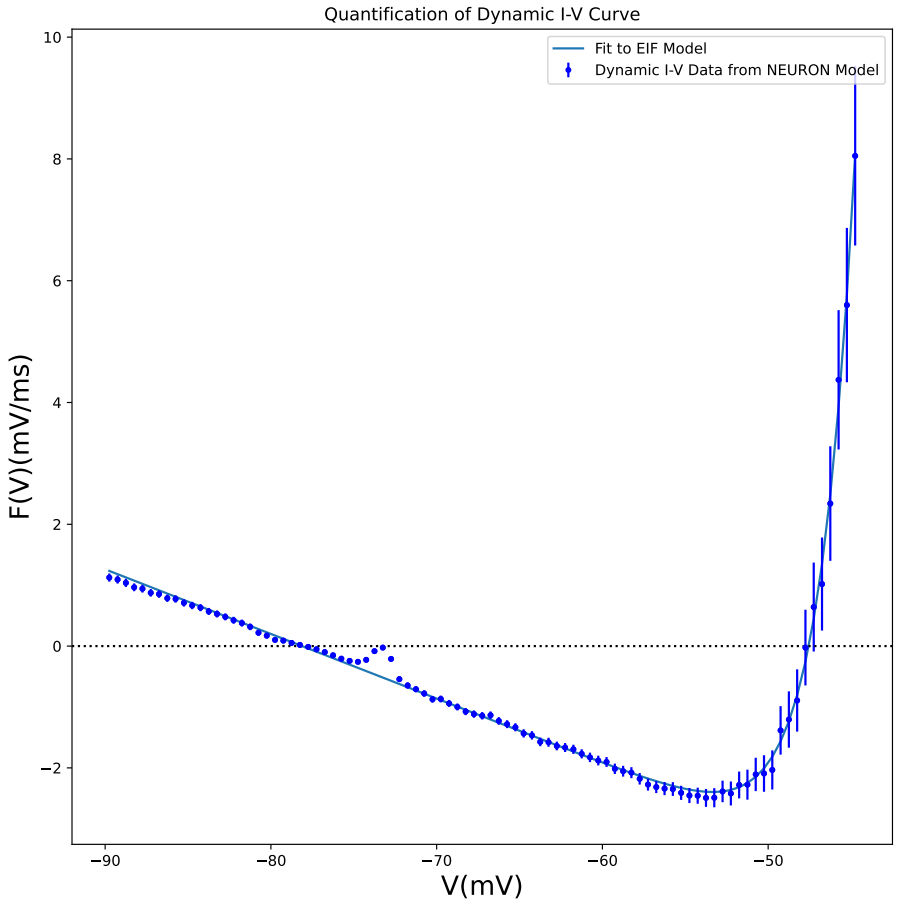

Figure 81: here it is shown the graph for the estimation of the dT parameter of the EIF model of the *in silico* data. The neuronal model is L23_PC_cADpyr229_2, dT value is in the figure 62 in the extremes range of -90, -44 mV

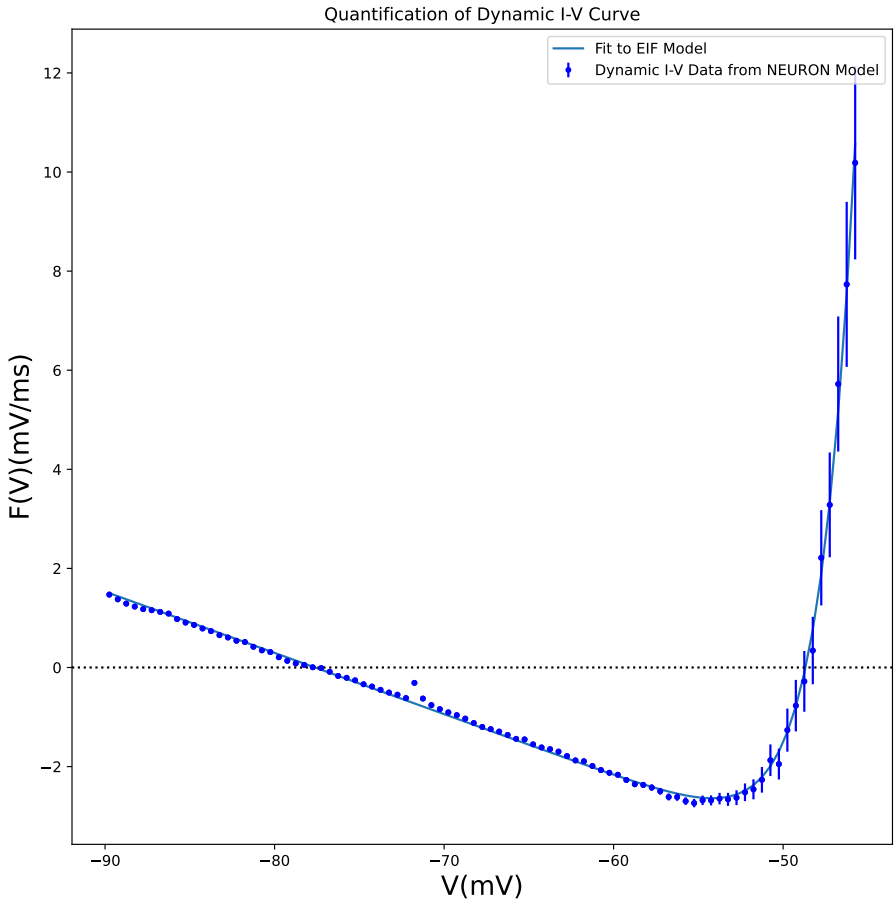

Figure 82: here it is shown the graph for the estimation of the dT parameter of the EIF model of the *in silico* data. The neuronal model is L23_PC_cADpyr229_3, dT value is in the figure 62 in the extremes range of -90, -44 mV

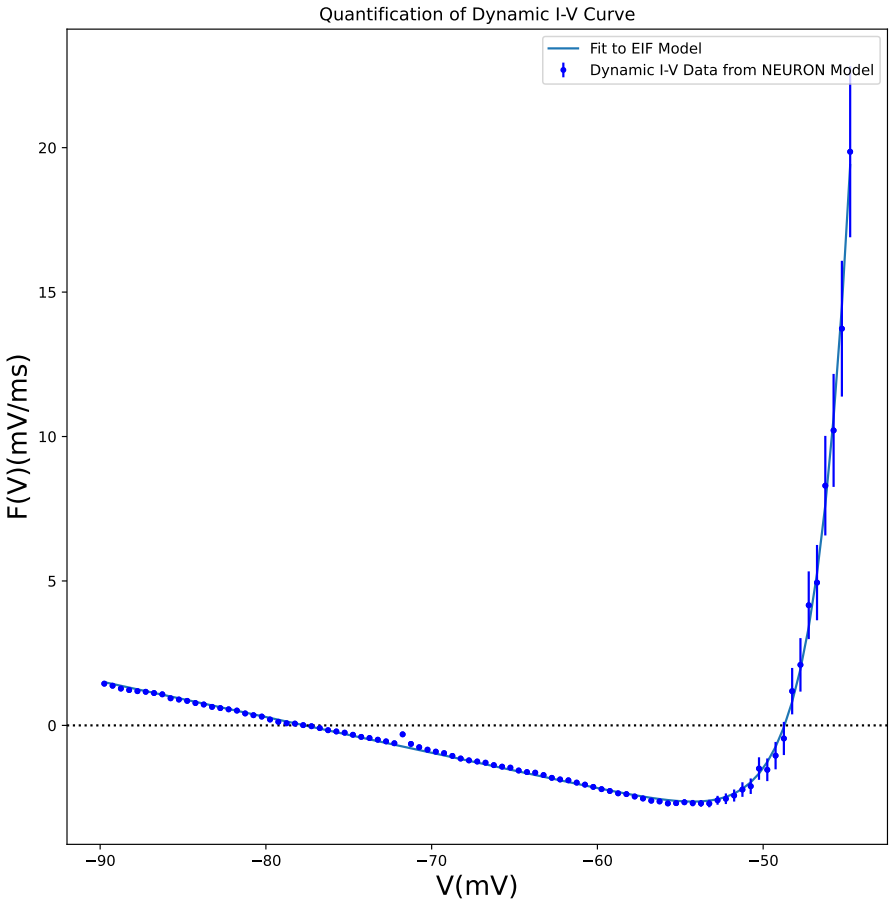

Figure 83: here it is shown the graph for the estimation of the dT parameter of the EIF model of the *in silico* data. The neuronal model is L23_PC_cADpyr229_3, dT value is in the figure 62 in the extremes range of -90, -45 mV

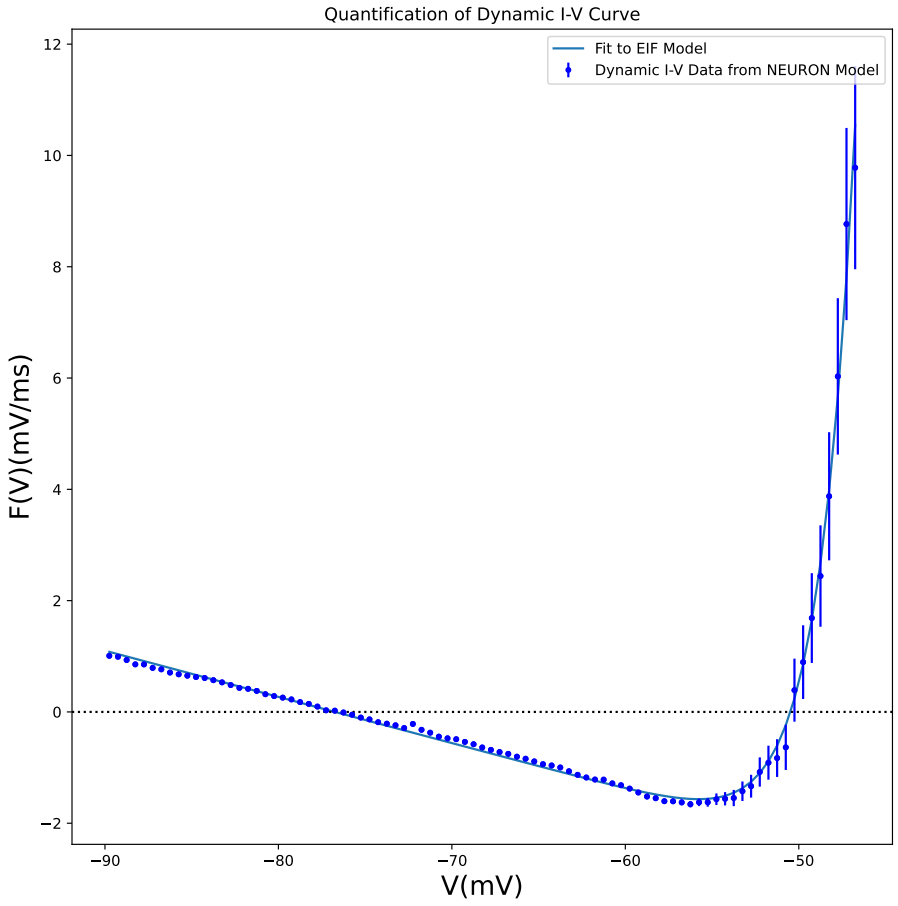

Figure 84: here it is shown the graph for the estimation of the dT parameter of the EIF model of the *in silico* data.The neuronal model is L23_PC_cADpyr229_5, dT value is in the figure 62 in the extremes range of -90, -45 mV

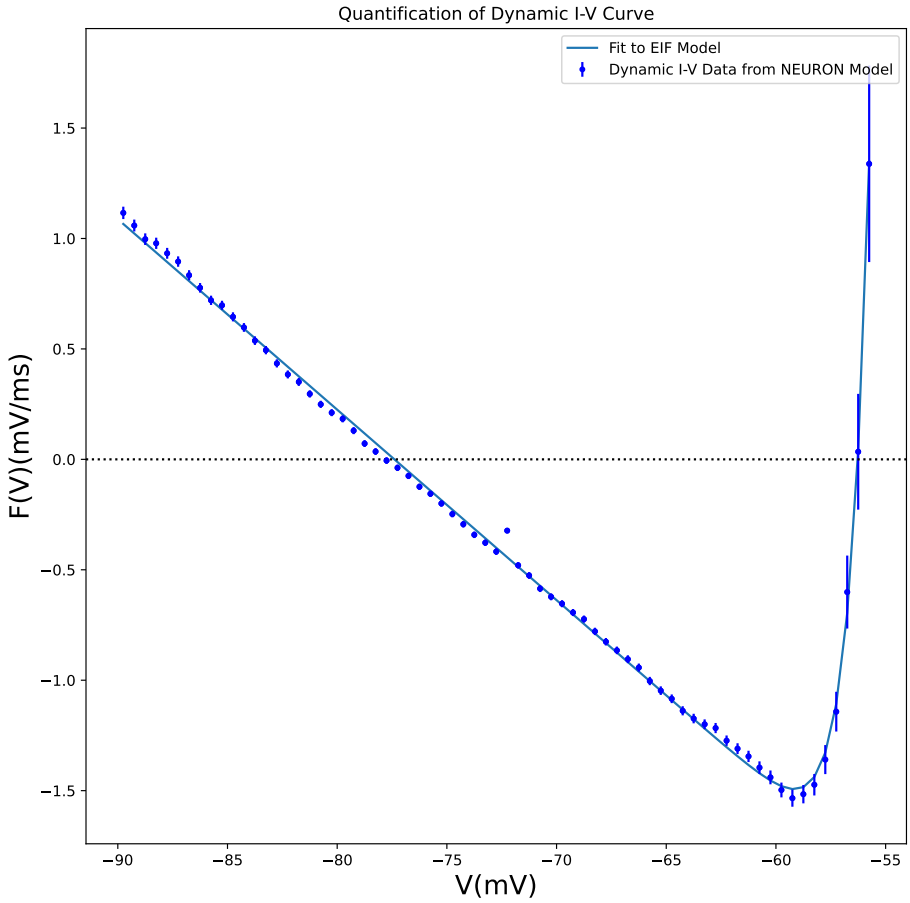

Figure 85: here it is shown the graph for the estimation of the dT parameter of the EIF model of the *in silico* data.The neuronal model is L4_PC_cADpyr230_1, dT value is in the figure 62 in the extremes range of -90, -45 mV

miao bau

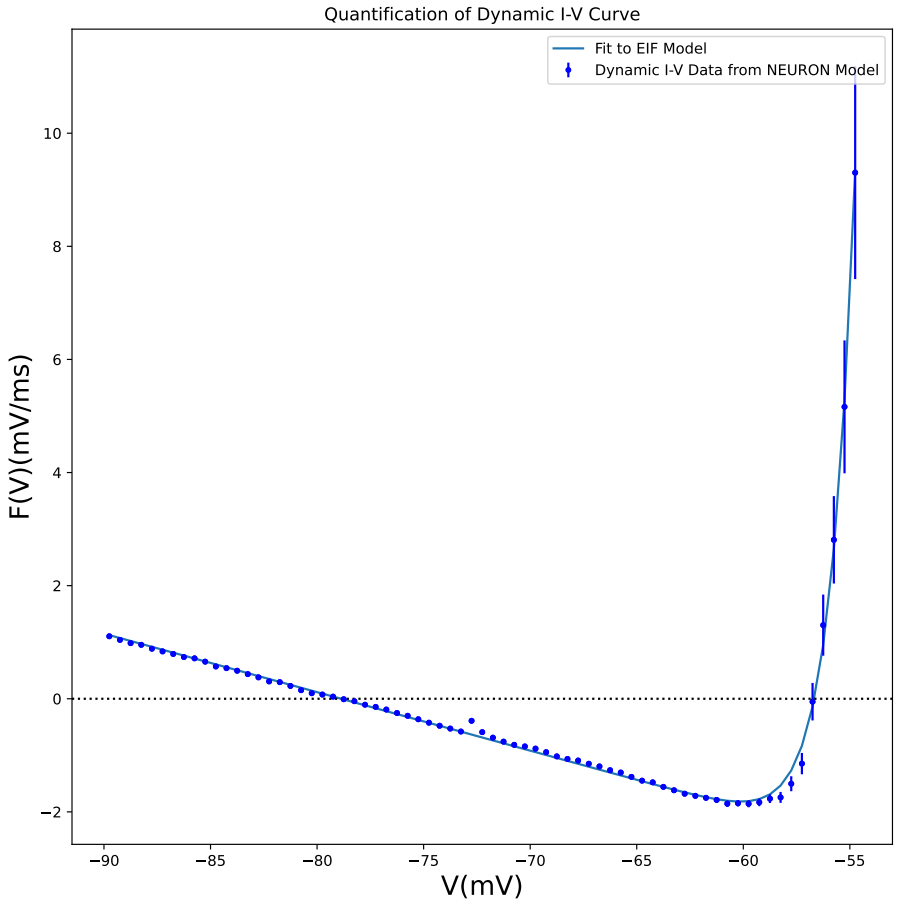

Figure 86: here it is shown the graph for the estimation of the dT parameter of the EIF model of the *in silico* data.The neuronal model is L4_PC_cADpyr230_2, dT value is in the figure 62 in the extremes range of -90, -45 mV

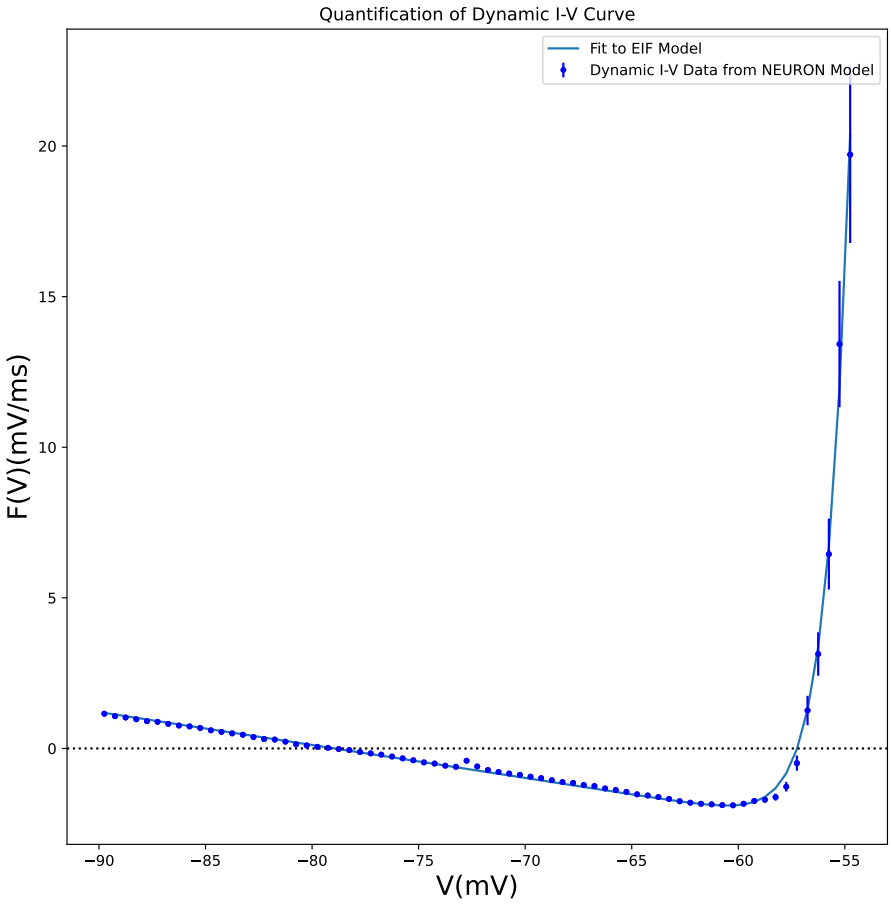

Figure 87: here it is shown the graph for the estimation of the dT parameter of the EIF model of the *in silico* data.The neuronal model is L4_PC_cADpyr230_3, dT value is in the figure 62 in the extremes range of -90, -45 mV

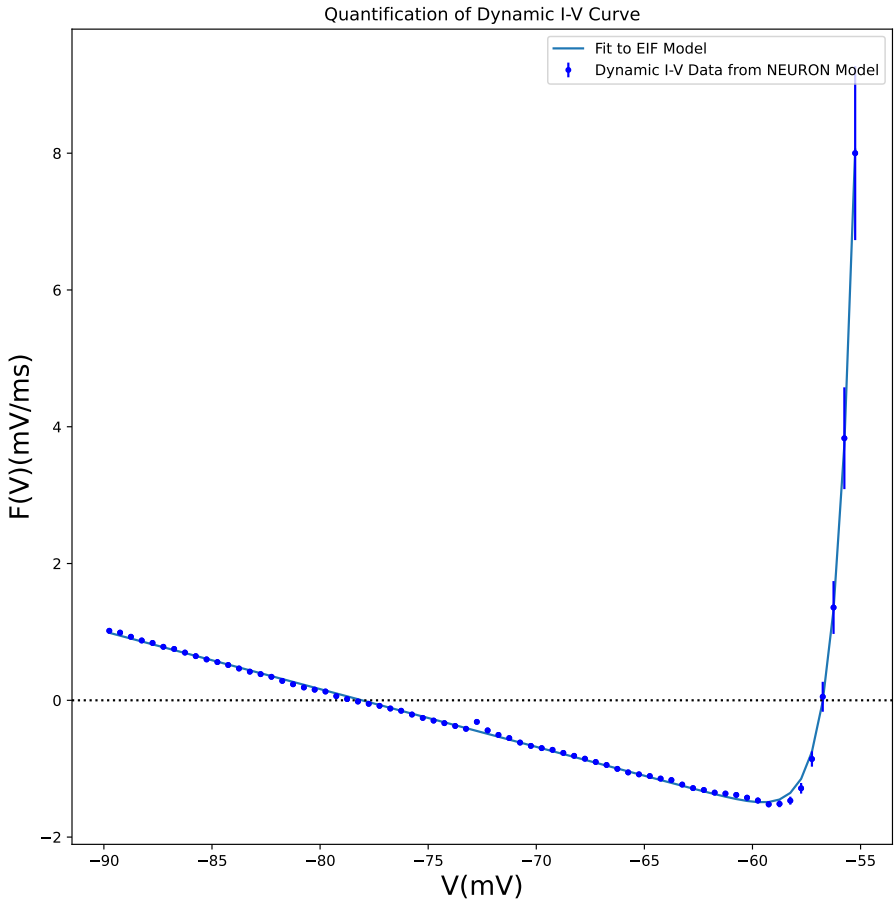

Figure 88: here it is shown the graph for the estimation of the dT parameter of the EIF model of the *in silico* data.The neuronal model is L4_PC_cADpyr230_4, dT value is in the figure 62 in the extremes range of -90, -45 mV

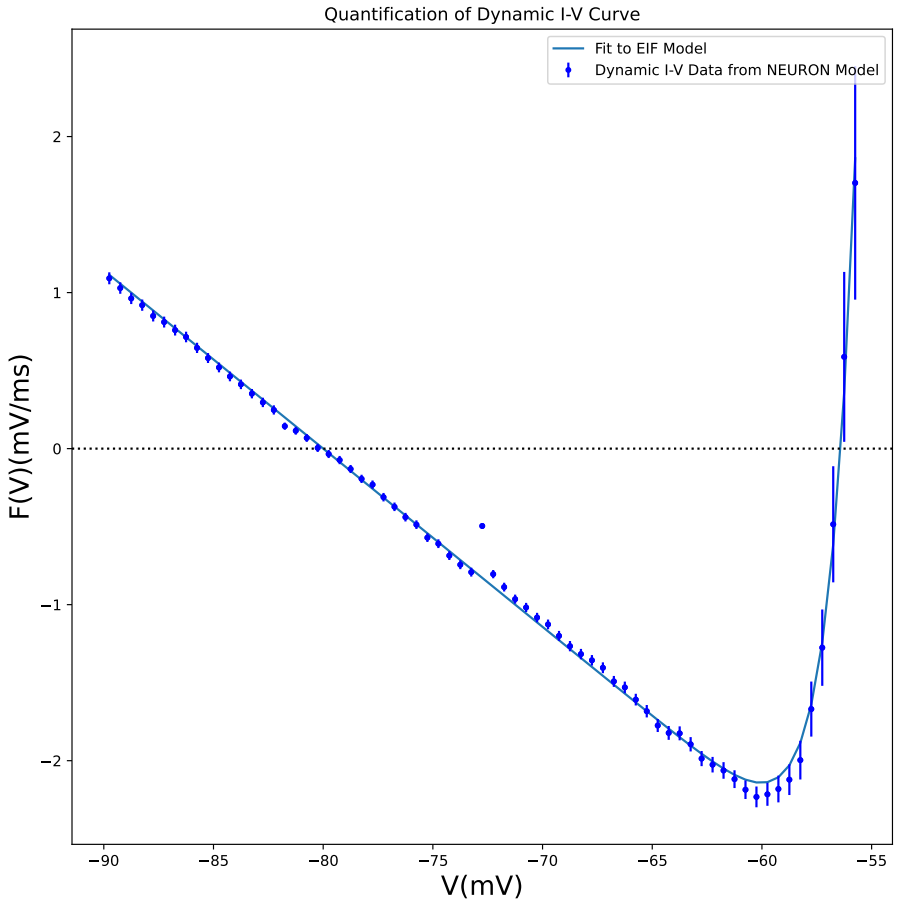

Figure 89: here it is shown the graph for the estimation of the dT parameter of the EIF model of the *in silico* data.The neuronal model is L4_PC_cADpyr230_5, dT value is in the figure 62 in the extremes range of -90, -45 mV

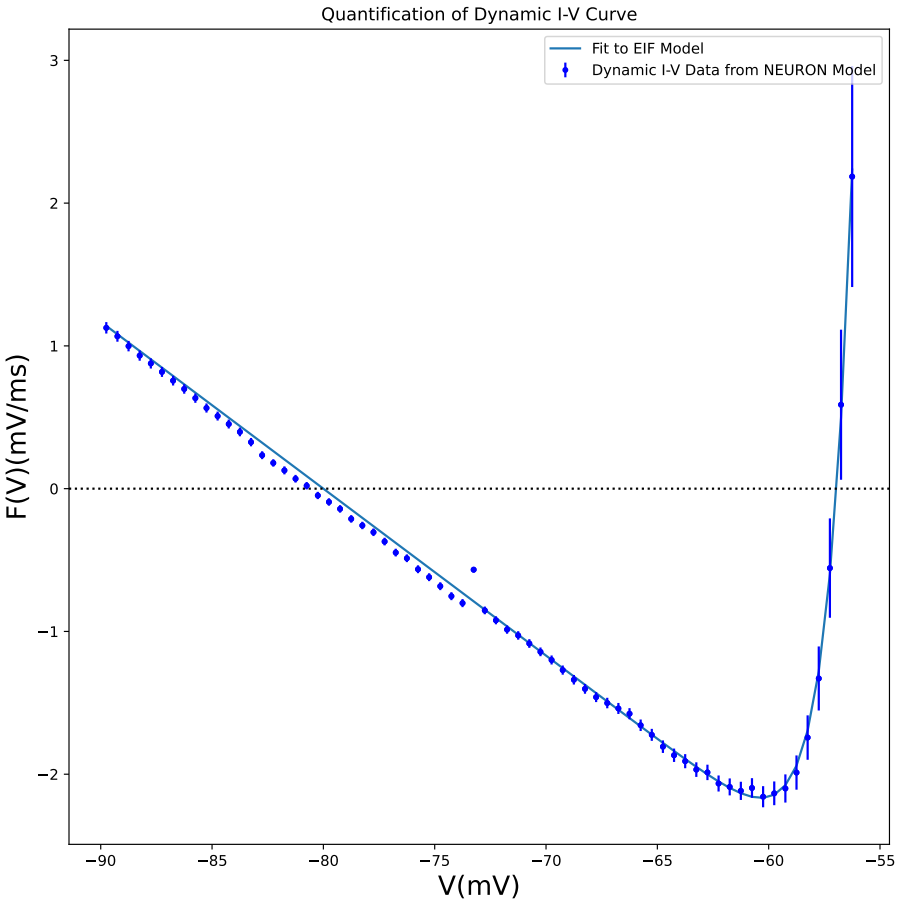

Figure 90: here it is shown the graph for the estimation of the dT parameter of the EIF model of the *in silico* data.The neuronal model is L4_SP_cADpyr230_1, dT value is in the figure 62 in the extremes range of -90, -55.5 mV

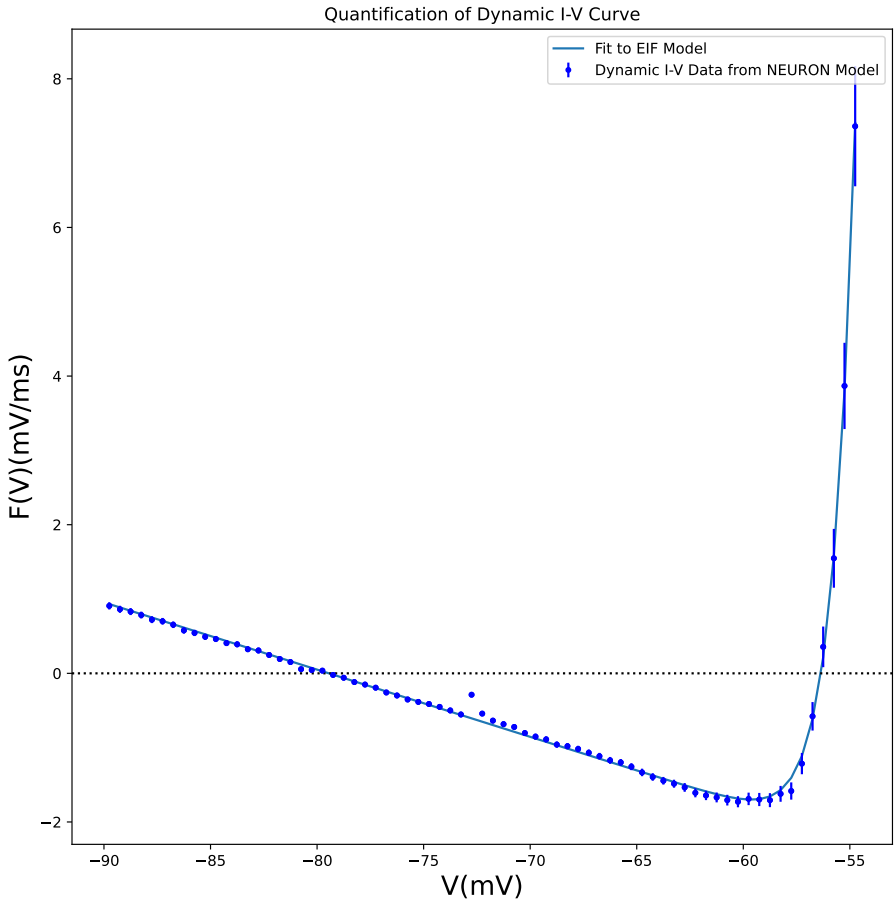

Figure 91: here it is shown the graph for the estimation of the dT parameter of the EIF model of the *in silico* data.The neuronal model is L4_SP_cADpyr230_2, dT value is in the figure 62 in the extremes range of -90, -54 mV

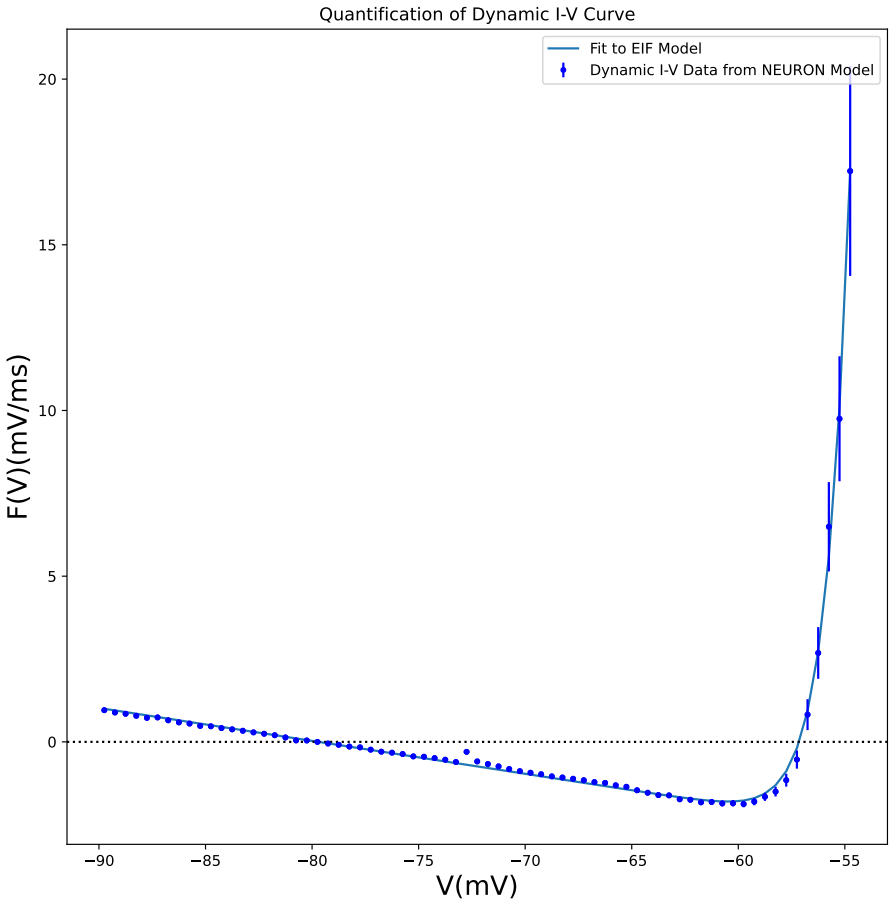

Figure 92: here it is shown the graph for the estimation of the dT parameter of the EIF model of the *in silico* data.The neuronal model is L4_SP_cADpyr230_3, dT value is in the figure 62 in the extremes range of -90, -54 mV

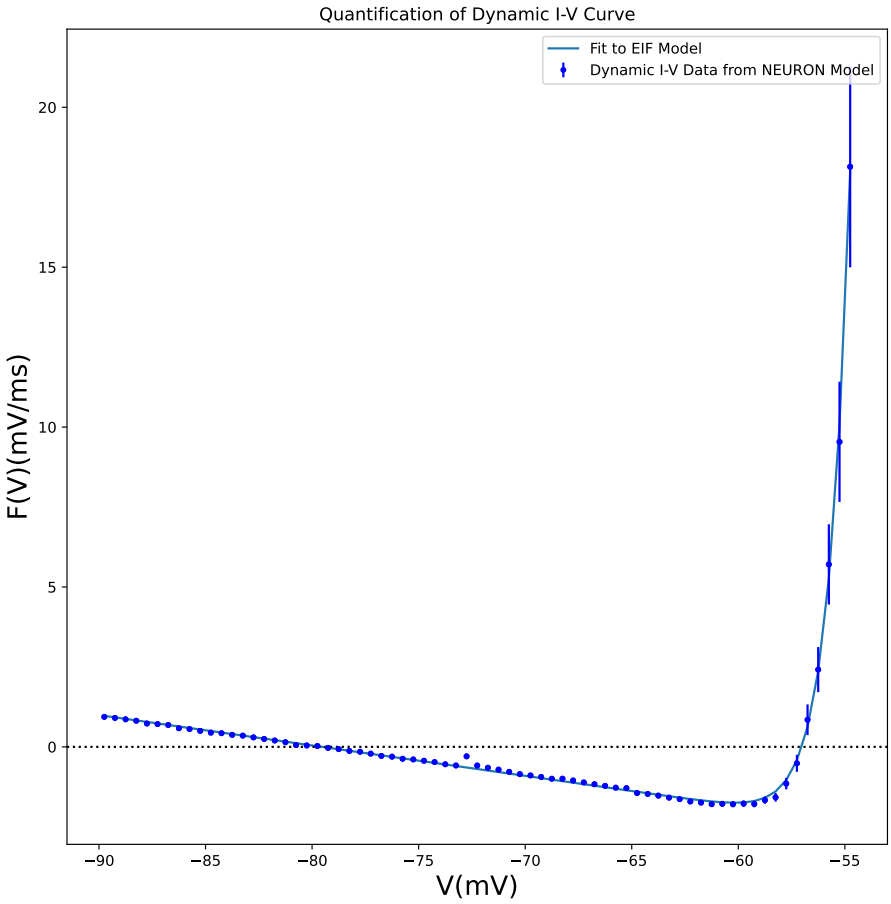

Figure 93: here it is shown the graph for the estimation of the dT parameter of the EIF model of the *in silico* data.The neuronal model is L4_SP_cADpyr230_4, dT value is in the figure 62 in the extremes range of -90, -54 mV

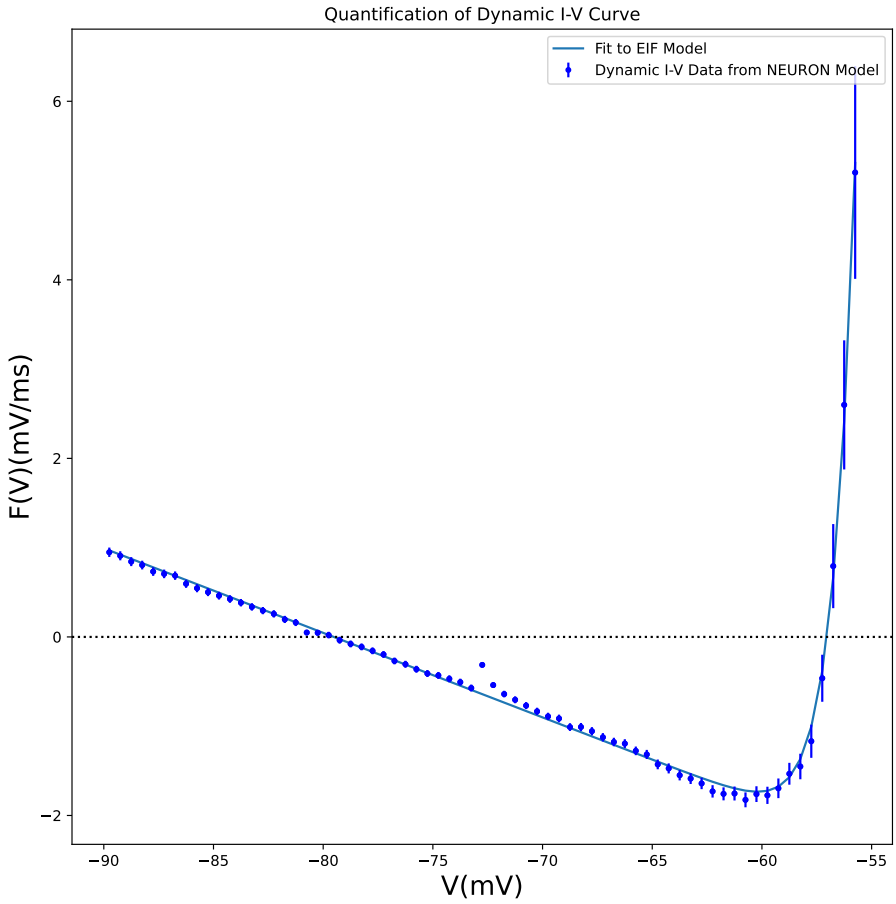

Figure 94: here it is shown the graph for the estimation of the dT parameter of the EIF model of the *in silico* data.The neuronal model is L4_SP_cADpyr230_5, dT value is in the figure 62 in the extremes range of -90, -55 mV

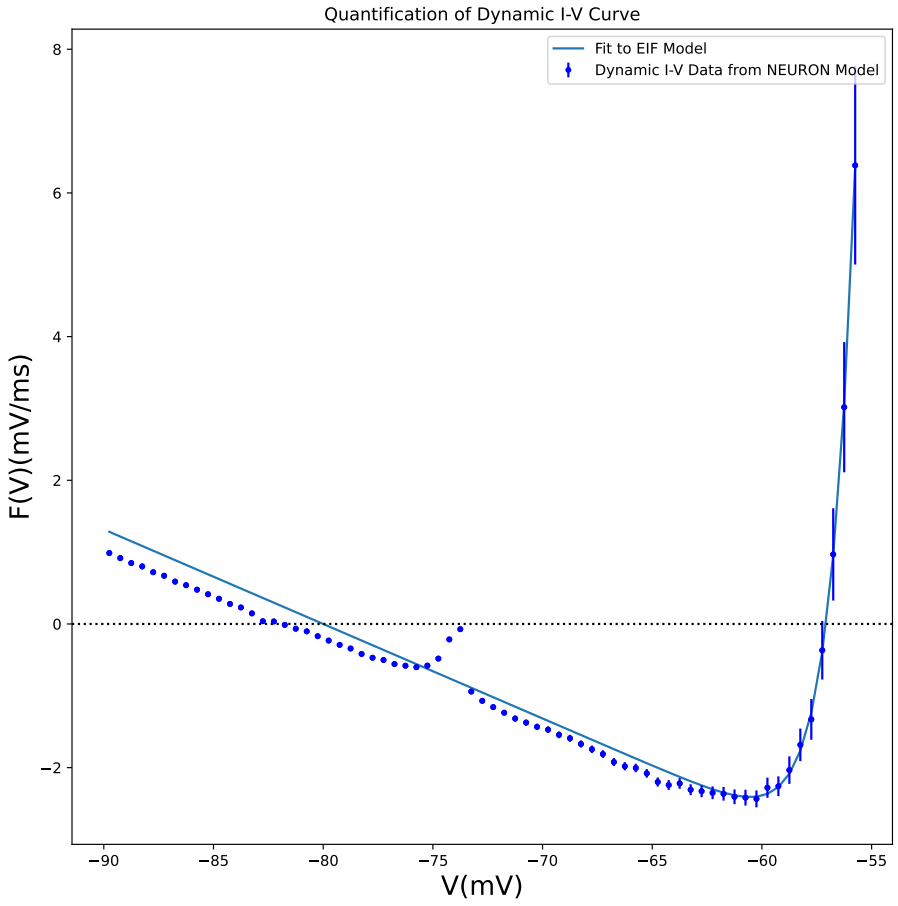

Figure 95: here it is shown the graph for the estimation of the dT parameter of the EIF model of the *in silico* data.The neuronal model is L4_SP_cADpyr230_1, dT value is in the figure 62 in the extremes range of -90, -54 mV

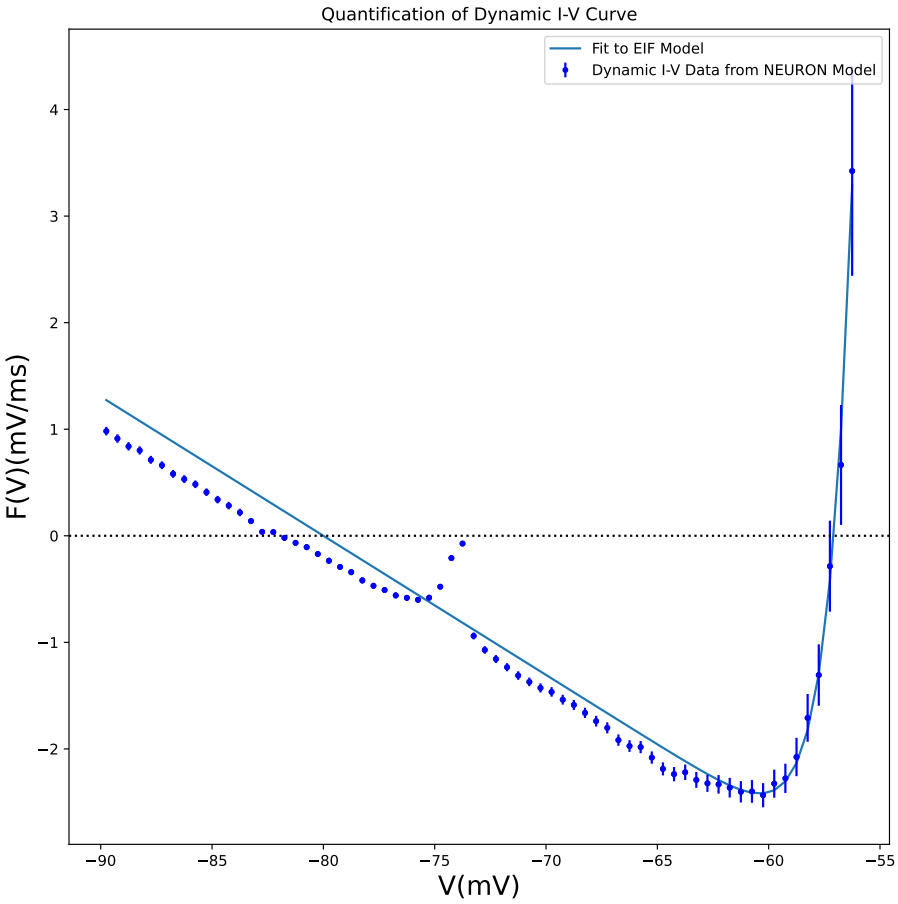

Figure 96: here it is shown the graph for the estimation of the dT parameter of the EIF model of the *in silico* data.The neuronal model is L4_SP_cADpyr230_2, dT value is in the figure 62 in the extremes range of -90, -55.5 mV

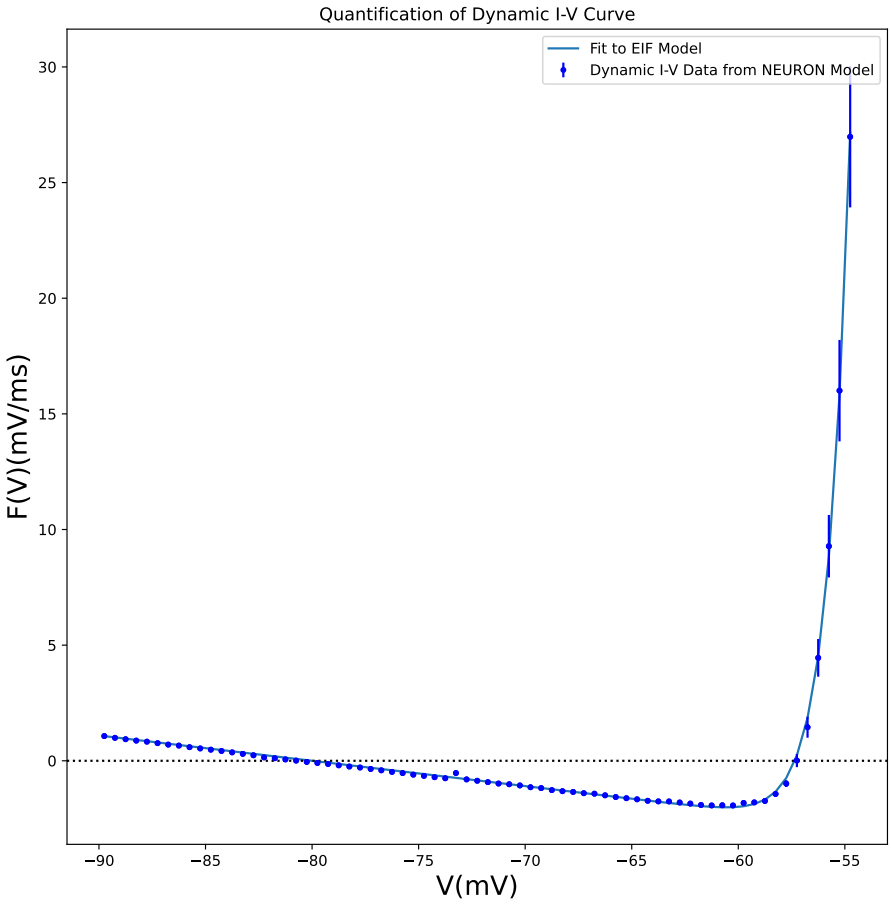

Figure 97: here it is shown the graph for the estimation of the dT parameter of the EIF model of the *in silico* data.The neuronal model is L4_SS_cADpyr230_3, dT value is in the figure 62 in the extremes range of -90, -54 mV

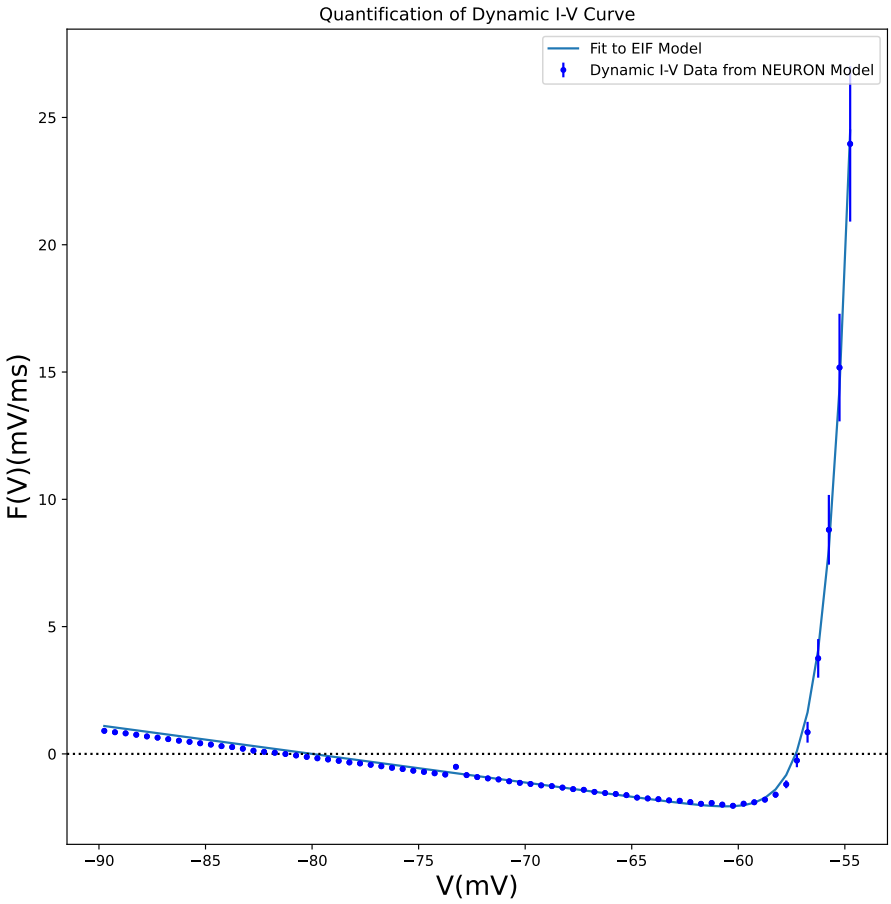

Figure 98: here it is shown the graph for the estimation of the dT parameter of the EIF model of the *in silico* data.The neuronal model is L4_SS_cADpyr230_4, dT value is in the figure 62 in the extremes range of -90, -54 mV

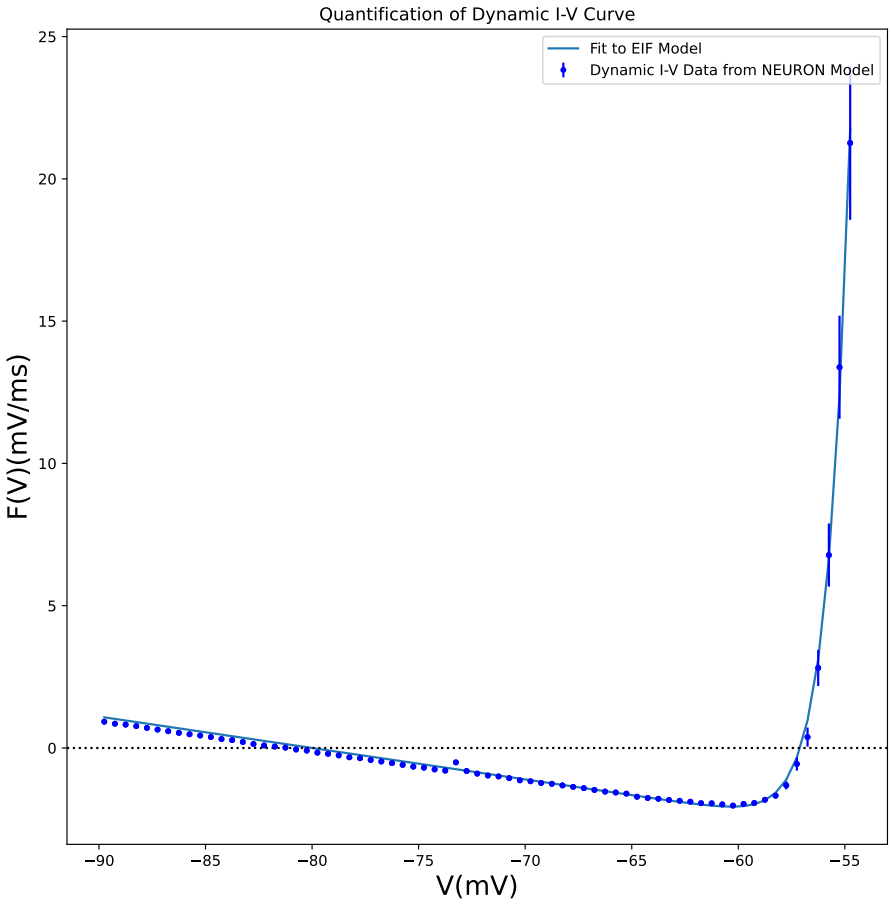

Figure 99: here it is shown the graph for the estimation of the dT parameter of the EIF model of the *in silico* data.The neuronal model is L4_SS_cADpyr230_5, dT value is in the figure 62 in the extremes range of -90, -54 mV

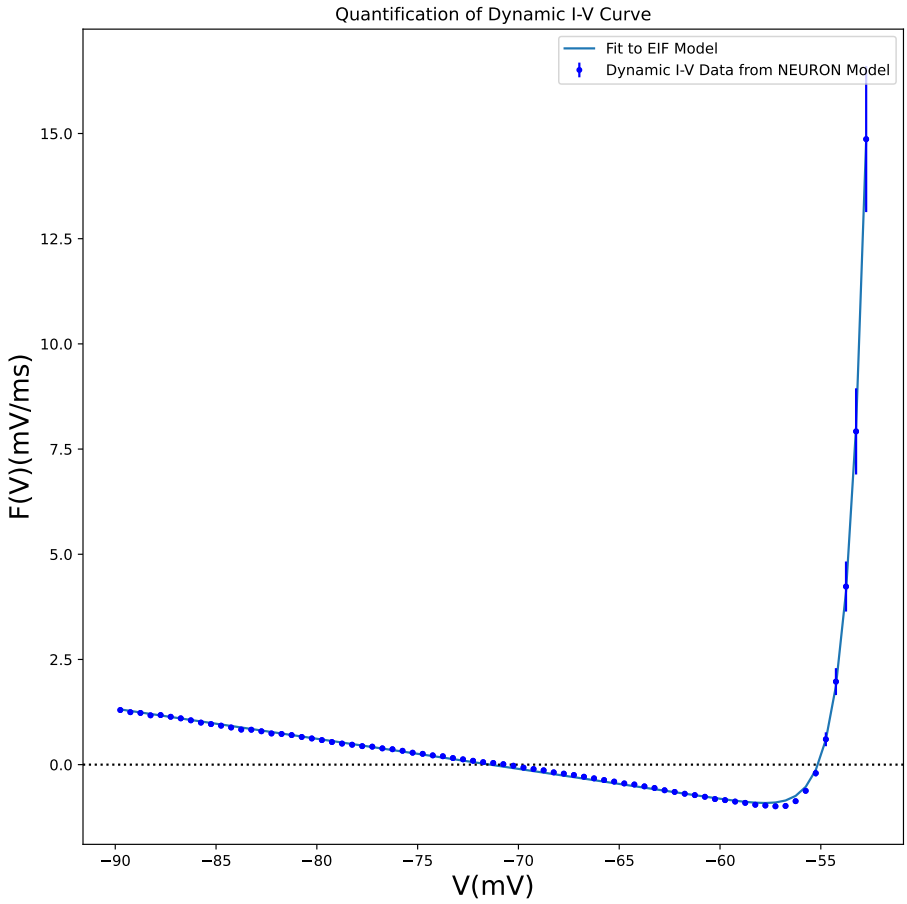

Figure 100: here it is shown the graph for the estimation of the dT parameter of the EIF model of the *in silico* data.The neuronal model is L5_STPC_cADpyr232_1, dT value is in the figure 62 in the extremes range of -90, -52 mV

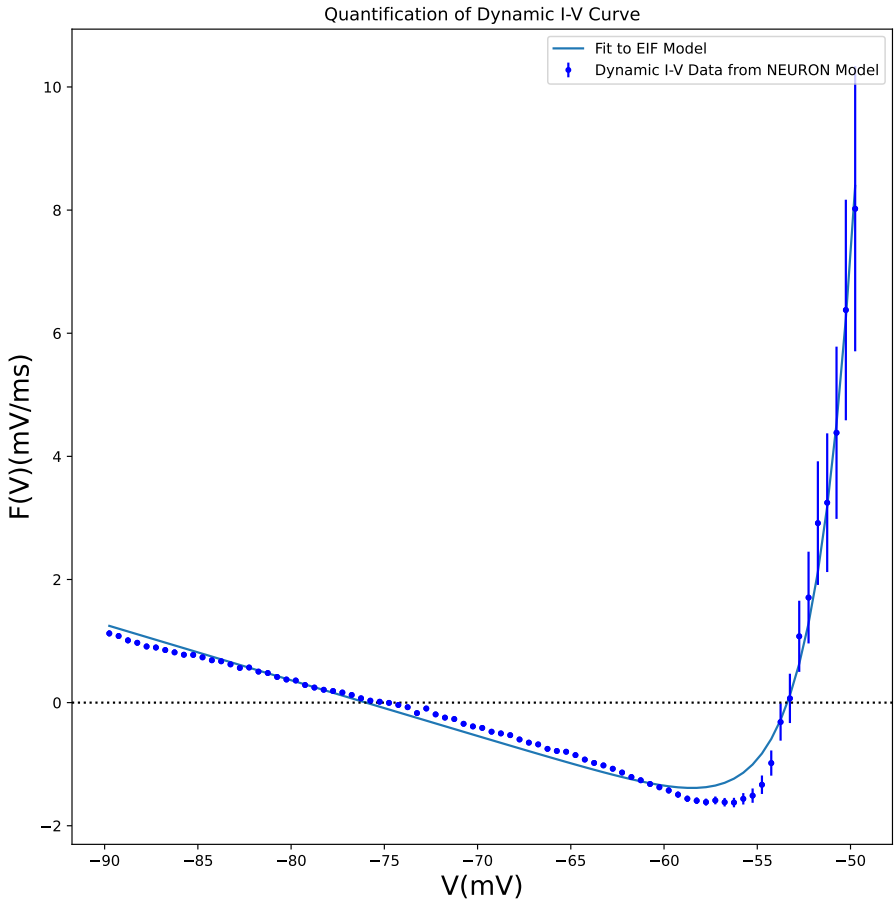

Figure 101: here it is shown the graph for the estimation of the dT parameter of the EIF model of the *in silico* data.The neuronal model is L5_STPC_cADpyr232_2, dT value is in the figure 62 in the extremes range of -90, -49 mV

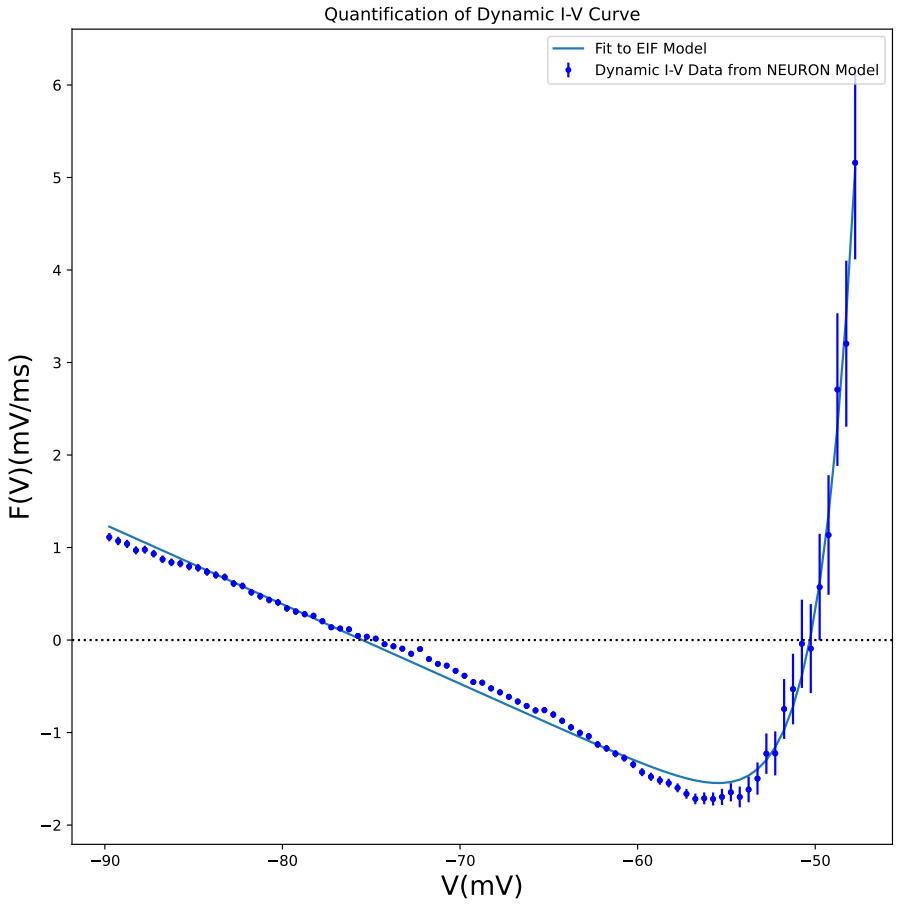

Figure 102: here it is shown the graph for the estimation of the dT parameter of the EIF model of the *in silico* data.The neuronal model is L5_STPC_cADpyr232_3, dT value is in the figure 62 in the extremes range of -90, -47 mV

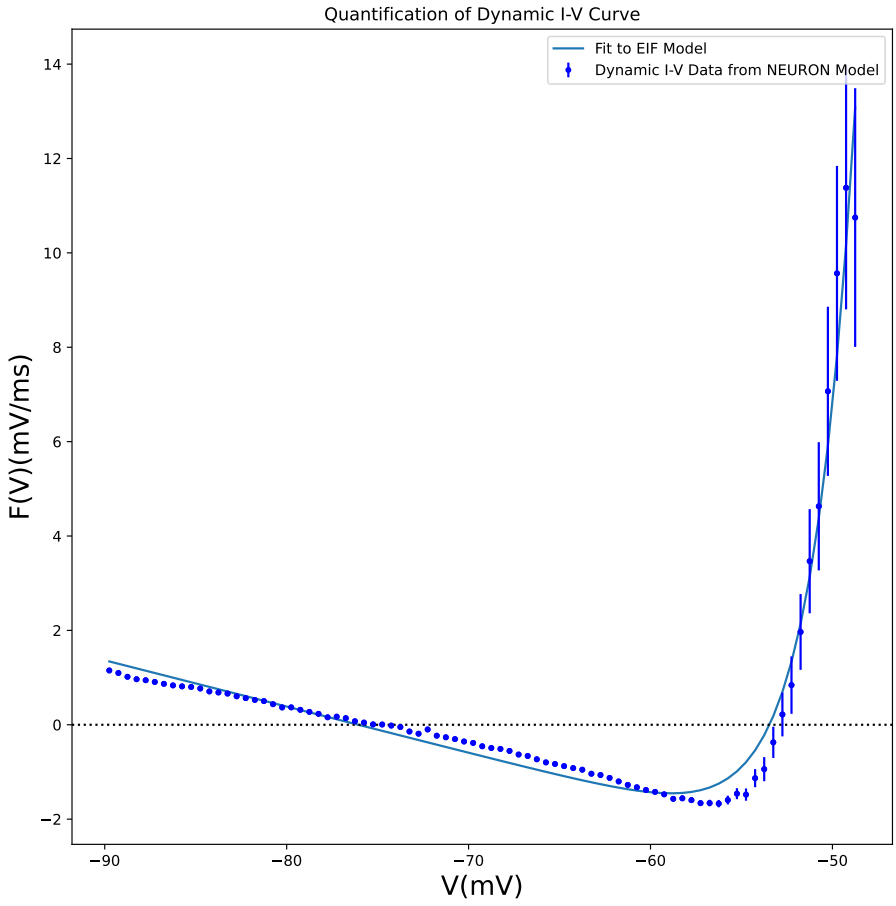

Figure 103: here it is shown the graph for the estimation of the dT parameter of the EIF model of the *in silico* data.The neuronal model is L5_STPC_cADpyr232_4, dT value is in the figure 62 in the extremes range of -90, -47 mV

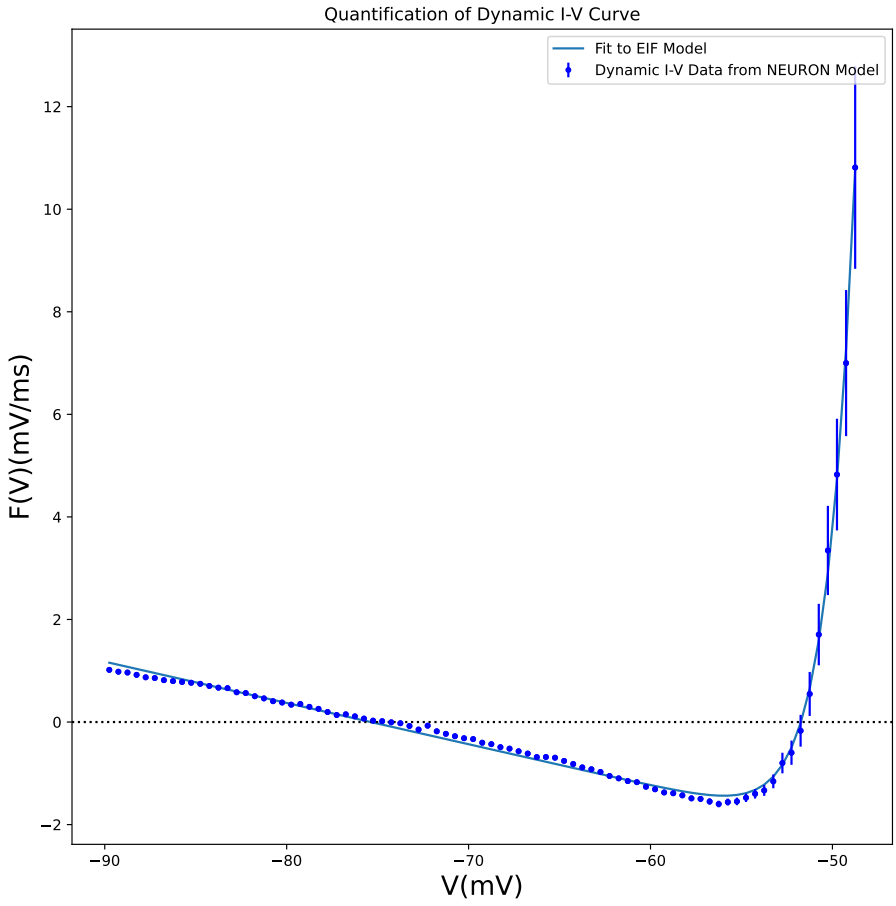

Figure 104: here it is shown the graph for the estimation of the dT parameter of the EIF model of the *in silico* data.The neuronal model is L5_STPC_cADpyr232_5, dT value is in the figure 62 in the extremes range of -90, -48 mV

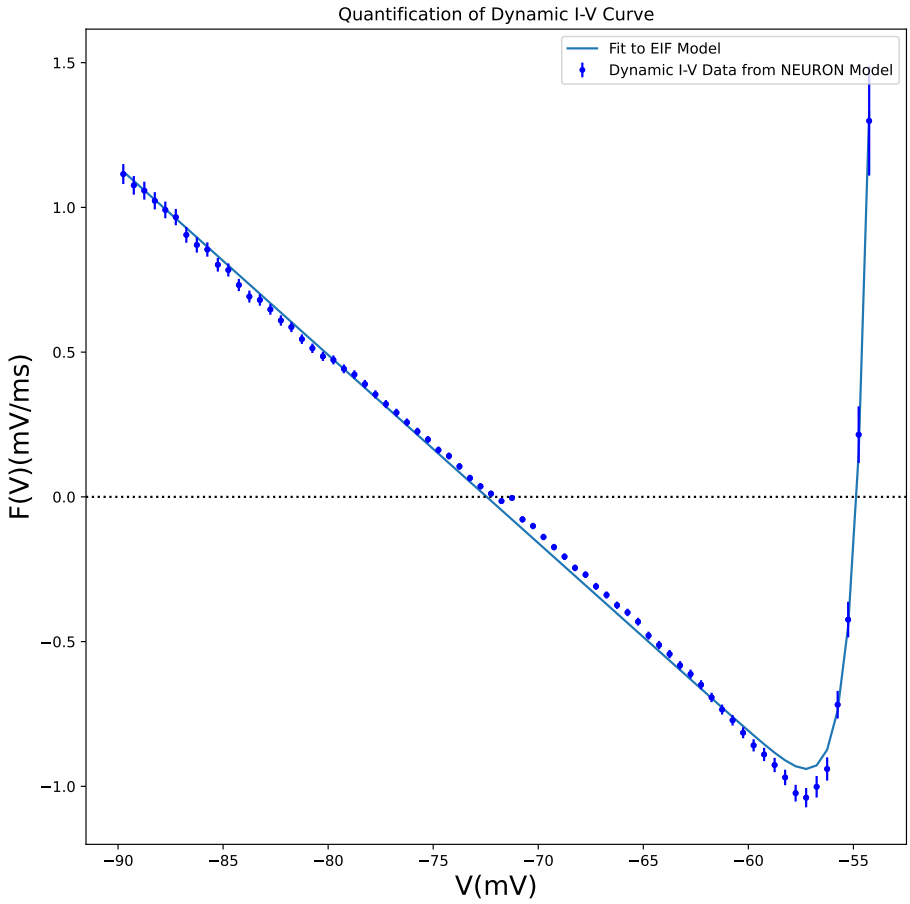

Figure 105: here it is shown the graph for the estimation of the dT parameter of the EIF model of the *in silico* data.The neuronal model is L5_TTPC1_cADpyr232_2, dT value is in the figure 62 in the extremes range of -90, -53.5 mV

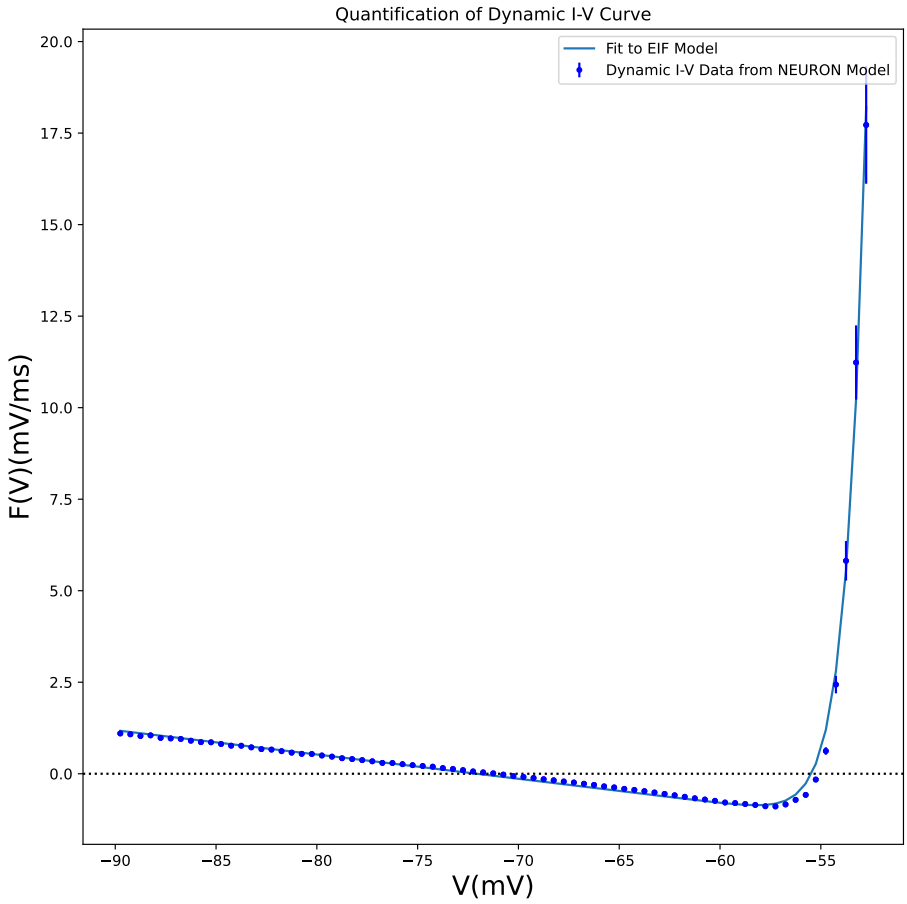

Figure 106: here it is shown the graph for the estimation of the dT parameter of the EIF model of the *in silico* data.The neuronal model is L5_TTPC1_cADpyr232_3, dT value is in the figure 62 in the extremes range of -90, -52 mV

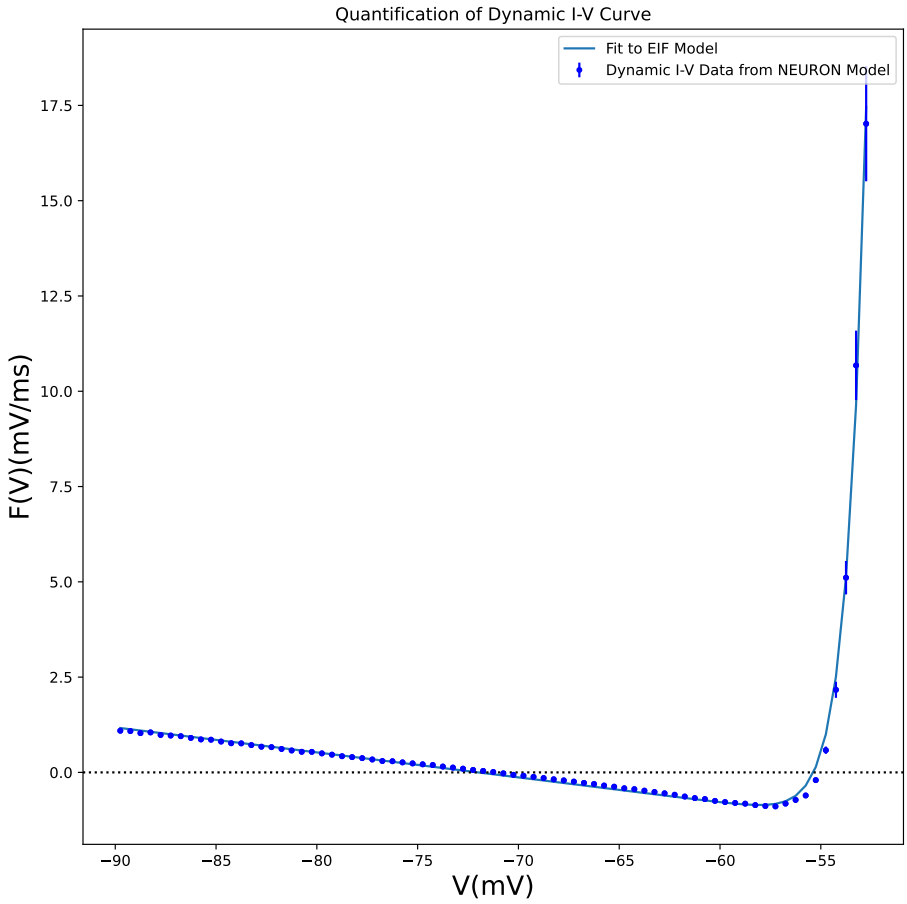

Figure 107: here it is shown the graph for the estimation of the dT parameter of the EIF model of the *in silico* data.The neuronal model is L5_TTPC1_cADpyr232_4, dT value is in the figure 62 in the extremes range of -90, -52 mV

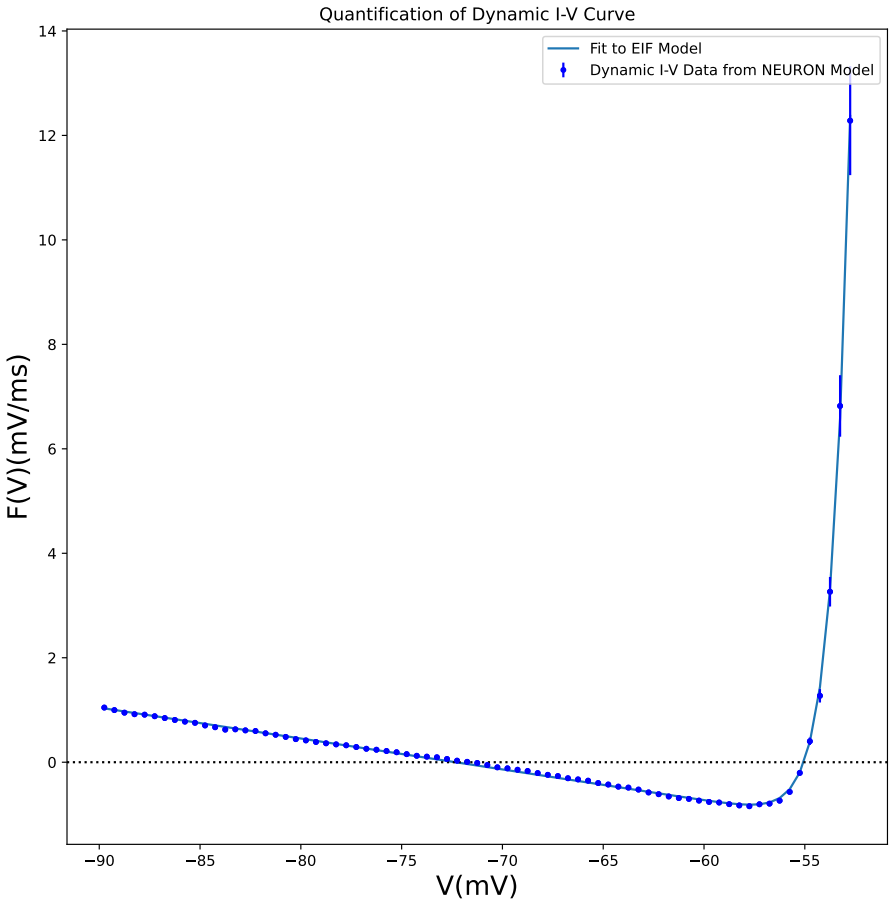

Figure 108: here it is shown the graph for the estimation of the dT parameter of the EIF model of the *in silico* data.The neuronal model is L5_TTPC1_cADpyr232_5, dT value is in the figure 62 in the extremes range of -90, -52 mV

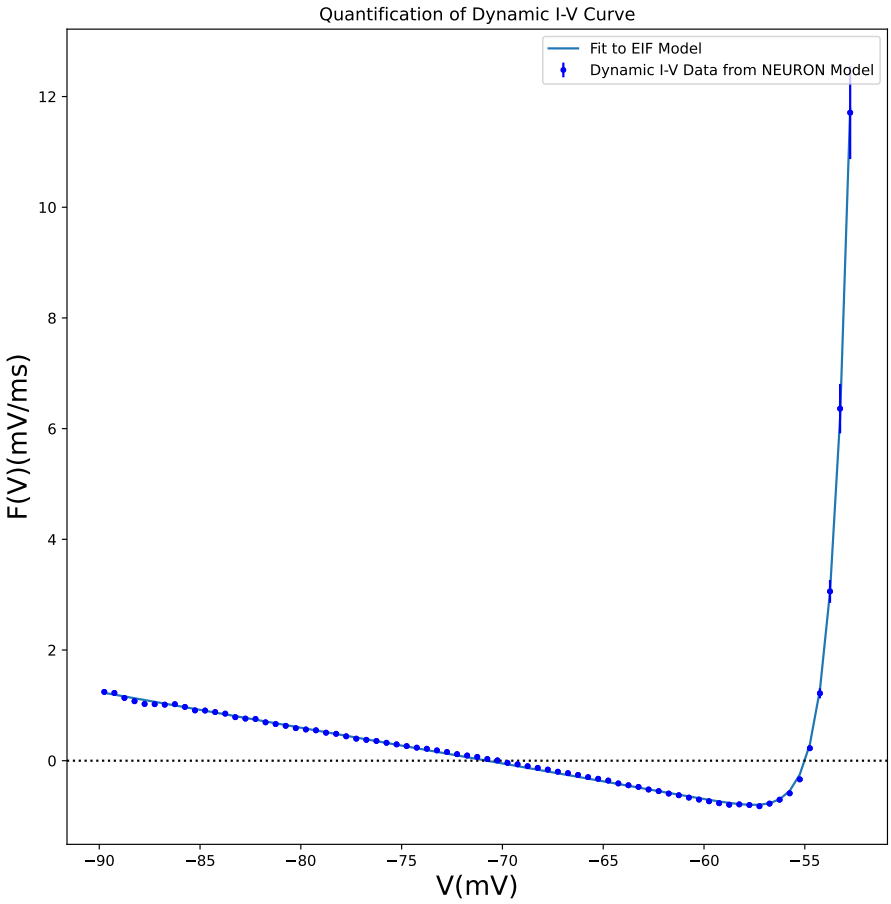

Figure 109: here it is shown the graph for the estimation of the dT parameter of the EIF model of the *in silico* data.The neuronal model is L5_TTPC2_cADpyr232_1, dT value is in the figure 62 in the extremes range of -90, -52 mV

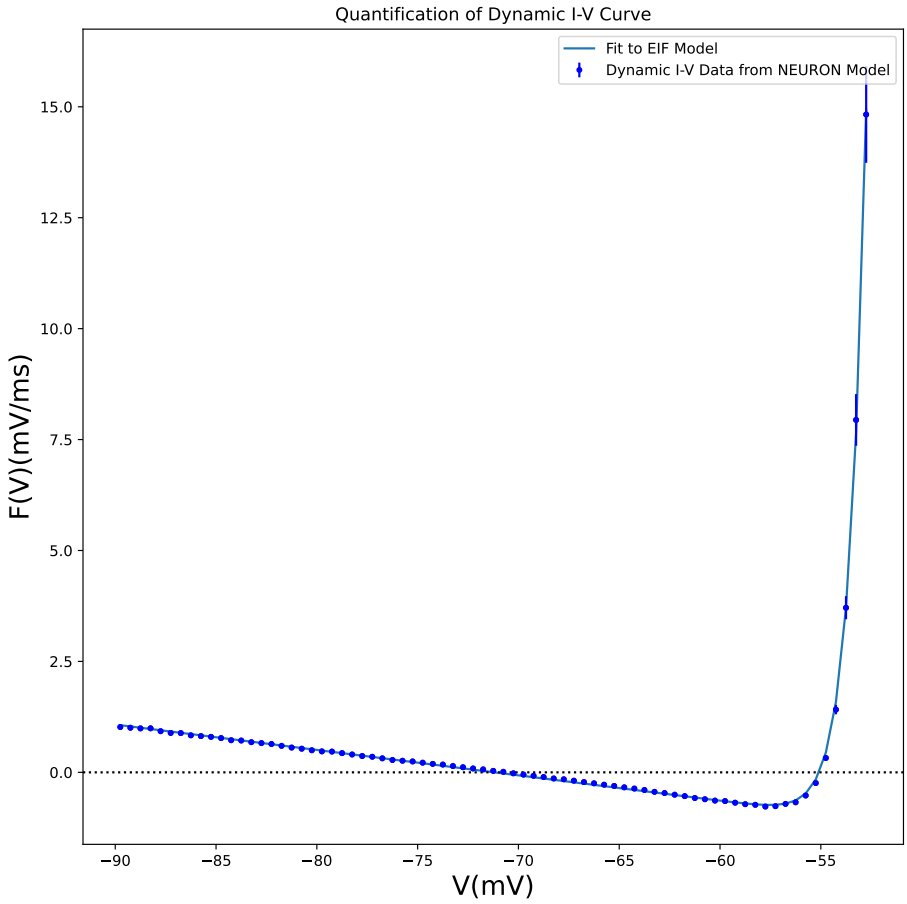

Figure 110: here it is shown the graph for the estimation of the dT parameter of the EIF model of the *in silico* data.The neuronal model is L5_TTPC2_cADpyr232_2, dT value is in the figure 62 in the extremes range of -90, -52 mV

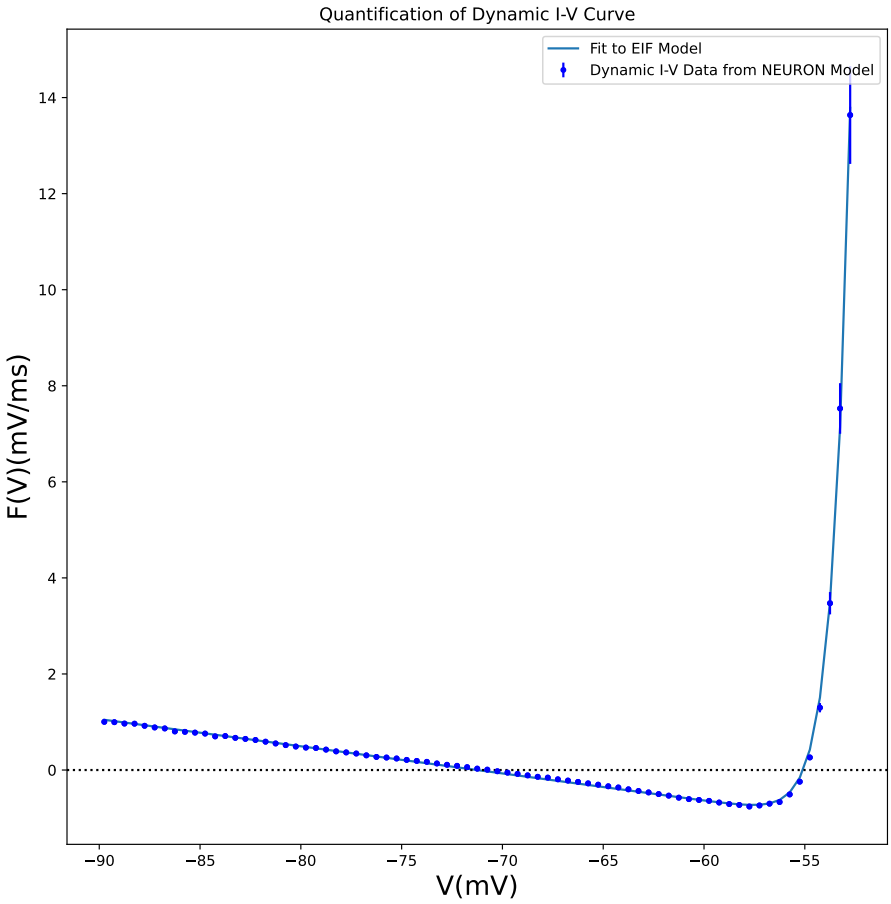

Figure 111: here it is shown the graph for the estimation of the dT parameter of the EIF model of the *in silico* data.The neuronal model is L5_TTPC2_cADpyr232_3, dT value is in the figure 62 in the extremes range of -90, -52 mV

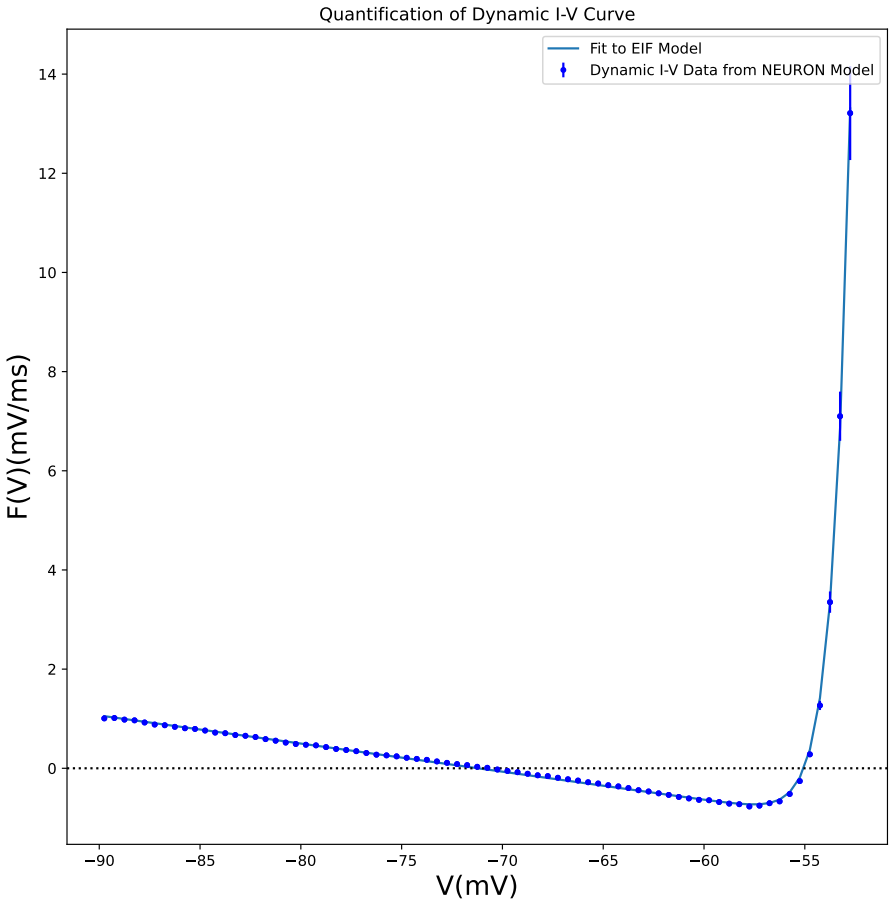

Figure 112: here it is shown the graph for the estimation of the dT parameter of the EIF model of the *in silico* data.The neuronal model is L5_TTPC2_cADpyr232_4, dT value is in the figure 62 in the extremes range of -90, -52 mV

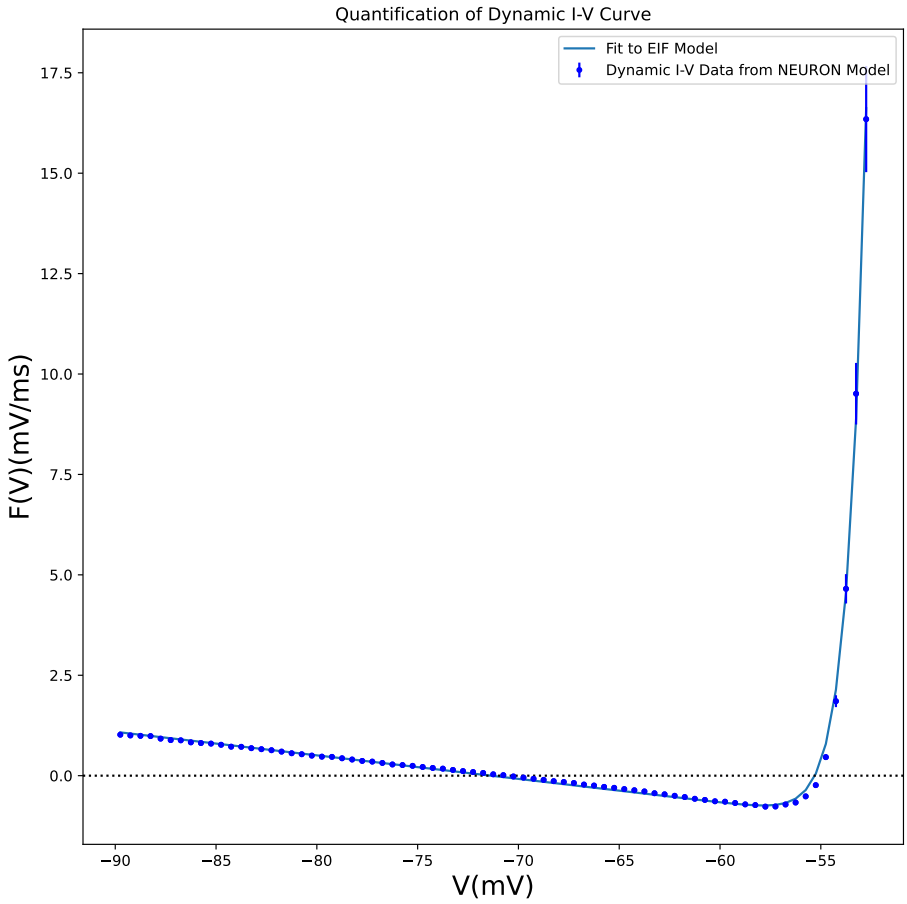

Figure 113: here it is shown the graph for the estimation of the dT parameter of the EIF model of the *in silico* data.The neuronal model is L5_TTPC2_cADpyr232_5, dT value is in the figure 62 in the extremes range of -90, -52 mV

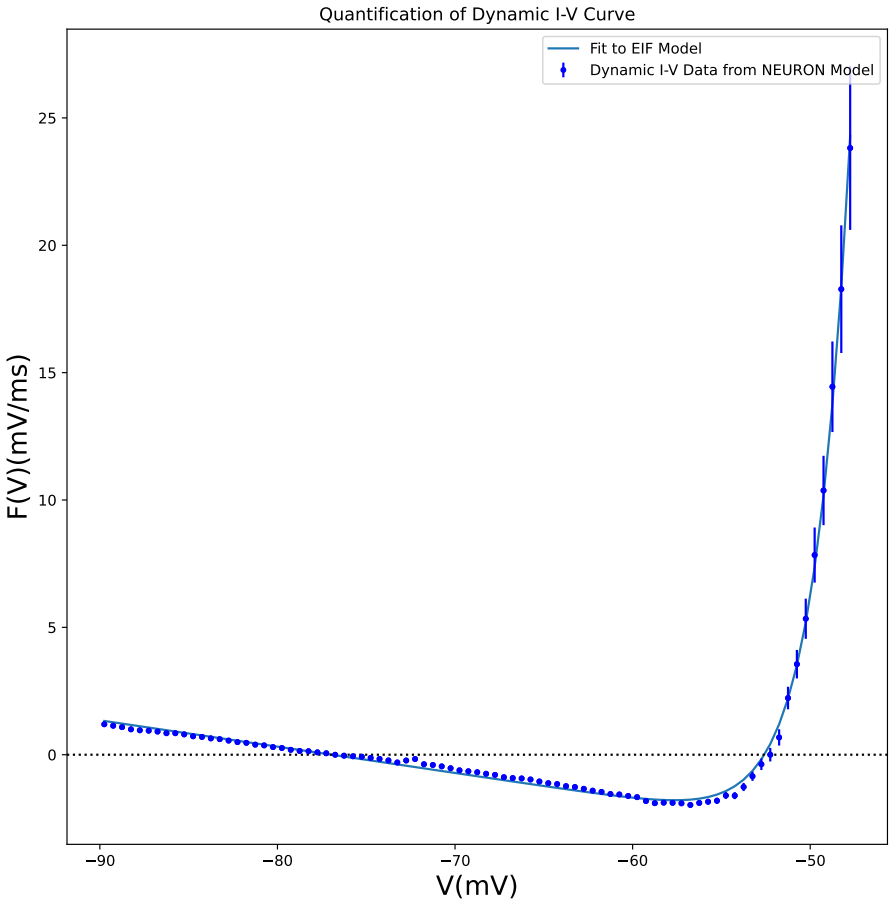

Figure 114: here it is shown the graph for the estimation of the dT parameter of the EIF model of the *in silico* data.The neuronal model is L5_UTPC_cADpyr232_1, dT value is in the figure 62 in the extremes range of -90, -47 mV

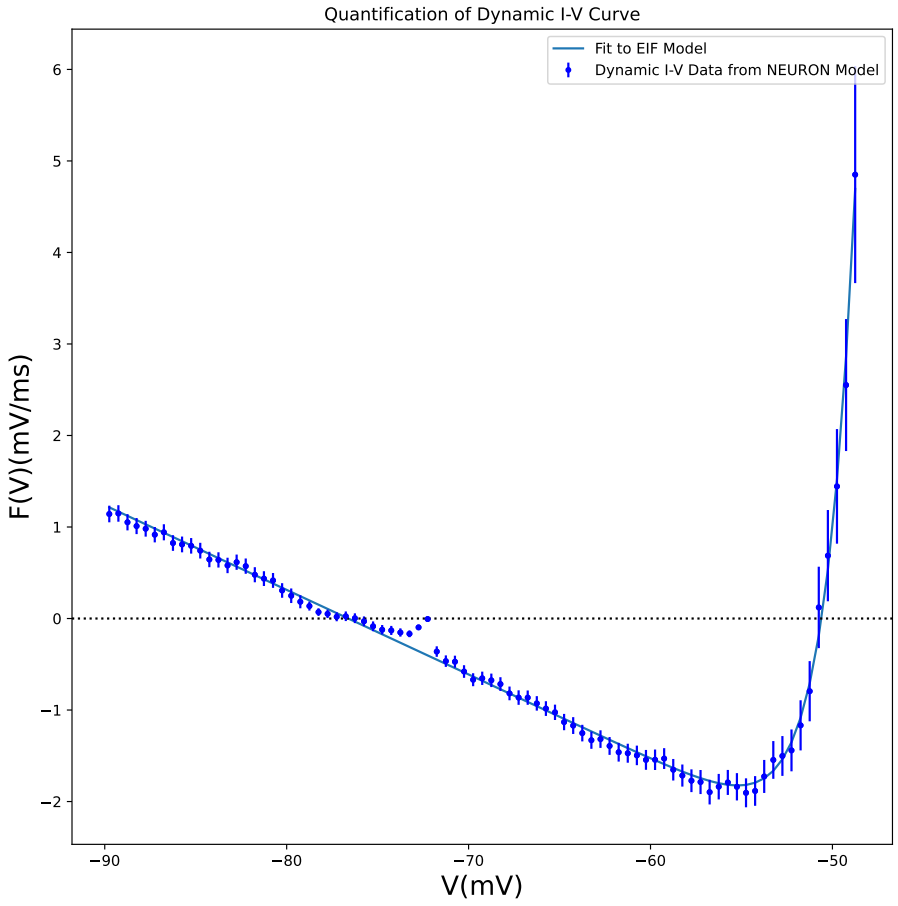

Figure 115: here it is shown the graph for the estimation of the dT parameter of the EIF model of the *in silico* data.The neuronal model is L5_UTPC_cADpyr232_2, dT value is in the figure 62 in the extremes range of -90, -47 mV

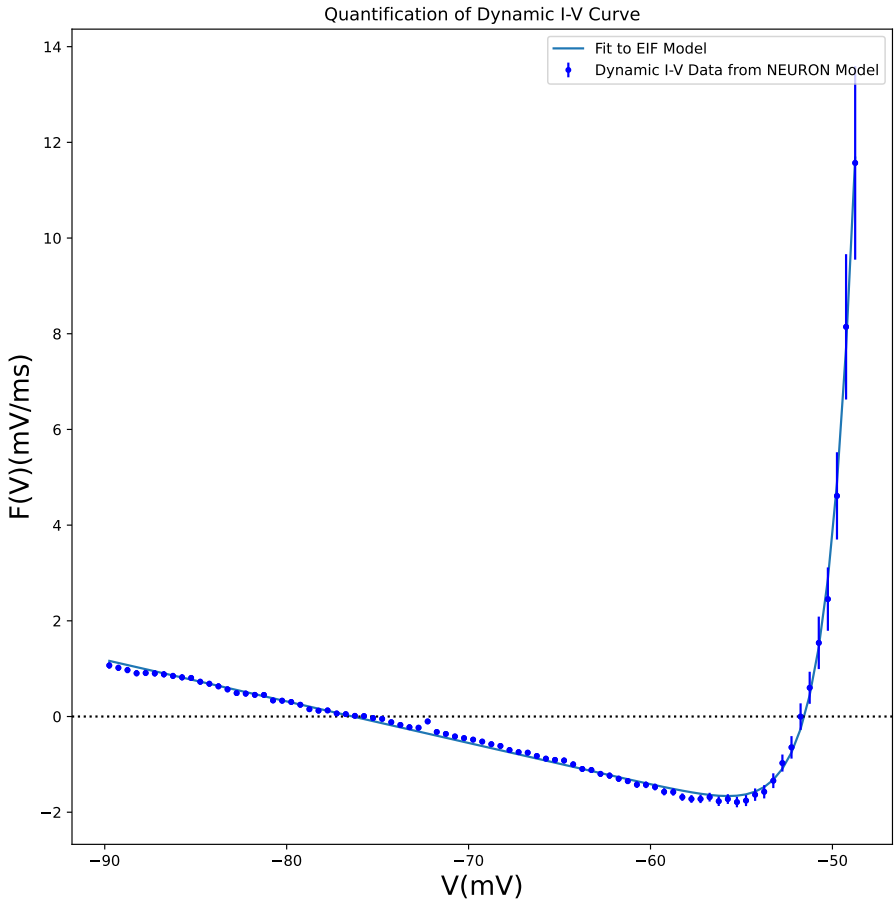

Figure 116: here it is shown the graph for the estimation of the dT parameter of the EIF model of the *in silico* data.The neuronal model is L5_UTPC_cADpyr232_3, dT value is in the figure 62 in the extremes range of -90, -48 mV

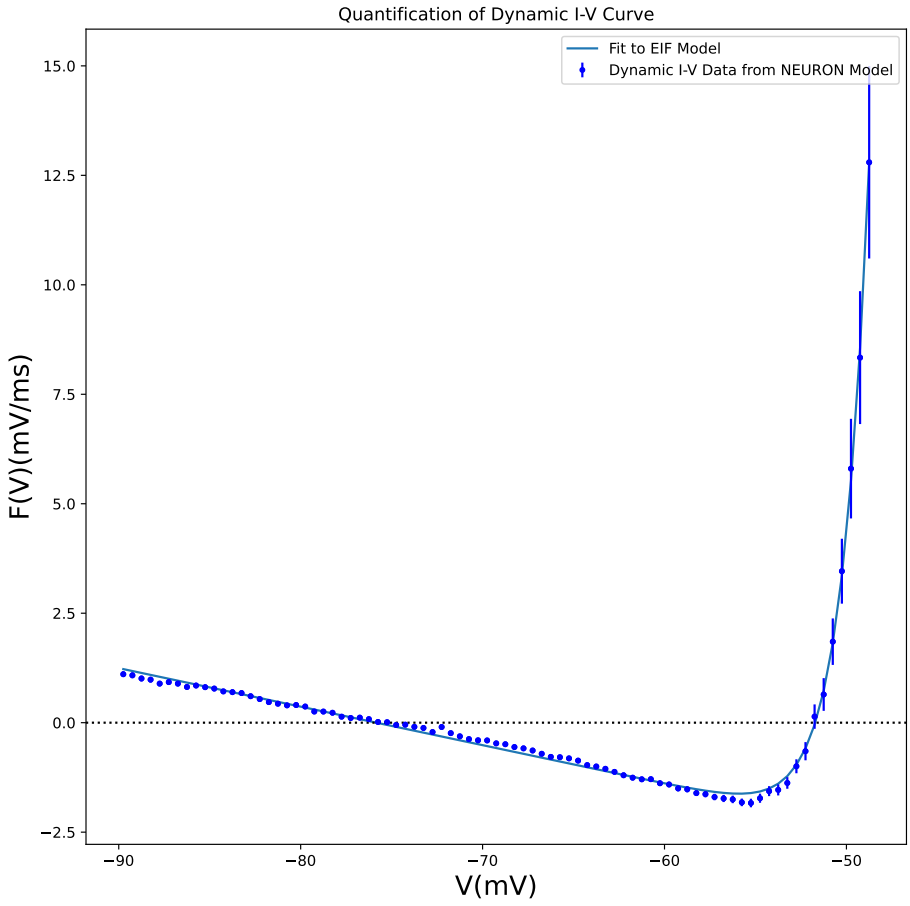

Figure 117: here it is shown the graph for the estimation of the dT parameter of the EIF model of the *in silico* data.The neuronal model is L5_UTPC_cADpyr232_4, dT value is in the figure 62 in the extremes range of -90, -48 mV

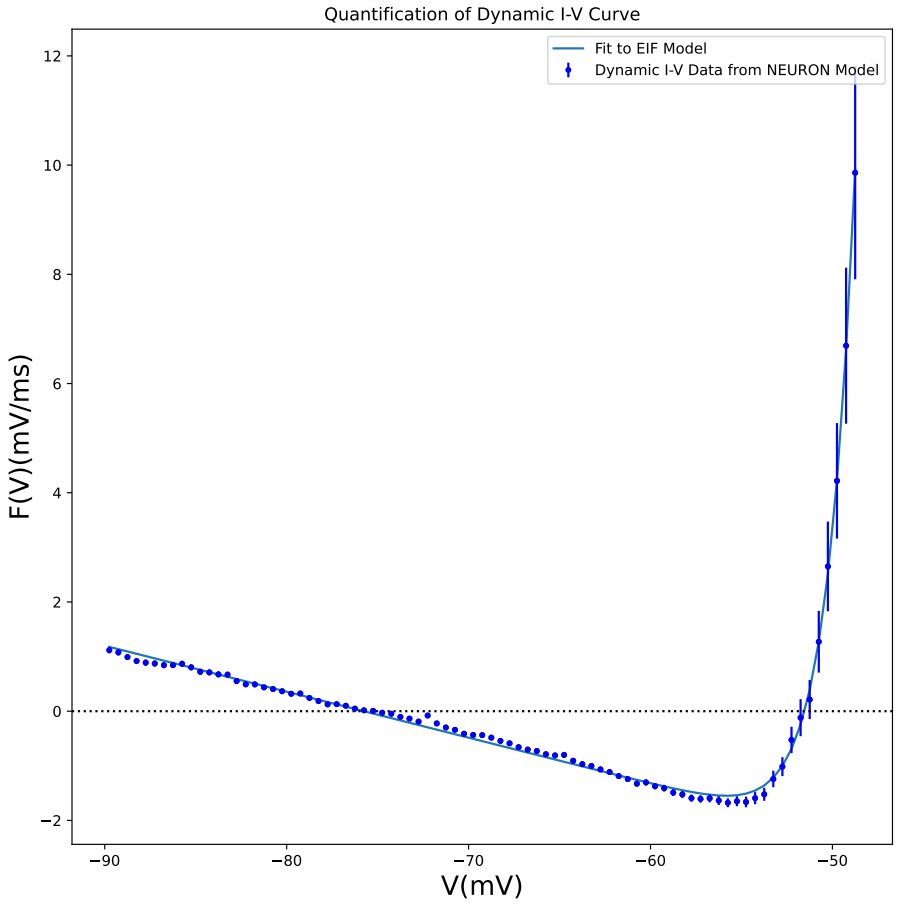

Figure 118: here it is shown the graph for the estimation of the dT parameter of the EIF model of the *in silico* data.The neuronal model is L5_UTPC_cADpyr232_5, dT value is in the figure 62 in the extremes range of -90, -48 mV

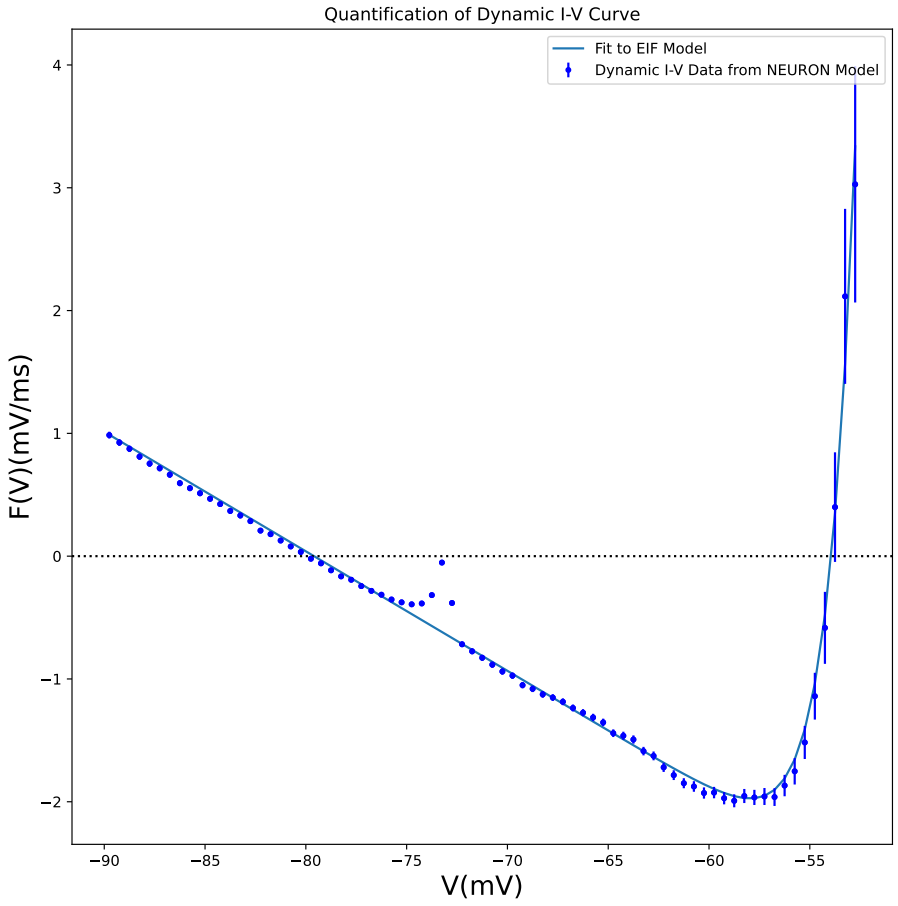

Figure 119: here it is shown the graph for the estimation of the dT parameter of the EIF model of the *in silico* data.The neuronal model is L6_BPC_cADpyr231_1, dT value is in the figure 62 in the extremes range of -90, -52 mV

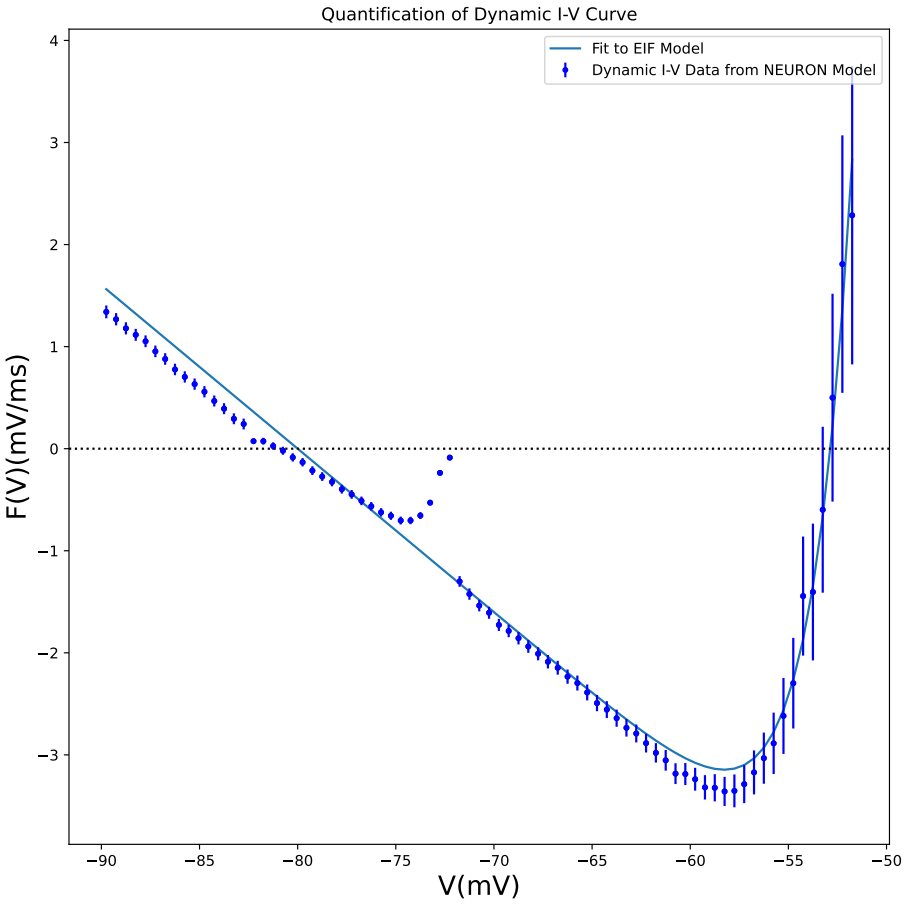

Figure 120: here it is shown the graph for the estimation of the dT parameter of the EIF model of the *in silico* data.The neuronal model is L6_BPC_cADpyr231_2, dT value is in the figure 62 in the extremes range of -90, -51 mV

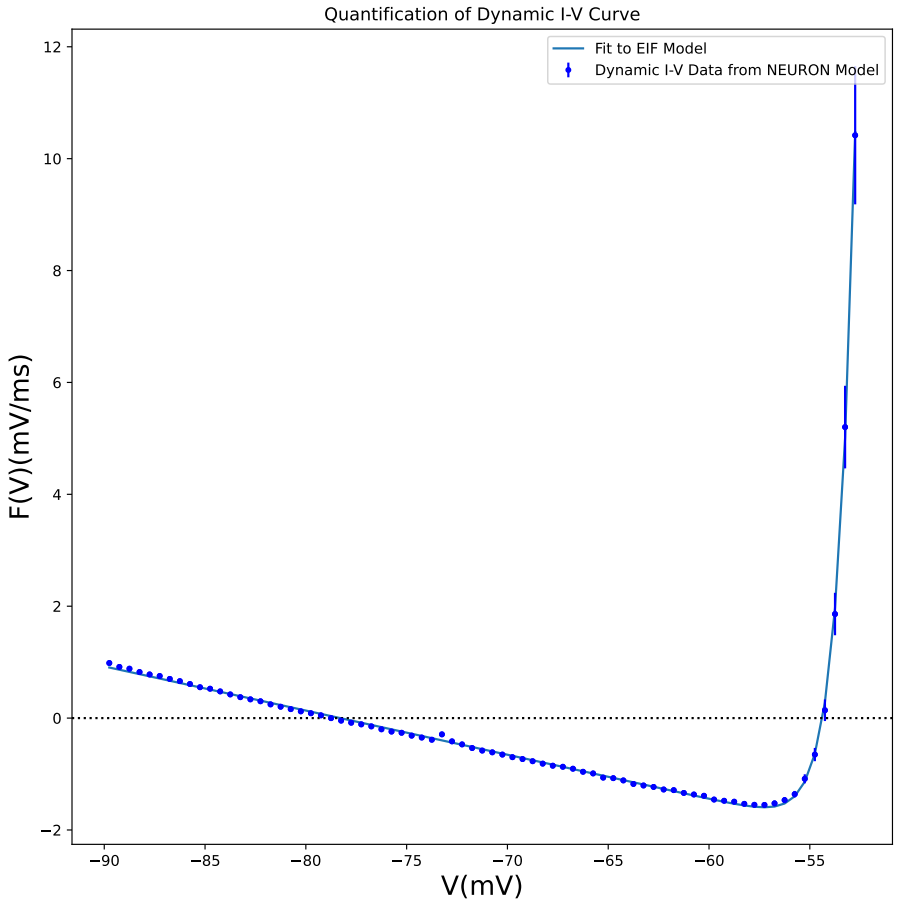

Figure 121: here it is shown the graph for the estimation of the dT parameter of the EIF model of the *in silico* data.The neuronal model is L6_BPC_cADpyr231_3, dT value is in the figure 62 in the extremes range of -90, -52 mV

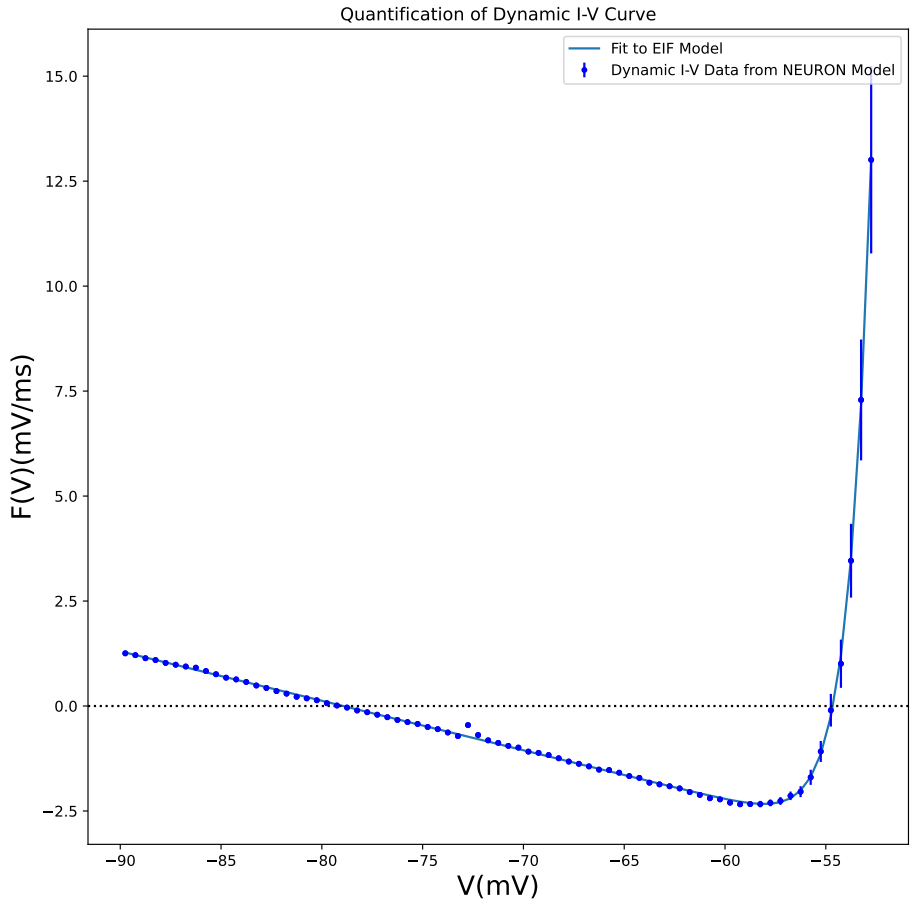

Figure 122: here it is shown the graph for the estimation of the dT parameter of the EIF model of the *in silico* data.The neuronal model is L6_BPC_cADpyr231_4, dT value is in the figure 62 in the extremes range of -90, -52 mV

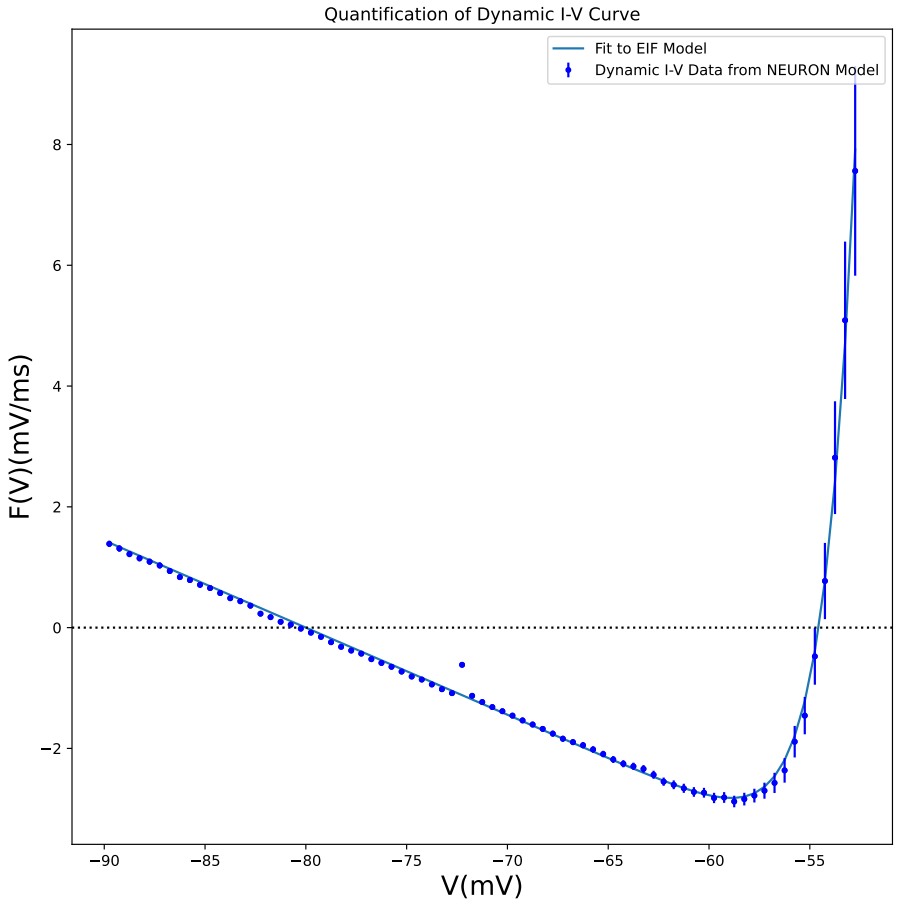

Figure 123: here it is shown the graph for the estimation of the dT parameter of the EIF model of the *in silico* data.The neuronal model is L6_BPC_cADpyr231_5, dT value is in the figure 62 in the extremes range of -90, -52 mV

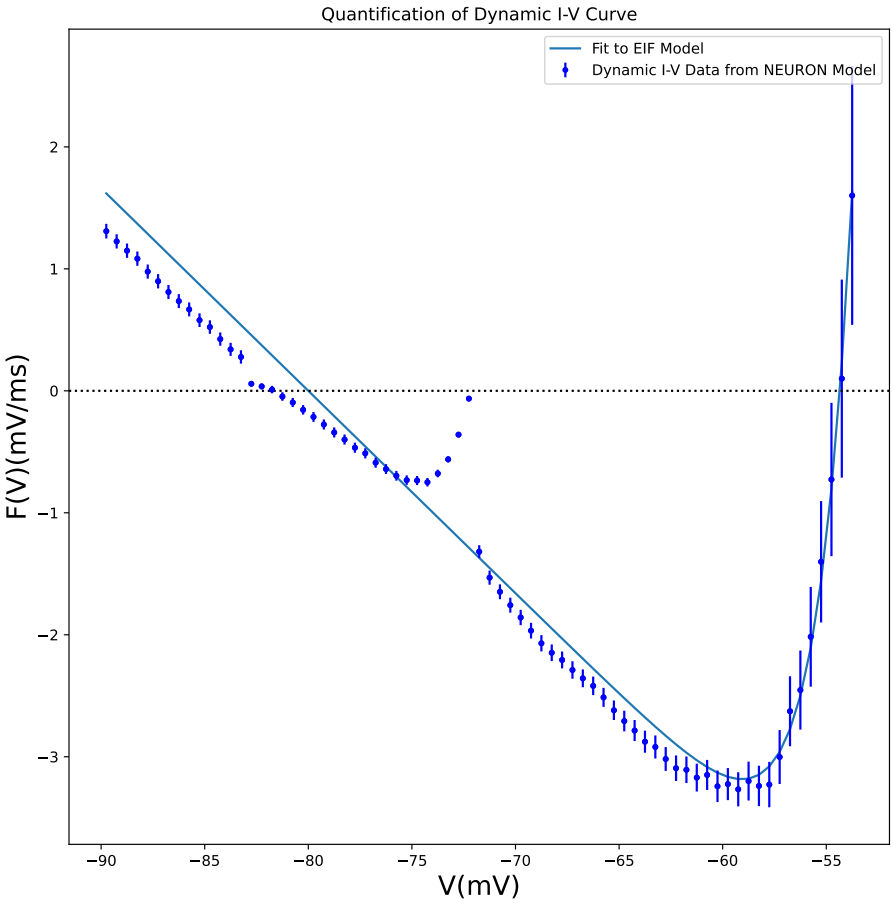

Figure 124: here it is shown the graph for the estimation of the dT parameter of the EIF model of the *in silico* data.The neuronal model is L6_IPC_cADpyr231_1, dT value is in the figure 62 in the extremes range of -90, -52 mV

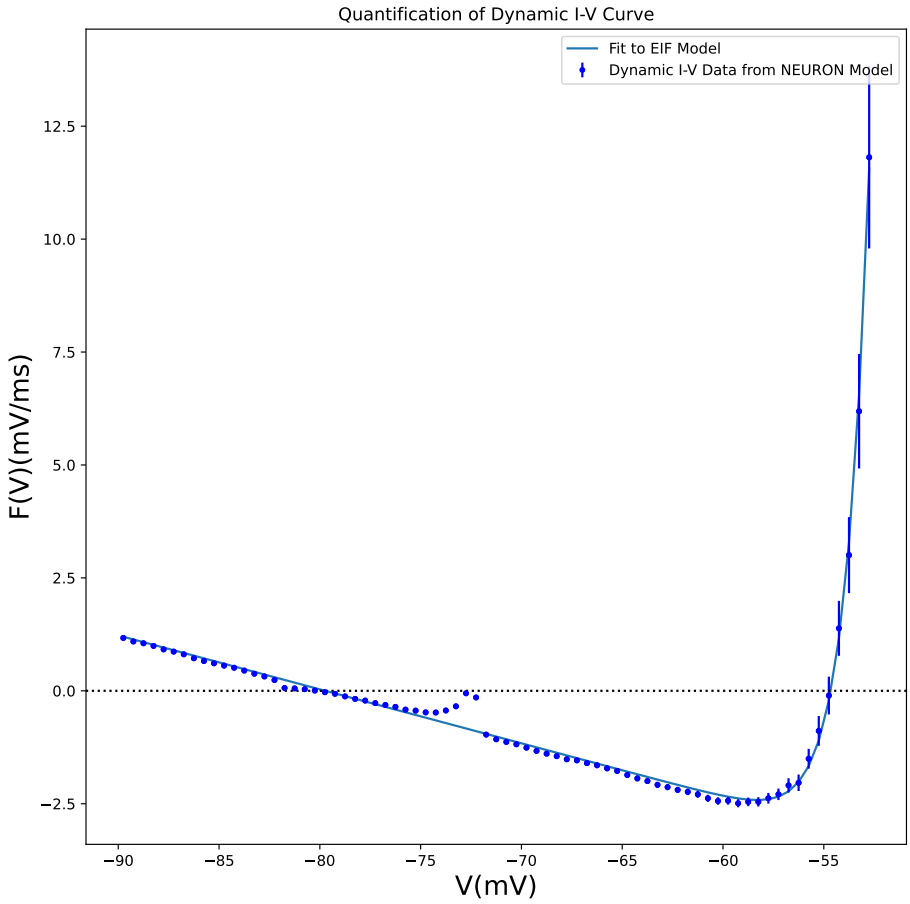

Figure 125: here it is shown the graph for the estimation of the dT parameter of the EIF model of the *in silico* data.The neuronal model is L6_IPC_cADpyr231_2, dT value is in the figure 62 in the extremes range of -90, -52 mV

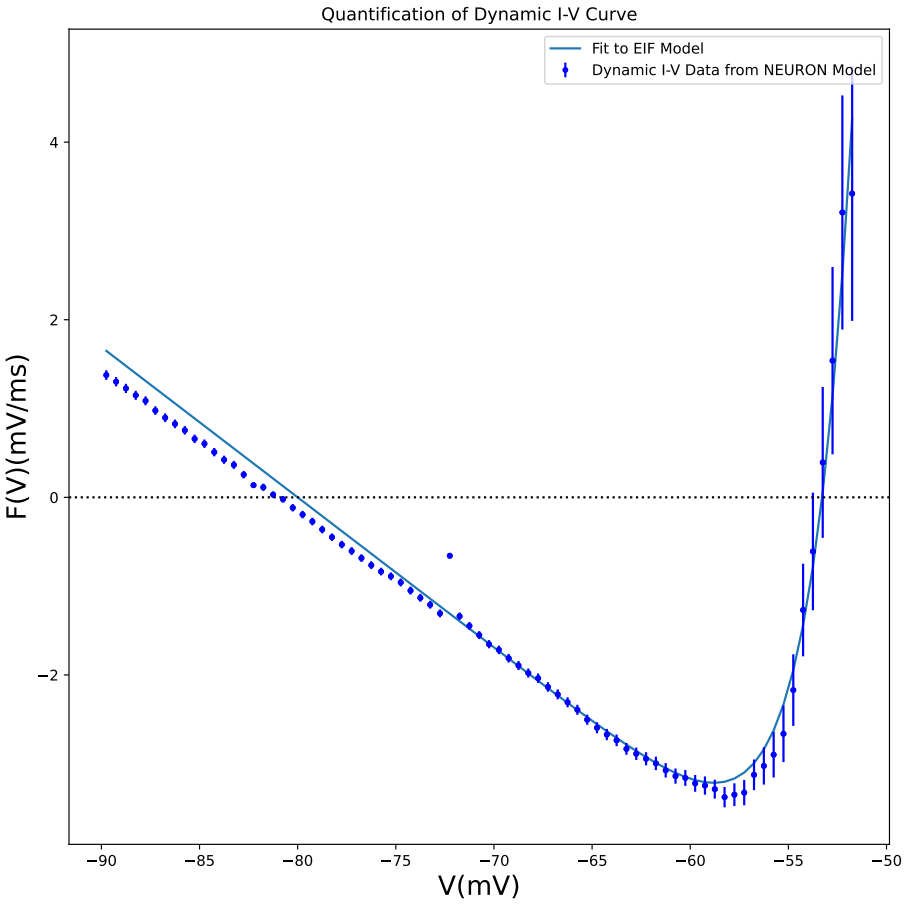

Figure 126: here it is shown the graph for the estimation of the dT parameter of the EIF model of the *in silico* data.The neuronal model is L6_IPC_cADpyr231_3, dT value is in the figure 62 in the extremes range of -90, -51 mV

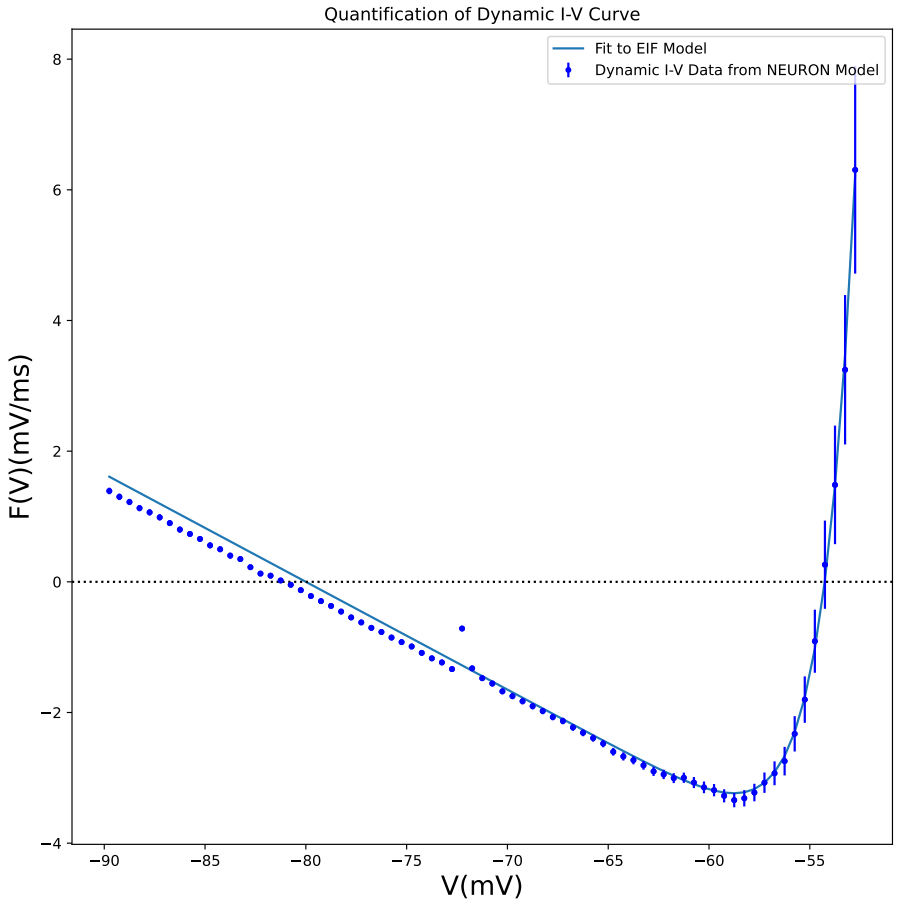

Figure 127: here it is shown the graph for the estimation of the dT parameter of the EIF model of the *in silico* data.The neuronal model is L6_IPC_cADpyr231_4, dT value is in the figure 62 in the extremes range of -90, -52 mV

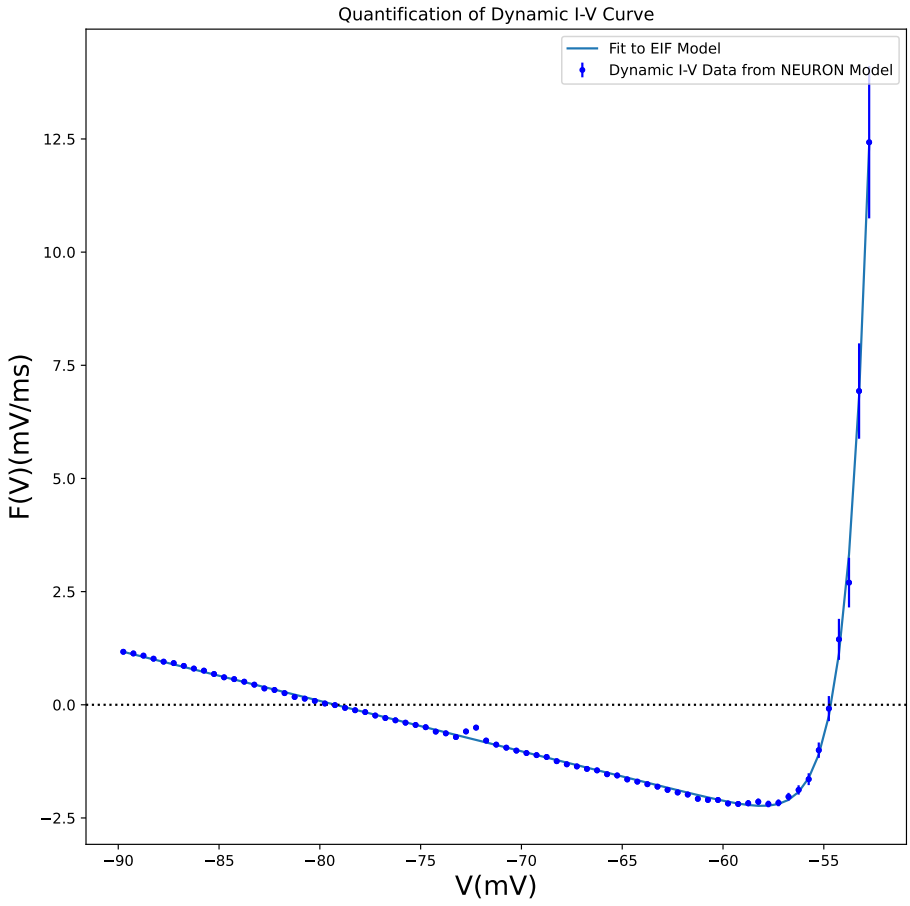

Figure 128: here it is shown the graph for the estimation of the dT parameter of the EIF model of the *in silico* data.The neuronal model is L6_IPC_cADpyr231_5, dT value is in the figure 62 in the extremes range of -90, -52 mV

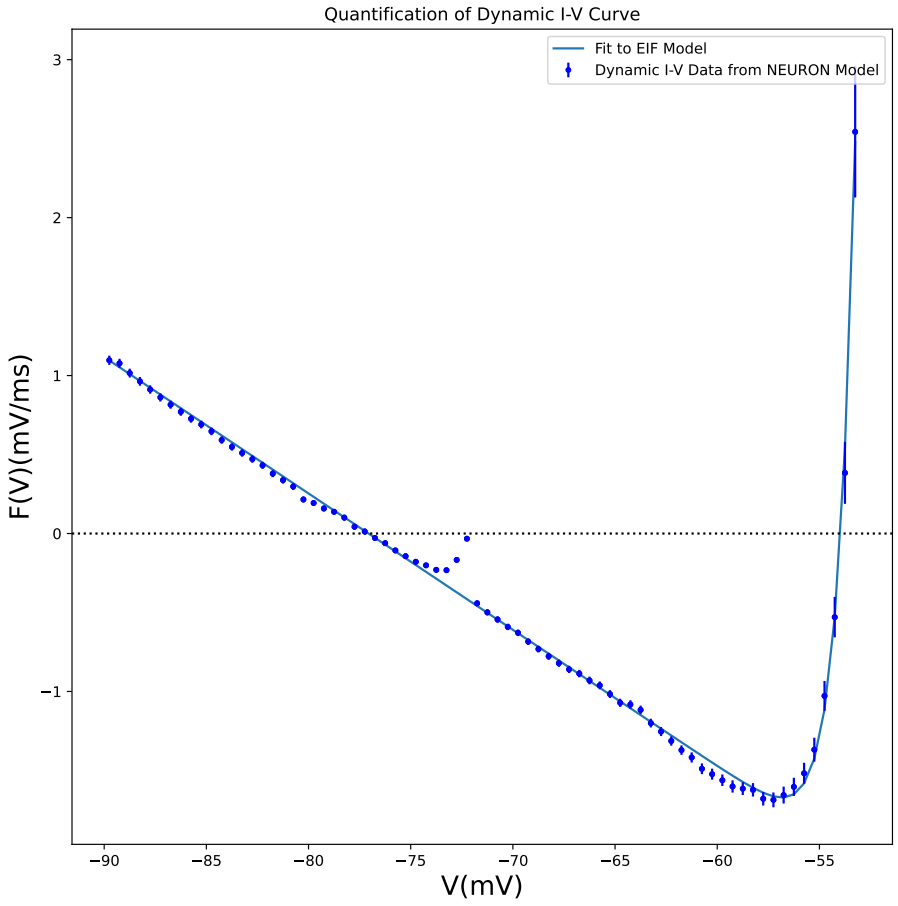

Figure 129: here it is shown the graph for the estimation of the dT parameter of the EIF model of the *in silico* data.The neuronal model is L6_TPC_L1_cADpyr231_1, dT value is in the figure 62 in the extremes range of -90, -52.5 mV

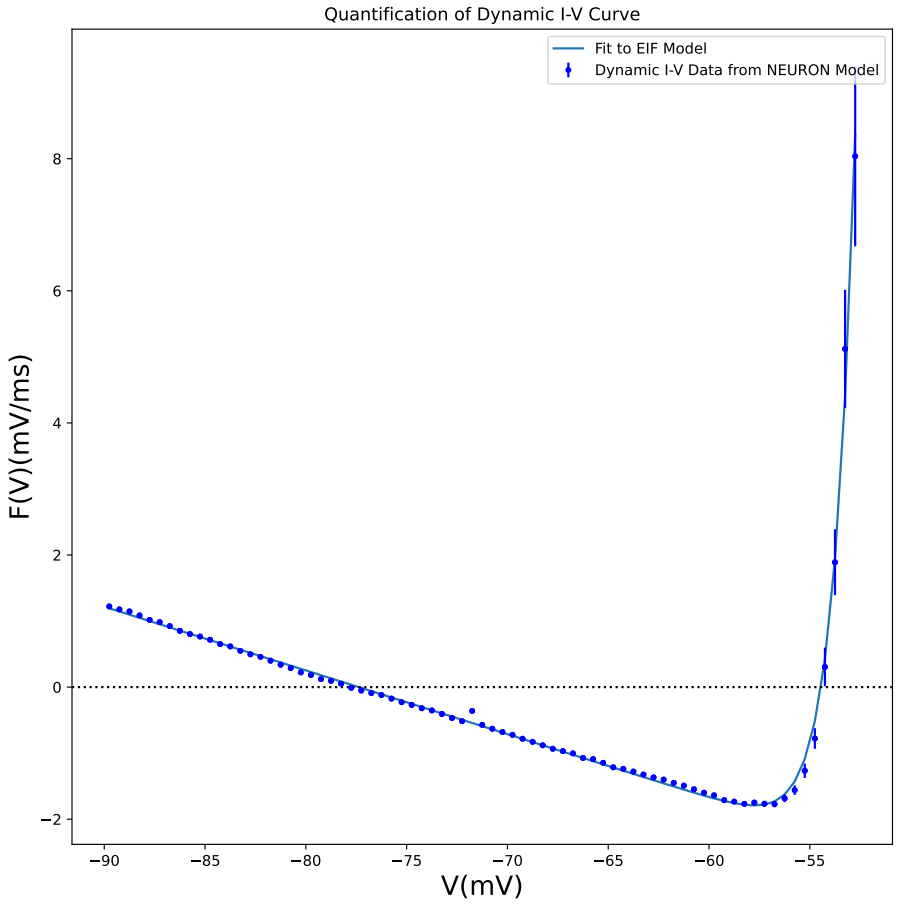

Figure 130: here it is shown the graph for the estimation of the dT parameter of the EIF model of the *in silico* data.The neuronal model is L6_TPC_L1_cADpyr231_2, dT value is in the figure 62 in the extremes range of -90, -52 mV

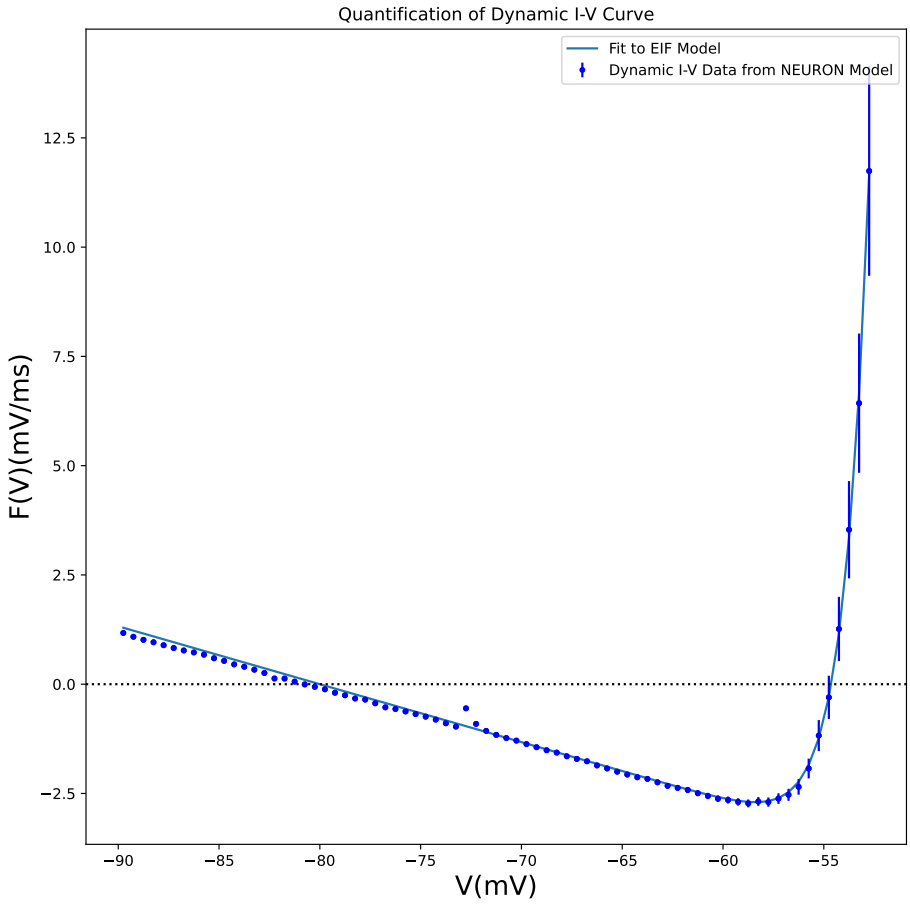

Figure 131: here it is shown the graph for the estimation of the dT parameter of the EIF model of the *in silico* data.The neuronal model is L6_TPC_L1_cADpyr231_3, dT value is in the figure 62 in the extremes range of -90, -52 mV

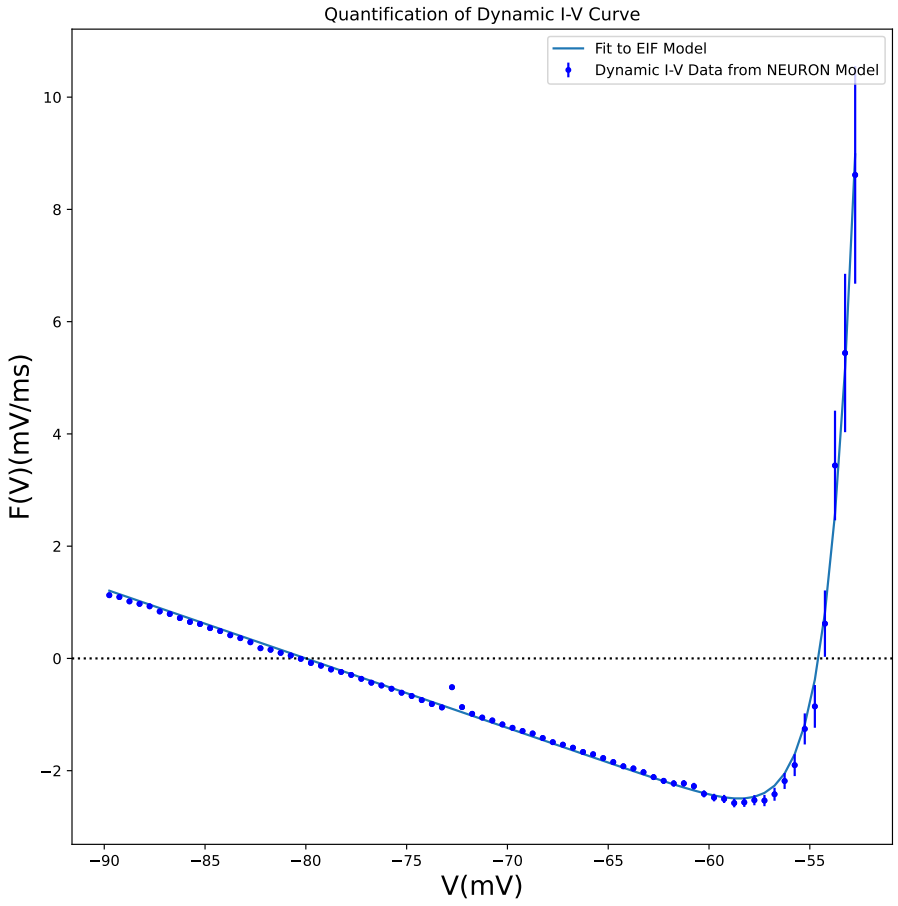

Figure 132: here it is shown the graph for the estimation of the dT parameter of the EIF model of the *in silico* data.The neuronal model is L6_TPC_L1_cADpyr231_4, dT value is in the figure 62 in the extremes range of -90, -52 mV

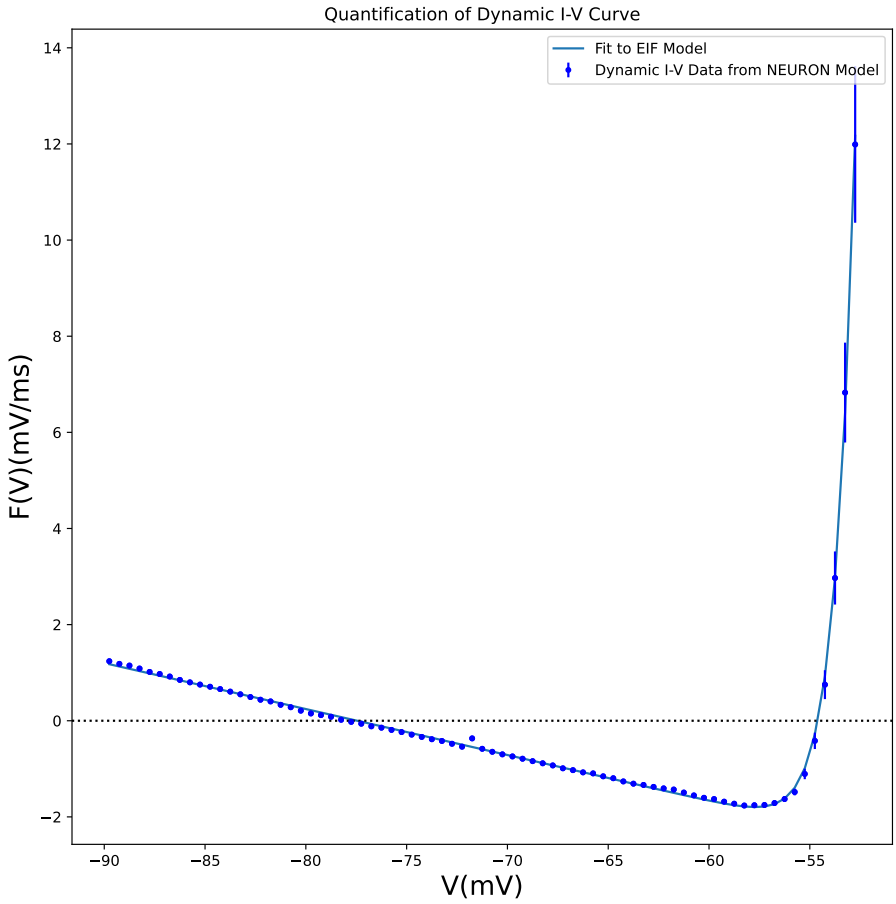

Figure 133: here it is shown the graph for the estimation of the dT parameter of the EIF model of the *in silico* data.The neuronal model is L6_TPC_L1_cADpyr231_5, dT value is in the figure 62 in the extremes range of -90, -52 mV

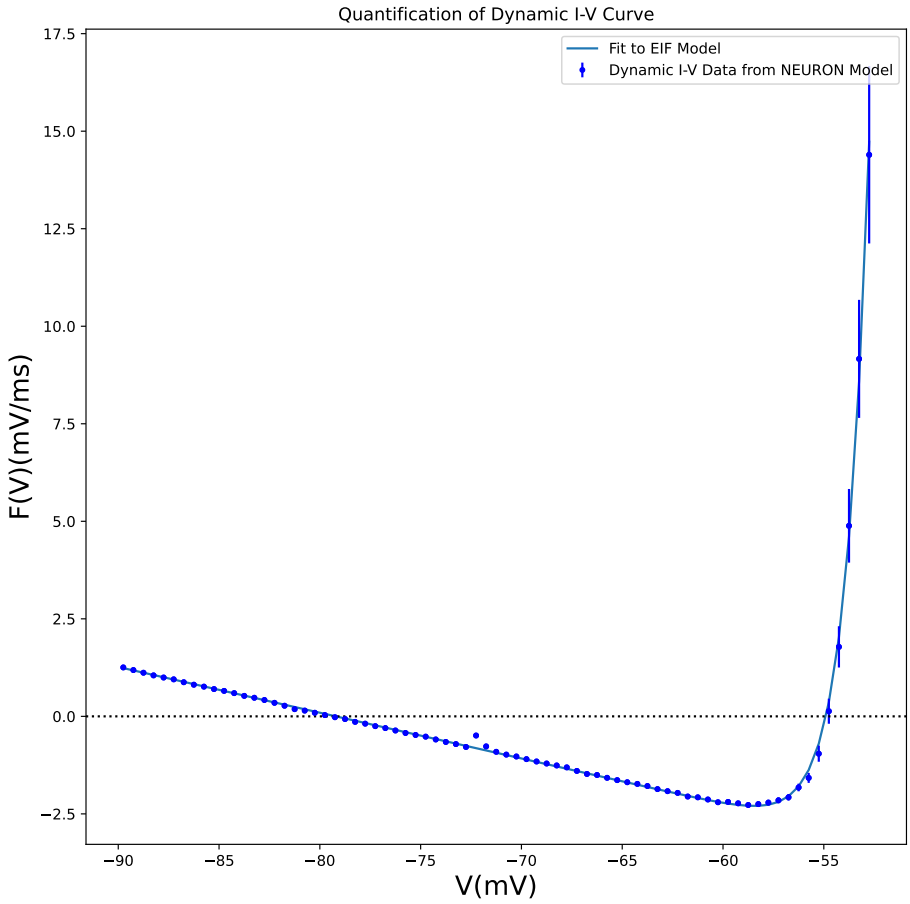

Figure 134: here it is shown the graph for the estimation of the dT parameter of the EIF model of the *in silico* data.The neuronal model is L6_TPC_L4_cADpyr231_1, dT value is in the figure 62 in the extremes range of -90, -52 mV

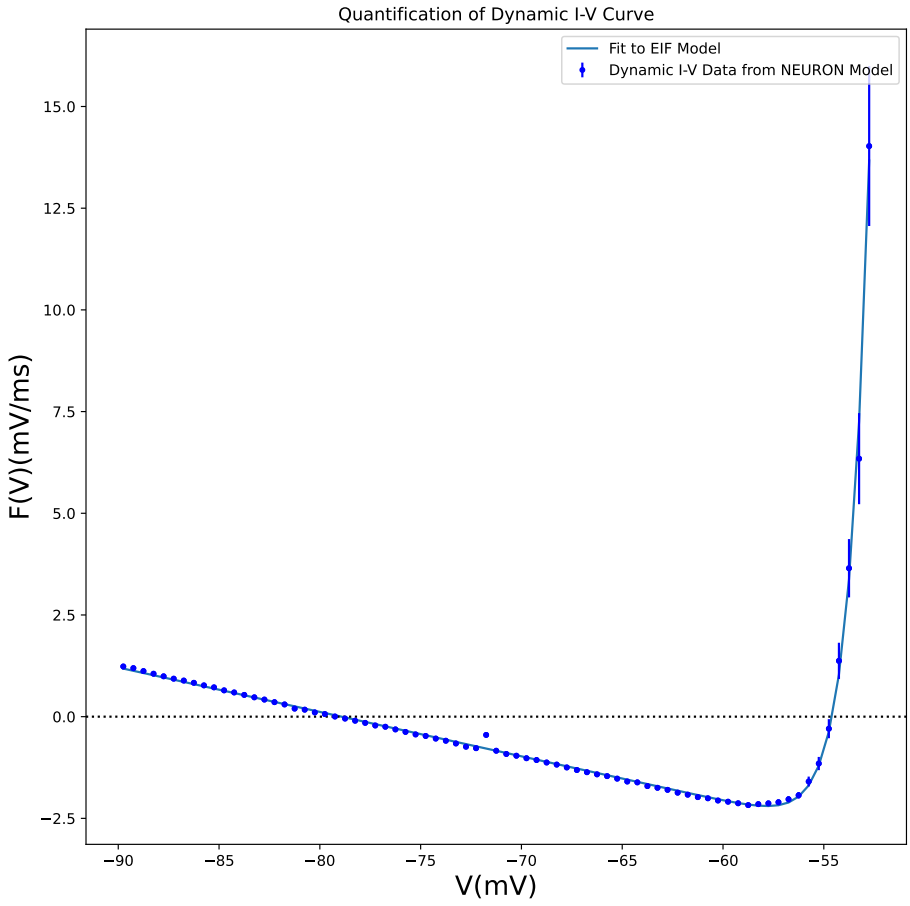

Figure 135: here it is shown the graph for the estimation of the dT parameter of the EIF model of the *in silico* data.The neuronal model is L6_TPC_L4_cADpyr231_2, dT value is in the figure 62 in the extremes range of -90, -52 mV

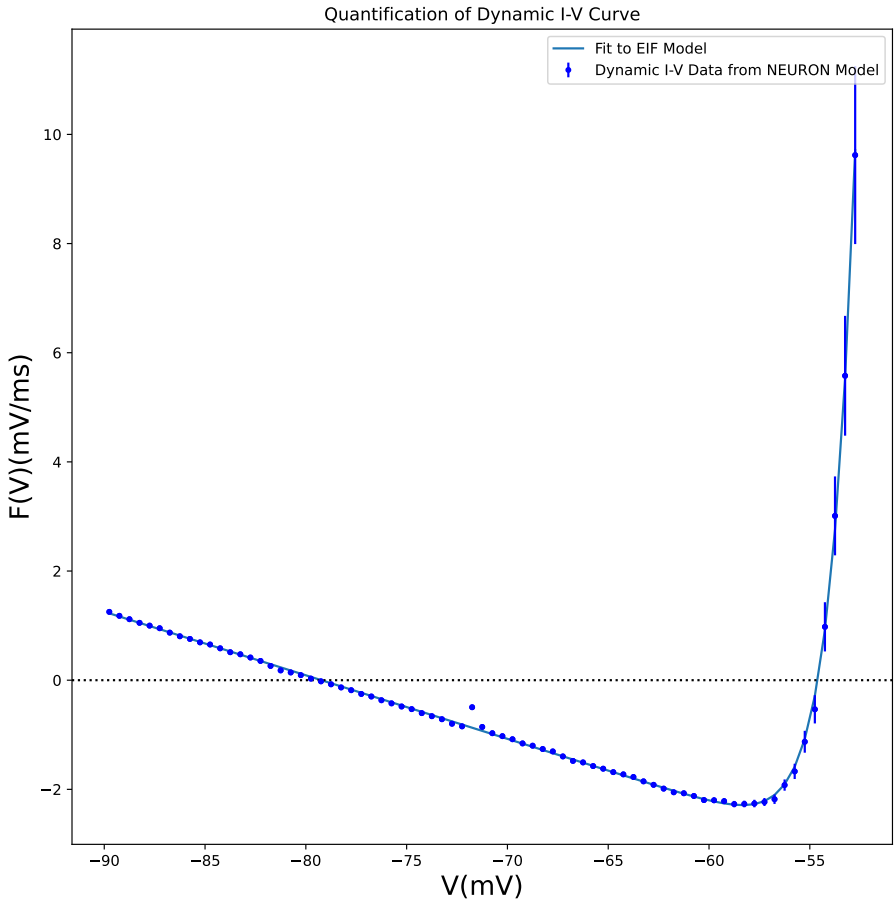

Figure 136: here it is shown the graph for the estimation of the dT parameter of the EIF model of the *in silico* data.The neuronal model is L6_TPC_L4_cADpyr231_3, dT value is in the figure 62 in the extremes range of -90, -52 mV

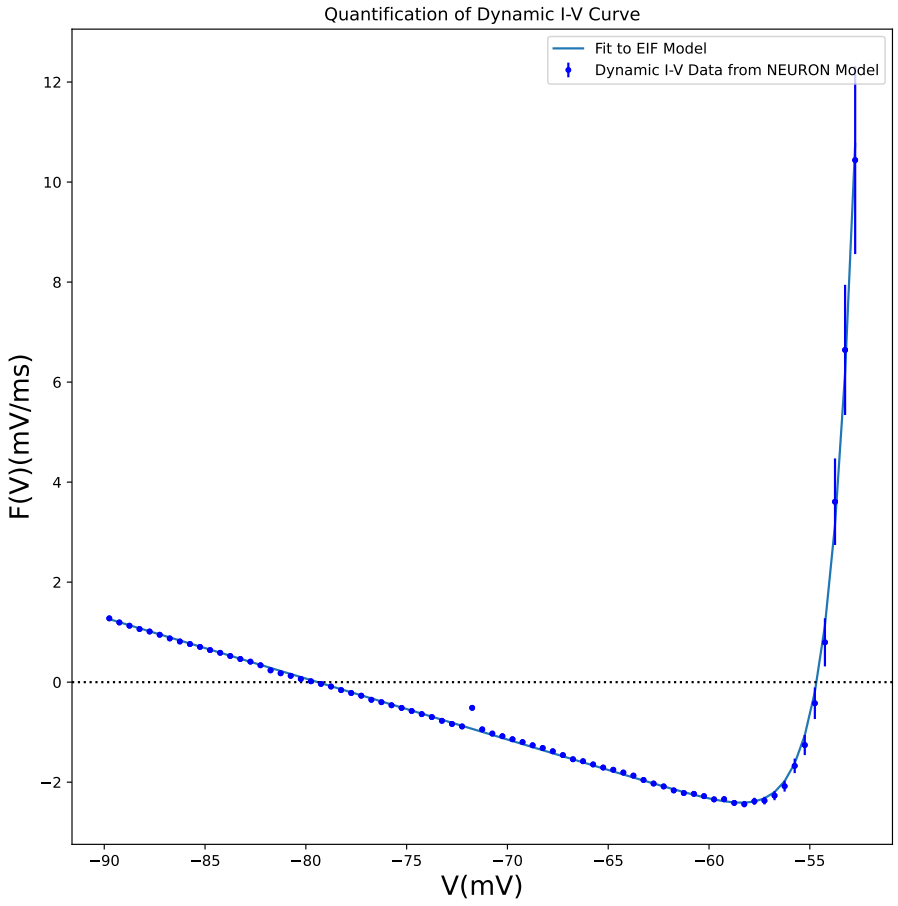

Figure 137: here it is shown the graph for the estimation of the dT parameter of the EIF model of the *in silico* data.The neuronal model is L6_TPC_L4_cADpyr231_4, dT value is in the figure 62 in the extremes range of -90, -52 mV

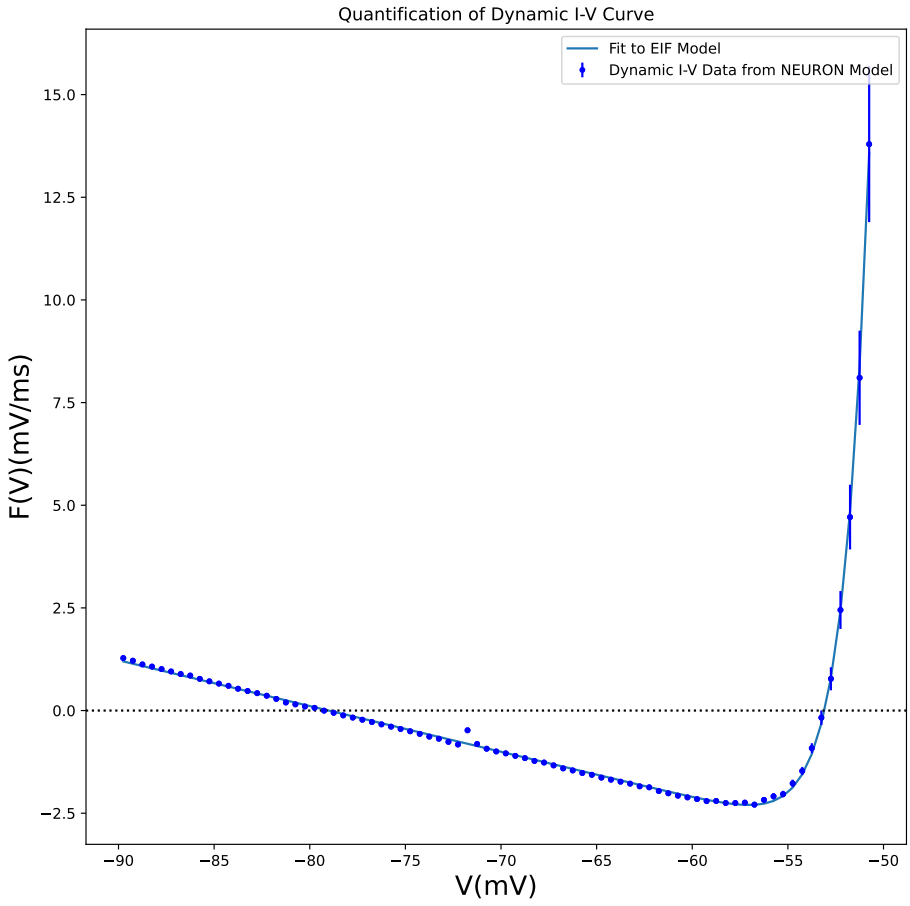

Figure 138: here it is shown the graph for the estimation of the dT parameter of the EIF model of the *in silico* data.The neuronal model is L6_TPC_L4_cADpyr231_5, dT value is in the figure 62 in the extremes range of -90, -50 mV

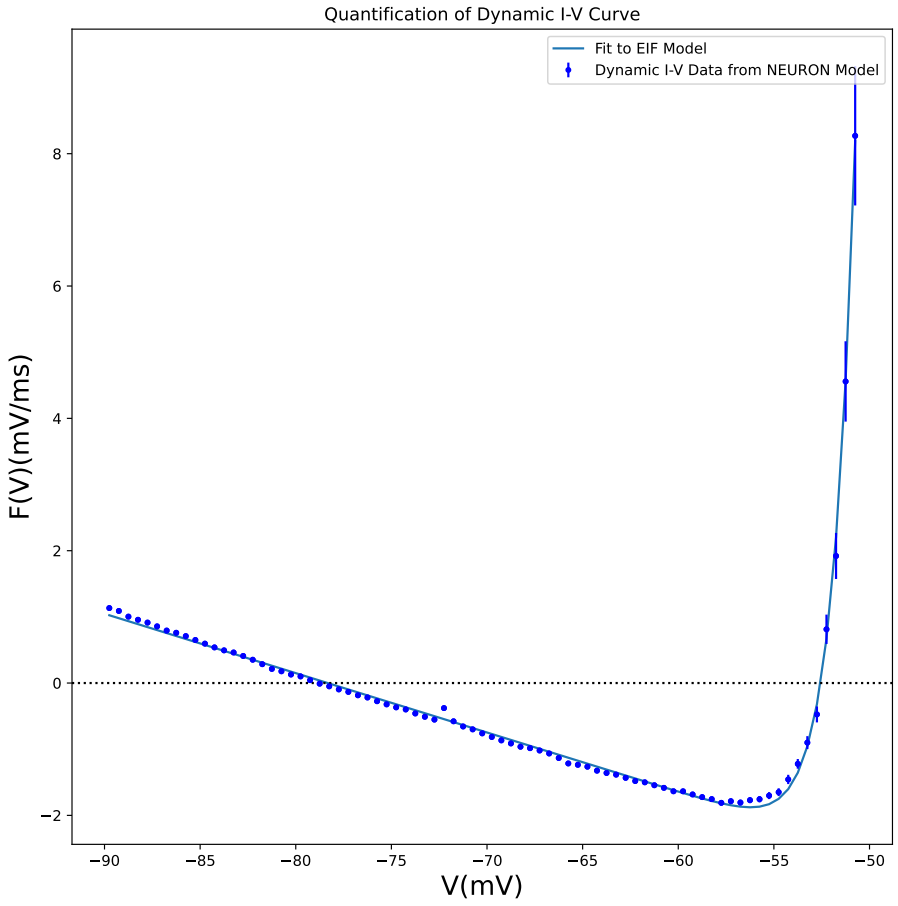

Figure 139: here it is shown the graph for the estimation of the dT parameter of the EIF model of the *in silico* data.The neuronal model is L6_UTPC_cADpyr231_1, dT value is in the figure 62 in the extremes range of -90, -50 mV

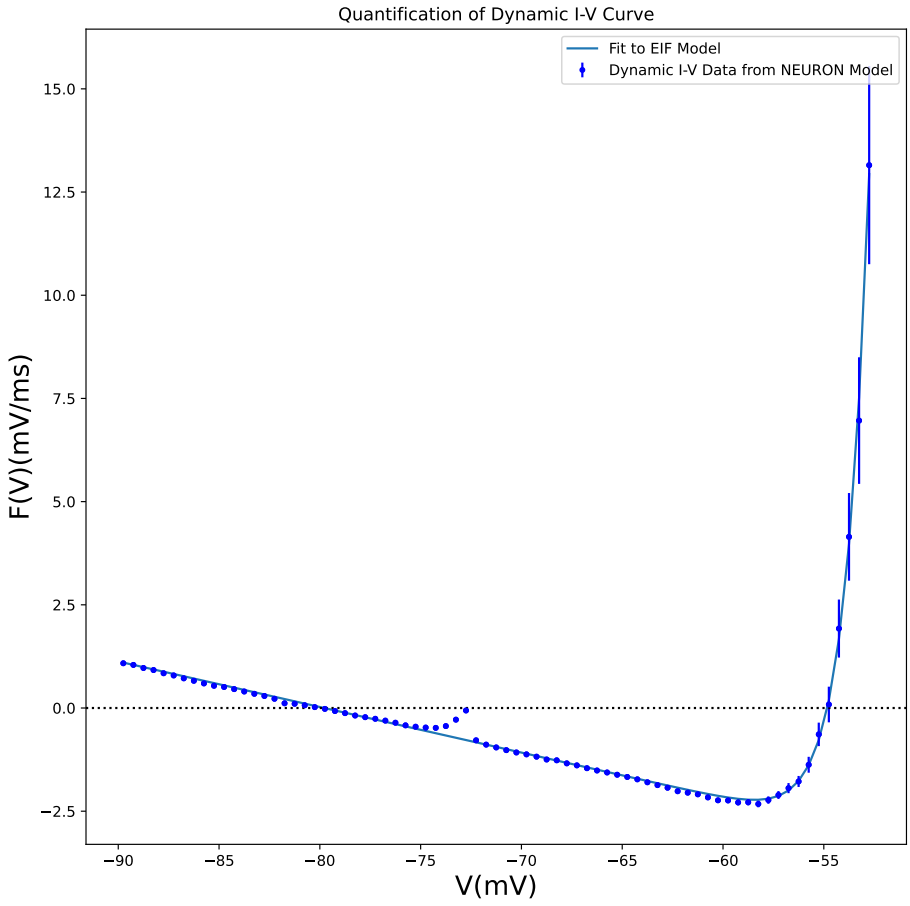

Figure 140: here it is shown the graph for the estimation of the dT parameter of the EIF model of the *in silico* data.The neuronal model is L6_UTPC_cADpyr231_2, dT value is in the figure 62 in the extremes range of -90, -50 mV

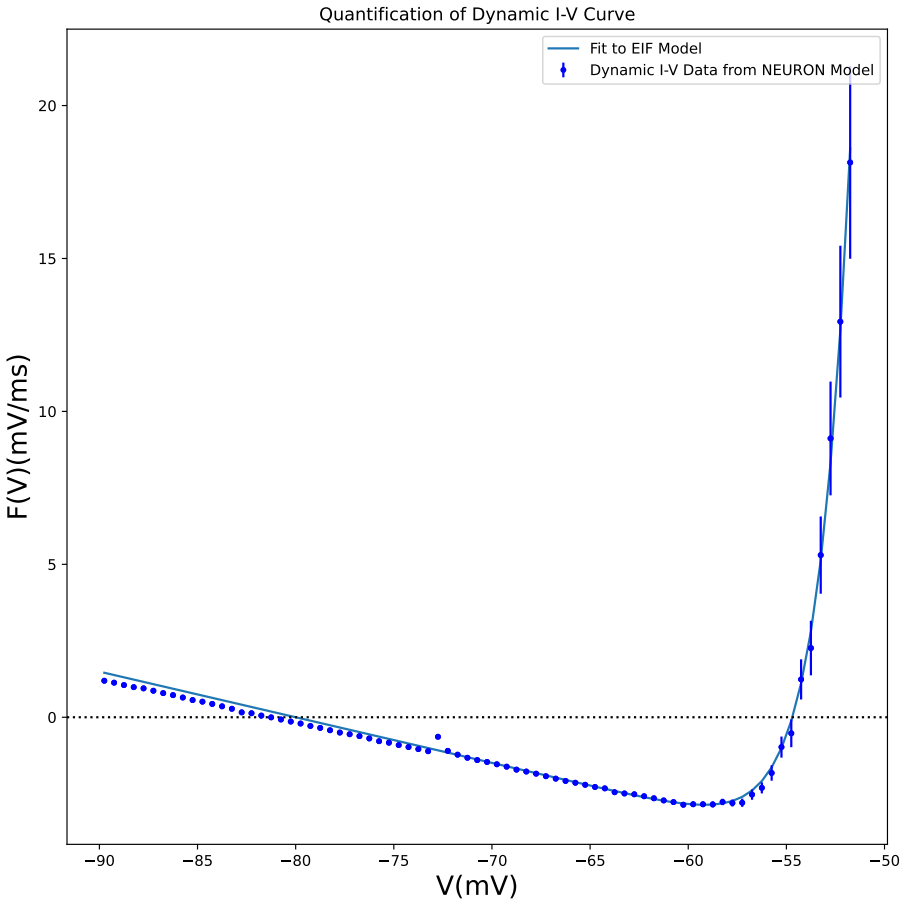

Figure 141: here it is shown the graph for the estimation of the dT parameter of the EIF model of the *in silico* data.The neuronal model is L6_UTPC_cADpyr231_3, dT value is in the figure 62 in the extremes range of -90, -50 mV

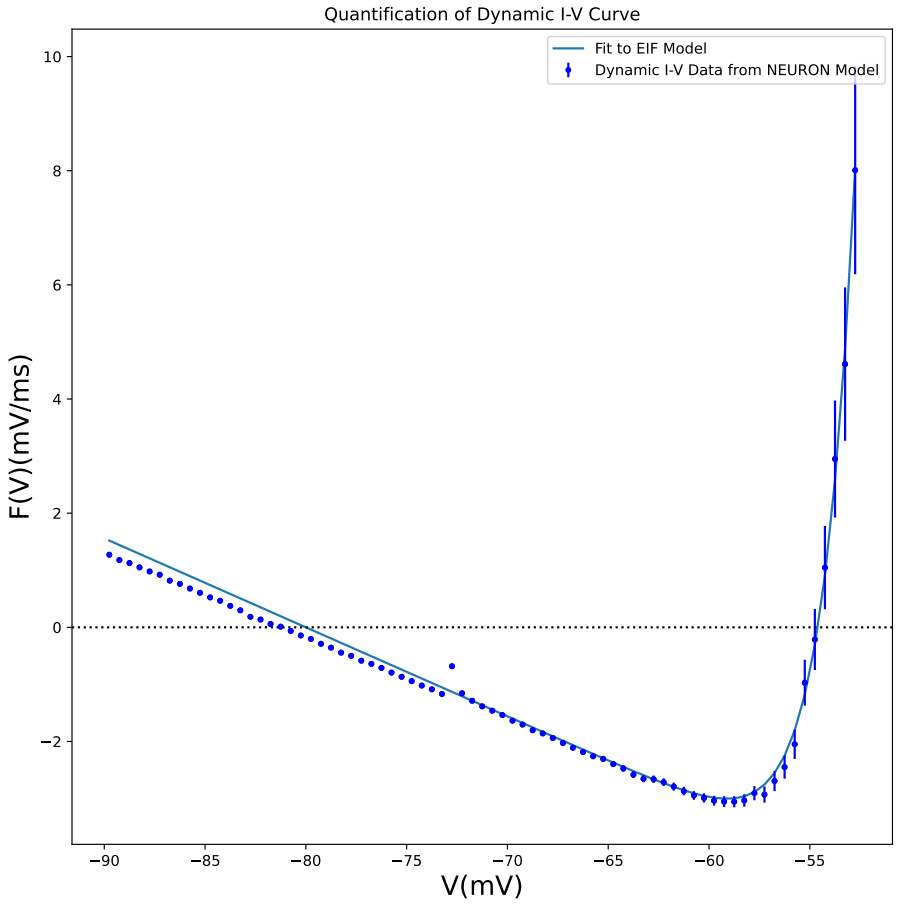

Figure 142: here it is shown the graph for the estimation of the dT parameter of the EIF model of the *in silico* data.The neuronal model is L6_UTPC_cADpyr231_4, dT value is in the figure 62 in the extremes range of -90, -51 mV

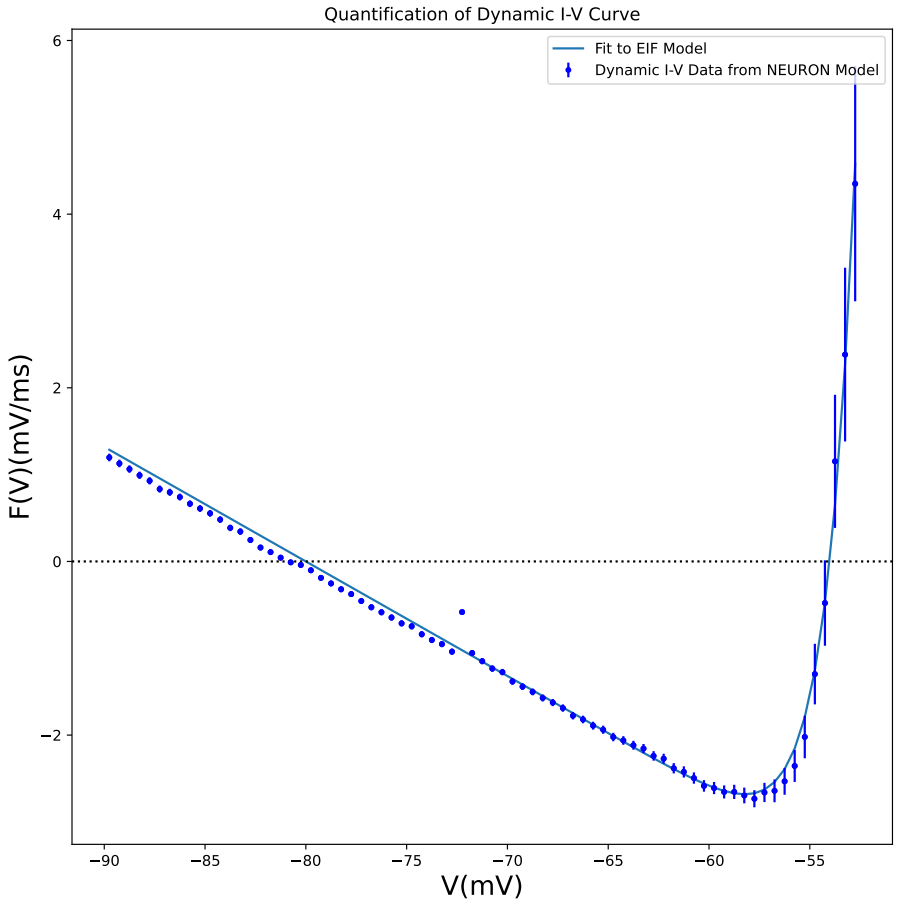

Figure 143: here it is shown the graph for the estimation of the dT parameter of the EIF model of the *in silico* data.The neuronal model is L6_UTPC_cADpyr231_5, dT value is in the figure 62 in the extremes range of -90, -51 mV

7.3 I-O properties at the HF for each neuronal models

here in this subsection are present all the figures regarding all the other neuronal models not showed in the subsectionTheory of Richardson verification on multi-compartmental models

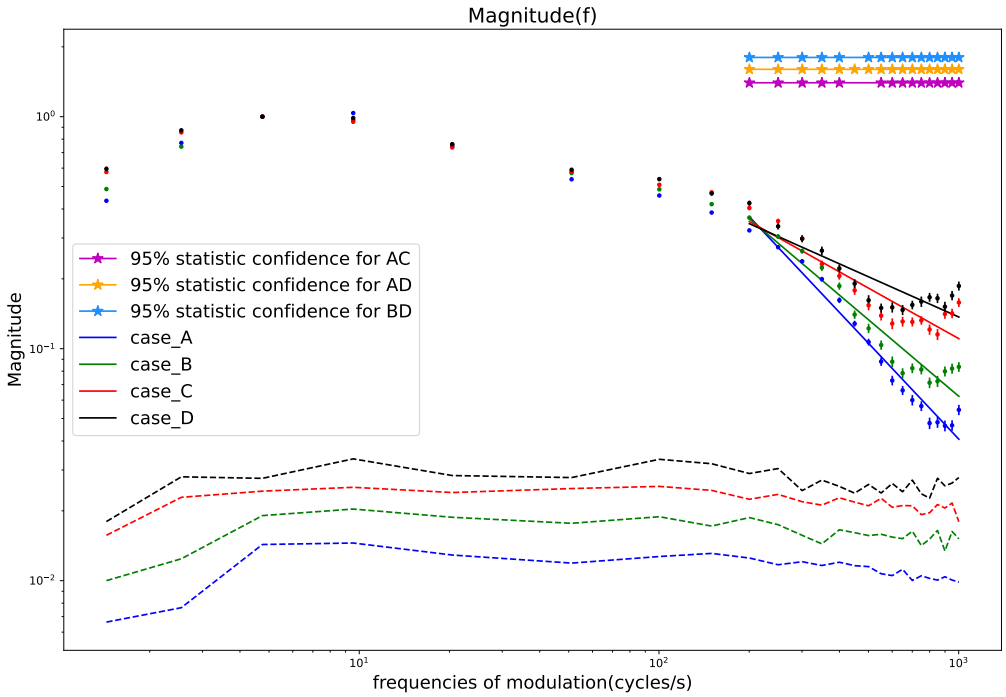

Figure 144: An example of a neuronal model, the L23_PC_cADpyr229_2, which shown the Richardson's effect at HF. The gain values are normalised over their maximum located around the $f_{mod} \sim$ 5Hz. The dashed lines stay for each cases as the minimal level of significance threshold. The magenta, yellow, blue lines and the stars indicate for each f_{mod} value that the cases A and C, A and D, B and D are not superimposable at the 95% of significance of the KS test. The solid lines of each color are the HF domain linear fit used to extrapolated the HF slope of the linear attenuation; the slopes values for each cases and neuronal models are in figure 70. The slopes values are shown in the figure 70.

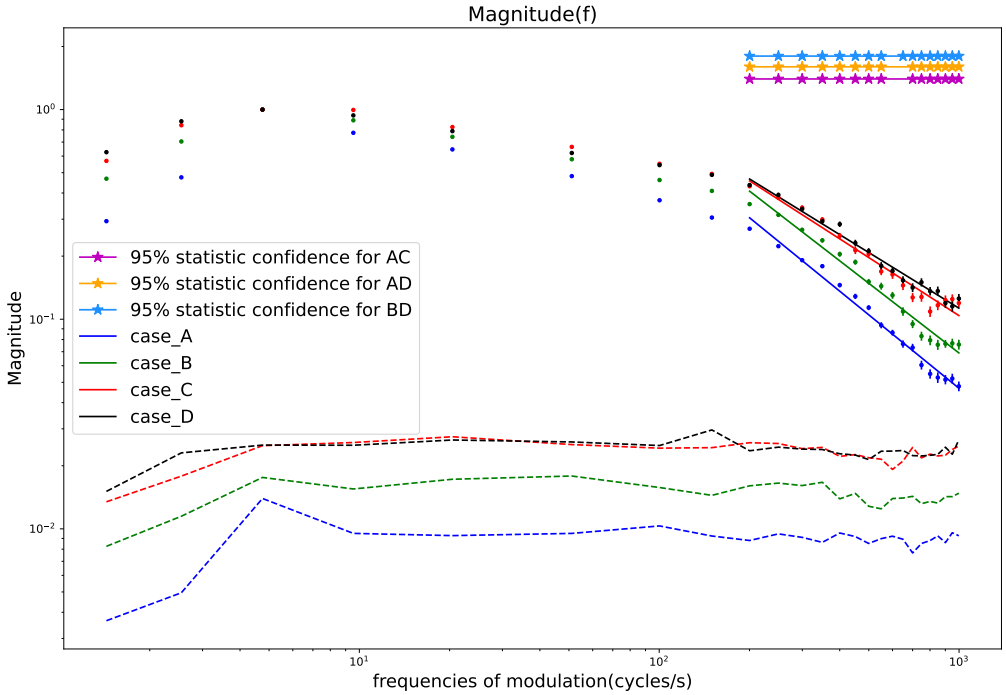

Figure 145: An example of a neuronal model, the L23_PC_cADpyr229_4, which shown the Richardson's effect at HF. The gain values are normalised over their maximum located around the $f_{mod} \sim$ 5Hz. The magenta, yellow, blue lines and the stars indicate for each f_{mod} value that the cases A and C, A and D, B and D are not superimposable at the 95% of significance of the KS test. The solid lines of each color are the HF domain linear fit used to extrapolated the HF slope of the linear attenuation; the slopes values for each cases and neuronal models are in figure 70.

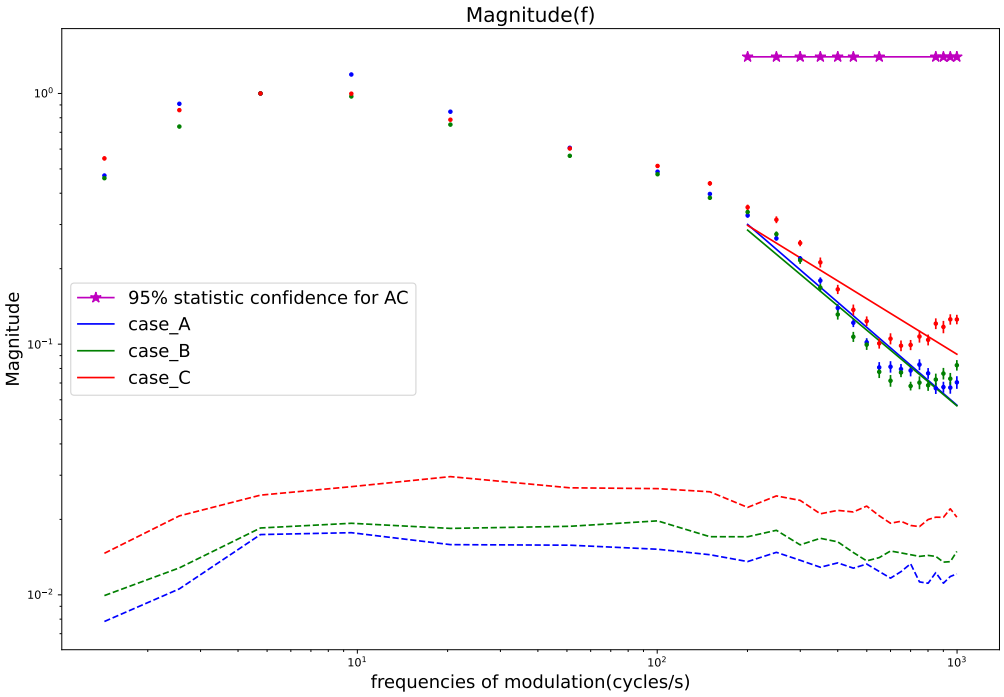

Figure 146: An example of a neuronal model, the L23_PC_cADpyr229_5, which even id the slopes are different the Richardson is not present since the gain amplitude of the case A is higher than the amplitude present in the case B. The gain values are normalised over their maximum located around the $f_{mod} \sim$ 5Hz. The magenta lines and the stars indicate for each f_{mod} value that the cases A and C, are not superimposable at the 95% of significance of the KS test. The solid lines of each color are the HF domain linear fit used to extrapolated the HF slope of the linear attenuation; the slopes values for each cases and neuronal models are in figure 70

.

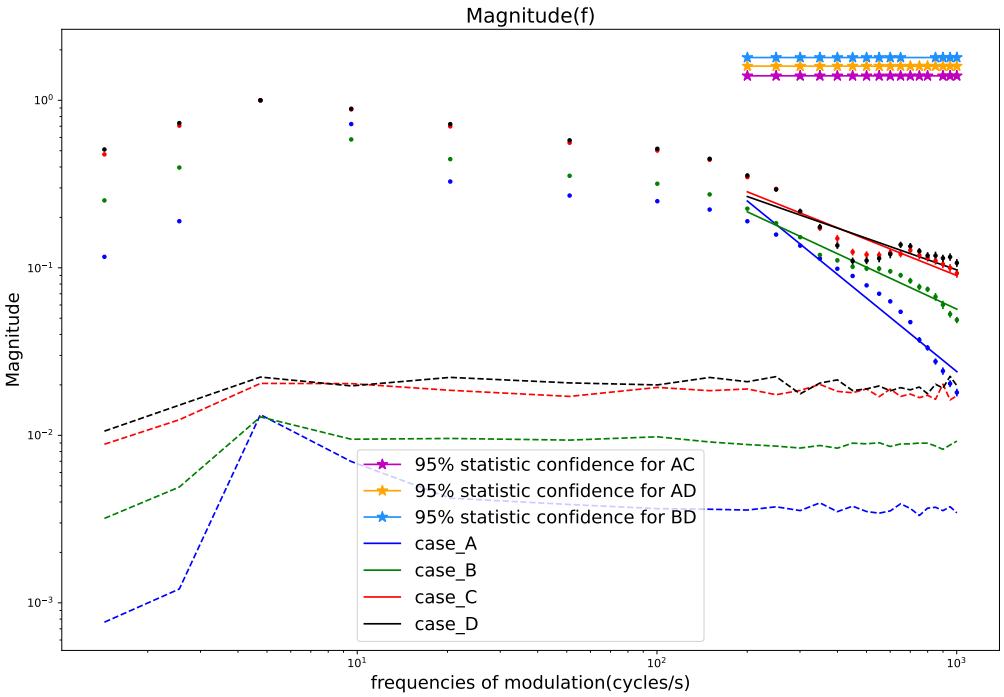

Figure 147: An example of a neuronal model, the L4_PC_cADpyr230_2, which even if the slopes are different the Richardson is not present since the gain amplitude of the case A is higher than the amplitude present in the case B. The gain values are normalised over their maximum located around the $f_{mod} \sim$ 5Hz. The magenta, yellow, blue lines and the stars indicate for each f_{mod} value that the cases A and C, A and D, B and D are not superimposable at the 95% of significance of the KS test. The solid lines of each color are the HF domain linear fit used to extrapolated the HF slope of the linear attenuation; the slopes values for each cases and neuronal models are in figure 70.

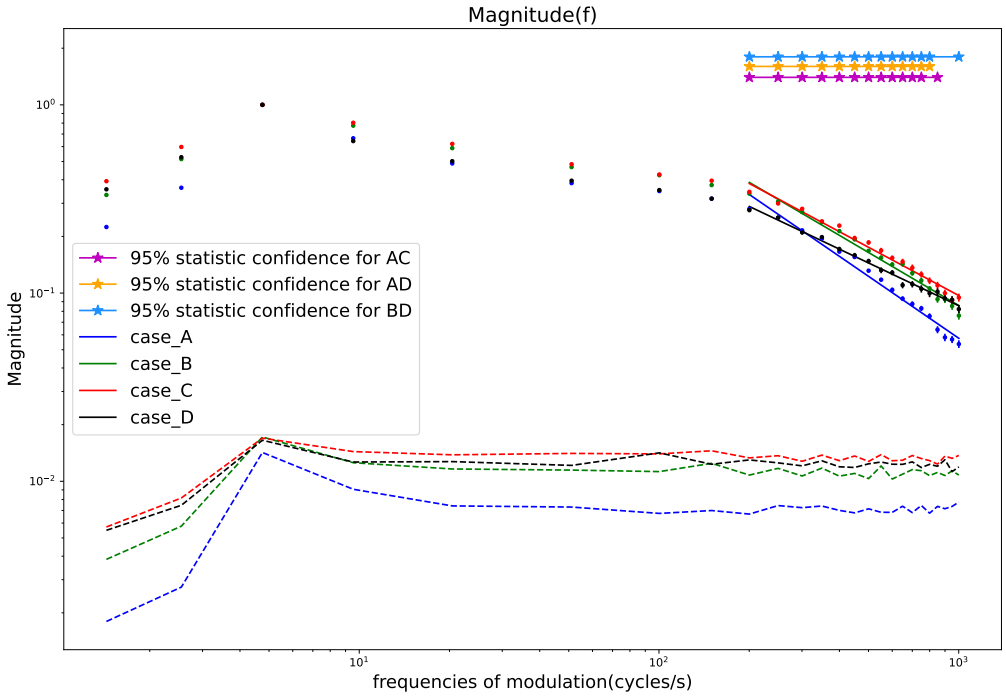

Figure 148: An example of a neuronal model, the L4_PC_cADpyr230_3, which even if the slopes are different the Richardson is not present since the gain amplitude of the case D is smaller than all the others. The gain values are normalised over their maximum located around the $f_{mod} \sim 5$Hz. The magenta, yellow, blue lines and the stars indicate for each f_{mod} value that the cases A and C, A and D, B and D are not superimposable at the 95% of significance of the KS test. The solid lines of each color are the HF domain linear fit used to extrapolated the HF slope of the linear attenuation; the slopes values for each cases and neuronal models are in figure 70.

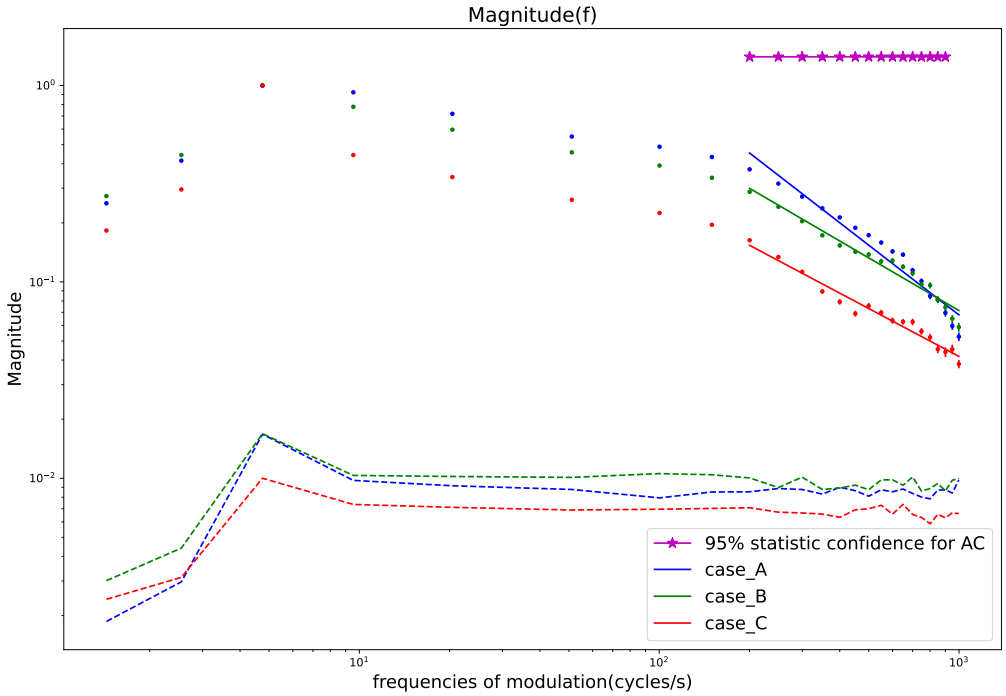

Figure 149: An example of a neuronal model, the L4_PC_cADpyr230_4, which even if the slopes are different the Richardson is not present since the gain amplitude of the case A is bigger than all the others. The gain values are normalised over their maximum located around the $f_{mod} \sim 5$Hz. The magenta line and the stars indicate for each f_{mod} value that the cases A and C, are not superimposable at the 95% of significance of the KS test. The solid lines of each color are the HF domain linear fit used to extrapolated the HF slope of the linear attenuation; the slopes values for each cases and neuronal models are in figure 70.

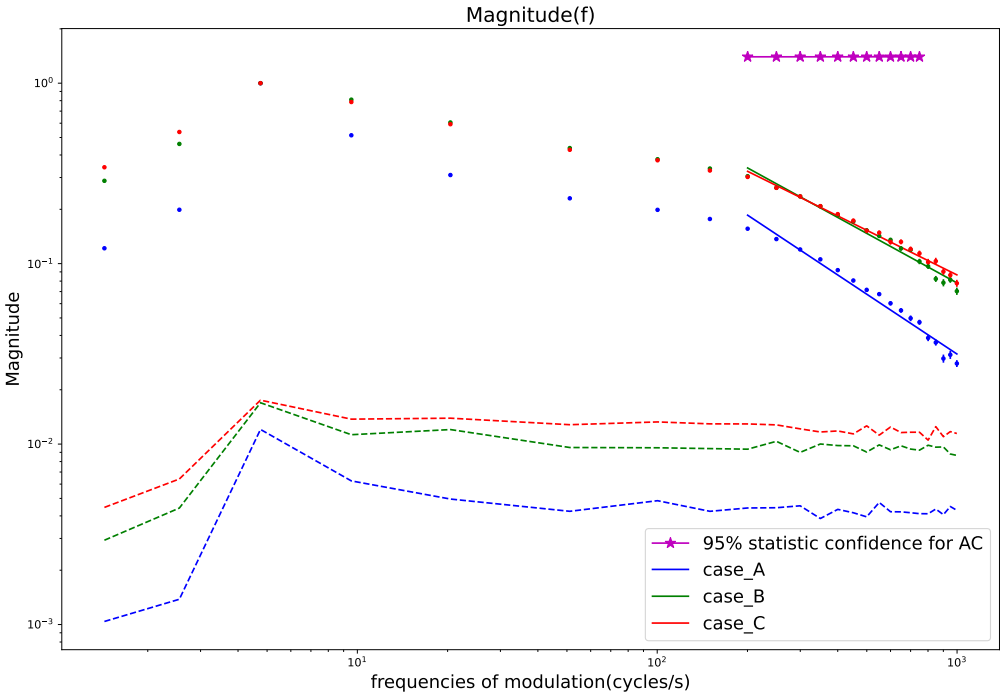

Figure 150: An example of a neuronal model, the L4_PC_cADpyr230_5, which even if the slopes are different the Richardson is not present since the gain amplitude of the case B is bigger than the case C. The gain values are normalised over their maximum located around the $f_{mod} \sim$ 5Hz. The magenta line and the stars indicate for each f_{mod} value that the cases A and C, are not superimposable at the 95% of significance of the KS test. The solid lines of each color are the HF domain linear fit used to extrapolated the HF slope of the linear attenuation; the slopes values for each cases and neuronal models are in figure 70.

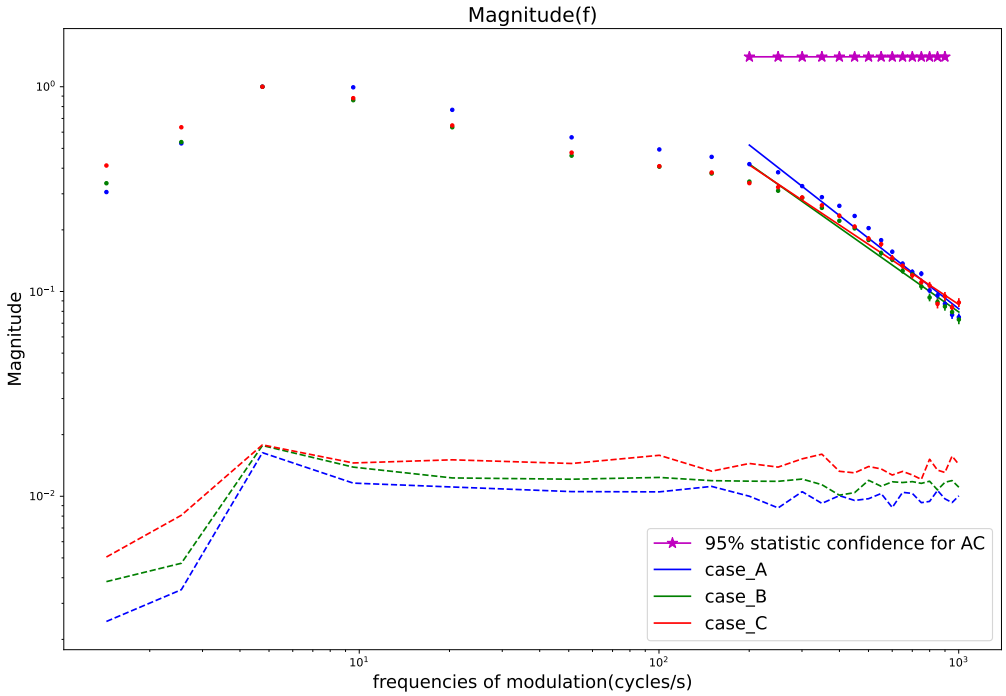

Figure 151: An example of a neuronal model, the L4_SP_cADpyr230_2, which even if the slopes are different the Richardson is not present since the gain amplitude of the case A is bigger than the others around 200 Cycles/s. The gain values are normalised over their maximum located around the $f_{mod} \sim 5$Hz. The magenta line and the stars indicate for each f_{mod} value that the cases A and C, are not superimposable at the 95% of significance of the KS test. The solid lines of each color are the HF domain linear fit used to extrapolated the HF slope of the linear attenuation; the slopes values for each cases and neuronal models are in figure 70.

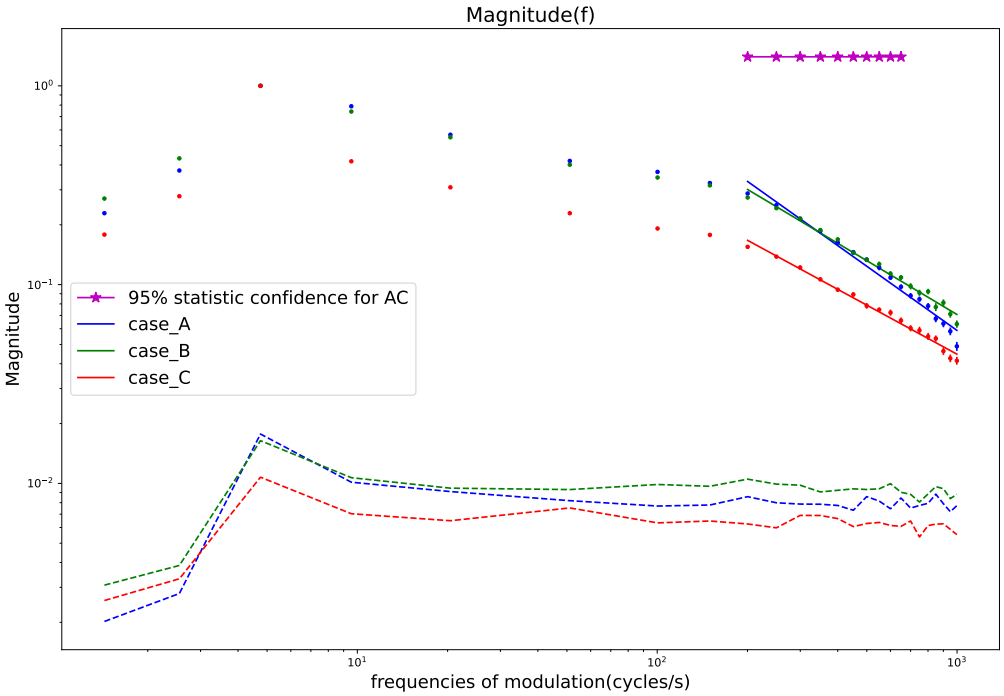

Figure 152: An example of a neuronal model, the L4_SP_cADpyr230_3, which even if the slopes are different the Richardson is not present since the gain amplitude of the case A is bigger than the others around 200 cycles/s. The gain values are normalised over their maximum located around the $f_{mod} \sim 5$Hz. The magenta line and the stars indicate for each f_{mod} value that the cases A and C, are not superimposable at the 95% of significance of the KS test. The solid lines of each color are the HF domain linear fit used to extrapolated the HF slope of the linear attenuation; the slopes values for each cases and neuronal models are in figure 70.

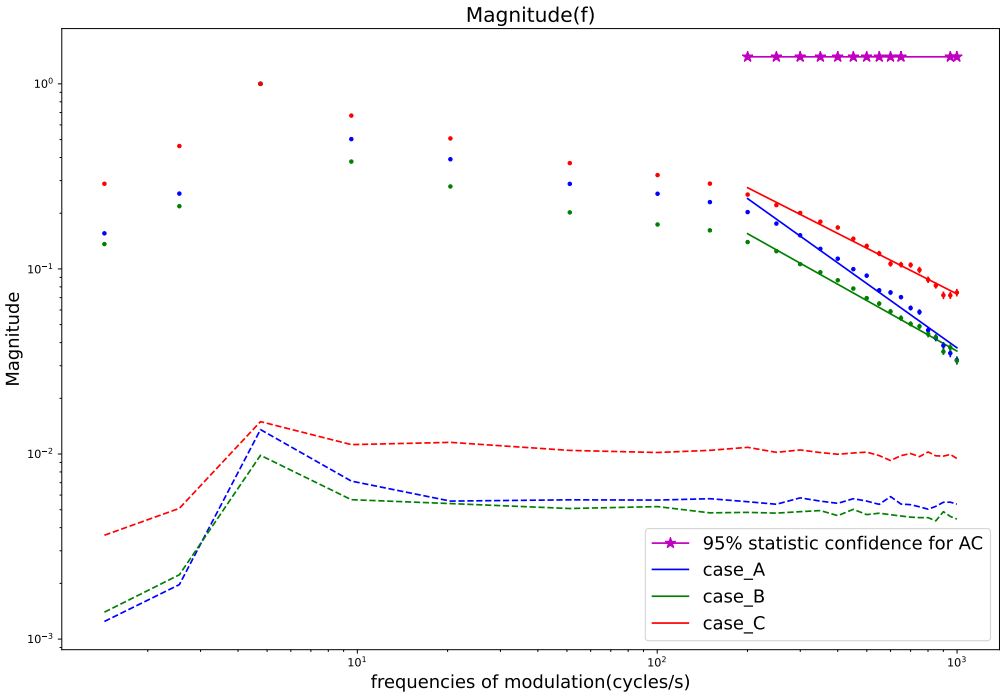

Figure 153: An example of a neuronal model, the L4_SP_cADpyr230_4, which even if the slopes are different the Richardson is not present since the gain amplitude of the case A is bigger than the case B. The gain values are normalised over their maximum located around the $f_{mod} \sim$ 5Hz. The magenta line and the stars indicate for each f_{mod} value that the cases A and C, are not superimposable at the 95% of significance of the KS test. The solid lines of each color are the HF domain linear fit used to extrapolated the HF slope of the linear attenuation; the slopes values for each cases and neuronal models are in figure 70.

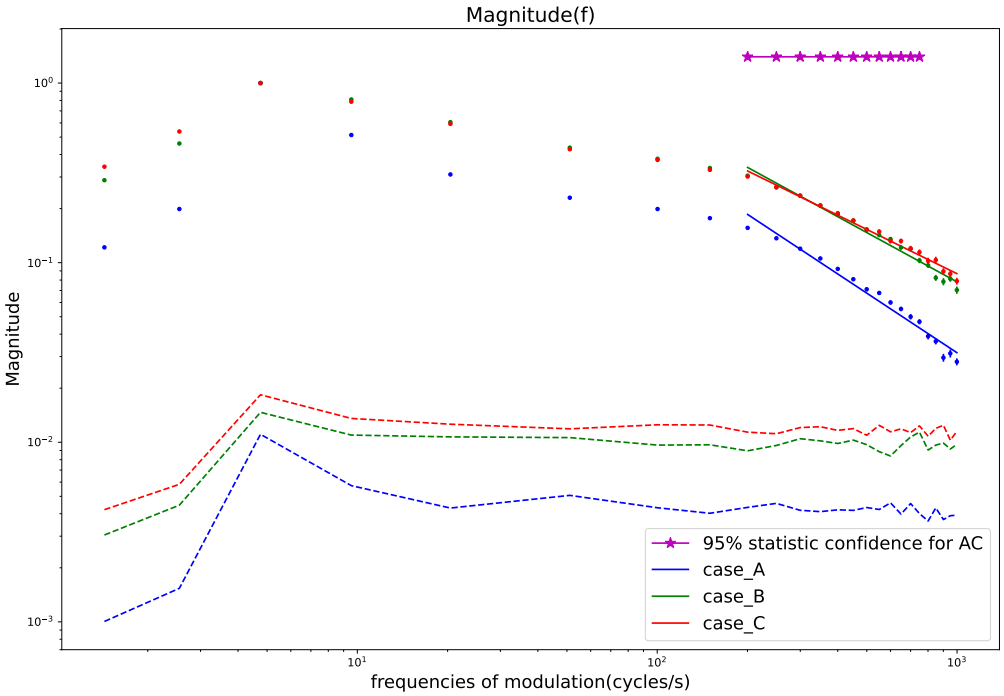

Figure 154: An example of a neuronal model, the L4_SP_cADpyr230_5, which even if the slopes are different the Richardson is not present since the gain amplitude of the case B is bigger than the case C around 200 Hz. The gain values are normalised over their maximum located around the $f_{mod} \sim 5$Hz. The magenta line and the stars indicate for each f_{mod} value that the cases A and C, are not superimposable at the 95% of significance of the KS test. The solid lines of each color are the HF domain linear fit used to extrapolated the HF slope of the linear attenuation; the slopes values for each cases and neuronal models are in figure 70.

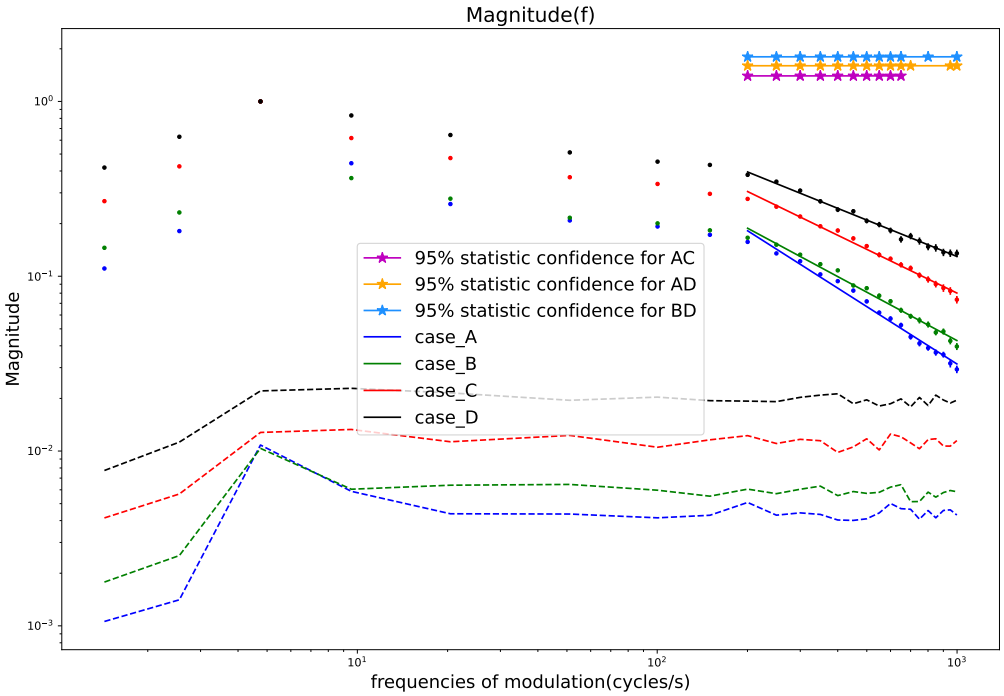

Figure 155: An example of a neuronal model, the L4_SS_cADpyr230_1, which shown the Richardson's effect at HF. The gain values are normalised over their maximum located around the $f_{mod} \sim$ 5Hz. The dashed lines stay for each cases as the minimal level of significance threshold. The magenta, yellow, blue lines and the stars indicate for each f_{mod} value that the cases A and C, A and D, B and D are not superimposable at the 95% of significance of the KS test. The solid lines of each color are the HF domain linear fit used to extrapolated the HF slope of the linear attenuation; the slopes values for each cases and neuronal models are in figure 70.

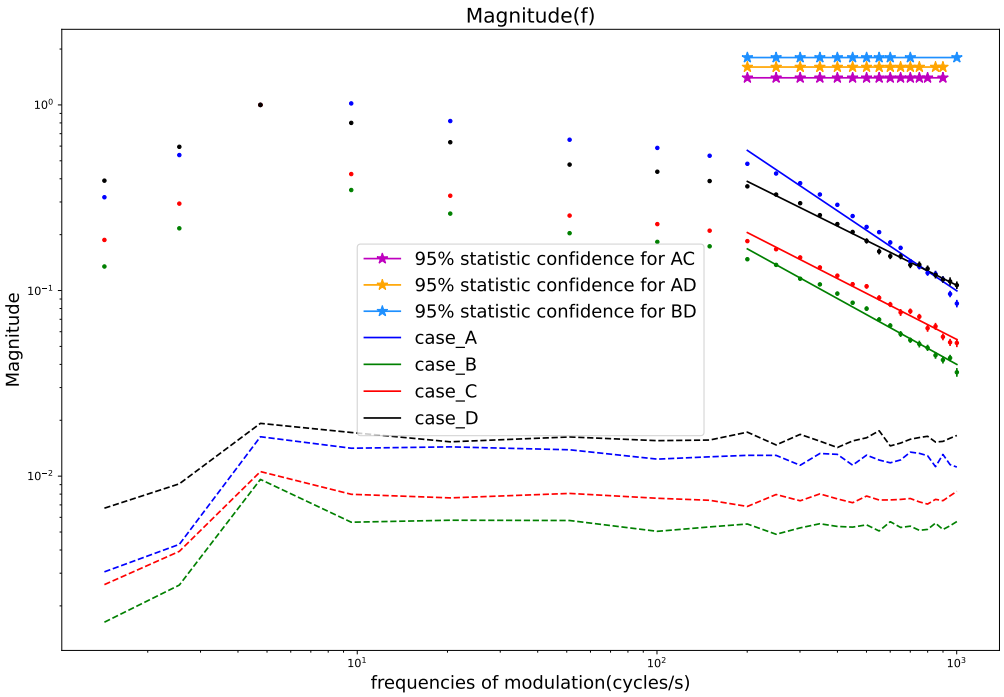

Figure 156: An example of a neuronal model, the L4_SS_cADpyr230_2, which doesn't have the RIchardson'effect since the amplitude of the case A is bigger than all the others. The gain values are normalised over their maximum located around the $f_{mod} \sim 5$Hz. The dashed lines stay for each cases as the minimal level of significance threshold. The magenta, yellow, blue lines and the stars indicate for each f_{mod} value that the cases A and C, A and D, B and D are not superimposable at the 95% of significance of the KS test. The solid lines of each color are the HF domain linear fit used to extrapolated the HF slope of the linear attenuation; the slopes values for each cases and neuronal models are in figure 70.

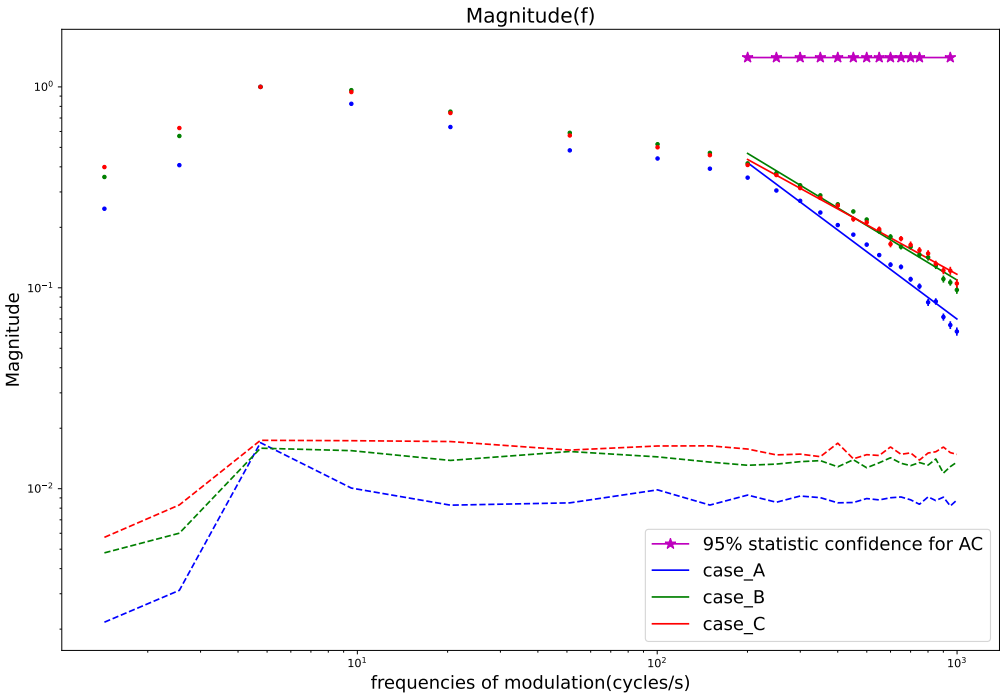

Figure 157: An example of a neuronal model, the L4_SS_cADpyr230_3, which doesn't have the RIchardson'effect since the amplitude of the case B is bigger than the case C ones. The gain values are normalised over their maximum located around the $f_{mod} \sim$ 5Hz. The dashed lines stay for each cases as the minimal level of significance threshold. The magenta line and the stars indicate for each f_{mod} value that the cases A and C are not superimposable at the 95% of significance of the KS test. The solid lines of each color are the HF domain linear fit used to extrapolated the HF slope of the linear attenuation; the slopes values for each cases and neuronal models are in figure 70.

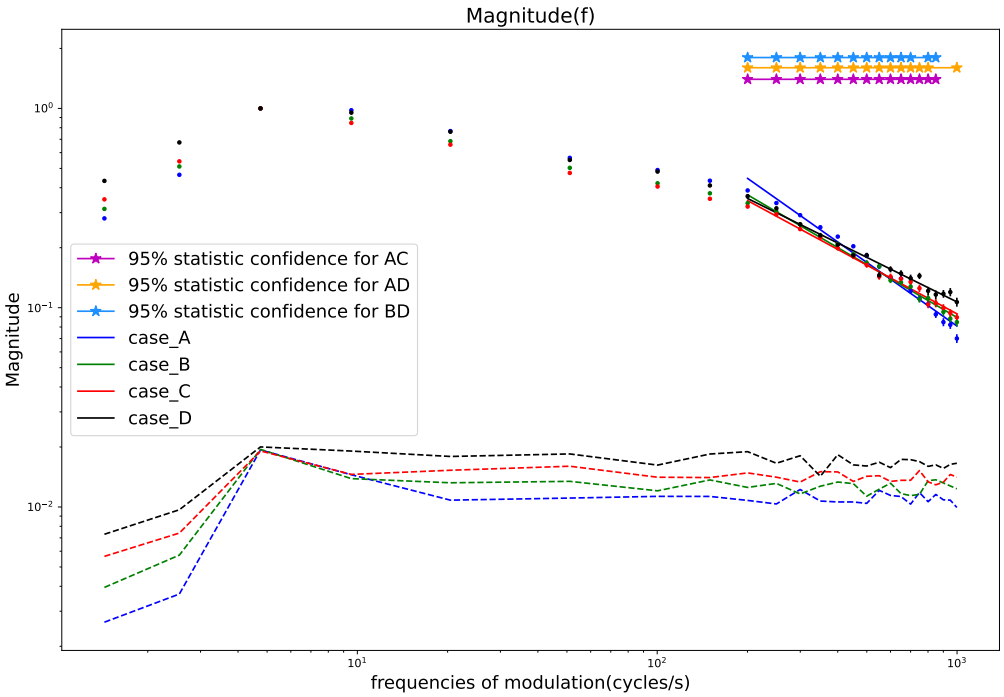

Figure 158: An example of a neuronal model, the L4_SS_cADpyr230_4, which doesn't have the RIchardson'effect since the amplitude of the case A is bigger than all the others. The gain values are normalised over their maximum located around the $f_{mod} \sim$ 5Hz. The dashed lines stay for each cases as the minimal level of significance threshold. The magenta,yellow and blue lines and the stars indicate for each f_{mod} value that the cases A and C,A and D and B and D are not superimposable at the 95% of significance of the KS test. The solid lines of each color are the HF domain linear fit used to extrapolated the HF slope of the linear attenuation; the slopes values for each cases and neuronal models are in figure 70.

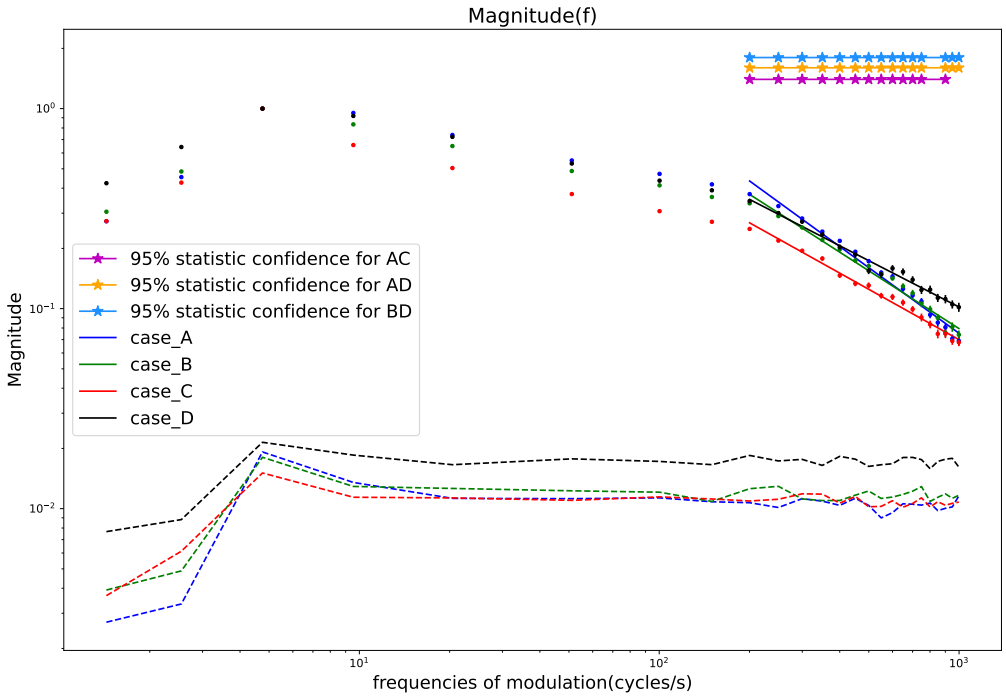

Figure 159: An example of a neuronal model, the L4_SS_cADpyr230_5, which doesn't have the RIchardson'effect since the amplitude of the case A is bigger than all the others. The gain values are normalised over their maximum located around the $f_{mod} \sim$ 5Hz. The dashed lines stay for each cases as the minimal level of significance threshold. The magenta,yellow and blue lines and the stars indicate for each f_{mod} value that the cases A and C,A and D and B and D are not superimposable at the 95% of significance of the KS test. The solid lines of each color are the HF domain linear fit used to extrapolated the HF slope of the linear attenuation; the slopes values for each cases and neuronal models are in figure 70.

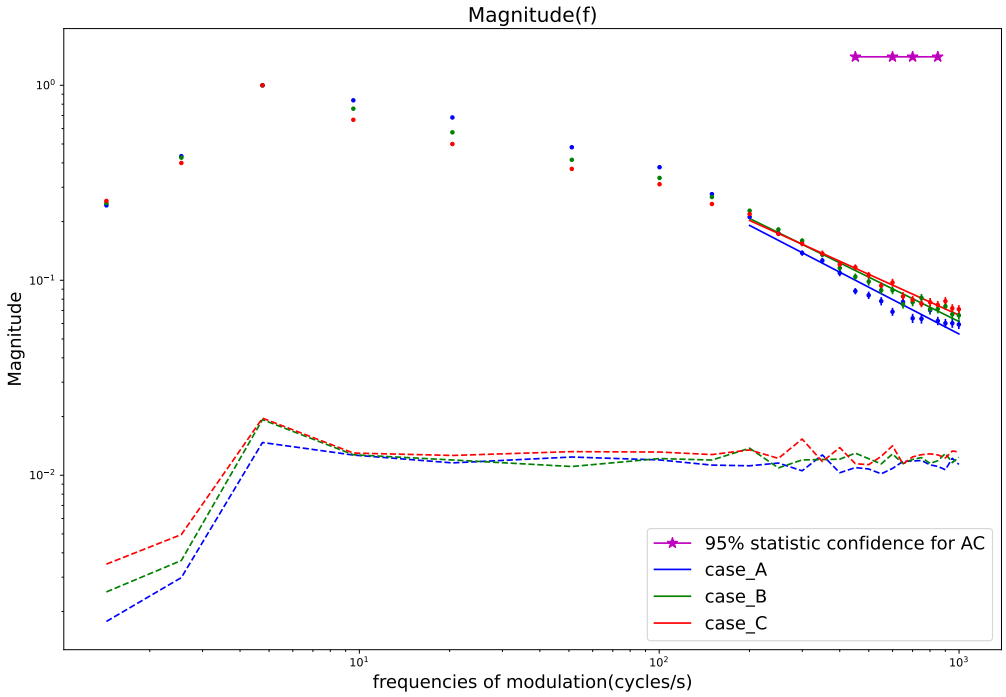

Figure 160: An example of a neuronal model, the L5_STPC_cADpyr232_1, which shown a tiny presence of the Richardson's effect at HF. The gain values are normalised over their maximum located around the $f_{mod} \sim 5$Hz. The dashed lines stay for each cases as the minimal level of significance threshold. The magenta line and the stars indicate for each f_{mod} value that the cases A and C are not superimposable at the 95% of significance of the KS test. The solid lines of each color are the HF domain linear fit used to extrapolated the HF slope of the linear attenuation; the slopes values for each cases and neuronal models are in figure 70.

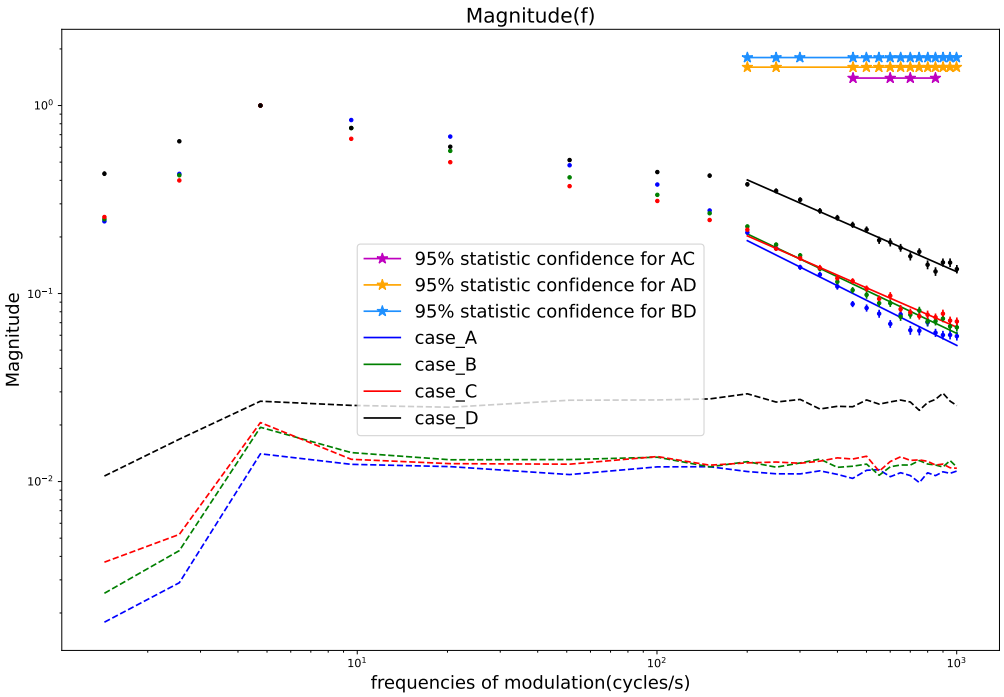

Figure 161: An example of a neuronal model, the L5_STPC_cADpyr232_2, which shown a tiny presence of the Richardson's effect at HF between the case and and C, but however a good evidence of it for the case D. The gain values are normalised over their maximum located around the $f_{mod} \sim 5$Hz. The dashed lines stay for each cases as the minimal level of significance threshold. The magenta line and the stars indicate for each f_{mod} value that the cases A and C are not superimposable at the 95% of significance of the KS test. The solid lines of each color are the HF domain linear fit used to extrapolated the HF slope of the linear attenuation; the slopes values for each cases and neuronal models are in figure 70.

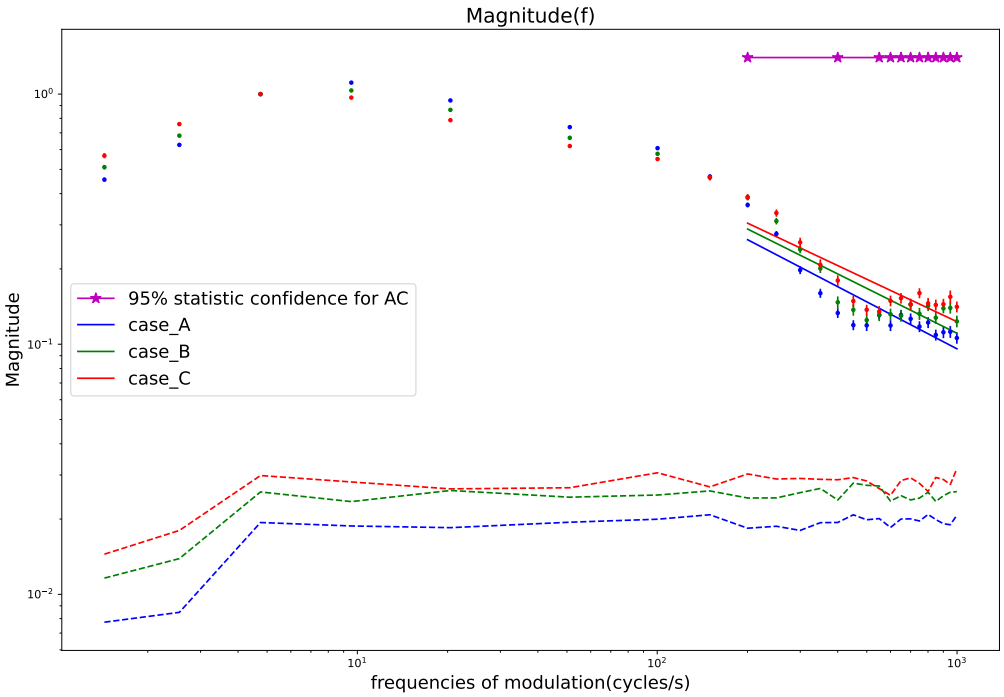

Figure 162: An example of a neuronal model, the L5_STPC_cADpyr232_3, which doesn't shown the Richardson's effect since all the line are parallel, hence the slopes aren't distinguishable. The gain values are normalised over their maximum located around the $f_{mod} \sim$ 5Hz. The dashed lines stay for each cases as the minimal level of significance threshold. The magenta line and the stars indicate for each f_{mod} value that the cases A and C are not superimposable at the 95% of significance of the KS test. The solid lines of each color are the HF domain linear fit used to extrapolated the HF slope of the linear attenuation; the slopes values for each cases and neuronal models are in figure 70.

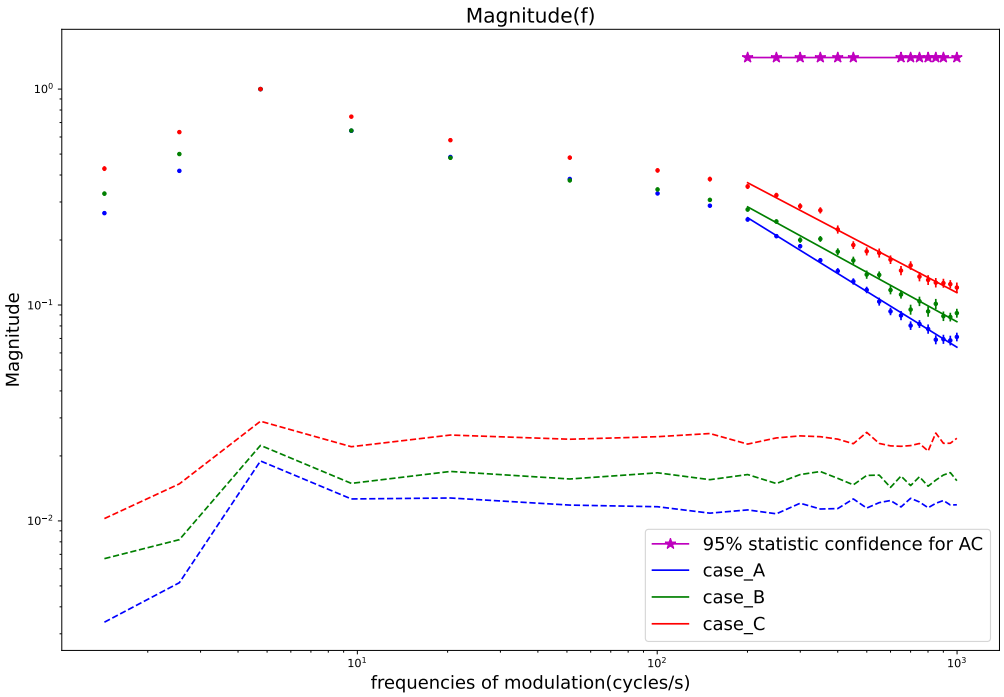

Figure 163: An example of a neuronal model, the L5_STPC_cADpyr232_4, which doesn't shown the Richardson's effect since all the line are parallel, hence the slopes aren't distinguishable. The gain values are normalised over their maximum located around the $f_{mod} \sim$ 5Hz. The dashed lines stay for each cases as the minimal level of significance threshold. The magenta line and the stars indicate for each f_{mod} value that the cases A and C are not superimposable at the 95% of significance of the KS test. The solid lines of each color are the HF domain linear fit used to extrapolated the HF slope of the linear attenuation; the slopes values for each cases and neuronal models are in figure 70.

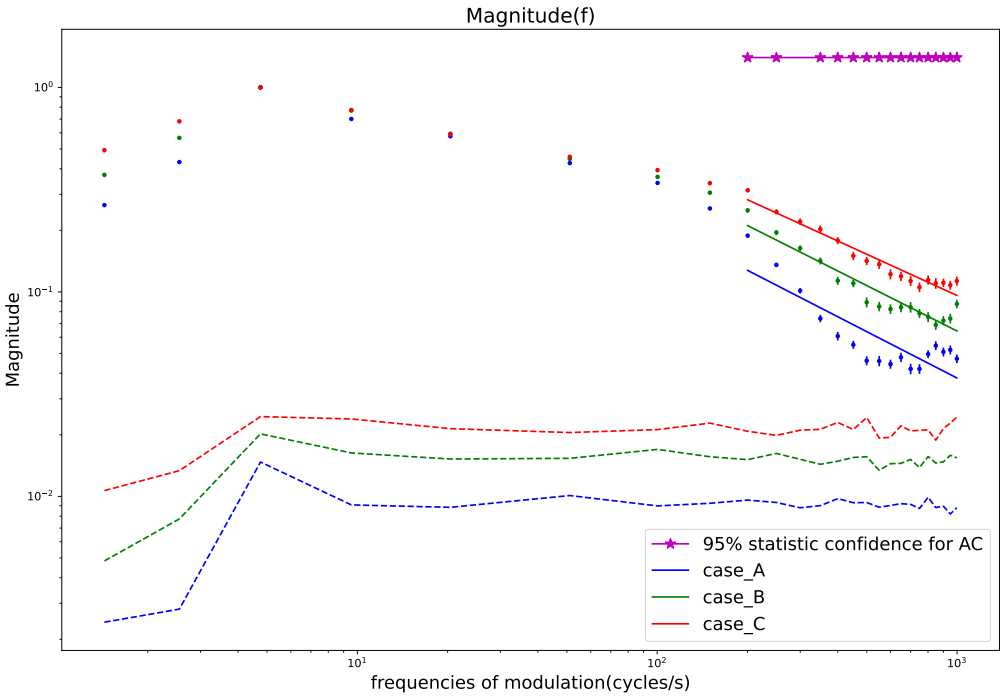

Figure 164: An example of a neuronal model, the L5_STPC_cADpyr232_5, which doesn't shown the Richardson's effect since all the line are parallel, hence the slopes aren't distinguishable. The gain values are normalised over their maximum located around the $f_{mod} \sim$ 5Hz. The dashed lines stay for each cases as the minimal level of significance threshold. The magenta line and the stars indicate for each f_{mod} value that the cases A and C are not superimposable at the 95% of significance of the KS test. The solid lines of each color are the HF domain linear fit used to extrapolated the HF slope of the linear attenuation; the slopes values for each cases and neuronal models are in figure 70.

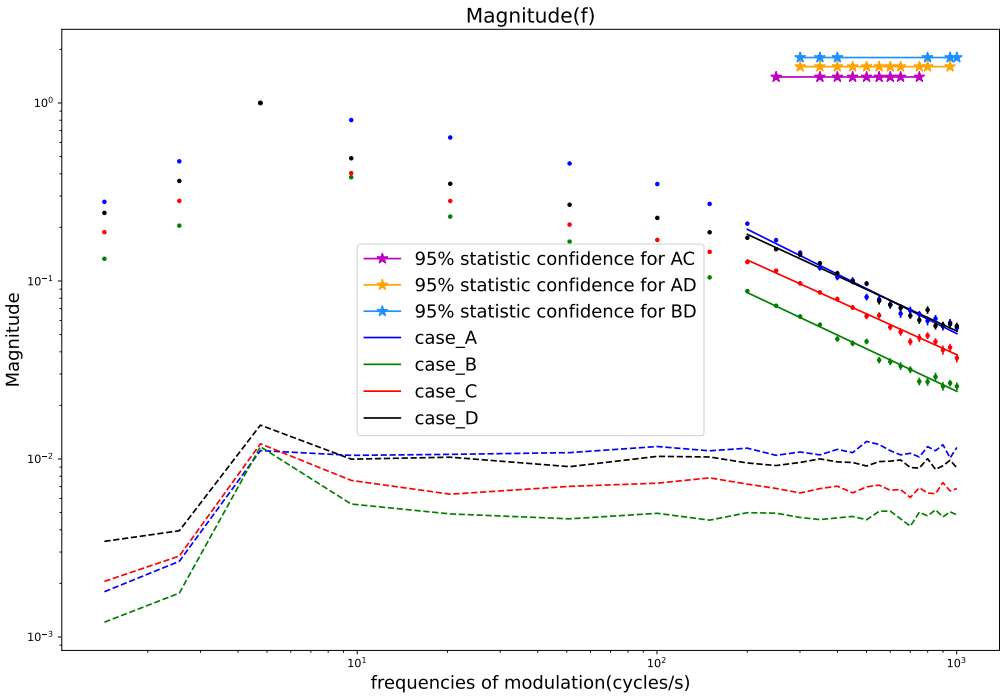

Figure 165: An example of a neuronal model, the L5_TTPC1_cADpyr232_2, which doesn't have the RIchardson'effect since the amplitude of the case A is bigger than all the others. The gain values are normalised over their maximum located around the $f_{mod} \sim$ 5Hz. The dashed lines stay for each cases as the minimal level of significance threshold. The magenta,yellow and blue lines and the stars indicate for each f_{mod} value that the cases A and C, A and D and B and D are not superimposable at the 95% of significance of the KS test. The solid lines of each color are the HF domain linear fit used to extrapolated the HF slope of the linear attenuation; the slopes values for each cases and neuronal models are in figure 70.

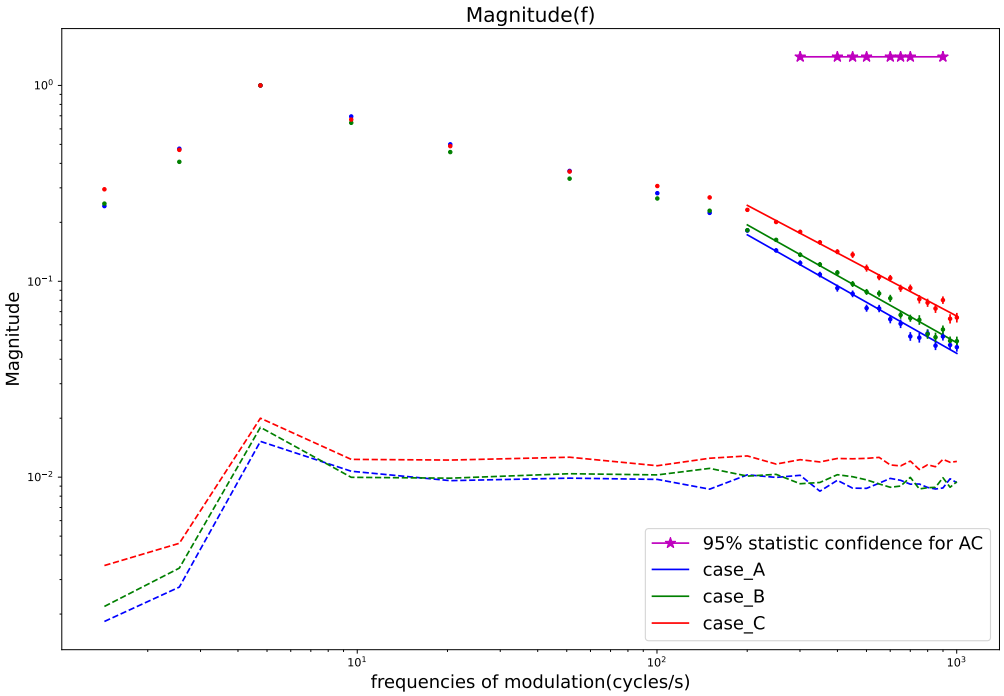

Figure 166: An example of a neuronal model, the L5_TTPC1_cADpyr232_3, hich shown a tiny presence of the Richardson's effect at HF. The gain values are normalised over their maximum located around the $f_{mod} \sim 5$Hz. The dashed lines stay for each cases as the minimal level of significance threshold. The magenta line and the stars indicate for each f_{mod} value that the cases A and C are not superimposable at the 95% of significance of the KS test. The solid lines of each color are the HF domain linear fit used to extrapolated the HF slope of the linear attenuation; the slopes values for each cases and neuronal models are in figure 70.

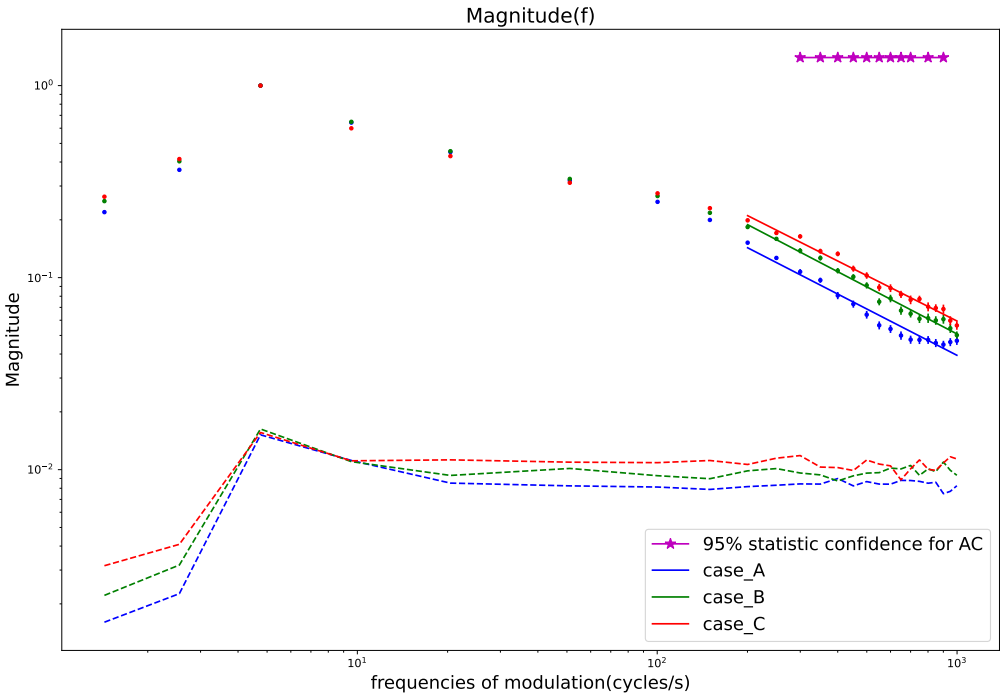

Figure 167: An example of a neuronal model, the L5_TTPC1_cADpyr232_4, hich doesn't shown the Richardson's effect since all the line are parallel, hence the slopes aren't distinguishable. The gain values are normalised over their maximum located around the $f_{mod} \sim$ 5Hz. The dashed lines stay for each cases as the minimal level of significance threshold. The magenta line and the stars indicate for each f_{mod} value that the cases A and C, are not superimposable at the 95% of significance of the KS test. The solid lines of each color are the HF domain linear fit used to extrapolated the HF slope of the linear attenuation; the slopes values for each cases and neuronal models are in figure 70.

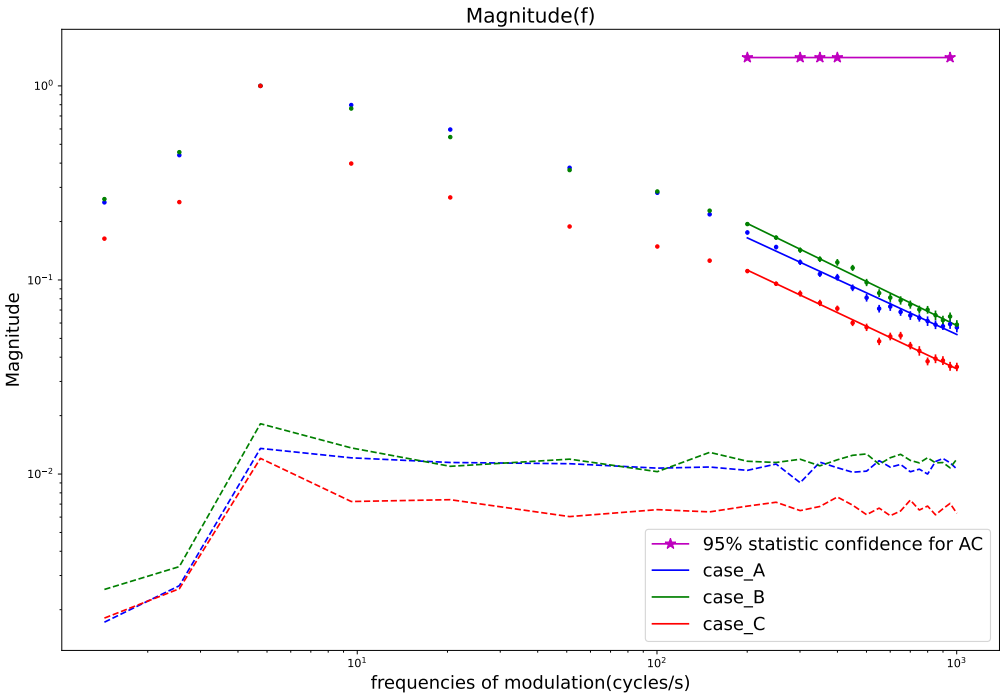

Figure 168: An example of a neuronal model, the L5_TTPC2_cADpyr232_1, which doesn't shown the Richardson's effect since the amplitude of the case C is smallest instead of being the biggest. The gain values are normalised over their maximum located around the $f_{mod} \sim$ 5Hz. The dashed lines stay for each cases as the minimal level of significance threshold. The magenta line and the stars indicate for each f_{mod} value that the cases A and C, are not superimposable at the 95% of significance of the KS test. The solid lines of each color are the HF domain linear fit used to extrapolated the HF slope of the linear attenuation; the slopes values for each cases and neuronal models are in figure 70.

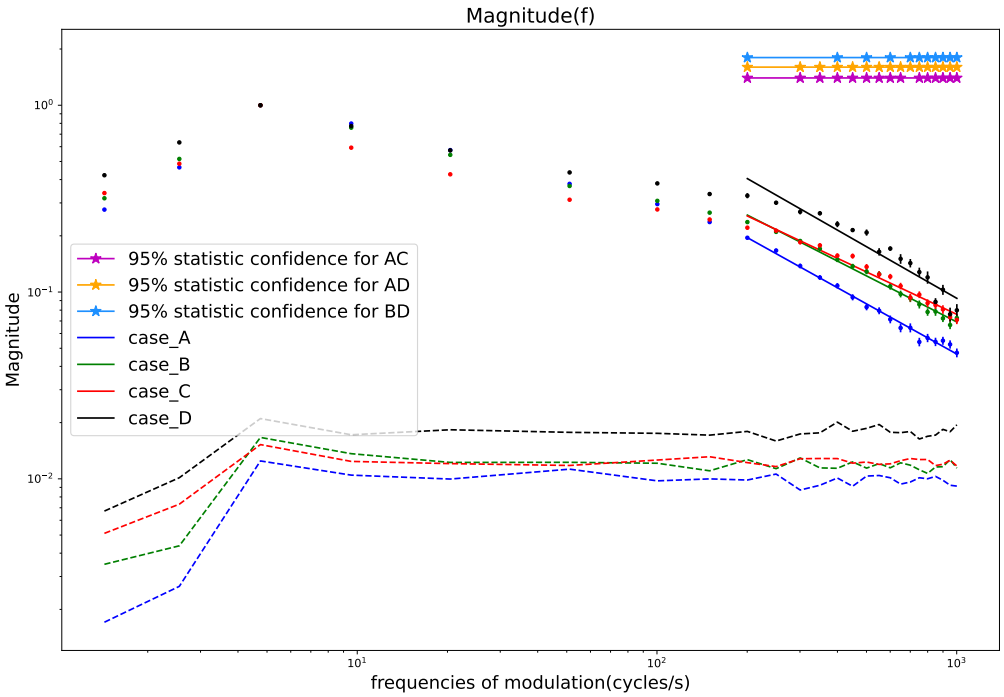

Figure 169: An example of a neuronal model, the L5_TTPC2_cADpyr232_2, which shown the Richardson's effect for exception the case D that has an higher slopes than other and not distinguishable from the case A. The gain values are normalised over their maximum located around the $f_{mod} \sim$ 5Hz. The dashed lines stay for each cases as the minimal level of significance threshold. The magenta, yellow and blue lines and the stars indicate for each f_{mod} value that the cases A and C, A and D and B and D, are not superimposable at the 95% of significance of the KS test. The solid lines of each color are the HF domain linear fit used to extrapolated the HF slope of the linear attenuation; the slopes values for each cases and neuronal models are in figure 70.

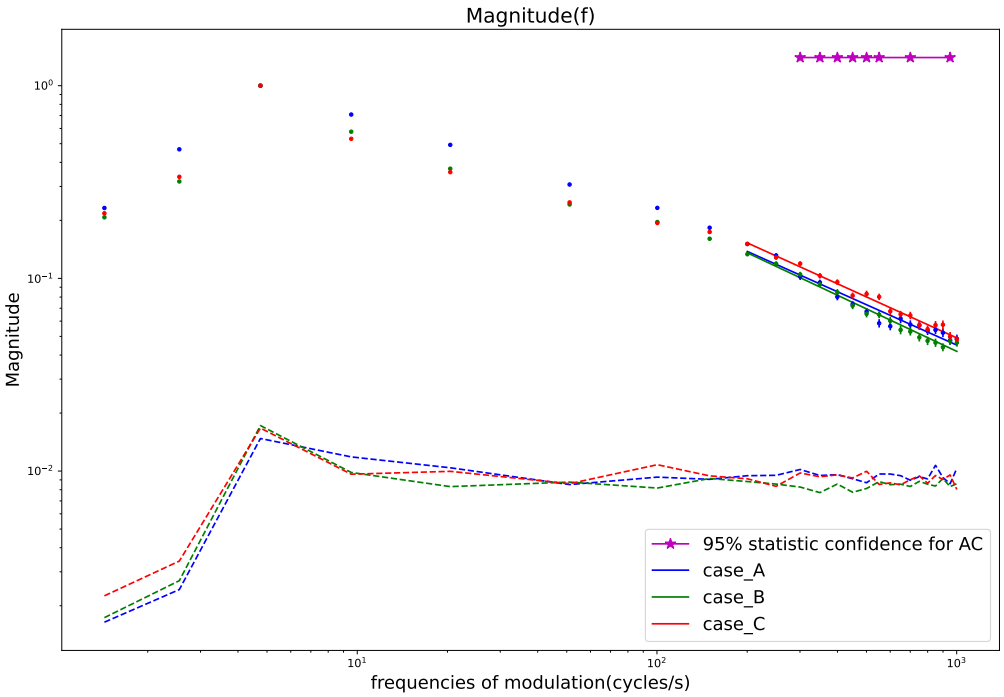

Figure 170: An example of a neuronal model, the L5_TTPC2_cADpyr232_3, which does not shown the Richardson effect, since the slops are not distinguishable. The gain values are normalised over their maximum located around the $f_{mod} \sim$ 5Hz. The dashed lines stay for each cases as the minimal level of significance threshold. The magenta, yellow and blue lines and the stars indicate for each f_{mod} value that the cases A and C, A and D and B and D, are not superimposable at the 95% of significance of the KS test. The solid lines of each color are the HF domain linear fit used to extrapolated the HF slope of the linear attenuation; the slopes values for each cases and neuronal models are in figure 70.

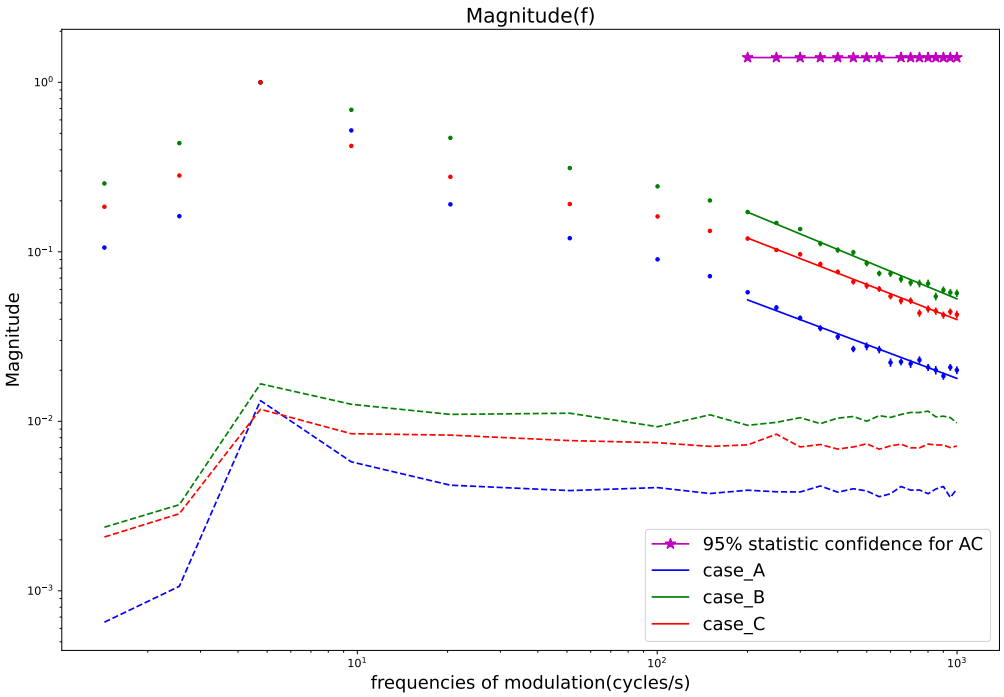

Figure 171: An example of a neuronal model, the L5_TTPC2_cADpyr232_4, which does not shown the Richardson effect, since the gain amplitude of the case B is bigger than the case C one. The gain values are normalised over their maximum located around the $f_{mod} \sim$ 5Hz. The dashed lines stay for each cases as the minimal level of significance threshold. The magenta, yellow and blue lines and the stars indicate for each f_{mod} value that the cases A and C, A and D and B and D, are not superimposable at the 95% of significance of the KS test. The solid lines of each color are the HF domain linear fit used to extrapolated the HF slope of the linear attenuation; the slopes values for each cases and neuronal models are in figure 70.

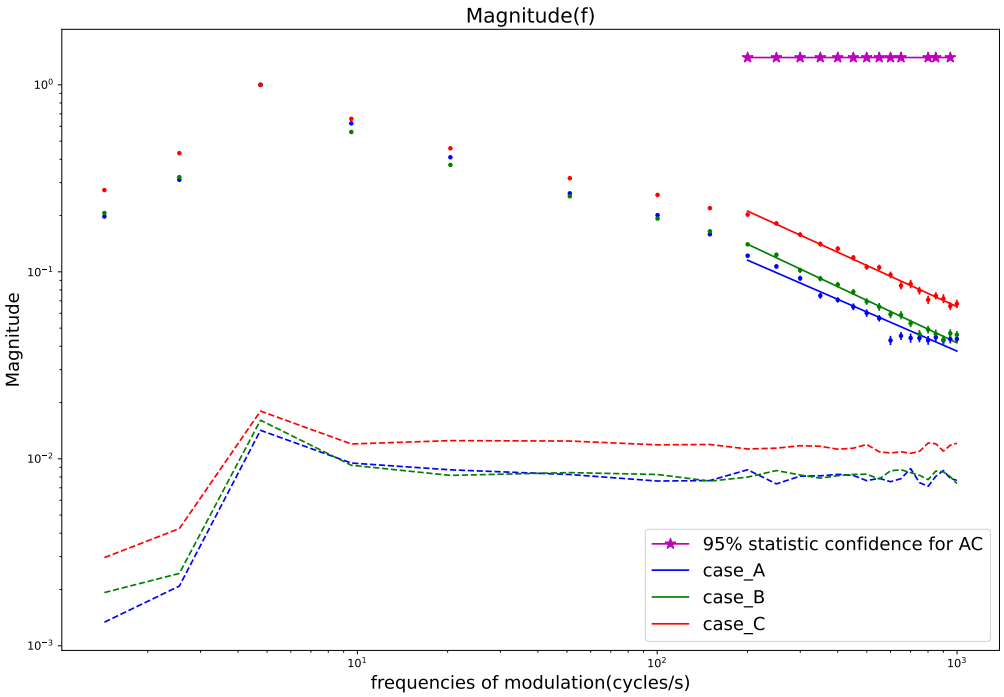

Figure 172: An example of a neuronal model, the L5_TTPC2_cADpyr232_5, which does not shown the Richardson effect, since the slopes are not distinguishable between each other. The gain values are normalised over their maximum located around the $f_{mod} \sim$ 5Hz. The dashed lines stay for each cases as the minimal level of significance threshold. The magenta, yellow and blue lines and the stars indicate for each f_{mod} value that the cases A and C, A and D and B and D, are not superimposable at the 95% of significance of the KS test. The solid lines of each color are the HF domain linear fit used to extrapolated the HF slope of the linear attenuation; the slopes values for each cases and neuronal models are in figure 70.

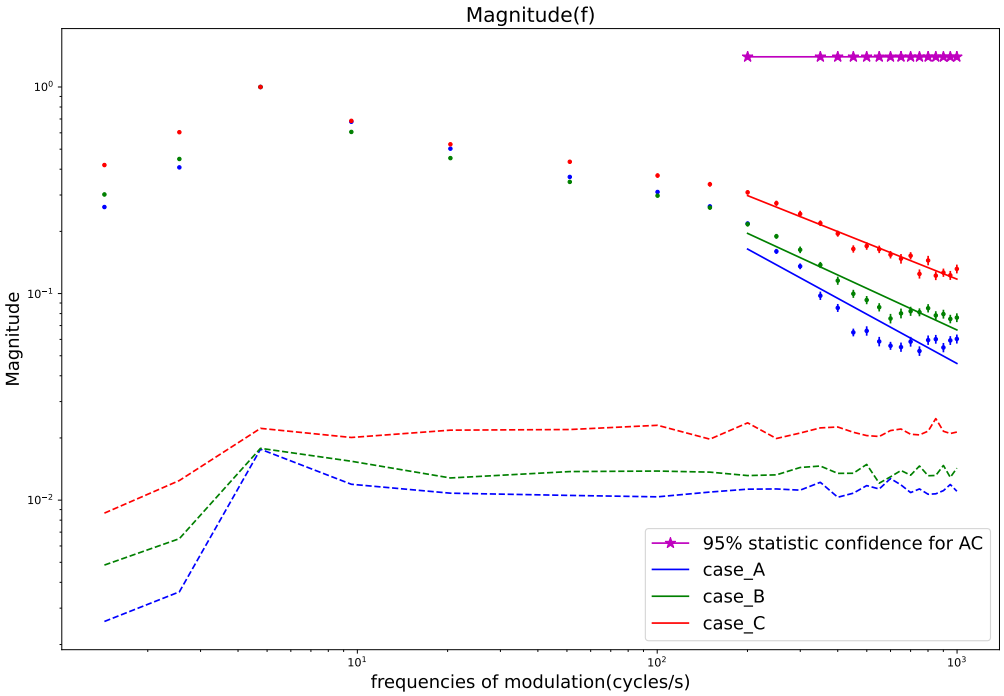

Figure 173: An example of a neuronal model, the L5_UTPC_cADpyr232_1, which shows the Richardson's effect. The gain values are normalised over their maximum located around the $f_{mod} \sim$ 5Hz. The dashed lines stay for each cases as the minimal level of significance threshold. The magenta, line and the stars indicate for each f_{mod} value that the cases A and C are not superimposable at the 95% of significance of the KS test. The solid lines of each color are the HF domain linear fit used to extrapolated the HF slope of the linear attenuation; the slopes values for each cases and neuronal models are in figure 70.

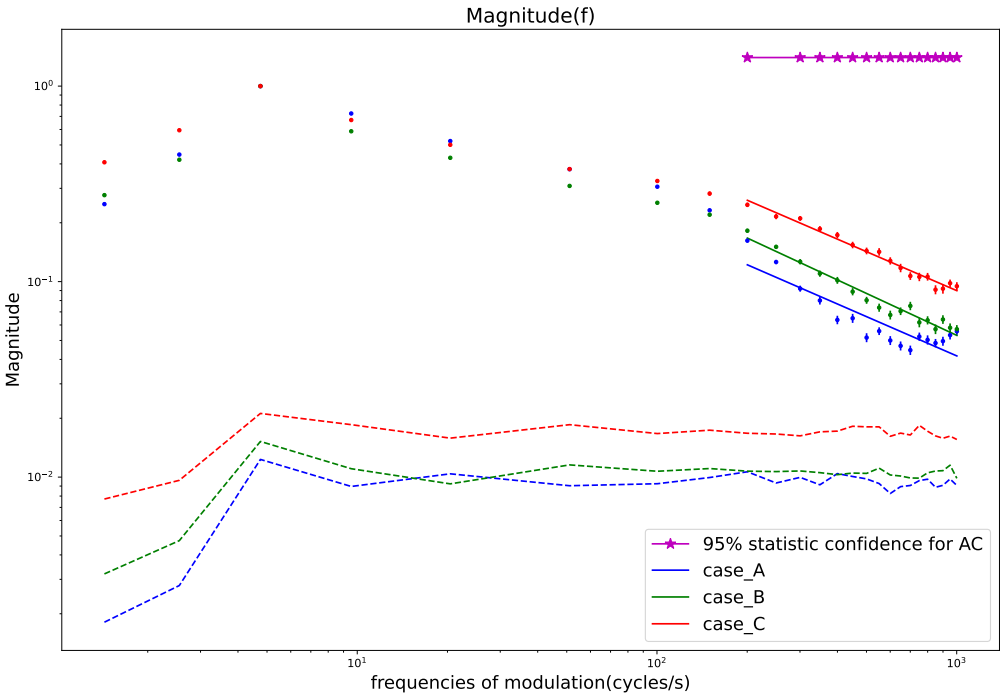

Figure 174: An example of a neuronal model, the L5_UTPC_cADpyr232_2, which doesn't shown the Richardson's effect since all the line are parallel, hence the slopes aren't distinguishable. The gain values are normalised over their maximum located around the $f_{mod} \sim$ 5Hz. The dashed lines stay for each cases as the minimal level of significance threshold. The magenta, line and the stars indicate for each f_{mod} value that the cases A and C are not superimposable at the 95% of significance of the KS test. The solid lines of each color are the HF domain linear fit used to extrapolated the HF slope of the linear attenuation; the slopes values for each cases and neuronal models are in figure 70.

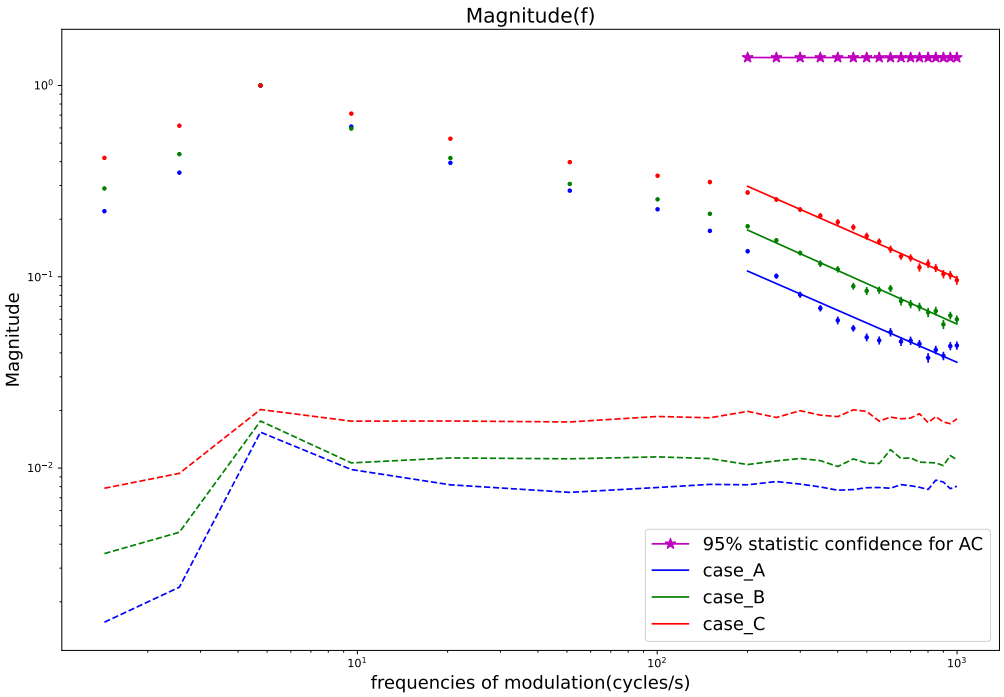

Figure 175: An example of a neuronal model, the L5_UTPC_cADpyr232_3, which doesn't shown the Richardson's effect since all the line are parallel, hence the slopes aren't distinguishable. The gain values are normalised over their maximum located around the $f_{mod} \sim$ 5Hz. The dashed lines stay for each cases as the minimal level of significance threshold. The magenta, line and the stars indicate for each f_{mod} value that the cases A and C are not superimposable at the 95% of significance of the KS test. The solid lines of each color are the HF domain linear fit used to extrapolated the HF slope of the linear attenuation; the slopes values for each cases and neuronal models are in figure 70.

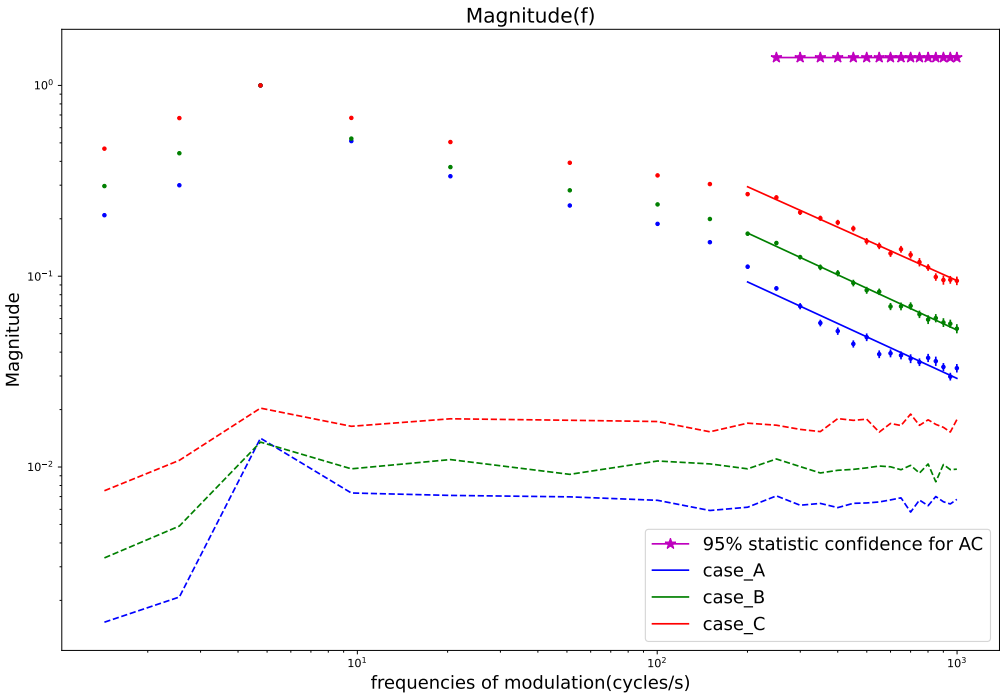

Figure 176: An example of a neuronal model, the L5_UTPC_cADpyr232_4, which doesn't shown the Richardson's effect since all the line are parallel, hence the slopes aren't distinguishable. The gain values are normalised over their maximum located around the $f_{mod} \sim$ 5Hz. The dashed lines stay for each cases as the minimal level of significance threshold. The magenta, line and the stars indicate for each f_{mod} value that the cases A and C are not superimposable at the 95% of significance of the KS test. The solid lines of each color are the HF domain linear fit used to extrapolated the HF slope of the linear attenuation; the slopes values for each cases and neuronal models are in figure 70.

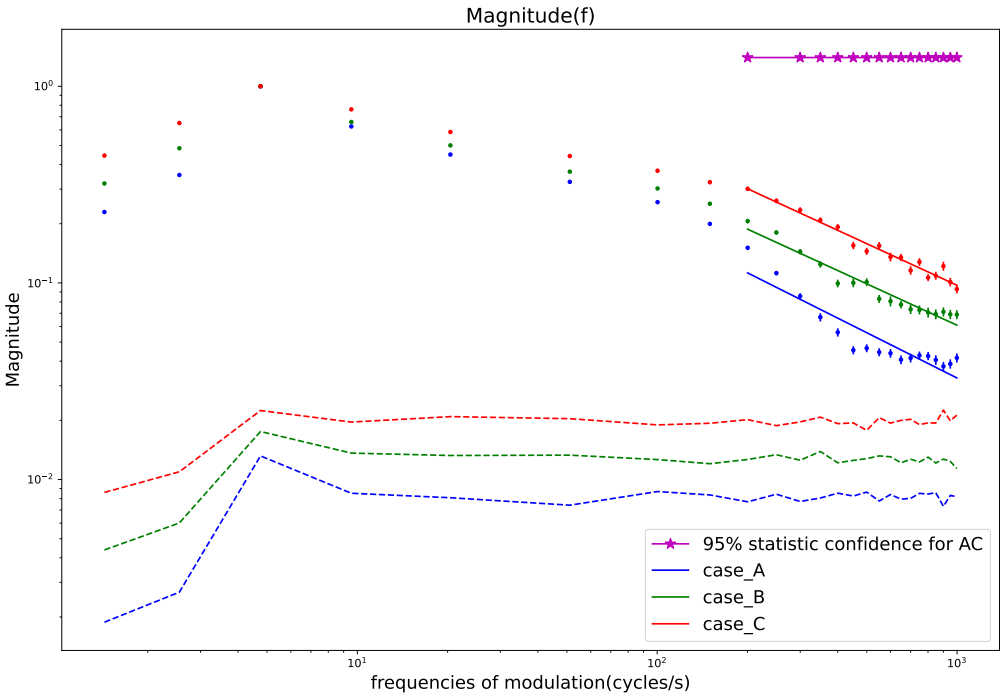

Figure 177: An example of a neuronal model, the L5_UTPC_cADpyr232_5, which doesn't shown the Richardson's effect since all the line are parallel, hence the slopes aren't distinguishable. The gain values are normalised over their maximum located around the $f_{mod} \sim$ 5Hz. The dashed lines stay for each cases as the minimal level of significance threshold. The magenta, line and the stars indicate for each f_{mod} value that the cases A and C are not superimposable at the 95% of significance of the KS test. The solid lines of each color are the HF domain linear fit used to extrapolated the HF slope of the linear attenuation; the slopes values for each cases and neuronal models are in figure 70.

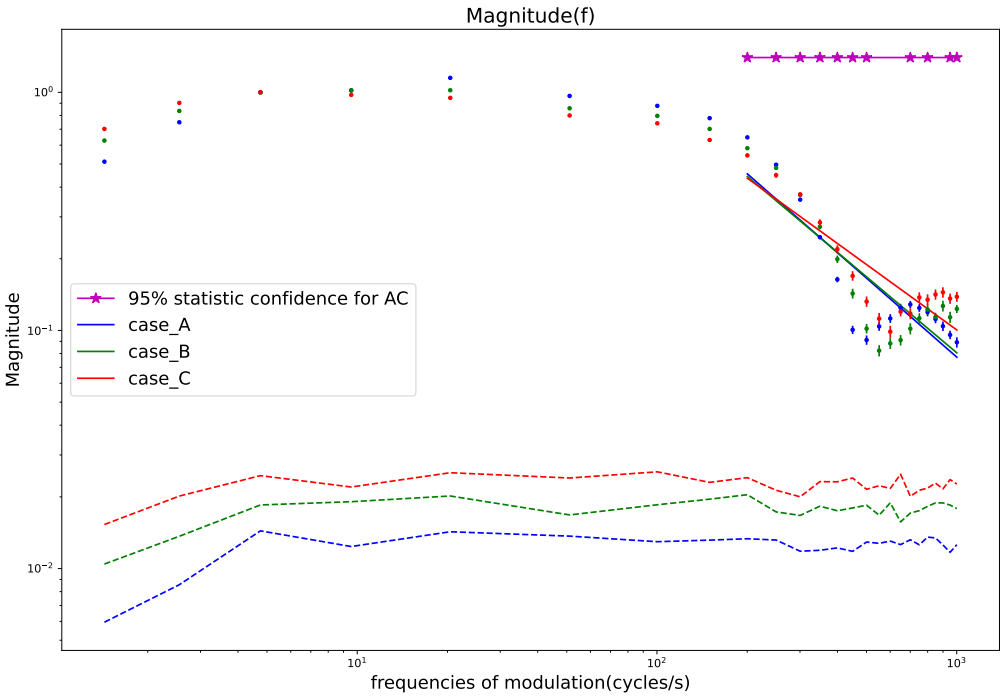

Figure 178: An example of a neuronal model, the L6_BPC_cADpyr231_2, which doesn't shown the Richardson's effect since the case B amplitude is bigger than case one. The gain values are normalised over their maximum located around the $f_{mod} \sim$ 5Hz. The dashed lines stay for each cases as the minimal level of significance threshold. The magenta line and the stars indicate for each f_{mod} value that the cases A and C are not superimposable at the 95% of significance of the KS test. The solid lines of each color are the HF domain linear fit used to extrapolated the HF slope of the linear attenuation; the slopes values for each cases and neuronal models are in figure 70.

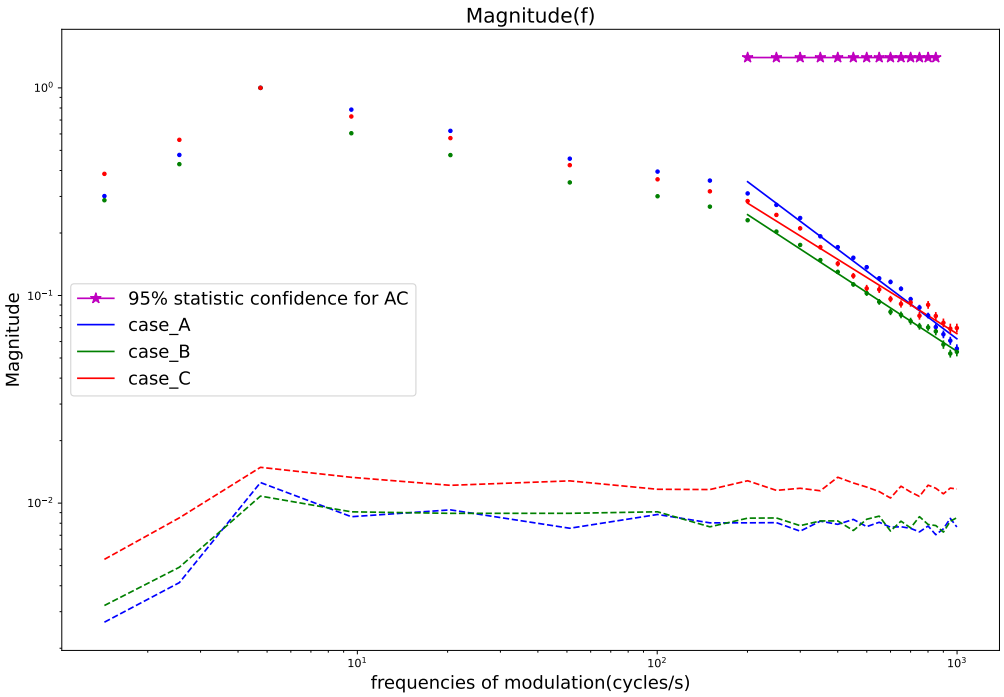

Figure 179: An example of a neuronal model, the L6_BPC_cADpyr231_3, which doesn't shown the Richardson's effect since the case A amplitude is bigger thanthe other ones. The gain values are normalised over their maximum located around the $f_{mod} \sim$ 5Hz. The dashed lines stay for each cases as the minimal level of significance threshold. The magenta line and the stars indicate for each f_{mod} value that the cases A and C are not superimposable at the 95% of significance of the KS test. The solid lines of each color are the HF domain linear fit used to extrapolated the HF slope of the linear attenuation; the slopes values for each cases and neuronal models are in figure 70.

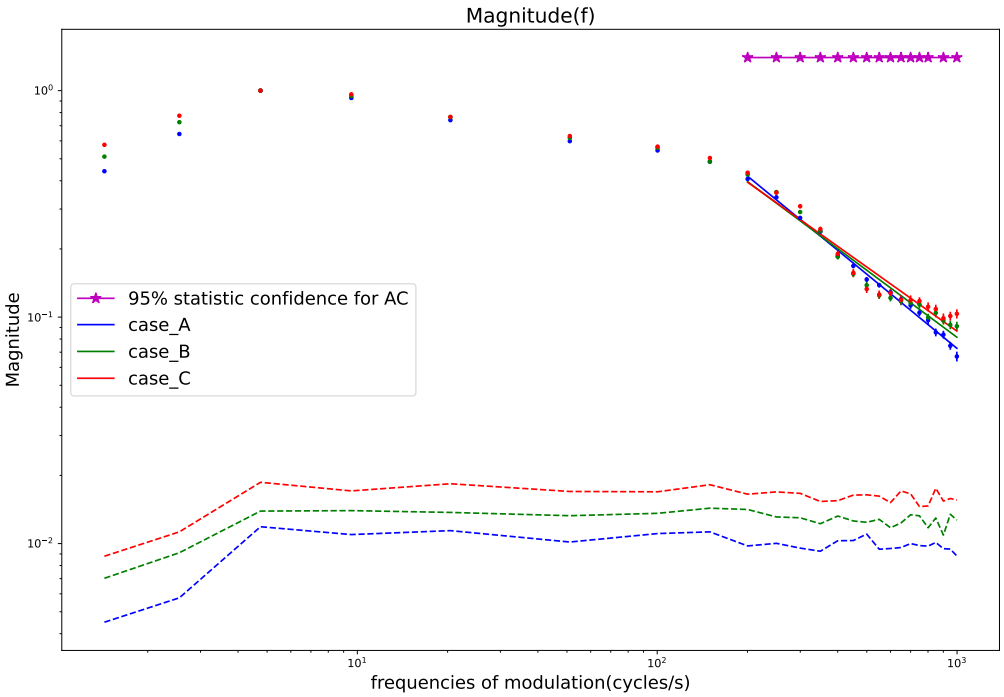

Figure 180: An example of a neuronal model, the L6_BPC_cADpyr231_4, which doesn't shown the Richardson's effect since the case A amplitude is bigger than the other ones. The gain values are normalised over their maximum located around the $f_{mod} \sim 5$Hz. The dashed lines stay for each cases as the minimal level of significance threshold. The magenta line and the stars indicate for each f_{mod} value that the cases A and C are not superimposable at the 95% of significance of the KS test. The solid lines of each color are the HF domain linear fit used to extrapolated the HF slope of the linear attenuation; the slopes values for each cases and neuronal models are in figure 70.

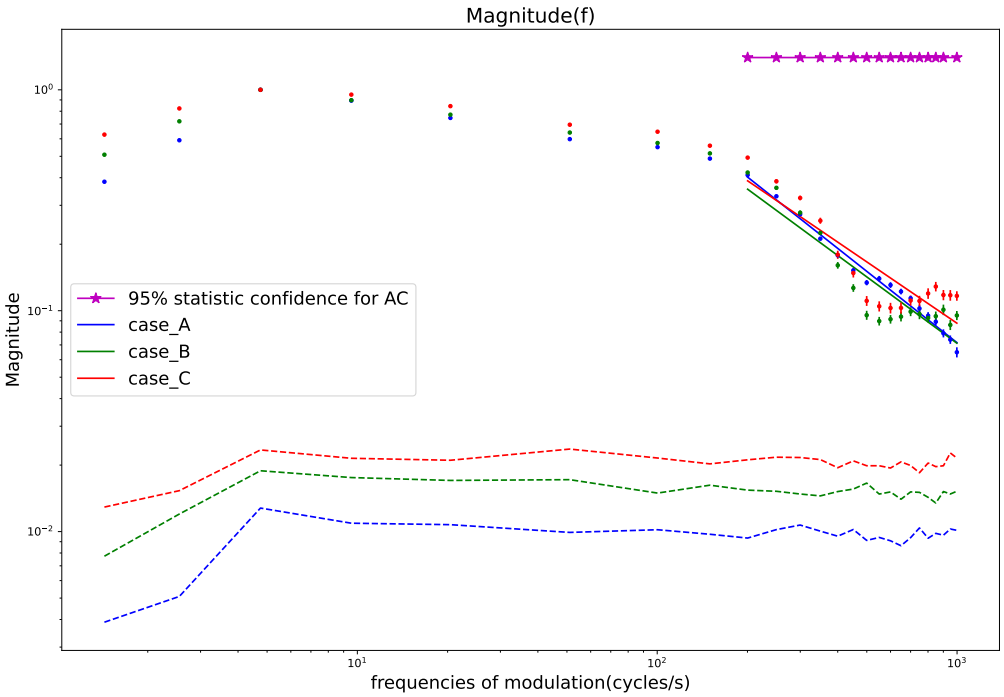

Figure 181: An example of a neuronal model, the L6_BPC_cADpyr231_5, which doesn't shown the Richardson's effect since the case A amplitude is bigger than the other ones. The gain values are normalised over their maximum located around the $f_{mod} \sim 5$Hz. The dashed lines stay for each cases as the minimal level of significance threshold. The magenta line and the stars indicate for each f_{mod} value that the cases A and C are not superimposable at the 95% of significance of the KS test. The solid lines of each color are the HF domain linear fit used to extrapolated the HF slope of the linear attenuation; the slopes values for each cases and neuronal models are in figure 70.

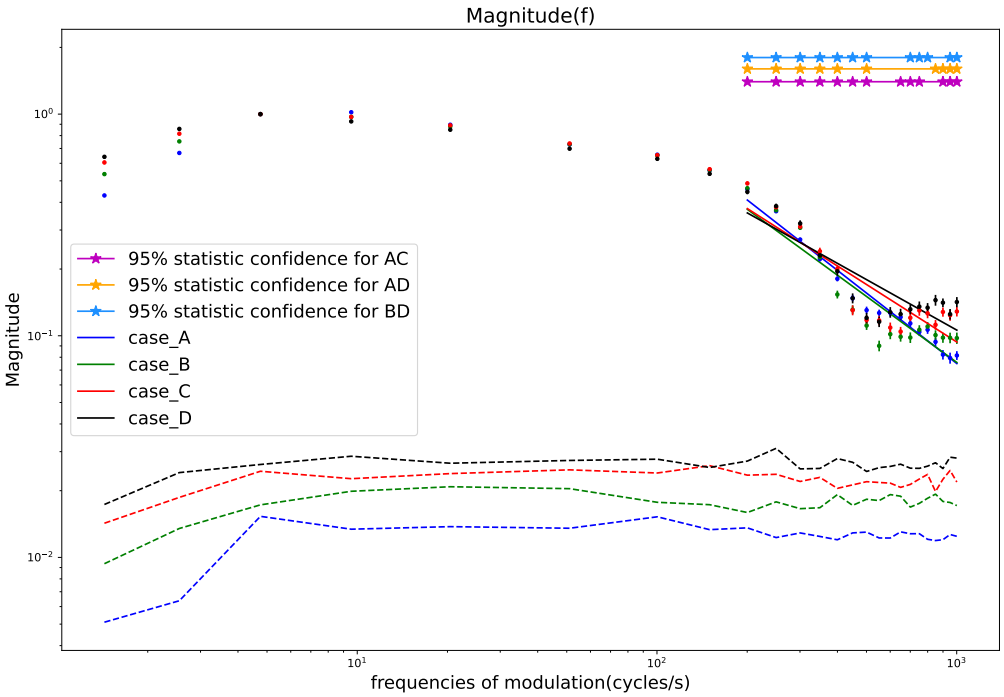

Figure 182: An example of a neuronal model, the L6_IPC_cADpyr231_1, which doesn't shown the Richardson's effect since the case A amplitude is bigger than the other ones. The gain values are normalised over their maximum located around the $f_{mod} \sim 5$Hz. The dashed lines stay for each cases as the minimal level of significance threshold. The magenta, yellow and blue lines and the stars indicate for each f_{mod} value that the cases A and C, A and D and B and D are not superimposable at the 95% of significance of the KS test. The solid lines of each color are the HF domain linear fit used to extrapolated the HF slope of the linear attenuation; the slopes values for each cases and neuronal models are in figure 70.

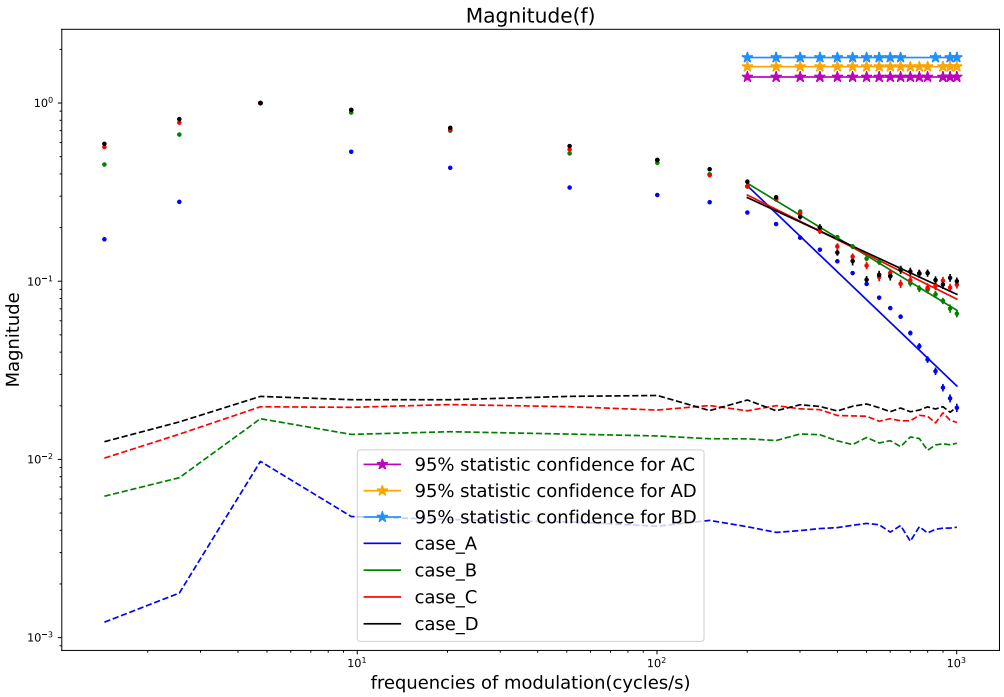

Figure 183: An example of a neuronal model, the L6_IPC_cADpyr231_2, which shows a tiny presence of the Richardson's effect at HF. The gain values are normalised over their maximum located around the $f_{mod} \sim 5$Hz. The dashed lines stay for each cases as the minimal level of significance threshold. The magenta, yellow and blue lines and the stars indicate for each f_{mod} value that the cases A and C, A and D and B and D are not superimposable at the 95% of significance of the KS test. The solid lines of each color are the HF domain linear fit used to extrapolated the HF slope of the linear attenuation; the slopes values for each cases and neuronal models are in figure 70.

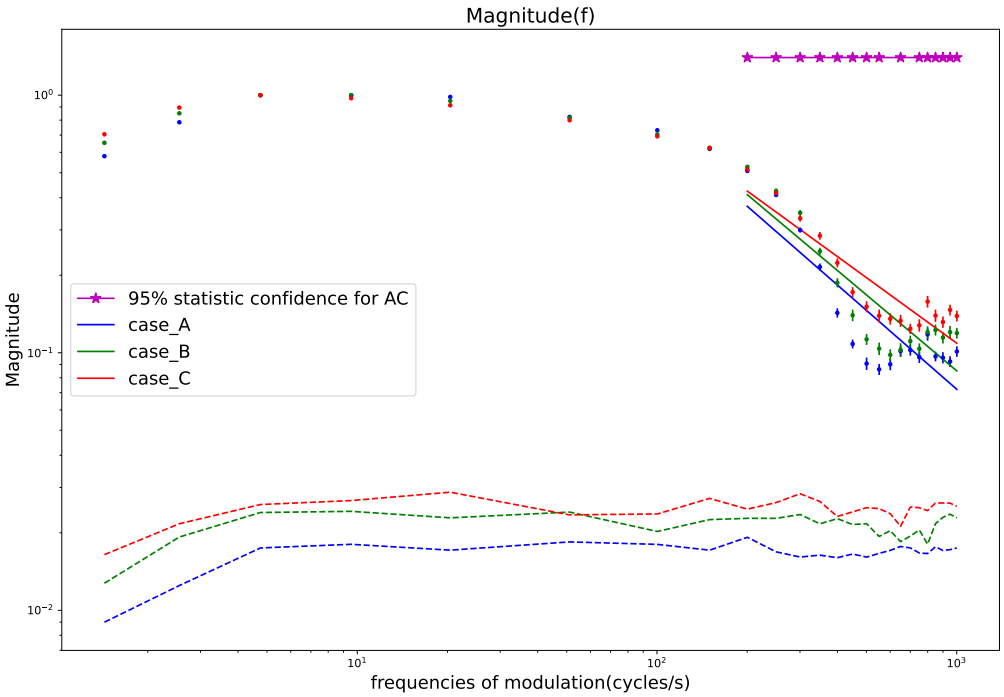

Figure 184: An example of a neuronal model, the L6_IPC_cADpyr231_3, which doesn't shown the Richardson's effect since the slopes of th straight lines are not distinguishable. The gain values are normalised over their maximum located around the $f_{mod} \sim$ 5Hz. The dashed lines stay for each cases as the minimal level of significance threshold. The magenta, yellow and blue lines and the stars indicate for each f_{mod} value that the cases A and C, A and D and B and D are not superimposable at the 95% of significance of the KS test. The solid lines of each color are the HF domain linear fit used to extrapolated the HF slope of the linear attenuation; the slopes values for each cases and neuronal models are in figure 70.

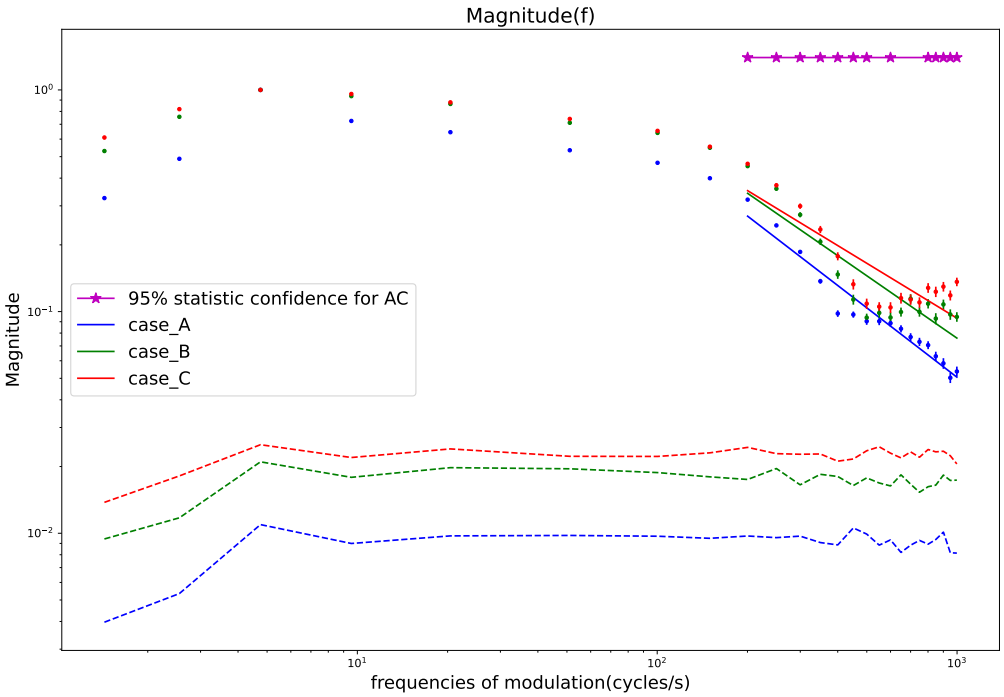

Figure 185: An example of a neuronal model, the L6_IPC_cADpyr231_4, which shows a tiny presence of the Richardson's effect at HF. The gain values are normalised over their maximum located around the $f_{mod} \sim 5$Hz. The dashed lines stay for each cases as the minimal level of significance threshold. The magenta, yellow and blue lines and the stars indicate for each f_{mod} value that the cases A and C, A and D and B and D are not superimposable at the 95% of significance of the KS test. The solid lines of each color are the HF domain linear fit used to extrapolated the HF slope of the linear attenuation; the slopes values for each cases and neuronal models are in figure 70.

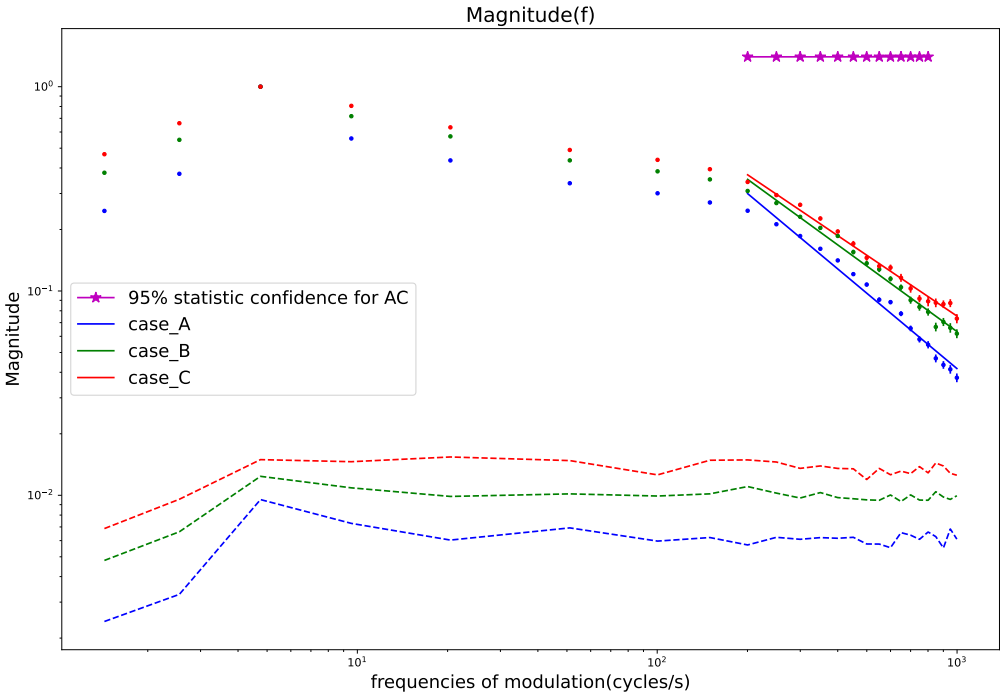

Figure 186: An example of a neuronal model, the L6_IPC_cADpyr231_5, which shows the Richardson's effect at HF. The gain values are normalised over their maximum located around the $f_{mod} \sim$ 5Hz. The dashed lines stay for each cases as the minimal level of significance threshold. The magenta, yellow and blue lines and the stars indicate for each f_{mod} value that the cases A and C, A and D and B and D are not superimposable at the 95% of significance of the KS test. The solid lines of each color are the HF domain linear fit used to extrapolated the HF slope of the linear attenuation; the slopes values for each cases and neuronal models are in figure 70.

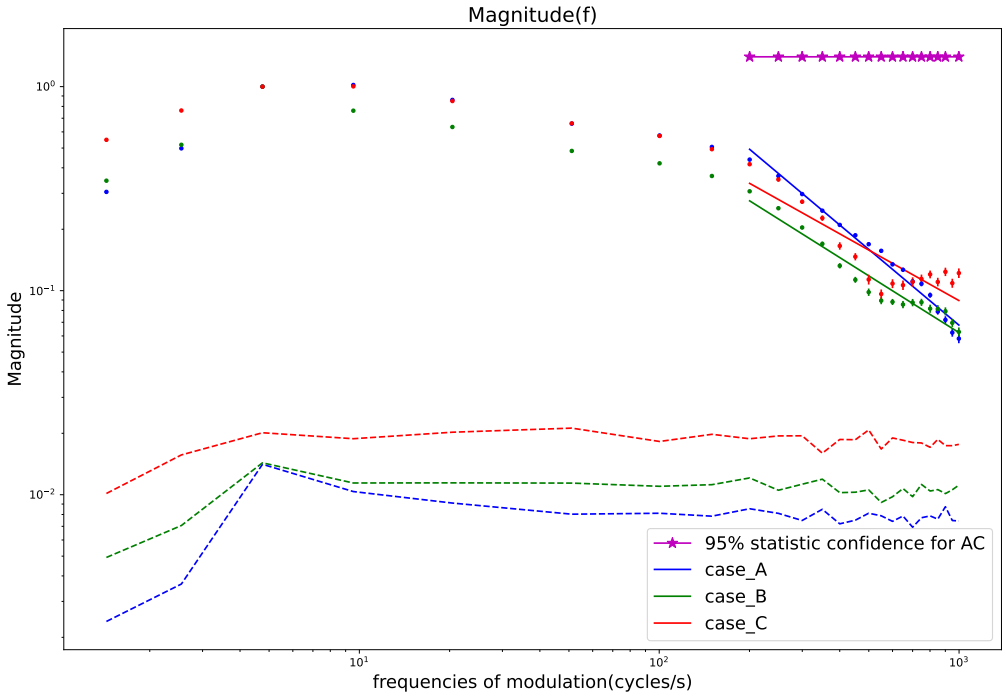

Figure 187: An example of a neuronal model, the L6_TPC_L1_cADpyr231_1, which shows the Richardson's effect at HF. The gain values are normalised over their maximum located around the $f_{mod} \sim$ 5Hz. The dashed lines stay for each cases as the minimal level of significance threshold. The magenta line and the stars indicate for each f_{mod} value that the cases A and C are not superimposable at the 95% of significance of the KS test. The solid lines of each color are the HF domain linear fit used to extrapolated the HF slope of the linear attenuation; the slopes values for each cases and neuronal models are in figure 70.

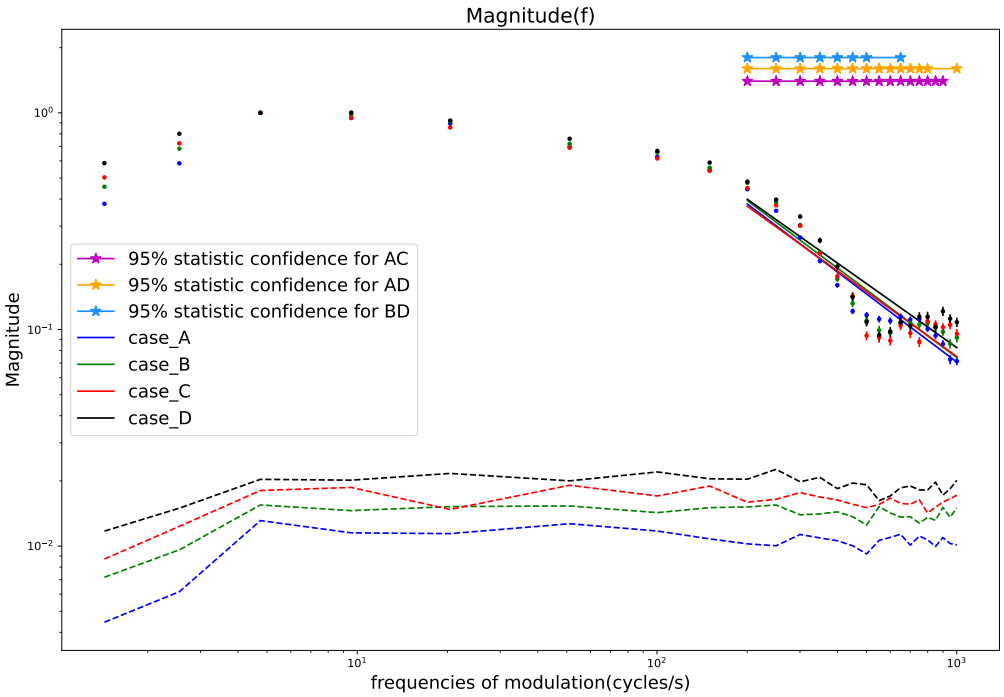

Figure 188: An example of a neuronal model, the L6_TPC_L1_cADpyr231_2, which does not show the Richardson's effect at HF, since the case B amplitude is bigger than all the others. The gain values are normalised over their maximum located around the $f_{mod} \sim$ 5Hz. The dashed lines stay for each cases as the minimal level of significance threshold. The magenta line and the stars indicate for each f_{mod} value that the cases A and C are not superimposable at the 95% of significance of the KS test. The solid lines of each color are the HF domain linear fit used to extrapolated the HF slope of the linear attenuation; the slopes values for each cases and neuronal models are in figure 70.

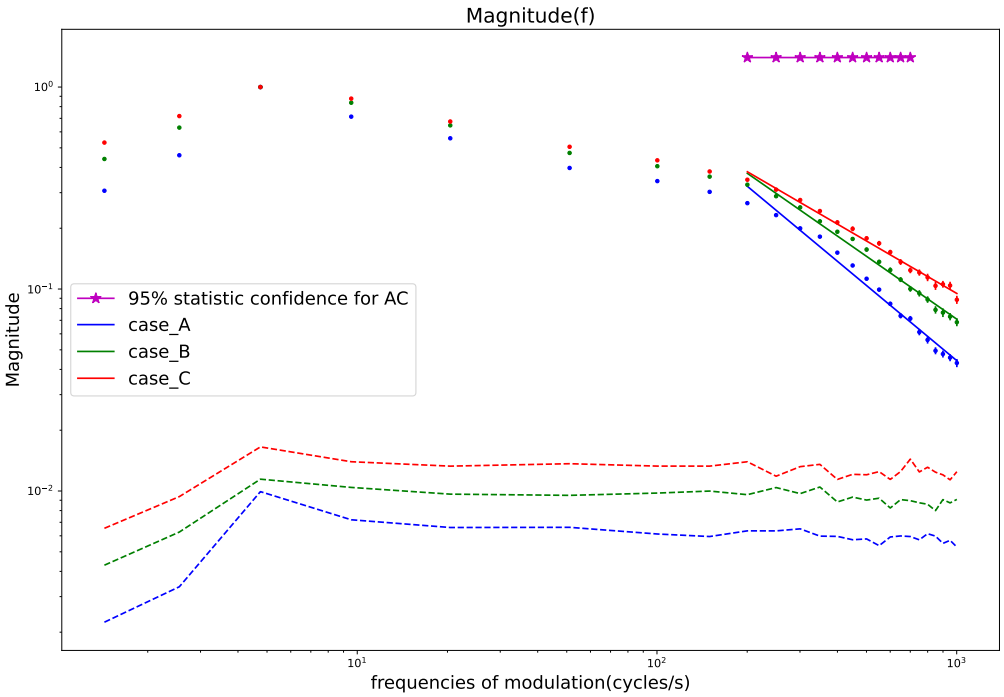

Figure 189: An example of a neuronal model, the L6_TPC_L1_cADpyr231_3, which does not show the Richardson's effect at HF, since the case A amplitude is bigger than all the others. The gain values are normalised over their maximum located around the $f_{mod} \sim$ 5Hz. The dashed lines stay for each cases as the minimal level of significance threshold. The magenta line and the stars indicate for each f_{mod} value that the cases A and C are not superimposable at the 95% of significance of the KS test. The solid lines of each color are the HF domain linear fit used to extrapolated the HF slope of the linear attenuation; the slopes values for each cases and neuronal models are in figure 70.

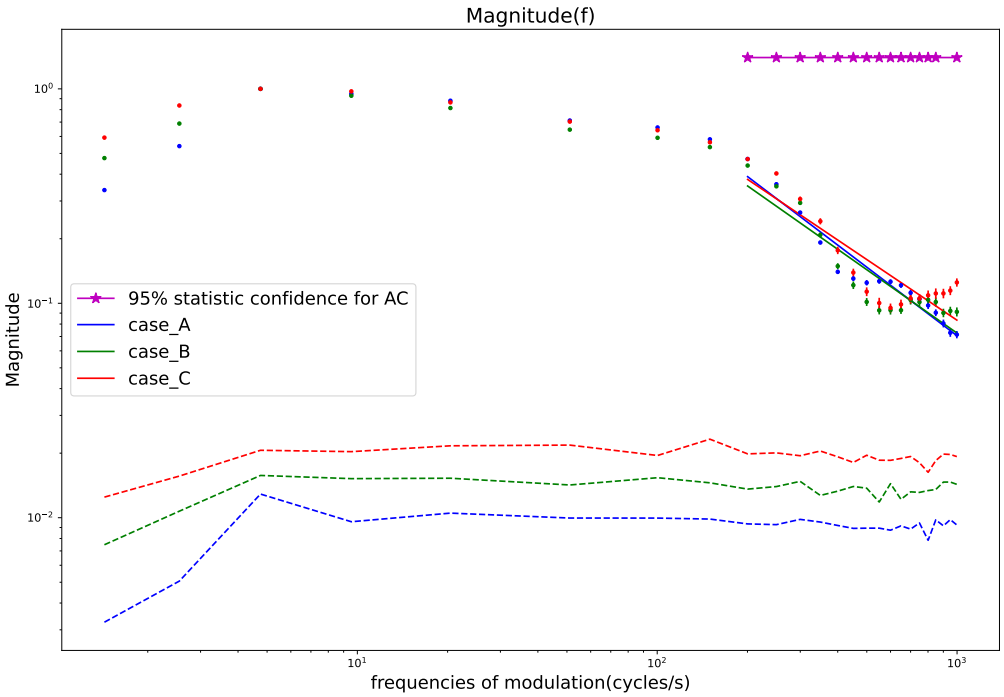

Figure 190: An example of a neuronal model, the L6_TPC_L1_cADpyr231_4, which does not show the Richardson's effect at HF, since the case A amplitude is bigger than all the others. The gain values are normalised over their maximum located around the $f_{mod} \sim 5$Hz. The dashed lines stay for each cases as the minimal level of significance threshold. The magenta line and the stars indicate for each f_{mod} value that the cases A and C are not superimposable at the 95% of significance of the KS test. The solid lines of each color are the HF domain linear fit used to extrapolated the HF slope of the linear attenuation; the slopes values for each cases and neuronal models are in figure 70.

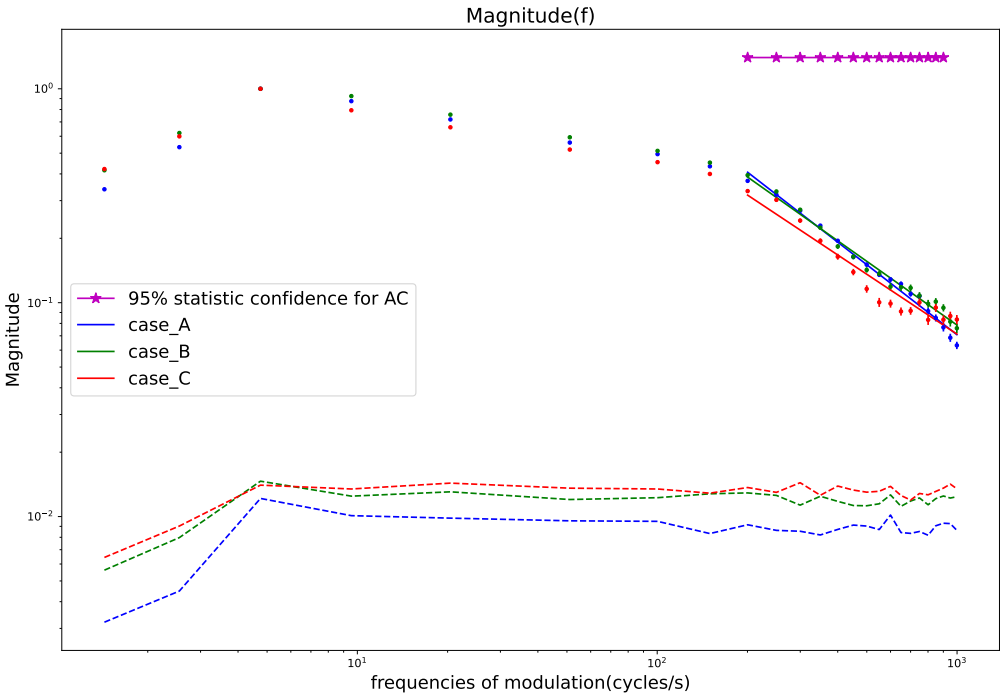

Figure 191: An example of a neuronal model, the L6_TPC_L1_cADpyr231_5, which does not show the Richardson's effect at HF, since the case A amplitude is bigger than all the others. The gain values are normalised over their maximum located around the $f_{mod} \sim$ 5Hz. The dashed lines stay for each cases as the minimal level of significance threshold. The magenta line and the stars indicate for each f_{mod} value that the cases A and C are not superimposable at the 95% of significance of the KS test. The solid lines of each color are the HF domain linear fit used to extrapolated the HF slope of the linear attenuation; the slopes values for each cases and neuronal models are in figure 70.

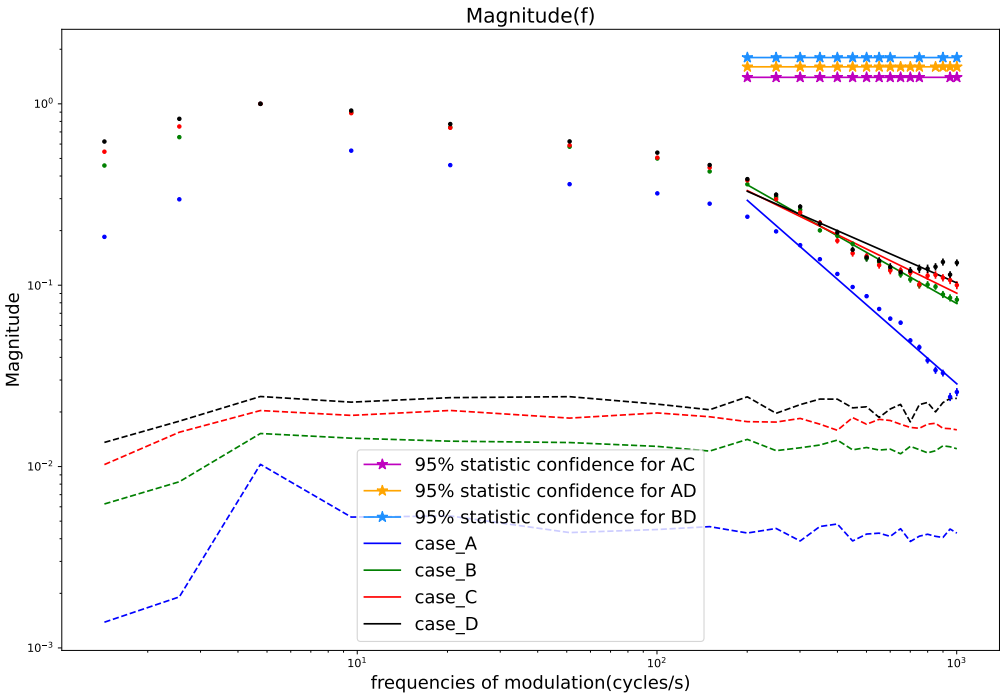

Figure 192: An example of a neuronal model, the L6_TPC_L4_cADpyr231_1, which does not show the Richardson's effect at HF, since the case B amplitude is bigger than all the others. The gain values are normalised over their maximum located around the $f_{mod} \sim$ 5Hz. The dashed lines stay for each cases as the minimal level of significance threshold. The magenta, yellow,blue lines and the stars indicate for each f_{mod} value that the cases A and C, A and D and B and D are not superimposable at the 95% of significance of the KS test. The solid lines of each color are the HF domain linear fit used to extrapolated the HF slope of the linear attenuation; the slopes values for each cases and neuronal models are in figure 70.

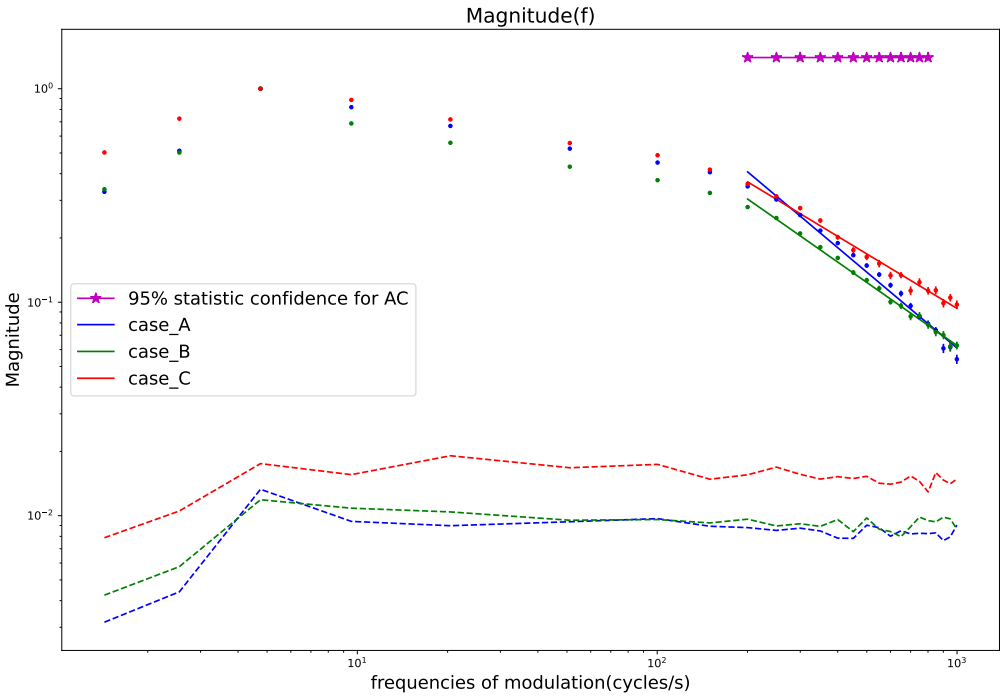

Figure 193: An example of a neuronal model, the L6_TPC_L4_cADpyr231_2, which does not show the Richardson's effect at HF, since the case B amplitude is bigger than all the others. The gain values are normalised over their maximum located around the $f_{mod} \sim$ 5Hz. The dashed lines stay for each cases as the minimal level of significance threshold. The magenta line and the stars indicate for each f_{mod} value that the cases A and C are not superimposable at the 95% of significance of the KS test. The solid lines of each color are the HF domain linear fit used to extrapolated the HF slope of the linear attenuation; the slopes values for each cases and neuronal models are in figure 70.

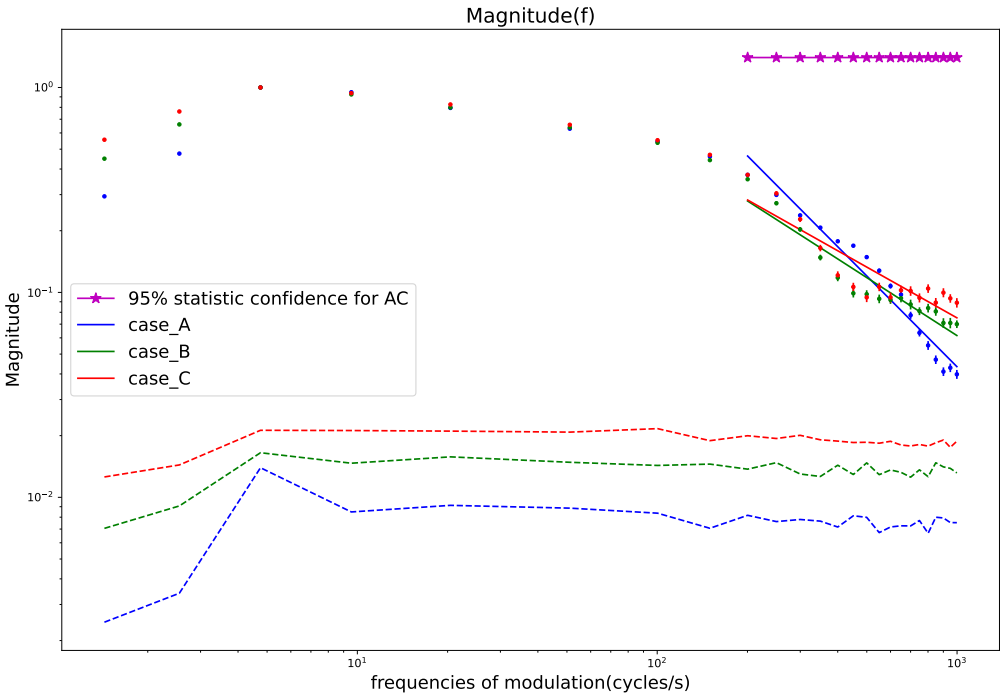

Figure 194: An example of a neuronal model, the L6_TPC_L4_cADpyr231_3, which does not show the Richardson's effect at HF, since the case A amplitude is bigger than all the others. The gain values are normalised over their maximum located around the $f_{mod} \sim$ 5Hz. The dashed lines stay for each cases as the minimal level of significance threshold. The magenta line and the stars indicate for each f_{mod} value that the cases A and C are not superimposable at the 95% of significance of the KS test. The solid lines of each color are the HF domain linear fit used to extrapolated the HF slope of the linear attenuation; the slopes values for each cases and neuronal models are in figure 70.

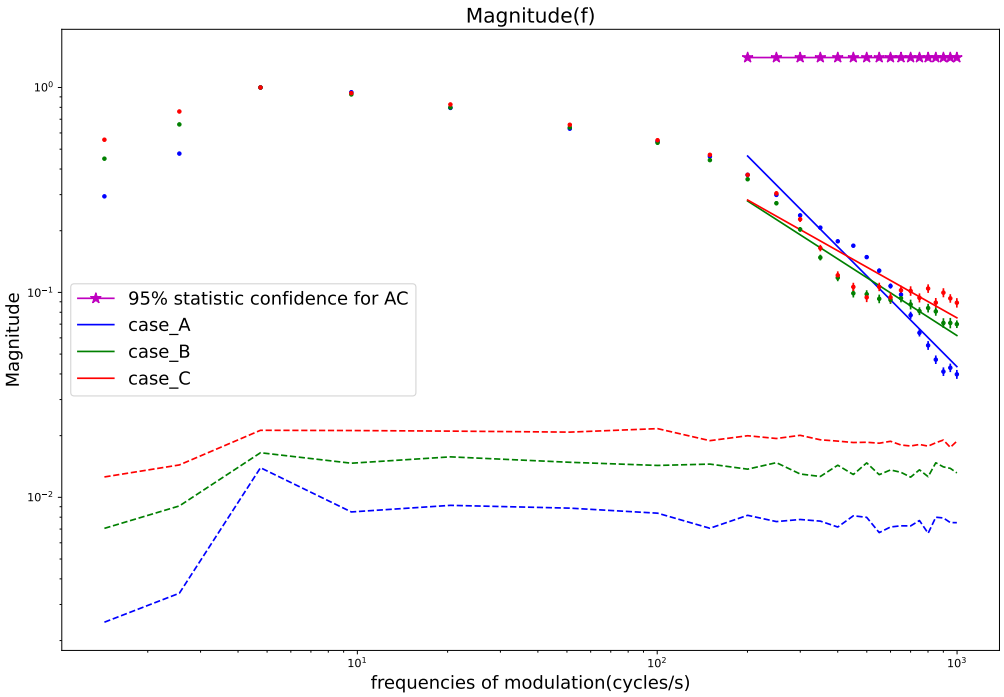

Figure 195: An example of a neuronal model, the L6_TPC_L4_cADpyr231_4, which does not show the Richardson's effect at HF, since the case A amplitude is bigger than all the others. The gain values are normalised over their maximum located around the $f_{mod} \sim$ 5Hz. The dashed lines stay for each cases as the minimal level of significance threshold. The magenta line and the stars indicate for each f_{mod} value that the cases A and C are not superimposable at the 95% of significance of the KS test. The solid lines of each color are the HF domain linear fit used to extrapolated the HF slope of the linear attenuation; the slopes values for each cases and neuronal models are in figure 70.

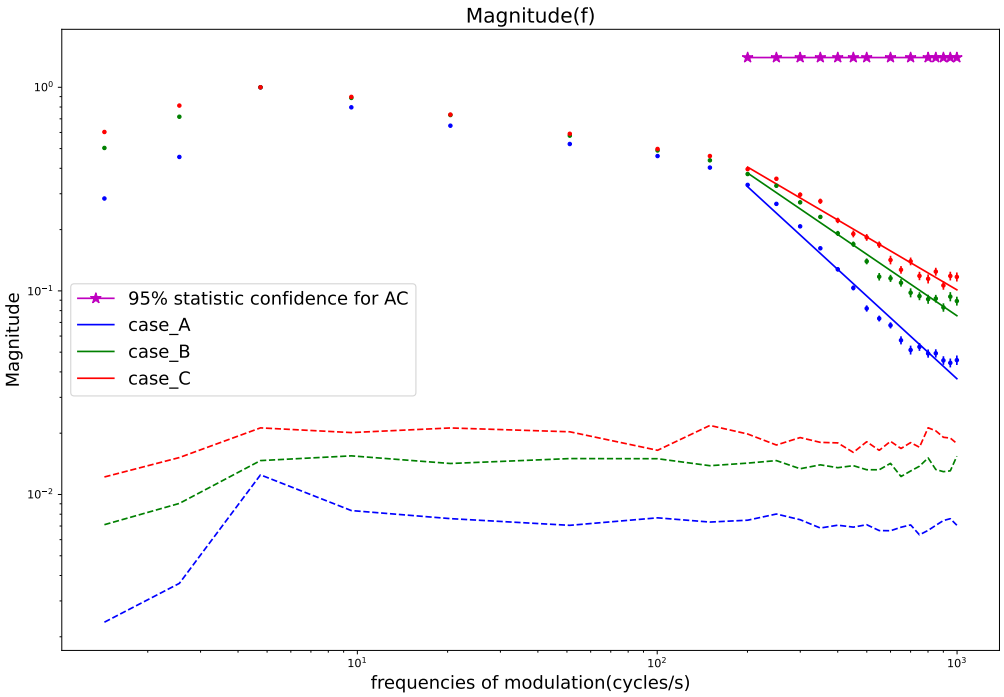

Figure 196: An example of a neuronal model, the L6_TPC_L4_cADpyr231_5, which does not show the Richardson's effect at HF, since the case A amplitude is bigger than all the others. The gain values are normalised over their maximum located around the $f_{mod} \sim$ 5Hz. The dashed lines stay for each cases as the minimal level of significance threshold. The magenta line and the stars indicate for each f_{mod} value that the cases A and C are not superimposable at the 95% of significance of the KS test. The solid lines of each color are the HF domain linear fit used to extrapolated the HF slope of the linear attenuation; the slopes values for each cases and neuronal models are in figure 70.

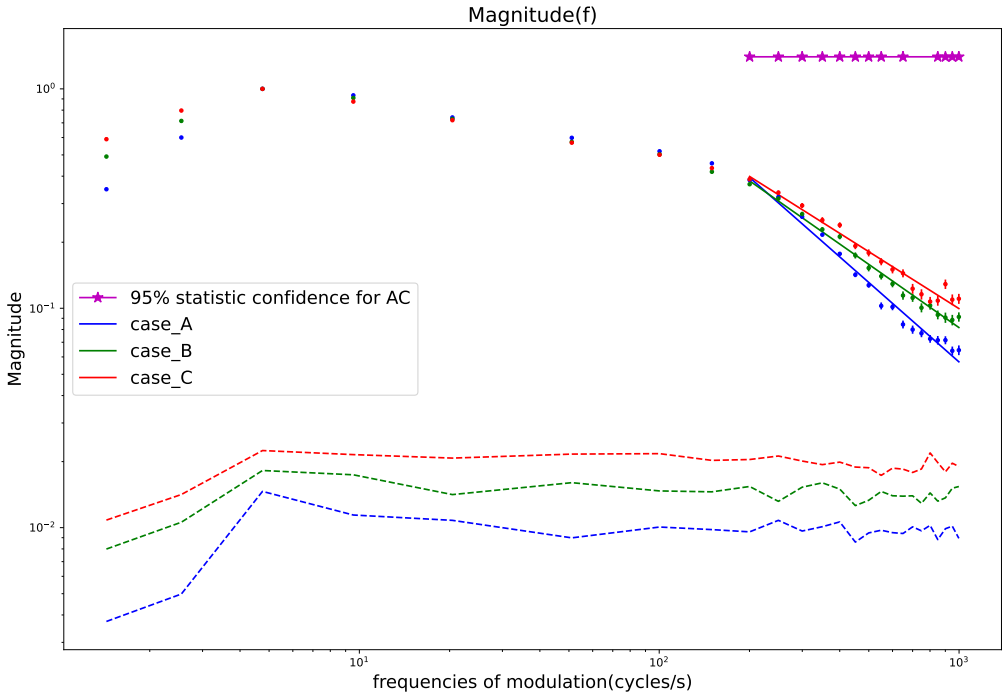

Figure 197: An example of a neuronal model, the L6_UTPC_cADpyr231_1, which shows the Richardson's effect at HF. The gain values are normalised over their maximum located around the $f_{mod} \sim$ 5Hz. The dashed lines stay for each cases as the minimal level of significance threshold. The magenta line and the stars indicate for each f_{mod} value that the cases A and C are not superimposable at the 95% of significance of the KS test. The solid lines of each color are the HF domain linear fit used to extrapolated the HF slope of the linear attenuation; the slopes values for each cases and neuronal models are in figure 70.

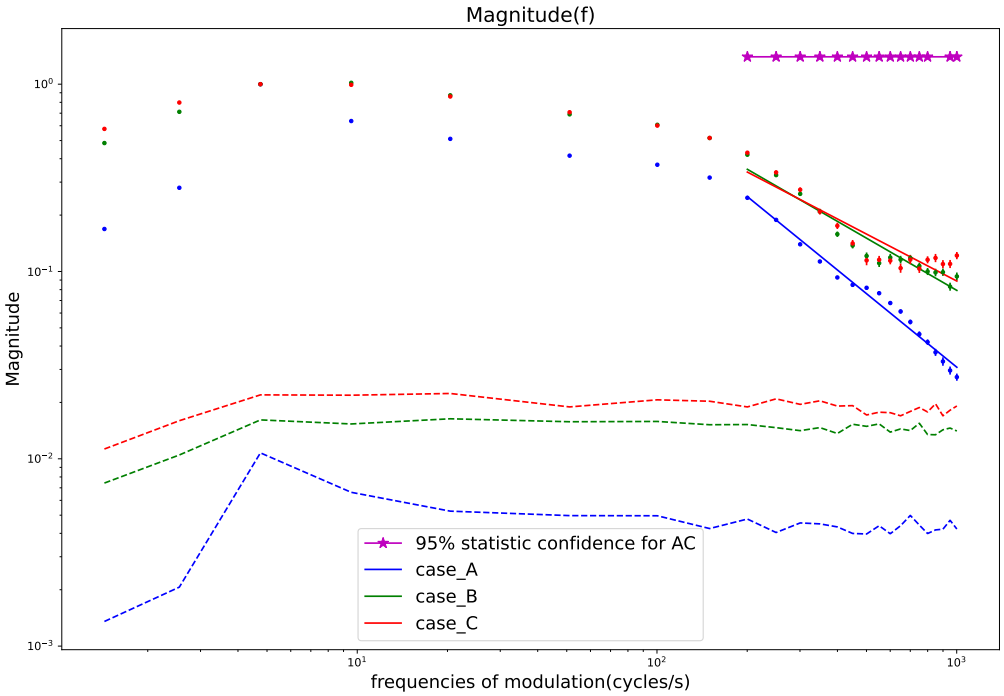

Figure 198: An example of a neuronal model, the L6_UTPC_cADpyr231_2, which shows a tiny presence of the Richardson's effect at HF. The gain values are normalised over their maximum located around the $f_{mod} \sim 5$Hz. The dashed lines stay for each cases as the minimal level of significance threshold. The magenta line and the stars indicate for each f_{mod} value that the cases A and C are not superimposable at the 95% of significance of the KS test. The solid lines of each color are the HF domain linear fit used to extrapolated the HF slope of the linear attenuation; the slopes values for each cases and neuronal models are in figure 70.

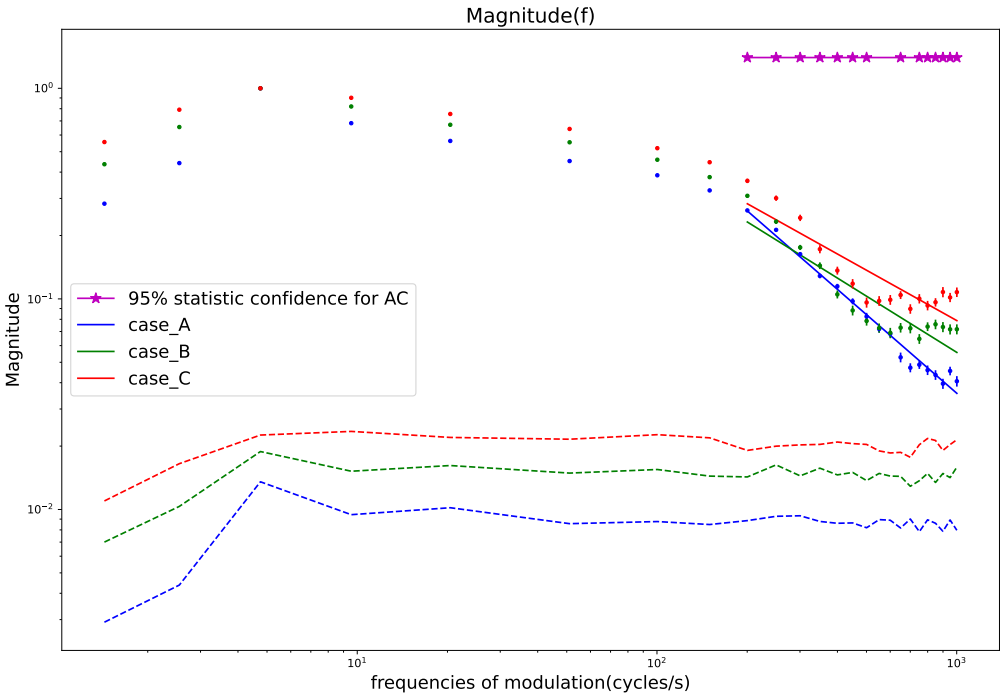

Figure 199: An example of a neuronal model, the L6_UTPC_cADpyr231_3, which does not show the Richardson's effect at HF, since the case A gain amplitude is bigger than the case B one. The gain values are normalised over their maximum located around the $f_{mod} \sim 5$Hz. The dashed lines stay for each cases as the minimal level of significance threshold. The magenta line and the stars indicate for each f_{mod} value that the cases A and C are not superimposable at the 95% of significance of the KS test. The solid lines of each color are the HF domain linear fit used to extrapolated the HF slope of the linear attenuation; the slopes values for each cases and neuronal models are in figure 70.

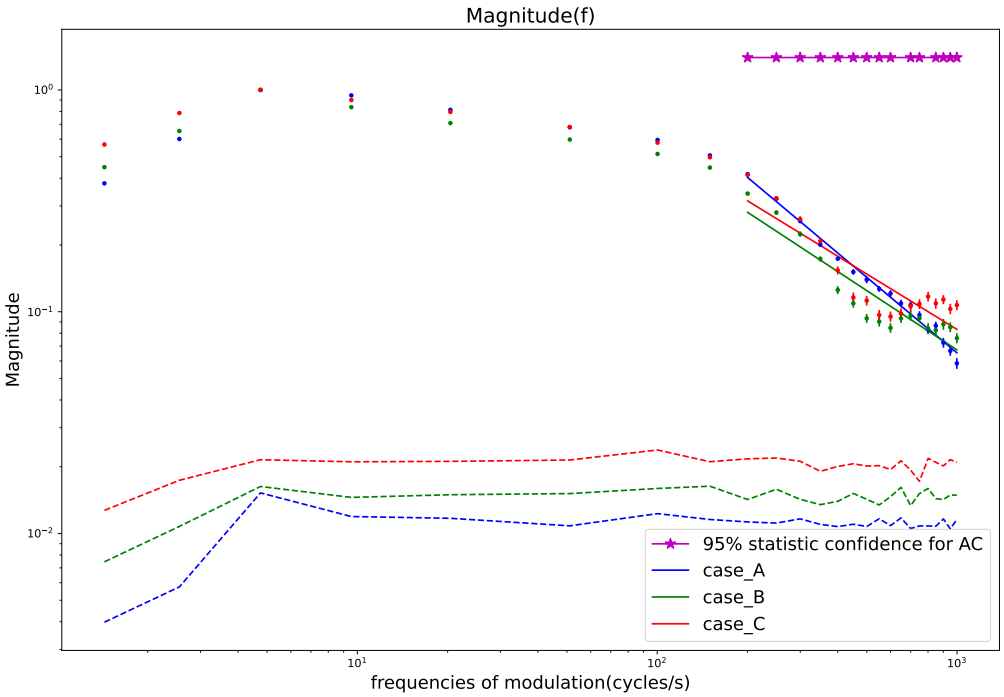

Figure 200: An example of a neuronal model, the L6_UTPC_cADpyr231_4, which does not show the Richardson's effect at HF, since the case A gain amplitude is bigger than the other ones. The gain values are normalised over their maximum located around the $f_{mod} \sim 5$Hz. The dashed lines stay for each cases as the minimal level of significance threshold. The magenta line and the stars indicate for each f_{mod} value that the cases A and C are not superimposable at the 95% of significance of the KS test. The solid lines of each color are the HF domain linear fit used to extrapolated the HF slope of the linear attenuation; the slopes values for each cases and neuronal models are in figure 70.

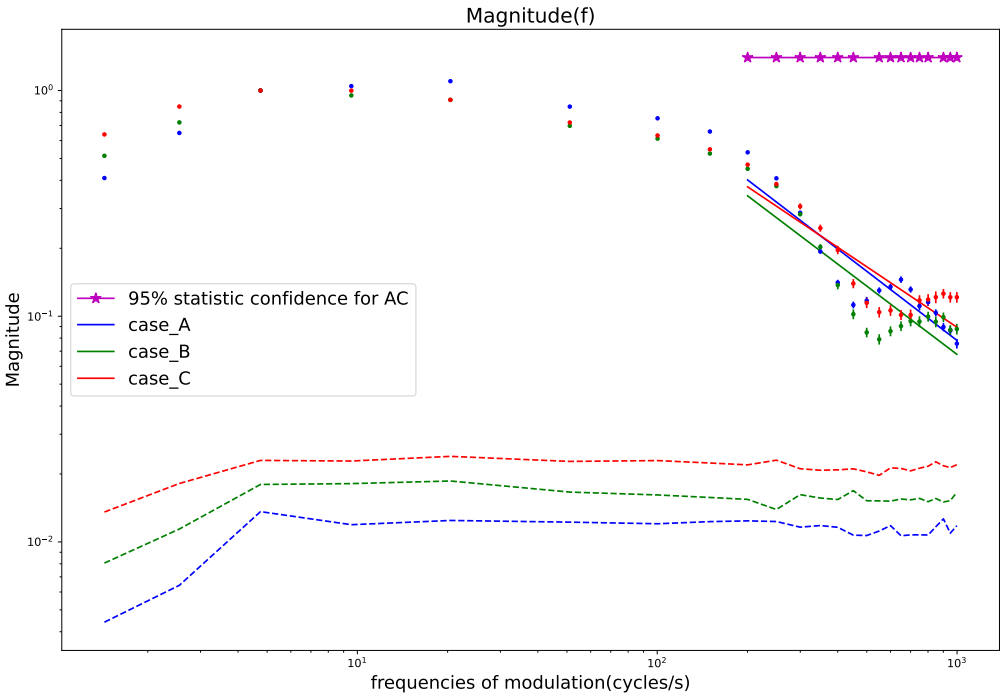

Figure 201: An example of a neuronal model, the L6_UTPC_cADpyr231_5, which does not show the Richardson's effect at HF, since the case A gain amplitude is bigger than the other ones. The gain values are normalised over their maximum located around the $f_{mod} \sim 5$Hz. The dashed lines stay for each cases as the minimal level of significance threshold. The magenta line and the stars indicate for each f_{mod} value that the cases A and C are not superimposable at the 95% of significance of the KS test. The solid lines of each color are the HF domain linear fit used to extrapolated the HF slope of the linear attenuation; the slopes values for each cases and neuronal models are in figure 70.

References

Abbott, L. F., Varela, J. A., Sen, K., and Nelson, S. B. (1997). Synaptic depression and cortical gain control. *Science*, 275(5297):221–224.

Arbib, M. A. (1998). *The Handbook of Brain Theory and Neural Networks (Bradford Book)*. The MIT Press.

Arsiero, M., Lüscher, H.-R., Lundstrom, B. N., and Giugliano, M. (2007). The impact of input fluctuations on the frequency–current relationships of layer 5 pyramidal neurons in the rat medial prefrontal cortex. *The Journal of Neuroscience*, 27(12):3274–3284.

Ascoli, G. A., Alonso-Nanclares, L., Anderson, S. A., Barrionuevo, G., Benavides-Piccione, R., Burkhalter, A., ki, G., Cauli, B., Defelipe, J., n, A., Feldmeyer, D., Fishell, G., Fregnac, Y., Freund, T. F., Gardner, D., Gardner, E. P., Goldberg, J. H., Helmstaedter, M., Hestrin, S., Karube, F., rday, Z. F., Lambolez, B., Lewis, D. A., Marin, O., Markram, H., oz, A., Packer, A., Petersen, C. C., Rockland, K. S., Rossier, J., Rudy, B., Somogyi, P., Staiger, J. F., Tamas, G., Thomson, A. M., Toledo-Rodriguez, M., Wang, Y., West, D. C., and Yuste, R. (2008). Petilla terminology: nomenclature of features of GABAergic interneurons of the cerebral cortex. *Nature Reviews Neuroscience*, 9(7):557–568.

Badel, L., Lefort, S., Berger, T. K., Petersen, C. C. H., Gerstner, W., and Richardson, M. J. E. (2008a). Extracting non-linear integrate-and-fire models from experimental data using dynamic i–v curves. *Biological Cybernetics*, 99(4-5):361–370.

Badel, L., Lefort, S., Brette, R., Petersen, C. C. H., Gerstner, W., and Richardson, M. J. E. (2008b). Dynamic i-v curves are reliable predictors of naturalistic pyramidal-neuron voltage traces. *Journal of Neurophysiology*, 99(2):656–666.

Bal, T. and Destexhe, A., editors (2009). *Dynamic-Clamp*. Springer US.

Baranyi, A., Szente, M. B., and Woody, C. D. (1993). Electrophysiological characterization of different types of neurons recorded in vivo in the motor cortex of the cat. II. membrane parameters, action potentials, current-induced voltage responses and electrotonic structures. *Journal of Neurophysiology*, 69(6):1865–1879.

Ben-Shalom, R., Ladd, A., Artherya, N. S., Cross, C., Kim, K. G., Sanghevi, H., Korngreen, A., Bouchard, K. E., and Bender, K. J. (2022). NeuroGPU: Accelerating multi-compartment, biophysically detailed neuron simulations on GPUs. *Journal of Neuroscience Methods*, 366:109400.

Bernander, O., Douglas, R. J., Martin, K. A., and Koch, C. (1991). Synaptic background activity influences spatiotemporal integration in single pyramidal cells. *Proceedings of the National Academy of Sciences*, 88(24):11569–11573.

Bessai, H. J. (2005). *MIMO Signals and Systems*. Springer US.

Biró, I. and Giugliano, M. (2015). A reconfigurable visual-programming library for real-time closed-loop cellular electrophysiology. *Frontiers in Neuroinformatics*, 9.

Boucsein, C., Tetzlaff, T., Meier, R., Aertsen, A., and Naundorf, B. (2009). Dynamical response properties of neocortical neuron ensembles: Multiplicative versus additive noise. *The Journal of Neuroscience*, 29(4):1006–1010.

Bower, J. M. and Woolston, D. C. (1983). Congruence of spatial organization of tactile projections to granule cell and purkinje cell layers of cerebellar hemispheres of the albino rat: vertical organization of cerebellar cortex. *Journal of Neurophysiology*, 49(3):745–766.

Brock, L. G., Coombs, J. S., and Eccles, J. C. (1952). The recording of potentials from motoneurones with an intracellular electrode. *The Journal of Physiology*, 117(4):431–460.

Brown, R. E., Basheer, R., McKenna, J. T., Strecker, R. E., and McCarley, R. W. (2012). Control of sleep and wakefulness. *Physiological Reviews*, 92(3):1087–1187.

Brunel, N., Chance, F. S., Fourcaud, N., and Abbott, L. F. (2001a). Effects of synaptic noise and filtering on the frequency response of spiking neurons. *Phys. Rev. Lett.*, 86:2186–2189.

Brunel, N., Chance, F. S., Fourcaud, N., and Abbott, L. F. (2001b). Effects of synaptic noise and filtering on the frequency response of spiking neurons. *Physical Review Letters*, 86(10):2186–2189.

Brunel, N. and Wang, X.-J. (2003). What determines the frequency of fast network oscillations with irregular neural discharges? i. synaptic dynamics and excitation-inhibition balance. *Journal of Neurophysiology*, 90(1):415–430.

Buzsáki, G. (2006). *Rhythms of the Brain*. Oxford University Press.

Cain, N., Iyer, R., Koch, C., and Mihalas, S. (2016). The computational properties of a simplified cortical column model. *PLOS Computational Biology*, 12(9):e1005045.

Camera, G. L., Giugliano, M., Senn, W., and Fusi, S. (2008). The response of cortical neurons to in vivo-like input current: theory and experiment. *Biological Cybernetics*, 99(4-5):279–301.

Carnevale, N. T. and Hines, M. L. (2006). *The NEURON Book*. Cambridge University Press.

Carslaw, H. S. (1986). *Conduction of heat in solids*. Clarendon Press.

Cheng, F.-Y., Xu, C., Gold, L., and Smith, S. (2021). Rapid enhancement of subcortical neural responses to sine-wave speech. *Frontiers in Neuroscience*, 15.

Cohen, S. and Hindmarsh (1994). Cvode. stiff/nonstiff ordinary differential eqn solver in c, direct and iterative metho. ″″.

Crank, J. (1980). *The Mathematics of Diffusion*. Oxford University Press, USA.

Cunningham, M. O., Whittington, M. A., Bibbig, A., Roopun, A., LeBeau, F. E. N., Vogt, A., Monyer, H., Buhl, E. H., and Traub, R. D. (2004). A role for fast rhythmic bursting neurons in cortical gamma oscillations in vitro. *Proceedings of the National Academy of Sciences*, 101(18):7152–7157.

Dasgupta, N. and Greenwald, A. G. (2001). On the malleability of automatic attitudes: Combating automatic prejudice with images of admired and disliked individuals. *Journal of Personality and Social Psychology*, 81(5):800–814.

Dean, P., Porrill, J., Ekerot, C.-F., and Jörntell, H. (2009). The cerebellar microcircuit as an adaptive filter: experimental and computational evidence. *Nature Reviews Neuroscience*, 11(1):30–43.

DeFelipe, J. (1993). Neocortical neuronal diversity: Chemical heterogeneity revealed by colocalization studies of classic neurotransmitters, neuropeptides, calcium-binding proteins, and cell surface molecules. *Cerebral Cortex*, 3(4):273–289.

DeFelipe, J. and Fariñas, I. (1992). The pyramidal neuron of the cerebral cortex: Morphological and chemical characteristics of the synaptic inputs. *Progress in Neurobiology*, 39(6):563–607.

Deniz, T. and Rotter, S. (2017). Joint statistics of strongly correlated neurons via dimensionality reduction. *Journal of Physics A: Mathematical and Theoretical*, 50(25):254002.

Destexhe, A. and Paré, D. (1999). Impact of network activity on the integrative properties of neocortical pyramidal neurons in vivo. *Journal of Neurophysiology*, 81(4):1531–1547.

Destexhe, A., Rudolph, M., Fellous, J.-M., and Sejnowski, T. (2001). Fluctuating synaptic conductances recreate in vivo-like activity in neocortical neurons. *Neuroscience*, 107(1):13–24.

Destexhe, A., Rudolph, M., and Paré, D. (2003). The high-conductance state of neocortical neurons in vivo. *Nature Reviews Neuroscience*, 4(9):739–751.

DeWeese, M. R. and Zador, A. M. (2006). Non-gaussian membrane potential dynamics imply sparse, synchronous activity in auditory cortex. *The Journal of Neuroscience*, 26(47):12206–12218.

Doiron, B., Longtin, A., Berman, N., and Maler, L. (2001). Subtractive and divisive inhibition: Effect of voltage-dependent inhibitory conductances and noise. *Neural Computation*, 13(1):227–248.

Eyal, G., Mansvelder, H. D., de Kock, C. P. J., and Segev, I. (2014). Dendrites impact the encoding capabilities of the axon. *Journal of Neuroscience*, 34(24):8063–8071.

Fick, A. (1855). Ueber diffusion. *Annalen der Physik und Chemie*, 170(1):59–86.

Fourcaud-Trocmé, N., Hansel, D., van Vreeswijk, C., and Brunel, N. (2003). How spike generation mechanisms determine the neuronal response to fluctuating inputs. *The Journal of Neuroscience*, 23(37):11628–11640.

Fourcaud-Trocmé, N. and Brunel, N. (2005). Dynamics of the instantaneous firing rate in response to changes in input statistics. *Journal of Computational Neuroscience*, 18(3):311–321.

Frick, A., Feldmeyer, D., Helmstaedter, M., and Sakmann, B. (2007). Monosynaptic connections between pairs of l5a pyramidal neurons in columns of juvenile rat somatosensory cortex. *Cerebral Cortex*, 18(2):397–406.

Fuhrmann, G., Markram, H., and Tsodyks, M. (2002). Spike frequency adaptation and neocortical rhythms. *Journal of Neurophysiology*.

Gentet, L. J., Stuart, G. J., and Clements, J. D. (2000). Direct measurement of specific membrane capacitance in neurons. *Biophysical Journal*, 79(1):314–320.

Gerstner, W. (2000). Population dynamics of spiking neurons: Fast transients, asynchronous states, and locking. *Neural Computation*, 12(1):43–89.

Gerstner, W., Kempter, R., van Hemmen, J. L., and Wagner, H. (1996). A neuronal learning rule for sub-millisecond temporal coding. *Nature*, 383(6595):76–78.

Gerstner, W., Sprekeler, H., and Deco, G. (2012). Theory and simulation in neuroscience. *Science*, 338(6103):60–65.

Gevertz, J. L., Aminzare, Z., Norton, K.-A., Pérez-Velázquez, J., Volkening, A., and Rejniak, K. A. (2015). Emergence of anti-cancer drug resistance: Exploring the importance of the microenvironmental niche via a spatial model. In *The IMA Volumes in Mathematics and its Applications*, pages 1–34. Springer New York.

Ghosh, A. and Shatz, C. J. (1993). A role for subplate neurons in the patterning of connections from thalamus to neocortex. *Development*, 117(3):1031–1047.

Gilman, S. and Arbor, A. (1983). Handbook of physiology. section 1: The nervous system, vol II. motor control, parts 1 and 2. section editors: John m. brookhart

and vernon b. mountcastle volume editor: Vernon b. brooks bethesda, MD, american physiological society, 1981 1480 pp, illustrated. *Annals of Neurology*, 13(1):111–111.

Giugliano, M., Camera, G. L., Fusi, S., and Senn, W. (2008). The response of cortical neurons to in vivo-like input current: theory and experiment: II. time-varying and spatially distributed inputs. *Biological Cybernetics*, 99(4-5):303–318.

Giugliano, M., Darbon, P., Arsiero, M., Lüscher, H.-R., and Streit, J. (2004). Single-neuron discharge properties and network activity in dissociated cultures of neocortex. *Journal of Neurophysiology*, 92(2):977–996.

Granit, R., Kernell, D., and Lamarre, Y. (1966). Algebraical summation in synaptic activation of motoneurones firing within the 'primary range' to injected currents. *The Journal of Physiology*, 187(2):379–399.

Granit, R., Kernell, D., and Shortess, G. K. (1963). Quantitative aspects of repetitive firing of mammalian motoneurones, caused by injected currents. *The Journal of Physiology*, 168(4):911–931.

Gupta, A., Wang, Y., and Markram, H. (2000). Organizing principles for a diversity of GABAergic interneurons and synapses in the neocortex. *Science*, 287(5451):273–278.

Hablitz, J. J. and Johnston, D. (1981). Endogenous nature of spontaneous bursting in hippocampal pyramidal neurons. *Cellular and Molecular Neurobiology*, 1(4):325–334.

Halliday, D. M. (2000). Weak, stochastic temporal correlation of large-scale synaptic input is a major determinant of neuronal bandwidth. *Neural Computation*, 12(3):693–707.

Harari, Y. N. (2015). *Sapiens: A Brief History of Humankind*. Dvir Publishing House Ltd. (Israel) Random House Harper.

Harris, K. D. and Shepherd, G. M. G. (2015). The neocortical circuit: themes and variations. *Nature Neuroscience*, 18(2):170–181.

Harrison, P. M., Badel, L., Wall, M. J., and Richardson, M. J. E. (2015). Experimentally verified parameter sets for modelling heterogeneous neocortical pyramidal-cell populations. *PLOS Computational Biology*, 11(8):e1004165.

Harvey, R. and Napper, R. (1991). Quantitatives studies on the mammalian cerebellum. *Progress in Neurobiology*, 36(6):437–463.

Hasenstaub, A., Shu, Y., Haider, B., Kraushaar, U., Duque, A., and McCormick, D. A. (2005). Inhibitory postsynaptic potentials carry synchronized frequency information in active cortical networks. *Neuron*, 47(3):423–435.

Helias, M., Deger, M., Rotter, S., and Diesmann, M. (2011). Finite post synaptic potentials cause a fast neuronal response. *Frontiers in Neuroscience*, 5.

Hevner, R. F., Shi, L., Justice, N., Hsueh, Y.-P., Sheng, M., Smiga, S., Bulfone, A., Goffinet, A. M., Campagnoni, A. T., and Rubenstein, J. L. (2001). Tbr1 regulates differentiation of the preplate and layer 6. *Neuron*, 29(2):353–366.

Hicks, R. D. (1907). *Aristotle: De anima; with translation, introduction and notes*. Cambridge: University Press.

Hines, M. (1984). Efficient computation of branched nerve equations. *International Journal of Bio-Medical Computing*, 15(1):69–76.

Hines, M. (1993). NEURON — a program for simulation of nerve equations. In *Neural Systems: Analysis and Modeling*, pages 127–136. Springer US.

Hines, M. (2009). NEURON and python. *Frontiers in Neuroinformatics*, 3.

Hines, M. L. and Carnevale, N. T. (1997). The NEURON simulation environment. *Neural Computation*, 9(6):1179–1209.

Hines, M. L. and Carnevale, N. T. (2000). Expanding NEURON's repertoire of mechanisms with NMODL. *Neural Computation*, 12(5):995–1007.

Hines, M. L. and Carnevale, N. T. (2001). Neuron: a tool for neuroscientists. *The Neuroscientist : a review journal bringing neurobiology, neurology and psychiatry*, 7:123–135.

Hodgkin, A. L. and Huxley, A. F. (1952). A quantitative description of membrane current and its application to conduction and excitation in nerve. *The Journal of Physiology*, 117(4):500–544.

Hohn, N. and Burkitt, A. N. (2001). Shot noise in the leaky integrate-and-fire neuron. *Physical Review E*, 63(3):031902.

Holmes, W. R. and Rall, W. (1992). Estimating the electrotonic structure of neurons with compartmental models. *Journal of Neurophysiology*, 68(4):1438–1452.

Huguenard, J. and McCormick, D. A. (1994). *Electrophysiologuy of the Neuron: An Interactive Tutorial*. Oxford University Press, Inc.

Häusser, M. and Roth, A. (1997). Estimating the time course of the excitatory synaptic conductance in neocortical pyramidal cells using a novel voltage jump method. *The Journal of Neuroscience*, 17(20):7606–7625.

Ilin, V., Malyshev, A., Wolf, F., and Volgushev, M. (2013). Fast computations in cortical ensembles require rapid initiation of action potentials. *Journal of Neuroscience*, 33(6):2281–2292.

Ito, M. (1984). *The cerebellum and neural control*. Raven Press.

Iyer, R., Menon, V., Buice, M., Koch, C., and Mihalas, S. (2013). The influence of synaptic weight distribution on neuronal population dynamics. *PLoS Computational Biology*, 9(10):e1003248.

Izhikevich, E. M. and Edelman, G. M. (2008). Large-scale model of mammalian thalamocortical systems. *Proceedings of the National Academy of Sciences*, 105(9):3593–3598.

Jack, J., Noble, D., and Tsien, R. (1975). Electric current flow in excitable cells. *Clarendon Press, Oxford*.

Johannesma, P. I. M. (1968). Diffusion models for the stochastic activity of neurons. In *Neural Networks*, pages 116–144. Springer Berlin Heidelberg.

Kasper, E. M., Larkman, A. U., Lübke, J., and Blakemore, C. (1994). Pyramidal neurons in layer 5 of the rat visual cortex. II. development of electrophysiological properties. *Journal of Comparative Neurology*, 339(4):475–494.

Kleppe, I. C. and Robinson, H. P. (1999). Determining the activation time course of synaptic AMPA receptors from openings of colocalized NMDA receptors. *Biophysical Journal*, 77(3):1418–1427.

Knight, B. (1972). Dynamics of encoding in a population of neurons. *J. Gen. Physiol*.

Knudsen, E. I. (1974). Behavioral thresholds to electric signals in high frequency electric fish. *Journal of Comparative Physiology*, 91(4):333–353.

Koch, C. and Segev, I. (1998). *Christof Koch and Idan Segev*. The MIT Press, 2 edition.

Köndgen, H., Geisler, C., Fusi, S., Wang, X.-J., Lüscher, H.-R., and Giugliano, M. (2008). The dynamical response properties of neocortical neurons to temporally modulated noisy inputs in vitro. *Cerebral Cortex*, 18(9):2086–2097.

Lamb, W. R. M. (1925). *Timaeus, in Plato in Twelve Volumes*. Harvard University Press.

Larkman, A. U. (1991). Dendritic morphology of pyramidal neurones of the visual cortex of the rat: I. branching patterns. *The Journal of Comparative Neurology*, 306(2):307–319.

Linaro, D., Biró, I., and Giugliano, M. (2017). Dynamical response properties of neocortical neurons to conductance-driven time-varying inputs. *European Journal of Neuroscience*, 47(1):17–32.

Linaro, D., Couto, J., and Giugliano, M. (2014). Command-line cellular electrophysiology for conventional and real-time closed-loop experiments. *Journal of Neuroscience Methods*, 230:5–19.

Lindner, B., Schimansky-Geier, L., and Longtin, A. (2002). Maximizing spike train coherence or incoherence in the leaky integrate-and-fire model. *Physical Review E*, 66(3):031916.

London, M. and Segev, I. (2001). Synaptic scaling in vitro and in vivo. *Nature Neuroscience*, 4(9):853–854.

Markram, H., Lübke, J., Frotscher, M., Roth, A., and Sakmann, B. (1997). Physiology and anatomy of synaptic connections between thick tufted pyramidal neurones in the developing rat neocortex. *The Journal of Physiology*, 500(2):409–440.

Markram, H., Muller, E., Ramaswamy, S., Reimann, M. W., Abdellah, M., Sanchez, C. A., Ailamaki, A., Alonso-Nanclares, L., Antille, N., Arsever, S., Kahou, G. A. A., Berger, T. K., Bilgili, A., Buncic, N., Chalimourda, A., Chindemi, G., Courcol, J.-D., Delalondre, F., Delattre, V., Druckmann, S., Dumusc, R., Dynes, J., Eilemann, S., Gal, E., Gevaert, M. E., Ghobril, J.-P., Gidon, A., Graham, J. W., Gupta, A., Haenel, V., Hay, E., Heinis, T., Hernando, J. B., Hines, M., Kanari, L.,

Keller, D., Kenyon, J., Khazen, G., Kim, Y., King, J. G., Kisvarday, Z., Kumbhar, P., Lasserre, S., Bé, J.-V. L., Magalhães, B. R., Merchán-Pérez, A., Meystre, J., Morrice, B. R., Muller, J., Muñoz-Céspedes, A., Muralidhar, S., Muthurasa, K., Nachbaur, D., Newton, T. H., Nolte, M., Ovcharenko, A., Palacios, J., Pastor, L., Perin, R., Ranjan, R., Riachi, I., Rodríguez, J.-R., Riquelme, J. L., Rössert, C., Sfyrakis, K., Shi, Y., Shillcock, J. C., Silberberg, G., Silva, R., Tauheed, F., Telefont, M., Toledo-Rodriguez, M., Tränkler, T., Geit, W. V., Díaz, J. V., Walker, R., Wang, Y., Zaninetta, S. M., DeFelipe, J., Hill, S. L., Segev, I., and Schürmann, F. (2015). Reconstruction and simulation of neocortical microcircuitry. *Cell*, 163(2):456–492.

Matsumura, M., Cope, T., and Fetz, E. (1988). Sustained excitatory synaptic input to motor cortex neurons in awake animals revealed by intracellular recording of membrane potentials. *Experimental Brain Research*, 70(3).

McCormick, D. A. (2004). Membrane properties and neurotransmitter actions. In *The Synaptic Organization of the Brain*, pages 39–78. Oxford University Press.

McCormick, D. A. and Bal, T. (1997). Sleep and arousal: thalamocortical mechanisms. *Annual Review of Neuroscience*, 20(1):185–215.

McCormick, D. A., Connors, B. W., Lighthall, J. W., and Prince, D. A. (1985). Comparative electrophysiology of pyramidal and sparsely spiny stellate neurons of the neocortex. *Journal of Neurophysiology*, 54(4):782–806.

McCormick, D. A. and Huguenard, J. R. (1992). A model of the electrophysiological properties of thalamocortical relay neurons. *Journal of Neurophysiology*, 68(4):1384–1400.

McCormick, D. A. and Prince, D. A. (1987). Post-natal development of electrophysiological properties of rat cerebral cortical pyramidal neurones. *The Journal of Physiology*, 393(1):743–762.

McCormick, D. A., Shu, Y., Hasenstaub, A., Sanchez-Vives, M., Badoual, M., and Bal, T. (2003). Persistent cortical activity: Mechanisms of generation and effects on neuronal excitability. *Cerebral Cortex*, 13(11):1219–1231.

Migliore, M., Cook, E. P., Jaffe, D. B., Turner, D. A., and Johnston, D. (1995). Computer simulations of morphologically reconstructed CA3 hippocampal neurons. *Journal of Neurophysiology*, 73(3):1157–1168.

Naundorf, B., Wolf, F., and Volgushev, M. (2006). Unique features of action potential initiation in cortical neurons. *Nature*, 440(7087):1060–1063.

Nowak, L. G., Azouz, R., Sanchez-Vives, M. V., Gray, C. M., and McCormick, D. A. (2003). Electrophysiological classes of cat primary visual cortical neurons in vivo as revealed by quantitative analyses. *Journal of Neurophysiology*, 89(3):1541–1566.

Palmer, L. M. and Stuart, G. J. (2006). Site of action potential initiation in layer 5 pyramidal neurons. *The Journal of Neuroscience*, 26(6):1854–1863.

Papyrus of Ani (1250 BC). *Book of the dead*.

Paré, D., Shink, E., Gaudreau, H., Destexhe, A., and Lang, E. J. (1998). Impact of spontaneous synaptic activity on the resting properties of cat neocortical pyramidal neurons in vivo. *Journal of Neurophysiology*, 79(3):1450–1460.

Perin, R., Berger, T. K., and Markram, H. (2011). A synaptic organizing principle for cortical neuronal groups. *Proceedings of the National Academy of Sciences*, 108(13):5419–5424.

Phillips, Charles L.and Parr, J. M. and Riskin, E. A. (2008). *Signals, Systems, and Transforms*. Pearson.

Qi, Y. and Gong, P. (2022). Fractional neural sampling as a theory of spatiotemporal probabilistic computations in neural circuits. *Nature Communications*, 13(1).

RaIl, W. (1964). Theoretical significance of dendritic trees for neuronal input-output relations (1964). In *4.2: Theoretical Significance of Dendritic Trees for Neuronal Input-Output Relations*. The MIT Press.

Rall, W. (1977). Core conductor theory and cable properties of neurons.

Rall, W., Burke, R. E., Smith, T. G., Nelson, P. G., and Frank, K. (1967). Dendritic location of synapses and possible mechanisms for the monosynaptic EPSP in motoneurons. *Journal of Neurophysiology*, 30(5):1169–1193.

Ramon y Cajal, R. (1909). *Histologie du système nerveux de l'homme des vertébrés*. Maloine.

Rapp, M., Segev, I., and Yarom, Y. (1994). Physiology, morphology and detailed passive models of guinea-pig cerebellar purkinje cells. *The Journal of Physiology*, 474(1):101–118.

Ravignani, A. and de Reus, K. (2019). Modelling animal interactive rhythms in communication. *Evolutionary Bioinformatics*, 15:117693431882355.

Regan, L. (1991). Voltage-dependent calcium currents in purkinje cells from rat cerebellar vermis. *The Journal of Neuroscience*, 11(7):2259–2269.

Reyes, A. and Sakmann, B. (1999). Developmental switch in the short-term modification of unitary EPSPs evoked in layer 2/3 and layer 5 pyramidal neurons of rat neocortex. *The Journal of Neuroscience*, 19(10):3827–3835.

Reyes-Puerta, V., Sun, J.-J., Kim, S., Kilb, W., and Luhmann, H. J. (2014). Laminar and columnar structure of sensory-evoked multineuronal spike sequences in adult rat barrel cortex in vivo. *Cerebral Cortex*, 25(8):2001–2021.

Ricciardi, L. M. (1977). Diffusion processes. In *Diffusion Processes and Related Topics in Biology*, pages 31–60. Springer Berlin Heidelberg.

Richardson, M. J. E. (2018). Spike shape and synaptic-amplitude distribution interact to set the high-frequency firing-rate response of neuronal populations. *Physical Review E*, 98(4):042405.

Richardson, M. J. E. and Swarbrick, R. (2010). Firing-rate response of a neuron receiving excitatory and inhibitory synaptic shot noise. *Physical Review Letters*, 105(17):178102.

Rudolph, M. and Destexhe, A. (2001). Do neocortical pyramidal neurons display stochastic resonance? *Journal of Computational Neuroscience*, 11(1):19–42.

Rudolph, M. and Destexhe, A. (2003a). A fast-conducting, stochastic integrative mode for neocortical neurons in vivo. *The Journal of Neuroscience*, 23(6):2466–2476.

Rudolph, M. and Destexhe, A. (2003b). Gain modulation and frequency locking under conductance noise. *Neurocomputing*, 52-54:907–912.

Rudolph, M. and Destexhe, A. (2004). Inferring network activity from synaptic noise. *Journal of Physiology-Paris*, 98(4-6):452–466.

Sah, P. and Faber, E. L. (2002). Channels underlying neuronal calcium-activated potassium currents. *Progress in Neurobiology*, 66(5):345–353.

Salinas, E. and Sejnowski, T. J. (2000). Impact of correlated synaptic input on output firing rate and variability in simple neuronal models. *The Journal of Neuroscience*, 20(16):6193–6209.

Sanchez-Vives, M. V. and McCormick, D. A. (2000). Cellular and network mechanisms of rhythmic recurrent activity in neocortex. *Nature Neuroscience*, 3(10):1027–1034.

Schutter, E. D. and Bower, J. M. (1994). An active membrane model of the cerebellar purkinje cell. i. simulation of current clamps in slice. *Journal of Neurophysiology*, 71(1):375–400.

Shadlen, M. N. and Newsome, W. T. (1998). The variable discharge of cortical neurons: Implications for connectivity, computation, and information coding. *The Journal of Neuroscience*, 18(10):3870–3896.

Silberberg, G., Wu, C., and Markram, H. (2004). Synaptic dynamics control the timing of neuronal excitation in the activated neocortical microcircuit. *The Journal of Physiology*, 556(1):19–27.

Solinas, S., Nieus, T., and D'Angelo, E. (2010). A realistic large-scale model of the cerebellum granular layer predicts circuit spatio-temporal filtering properties. *Frontiers in Cellular Neuroscience*.

Song, S., Sjöström, P. J., Reigl, M., Nelson, S., and Chklovskii, D. B. (2005). Highly nonrandom features of synaptic connectivity in local cortical circuits. *PLoS Biology*, 3(3):e68.

Stacey, W. C. and Durand, D. M. (2001). Synaptic noise improves detection of subthreshold signals in hippocampal CA1 neurons. *Journal of Neurophysiology*, 86(3):1104–1112.

Steriade, M. (2001). Impact of network activities on neuronal properties in corticothalamic systems. *Journal of Neurophysiology*, 86(1):1–39.

Sterratt, D., Graham, B., Gillies, A., and Willshaw, D. (2011). *Principles of Computational Modellingin Neuroscience*. Cambridge university press.

Sundararajan, D. (2008). *A Pratical Approach to Singnals and Systems*. Wiley.

Tannery, P. (1887). *Pour L'histoire de laScience Hellène Théophraste, sur les sensations*.

Tchumatchenko, T., Malyshev, A., Wolf, F., and Volgushev, M. (2011). Ultrafast population encoding by cortical neurons. *Journal of Neuroscience*, 31(34):12171–12179.

Testa-Silva, G., Verhoog, M. B., Linaro, D., de Kock, C. P. J., Baayen, J. C., Meredith, R. M., Zeeuw, C. I. D., Giugliano, M., and Mansvelder, H. D. (2014). High bandwidth synaptic communication and frequency tracking in human neocortex. *PLoS Biology*, 12(11):e1002007.

Tiesinga, P. H. E., José, J. V., and Sejnowski, T. J. (2000). Comparison of current-driven and conductance-driven neocortical model neurons with hodgkin-huxley voltage-gated channels. *Physical Review E*, 62(6):8413–8419.

Toledo-Rodriguez, M., Goodman, P., Illic, M., Wu, C., and Markram, H. (2005). Neuropeptide and calcium-binding protein gene expression profiles predict neuronal anatomical type in the juvenile rat. *The Journal of Physiology*, 567(2):401–413.

Traub, R. D., Wong, R. K., Miles, R., and Michelson, H. (1991). A model of a CA3 hippocampal pyramidal neuron incorporating voltage-clamp data on intrinsic conductances. *Journal of Neurophysiology*, 66(2):635–650.

Treves, A. (1993). Mean-field analysis of neuronal spike dynamics. *Network: Computation in Neural Systems*, 4(3):259–284.

Tuckwell, H. C. (1988). *Introduction to theoretical neurobiology: linear cable theory and dendritic structure*, volume 1. Cambridge University Press.

Uhlenbeck, G. E. and Ornstein, L. S. (1930). On the theory of the brownian motion. *Physical Review*, 36(5):823–841.

van Leeuwenhoek (1719). *Epistolae Physiologicae Super Compluribus NaturaeArcanis*. Adrianum Beman.

Vesalius, A. and van Calcar, J. S. (1543). *Andreae Vesalii Brvxellensis, Scholae medicorum Patauinae professoris, De humani corporis fabrica libri septem*. Ex officina Ioannis Oporini.

Waldeyer, W. (1891). Ueber einige neuere forschungen im gebiete der anatomie des central nerven systems. *DMW - Deutsche Medizinische Wochenschrift*, 17(44):1213–1218.

Wang, X.-J. and Buzsáki, G. (1996). Gamma oscillation by synaptic inhibition in a hippocampal interneuronal network model. *The Journal of Neuroscience*, 16(20):6402–6413.

Wang, Y. (2002). Anatomical, physiological, molecular and circuit properties of nest basket cells in the developing somatosensory cortex. *Cerebral Cortex*, 12(4):395–410.

Wang, Y., Toledo-Rodriguez, M., Gupta, A., Wu, C., Silberberg, G., Luo, J., and Markram, H. (2004). Anatomical, physiological and molecular properties of martinotti cells in the somatosensory cortex of the juvenile rat. *The Journal of Physiology*, 561(1):65–90.

Wiesenfeld, K. and Moss, F. (1995). Stochastic resonance and the benefits of noise: from ice ages to crayfish and SQUIDs. *Nature*, 373(6509):33–36.

Williams, S. R. and Stuart, G. J. (2003). Role of dendritic synapse location in the control of action potential output. *Trends in Neurosciences*, 26(3):147–154.

Wilson, N. R., Runyan, C. A., Wang, F. L., and Sur, M. (2012). Division and subtraction by distinct cortical inhibitory networks in vivo. *Nature*, 488(7411):343–348.

Wolff, L. and Lindner, B. (2008). Method to calculate the moments of the membrane voltage in a model neuron driven by multiplicative filtered shot noise. *Physical Review E*, 77(4):041913.

Wong, R. K. and Prince, D. A. (1981). Afterpotential generation in hippocampal pyramidal cells. *Journal of Neurophysiology*, 45(1):86–97.

Woody, C. and Gruen, E. (1978). Characterization of electrophysiological properties of intracellularly recorded neurons in the neocortex of awake cats: A comparison of the response to injected current in spike overshoot and undershoot neurons. *Brain Research*, 158(2):343–357.